Non Markovian behavior and spectral density measurement in optical quantum networks

Paul Renault

To cite this version:

Paul Renault. Non Markovian behavior and spectral density measurement in optical quantum networks. Optics [physics.optics]. Sorbonne Université, 2022. English. NNT : 2022SORUS246 . tel-03828914

HAL Id: tel-03828914
https://theses.hal.science/tel-03828914v1

Submitted on 25 Oct 2022

Thèse de Doctorat de
Sorbonne Université

présentée par

Paul Renault

le 25 avril 2022

pour obtenir le grade de Docteur de Sorbonne Université
sur le sujet:

NON MARKOVIAN BEHAVIOUR AND SPECTRAL DENSITY MEASUREMENT IN OPTICAL QUANTUM NETWORKS

Laboratoire Kastler Brossel
Physique quantique et applications

Membres du jury :

Pr. Susana HUELGA	Rapporteur
Dr. Jonathan MATTHEWS	Rapporteur
Pr. Nicolas JOLY	Membre du jury
Dr. Alex CHIN	Membre du jury
Dr. Valentina PARIGI	Membre invité
Pr. Nicolas TREPS	Directeur de thèse

" (...) Et là, normalement, il me faut une citation latine, mais pfff... j'en ai marre !"
Roi Loth d'Arcanie
Kaamelott, Livre V, tome 1

Remerciements

Je profite de ces premières lignes pour remercier les différentes personnes qui, au cours de ces 3 années et demi, m'auront soutenu, de près ou de loin, dans cette entreprise qu'est la thèse.
Tout d'abord, je souhaite remercier Nicolas Joly, Jonathan Matthews, Alex Chin et Susana Huelga d'avoir accepté puis rempli pleinement leur rôle de jury. Merci d'avoir fait une place dans vos emplois du temps chargés pour la relecture de ce manuscrit ainsi que pour vos remarques constructives, que ce soient lors de la soutenance ou à travers vos rapports.
Ensuite, je remercie chaleureusement les deux personnes qui m'ont encadré tout au long de cette thèse, Nicolas Treps et Valentina Parigi. Je m'estime très heureux pour ne pas dire chanceux d'avoir travaillé à vos côtés et ainsi avoir bénéficié de votre expérience, de votre rigueur, de votre pédagogie. Merci aussi aux deux autres permanents de l'équipe, Claude et Mattia qui ont toujours su se rendre disponibles pour mes questions d'expérimentateur.
Toutefois, un groupe de recherche ne se résume pas seulement aux membres permanents. J'ai été accueilli il y a 4 ans par une équipe chaleureuse et enthousiaste de doctorants et de postdocs : Francesco, Sayam, Luca, Tiphaine, Pauline sans oublier bien sûr la team SPOPO : Young-Sik, Adrien et Thibault. Mention spéciale à Thibault et Adrien pour m'avoir formé à l'art du clic-clac et de m'avoir légué tous les secrets que renfermait cette manip. J'aimerais aussi citer les personnes qui ont rejoint l'équipe au cours de l'aventure : Alex et ses tics si particuliers ; Ganael lobbyiste de la cantine à ses heures perdues, merci pour tout le temps passé à reprogrammer les codes Labview en python ; David. B qui je l'espère apprendra le français un jour ; sans oublier Clémentine, Manuel, David. F, Giacomo, Guillerme, Victor, Ilya ainsi que les tous nouveaux doctorants Niels et Johan qui je suis sûr seront aussi performants sur leur table optique qu'aux échecs. Enfin, parmi les personnes de l'équipe, je ne peux oublier de mentionner Matthieu qui a été d'abord camarade en master puis collègue au sein de l'équipe optique quantique multimode. On a ainsi traversé, si l'on peut dire, les épreuves de la thèse en parallèle que ce soient les galères, les doutes mais aussi les joies comme la découverte de la magnifique ville de Paderborn. Enfin, je me dois d'ajouter quelques mots pour Francesca. Il est évident que, sans toi, ma thèse aurait été plus monotone. Bien que ton caractère

ait eu tendance à tout renverser sur son passage, je ne peux que te remercier pour ta bonne humeur et ton dynamisme.

Je tiens aussi à remercier le personnel administratif du laboratoire ainsi que le personnel technique que ce soient les membres de l'atelier de mécanique mais aussi ceux de l'atelier d'électronique qui sont toujours à notre écoute et sans qui nos tables optiques seraient bien vides.

Enfin, tout doctorant vous le dira, une thése implique un fort engagement personnel qui nécessite parfois de savoir décompresser. Ainsi, ces années de dur labeur auront été moins savoureuses sans la présence de mes amis. Je ne peux citer tout le monde mais j'ai une pensée particulière pour certains d'entre eux qui se sont aussi retrouvés empêtrés dans les joies de la thèse : Alex Gourm, Guillaume Noat, Jean Charles, Cyril dit Saint Suaire, Romain Mons. Merci aussi à Alex. M et à ceux qui se sont détourner de la science au profit du Berry et de ses abeilles : Quille et Clément MdC. Enfin, je pense que je n'aurais écrit aucune de ces lignes sans le soutien inconditionnel de ma famille. Merci à mon frère Gabriel, à ma soeur Anaëlle et à mes parents de m'avoir poussé à persévérer dans mes études peu importe la finalité.

Abstract

Entanglement among multiple modes is a necessary resource in the field of quantum information technology. In this context, frequency comb sources of femtosecond pulsed light represent a useful resource, with approximately 10^5 individual frequency modes across the pulse bandwidth and it has been recently shown that a synchronously pumped optical parametric oscillator (SPOPO) can generate highly multimode nonclassical states of light. A high degree of control over the mode structure of the output can thus be achieved by shaping the spectral mode of the pump beam using a pulse shaper. The SPOPO setup is also a promising platform for the simulation of quantum optical networks. Energy exchanges have been characterized for several models of networks via the measurement of the spectral density function and the observation of quantum non-Markovian behavior.

Contents

Introduction

Optics is a wonderful tool to perform measurements and interact with the outside world. It has never stop evolving throughout history, which enabled many technological and scientific advances. First, engineering optical elements is a way to observe objects at long distances that are not accessible to human eye. In the Middle Ages, the development of telescopes and geometrical optics enabled the discoveries by Kepler and Galileo about planets paths and confirmed Copernic hypothesis, which had an important impact on society and ways of thinking at that time. Beside, optical instruments can also be used to measure objects of small size. Because of the short wavelengths in the visible regime, among the wave easily produceable, light offers better resolution than sound for example and is often used for imagery techniques on biological tissue or through complex medium[Anderson 58, Segev 13, John 84, Horstmeyer 15, Popoff 10]. In addition, the interference phenomenon, consequence of the wave model adoption [Maxwell 65, Maxwell 96], can push the resolution further for an optical detection setup. Indeed, at the end of XIX$^{\text{th}}$ century, A. A. Michelson and E. Morley build an interferometer and showed it was possible to measure small displacements [Michelson , Michelson 94].

The XX$^{\text{th}}$ century was also subject to high advances in physics and especially in optics. At the beginning of the century, a new field appeared, quantum physics, proposing a description of object at very low scale [de Broglie 24, Born 23, Heisenberg 25, Dirac 25]. The emergence of this field has been a source of debate because of some of its consequences, which may seem counterintuitive. We can quote the superposition property, the Heisenberg principle. Another property, entanglement, was firstly introduced as a paradox by A. Einstein B. Podolsky and N. Rosen to raise the question of the completeness of quantum theory [Einstein 35a]. J. S. Bell brought a new outlook to the problem showing that quantum physics is incompatible with hidden variable theories and introducing the inequality called by his name [Einstein 35b]. The violation of this inequality was experimentally observed few years later [Aspect 82]. In spite of these curious properties, quantum physics was still at the origin of some advances in industry, like for the laser [Maiman 60] or the transistor [Bardeen 57].

Nowadays, and for several years now, we saw a growth of the publications number related to quantum physics. This is partly the result of a remark made by Richard Feynman : "The nature is not classical". By this sentence, the author means that if you want to study phenomena involving object of small size, because of their quantum properties, the best way to simulate them would be to use a quantum platform [Feynman 86, Feynman 96]. From this observation, scientist started dreaming and working about a quantum computer, which we can define as a calculator working from quantum properties. Although, it firstly remained just an idea, after the exhibition of potential applications especially for cryptographic problems [Shor 94], more and more scientists have taken an interest in its design [Politi 09, Martin-Lopez 12, Knill 10]. The purpose of such a machine would be to perform calculations faster but also to tackle problems unsolvable for a classical computer.
Today, several ways to build a quantum computer are investigated with their own advantages and drawbacks: superconducting circuits [Devoret 13, You 05], trapped ions [Paul 90, Church 69, Leibfried 03, Blatt 12], NV centers [.Childress 13], photonics [P.Kok 07, O'Brien 07], cold atoms [Bloch 12]. Beside, if most of the work in this field is dedicated to produce and improve qubit (quantum bit) in discrete variable, some of them study quantum computing using continuous variable[Furusawa 98, Braunstein 05, Weedbrook 12, Raussendorf 01a, Raussendorf 01b, Menicucci 06].

Continuous variable optical qubits are based on non classical states of light called squeezed states[Ma 90, Walls 83, Lvovsky 09]. They are named that way because they exhibit noise below the standard quantum noise limit in one quadrature component. We can produce them in an optic laboratory using Optical Parametric Amplification (OPA)[Wu 87]. This is a source for squeezing or entanglement or both as depends on the measurement basis. Hence, for a large number of optical modes we can produce entanglement on a large ensemble of states using an ensemble of beam splitters. We call these states cluster states[Yokoyama 13, Chen 14, Cai 17]. The team, whose I was member all along my PhD, studied squeezed and cluster states for many years now: how we can produce them, their applications in term of metrology and quantum computing and how can we produce non Gaussian states, *i.e* continuous variable quantum states with non Gaussian distribution. They are key elements to get quantum advantage over classical computing [Mari 12, Bartlett 02]. Today, a part of the research on continuous variable quantum information is turning to the production of these exotic states [Ourjoumtsev 07, Ourjoumtsev 06, Ra 20, Walschaers 21a, Bourassa 21, Gottesman 01].

In this work, we restrict ourself to the gaussian states case. Although, this resource is not sufficient to overcome a classical computer, the aim is to try to compute simulations with a system over which we have a large control. The cluster states that we want to produce are based on optical frequency modes from a femtosecond laser. This kind of sources have the advantage to contain a high number of teeth in their frequency comb (around 10^5 modes), which ensures the ability to build large cluster states.

For the last three years and a half, I have been working on the experiment called SPOPO (Synchronously Pumped Optical Parametric Oscillator) whose central piece is an OPO cavity resonant for frequency combs and driven by blue pulse light [Roslund 14, Patera 09]. The purpose of this cavity is to produce a superposition of squeezed vacuum states among the optical modes of a frequency comb. I first took part to a project of optimizing the pump spectral shape using machine learning algorithms in order to obtain different forms of multimode squeezed states at the output of the SPOPO cavity. Then I worked on the implementation of a photonics crystal fiber that widens the optical spectrum of the frequency comb in order to increase the number of accessible frequency modes.
Then, the second and my main project was dedicated to the simulation of the evolution of open quantum system coupled to an environment modeled by an ensemble of harmonic oscillators. We performed measurement following the theoretical works made by J. Nokkala [Nokkala 18b, Nokkala 18a]. The purpose of this work is to take benefit of the large number and variety of cluster states available and characterize the energy exchanges between these two subsystems. If the presence of an environment was before synonym of losses, it has been recently shown that an environment suitably tailored could actually protect the system against losses or decoherence [Verstraete 09, Barreiro 02, Biercuk 09]. The first quantity that we look is the spectral density for a coupling environment as a function of the frequency of the system of interest. Finally the second point is to observe and quantify quantum non Markovianity between the open system and its environment which reflects a back flow of information.

0.1 Thesis Outlines

This thesis aims to highlight the evolution of the research works that occupied me throughout my PhD. It is organized in three parts as follows:

Part 1:
This part is composed by one chapter. The goal here is to introduce the different concepts and notations for a better understanding of the two next parts. The chapter discusses classical optics and more specifically the optical pulses and the physics of cavity. We also introduce the basics of quantum optics.

Part 2:
The purpose of this part is to present the whole SPOPO experiment. It is divided in three chapters. The first one shows the SPOPO cavity itself and the beam preparation

to obtain the desired states. Then, the second chapter discusses the detection part and its multimode aspect. Finally the third one shows squeezing measurements on characterization of the SPOPO output when the pump is optimized or not.

Part 3:
The last part is divided in two chapters dedicated to the simulation of harmonic oscillators networks and the characterization of the energy exchanges inside. The first chapter introduces the model used in this part and shows measurements of spectral density for different environments coupled to the open quantum system. Finally in the last chapter of this thesis, we highlight quantum non Markovianity behaviours for some of the networks that we simulate.

Part I

THEORETICAL BACKGROUND

Chapter 1

A toolbox for classical and quantum optics

Contents

Before presenting details about the experiment I had been working on during my PhD and its results, we have to introduce physical concepts and their notation for a better understanding of this manuscript. This is the object of this chapter. First, we start with tools from classical optics which are frequently used even for a quantum optics experiment and then, in a second part, we present notions of quantum optics: what are operators and Hamiltonians in quantum optics? How do we represent a state in this context?

This chapter aims to put definitions on words in order to get a better appreciation about what do we mean by “multimode quantum optics”.

1.1 A classical definition of the light

1.1.1 What is a mode?

The first term we introduce here is "multimode". Indeed what do we mean by multimode optics? And what is a mode exactly? To answer to these questions, let's take a function $\boldsymbol{g}(\mathbf{r}, t)$ where $\mathbf{r}$ and t are respectively the position vector in a Cartesian referential and the time. The function $\boldsymbol{g}$ is an optical mode if it is solution of the wave propagation equation [Fabre 20][Grynberg 10]:

$$\Delta \mathbf{g}(\mathbf{r}, t) - \frac{n^2}{c^2}\frac{\partial^2 \mathbf{g}(\mathbf{r}, t)}{\partial t^2} = 0 \tag{1.1}$$

Here, c is the speed of light in vacuum, n is the index of the propagation medium and Δ stands for Laplacian operator in Cartesian coordinate system. This equation is derived from Maxwell's equations [Maxwell 65] where the charge density and the current density are zero. The electric field $\boldsymbol{E}$ is solution of (1.1). Before writing the electric field, let us first set out the assumptions that will define a framework for this manuscript:

- we restrict ourself to the single mode and narowband solutions where ω_0 is the wave frequency.
- we assume $\boldsymbol{k}.\boldsymbol{r} = kz$ according to the paraxial approximation where $\boldsymbol{k}$ is the wave vector and k its component along z axis.

We have then

$$\mathbf{E}(\mathbf{r}, t) = E_0 f(\mathbf{r}, t)\boldsymbol{\epsilon}\exp(-i(\omega_0 t - kz)) \tag{1.2}$$

where E_0 is the amplitude of the wave, $\boldsymbol{\epsilon}$ is the polarization vector and f is a function dependent on t and $\boldsymbol{r}$ normalized in space. We can thus write:

$$\int_V \mathrm{d}^3\boldsymbol{r}\, |f(\boldsymbol{r}, t)| = 1 \tag{1.3}$$

where V denotes a large volume containing the wave. For sake of simplicity we call f the mode as it includes all the informations about the temporal and spatial aspects of the real one if we remove the exponential term responsible of the wave propagation.

1.1.2 Some examples of modes

1.1.2.1 Plane waves

If the function f is not dependent on time and spatial variables, it becomes just a constant function. This case is actually the most common one to study optics, called the plan-wave model. In this restriction, we have $\mathbf{E}(\mathbf{r}, t) = E_0\boldsymbol{\epsilon}\mathrm{e}^{-i(\omega_0 t - kz)}$.

1.1.2.2 Spatial modes

Now we only assume f is not dependent on time. The function f is a slowly varying envelope in the longitudinal direction, which is translated mathematically by $\left|\frac{\partial^2 f}{\partial z^2}\right| \ll \left|2k\frac{\partial f}{\partial z}\right|$. By injecting the field expression (1.2) deduced from these hypothesis in (1.1), we get:

$$\frac{\partial^2 f}{\partial x^2} + \frac{\partial^2 f}{\partial y^2} - 2ik\frac{\partial f}{\partial z} = 0 \tag{1.4}$$

This equation admits a family of solutions called the transverse electromagnetic modes (TEM) and denoted as $f_{n,m}$. They are actually the spatial eigenmodes of a laser cavity or a waveguide [Siegman 86]. We can write the mode $f_{n,m}$ as follows:

$$f_{n,m}(x,y,z) = \frac{C_{n,m}}{w(z)} H_n\left(\frac{\sqrt{2}x}{w(z)}\right) H_m\left(\frac{\sqrt{2}y}{w(z)}\right) \mathrm{e}^{-(x^2+y^2)/w(z)^2} \mathrm{e}^{-ik(x^2+y^2)/2R(z)} \mathrm{e}^{-i(m+n+1)\phi(z)} \tag{1.5}$$

where $C_{n,m}$ is a normalization factor, $w(z)$ is the beam width, $R(z)$ is the radius of curvature, H_n and H_m are Hermite Gaussian polynomials respectively of order n and m and $\phi(z)$ is the Gouy phase shift. The transverse shapes of the first order modes are represented in figure 1.1

To have a better understanding about these solutions and the parameters introduced, let's take the example of the first mode $f_{0,0}$:

$$f_{0,0}(x,y,z) = \frac{w_0}{w(z)} \mathrm{e}^{-(x^2+y^2)/w(z)^2} \mathrm{e}^{-ik(x^2+y^2)/2R(z)} \mathrm{e}^{-i\phi(z)} \tag{1.6}$$

the beam width can be derived as follows:

$$w(z)^2 = w_0^2\left(1 + z/z_R\right) \tag{1.7}$$

w_0 is the minimum and is called the waist. z_R is the Rayleigh length given by:

$$z_R = \frac{\pi w_0^2 n}{\lambda} \tag{1.8}$$

z_R represents the distance from the waist given by the relation $w(z_0 \pm z_R) = \sqrt{2}w_0$ where z_0 is the position of the waist. It's also possible to derive the radius of curvature and the phase:

$$\frac{1}{R(z)} = \frac{z}{z^2 + z_R^2} \tag{1.9}$$

$$\frac{1}{\phi(z)} = \arctan\left(\frac{z}{z_R}\right) \tag{1.10}$$

The figure represents an example of propagation along the axis Oz of this $f_{0,0}$ mode.

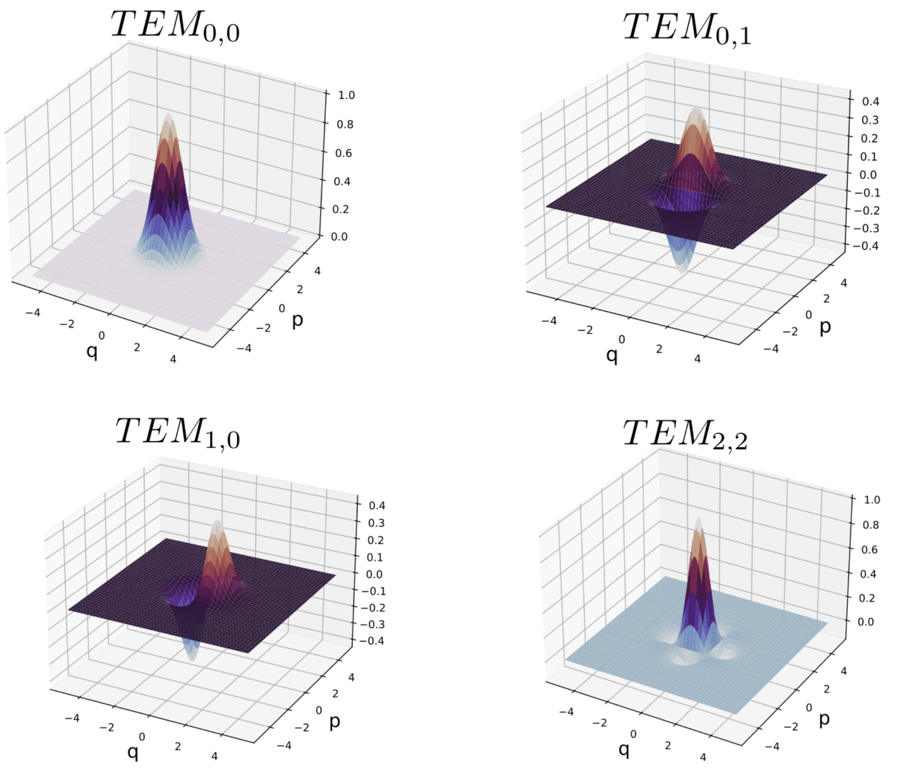

$TEM_{0,0}$ $TEM_{0,1}$ $TEM_{1,0}$ $TEM_{2,2}$

Figure 1.1 – Profile of TEM modes as a function of transverse position x and y.

1.1.2.3 Temporal and frequency modes

We have just seen the case where the function f only depends on spatial variables. Let us see now the temporal case. First, we introduce the Fourier transform, which makes the study of optical waves in frequency or temporal domains equivalent. $\mathcal{F}$ denotes this operation defined as:

$$\mathcal{F}[h(t)] = \int_{\mathbb{R}} \frac{\mathrm{d}t}{\sqrt{2\pi}} h(t) \mathrm{e}^{-i\omega t} = \tilde{h}(\omega) \tag{1.11}$$

where h is a function of time defined on $\mathbb{R}$. The inverse operation is given by:

$$\mathcal{F}^{-1}[\tilde{h}(\omega)] = \int_{\mathbb{R}} \frac{\mathrm{d}\omega}{\sqrt{2\pi}} \tilde{h}(\omega) \mathrm{e}^{i\omega t} = h(t) \tag{1.12}$$

Now, considering the electric field, we can write:

$$\mathbf{E}(\omega, \mathbf{r}) = \int_{\mathbb{R}} \frac{\mathrm{d}t}{\sqrt{2\pi}} \mathbf{E}(t, \mathbf{r}) \mathrm{e}^{-i\omega t} \tag{1.13}$$

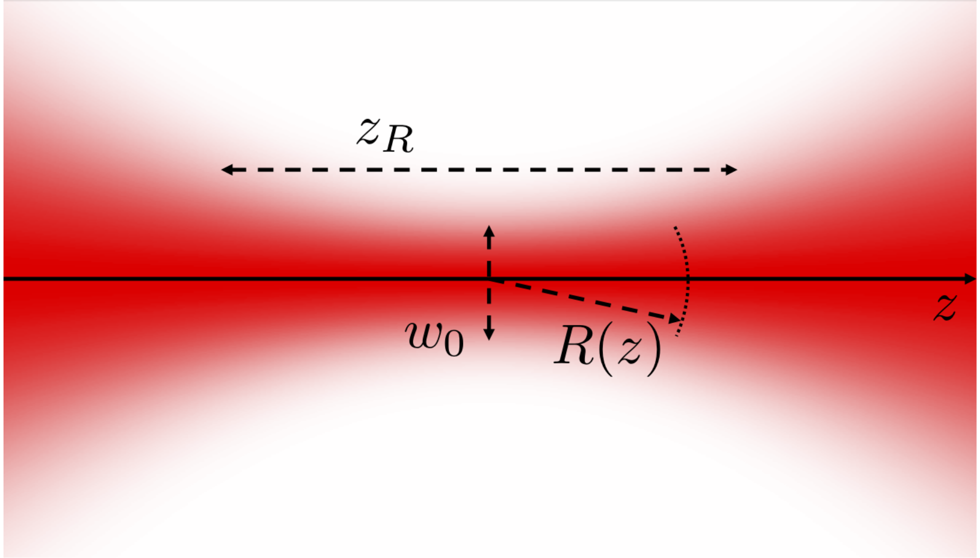

Figure 1.2 – Gaussian profile of the TEM mode $f_{0,0}$ along the direction of propagation z

For the complex expression of the electric field we have the relation: $[\mathbf{E}(\omega,\mathbf{r})]^* = \mathbf{E}(-\omega,\mathbf{r})$. Hence, all the necessary information about the frequency spectrum is contained in the $\mathbb{R}^+$ domain and in order to be more consistent we introduce the notation $\boldsymbol{E}^{(+)}$ which is the Fourier transform of the field in temporal domain only on $\mathbb{R}^+$:

$$\mathbf{E}^{(+)}(\omega,\mathbf{r}) = \int_{\mathbb{R}^+} \frac{\mathrm{d}t}{\sqrt{2\pi}} \mathbf{E}(t,\mathbf{r})\mathrm{e}^{-i\omega t} \tag{1.14}$$

The equivalent definition for $\mathbb{R}^-$ also stands and is denoted as $\boldsymbol{E}^{(-)}$:

$$\mathbf{E}^{(-)}(\omega,\mathbf{r}) = \int_{\mathbb{R}^-} \frac{\mathrm{d}t}{\sqrt{2\pi}} \mathbf{E}(t,\mathbf{r})\mathrm{e}^{-i\omega t} \tag{1.15}$$

Now that we have introduced the Fourier transform and the corresponding notation of the field, we can describe the pulsed modes. Here we will only focus on the temporal and frequency descriptions of the pulse, meaning we restrict the calculation to the $\boldsymbol{r} = \mathbf{0}$ case.

A pulse is defined as a wave at frequency ω_0 with an envelope depending on time. With our notation, f plays the role of the envelop so we can write the electric field as:

$$\mathbf{E}_p(t) = E_0 \boldsymbol{\epsilon} f(t)\mathrm{e}^{-i\omega_0 t} \tag{1.16}$$

We call τ the duration of the pulse. In the frequency domain, we have:

$$\mathbf{E}_p(\omega) = E_0\boldsymbol{\epsilon}\int_{\mathbb{R}} \frac{\mathrm{d}t}{\sqrt{2\pi}} f(t)\mathrm{e}^{-i(\omega-\omega_0)t} = E_0\boldsymbol{\epsilon}\tilde{f}(\omega-\omega_0) \tag{1.17}$$

where $\tilde{f}$ indicates the Fourier transform of the envelop function.

Now let us study the case of a pulse train. The temporal mode is not anymore composed by one pulse but a succession of pulses spaced by a time Δt. We define the repetition rate as $\omega_r := 1/\Delta t$. This example corresponds to the laser source of the SPOPO experiment described in the following chapters, with the particularity that the envelop $f(t)$ has a gaussian shape. It means we can write, for one pulse, $f(t)$ as:

$$f(t) = C_p\mathrm{e}^{-\frac{t^2}{4\tau^2}} \tag{1.18}$$

where C_p is a normalization constant, and τ is the standard deviation of the gaussian function. This parameter is usually called the pulse duration. One interesting property of gaussian functions is their Fourier transform. Indeed the Fourier transform of a gaussian function is a gaussian function. We thus have for the function $f(t)$:

$$\tilde{f}(\omega) = \tilde{C}_p\mathrm{e}^{-\frac{\omega^2}{\Delta\omega^2}} \tag{1.19}$$

where $\tilde{C}_p$ is also a normalization constant and $\Delta\omega$ is the spectral bandwidth in frequency domain. If we come back to the train of pulses, we can deduce the electric field in temporal and frequency domains. First, in temporal, we have [Thiel 15]:

$$\mathbf{E}(t) = E_0\boldsymbol{\epsilon}\sum_l f(t-l\Delta t)\mathrm{e}^{-i[\omega_0(t-l\Delta t)]} \tag{1.20}$$

Then, in frequency domain, we have:

$$\mathbf{E}(\omega) = E_0\boldsymbol{\epsilon}\tilde{f}(\omega)\sum_l \delta(\omega - l\omega_r) \tag{1.21}$$

Hence, the Fourier transform of a pulse train is a frequency comb with a gaussian envelope (figure 1.3). As we will see in chapter 2, these modes are the ones of our laser source. One of the other major benefit, if we compare with TEM beams, is about the number of modes. Indeed, as we saw in the expression (1.21) each element of the sum is actually a mode called tooth of the frequency comb. Let's now consider the experimental values of our laser source: we have $\omega_r = 75$ MHz, $\lambda_0 = 795$ nm and $\tau = 100$ fs. We obtain the quantity $N_{mode} \approx \frac{1}{\omega_r\Delta t} \approx 10^5$ modes. This number would be very difficult to reach for the TEM modes in term of scalability so the pulse train is a very good candidate for a multimode experiment as soon as we don't want to be limited by this quantity.

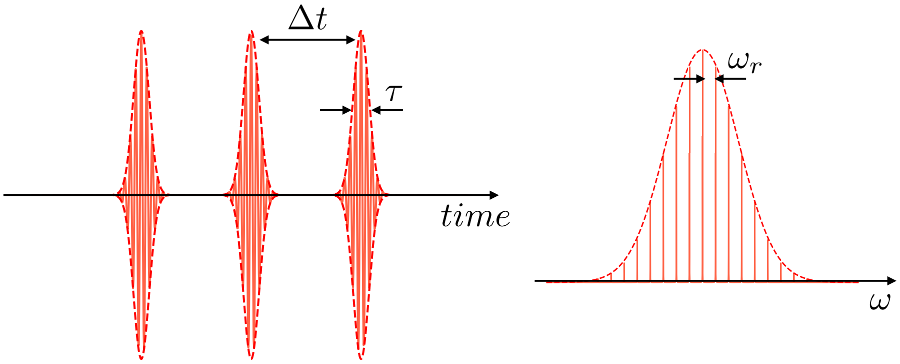

Figure 1.3 – An example of pulse-train (*left*) and the correspondingly Fourier transform, the gaussian frequency comb (*right*).

1.1.2.4 Dispersion in a frequency comb

The large number of modes of the frequency comb is a wonderful support, however this advantage comes with a non negligible drawback: the dispersion. Indeed if we refer to the mode definition (1.1), each tooth of the comb is a single solution of this equation. Nonetheless, the celerity depends on ω, which means that not all modes will propagate at the same speed. This effect is called dispersion and as a consequence, the phase velocity and the group velocity are different, *i.e.* when the speed of the envelope is different from the speed of the ω_0 wave inside this envelope.

Let us examine now in details the effect of the dispersion on the structure of the pulse. Here we will focus only on the scalar part of the electric field and we will still assume the case $z = 0$. We have thus:

$$E^{(+)}(t) = E_0 f(t) \mathrm{e}^{-i\omega_0 t} \tag{1.22}$$

$$E^{(+)}(\omega) = E_0 \tilde{f}(\Omega) \mathrm{e}^{-i\Omega t} \tag{1.23}$$

where $\Omega = \omega - \omega_0$. Because of phase shift between modes, we introduce the quantities $\phi(t)$ and $\Phi(\omega)$ such as:

$$E^{(+)}(t) = E_0 f(t) \mathrm{e}^{-i\phi(t)} \tag{1.24}$$

$$E^{(+)}(\omega) = E_0 \tilde{f}(\Omega) \mathrm{e}^{-i\Phi(\omega)} \tag{1.25}$$

We suppose the phase variation is small, we can thus proceed to Taylor expantion of the function $\Phi(\omega)$ around ω_0:

$$\Phi(\omega) = \Phi(\omega_0) + \Omega \frac{\partial \Phi}{\partial \omega}\bigg|_{\omega_0} + \frac{\Omega^2}{2} \frac{\partial^2 \Phi}{\partial \omega^2}\bigg|_{\omega_0} + ... \tag{1.26}$$

For the rest of the derivation we will denote Φ_n the derivative $\frac{\partial^n \Phi}{\partial \omega^n}\big|_{\omega_0}$. Now let's see the influence of each term on the pulse train:

Constant phase. It corresponds to the case $\Phi(\omega) = \Phi(\omega_0) = \Phi_0$. We thus have:

$$E^{(+)}(t) = E_0 a(t) \mathrm{e}^{-i(\omega_0 t - \Phi_0)} \tag{1.27}$$

It results in a delay between the envelope and the wave. As represented in the figure 1.4. the two local maximums of both functions does not match.

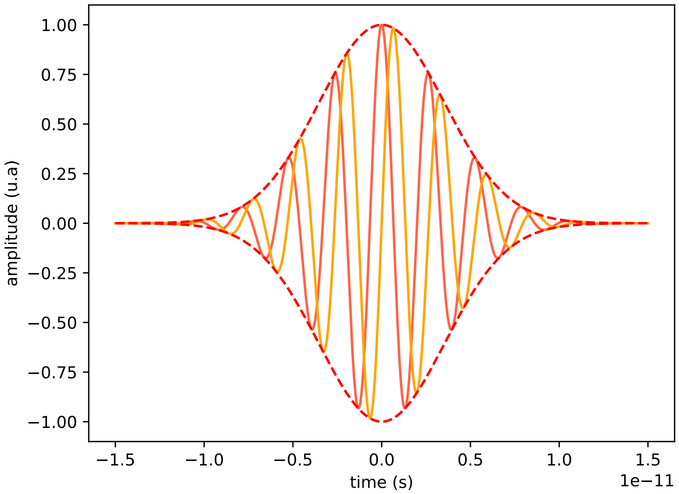

Figure 1.4 – Effect of a constant phase in the dispersion on a 2.5 fs duration pulse with $\omega_0 = 2.37$ THz. The red curve has no temporal dispersion and the orange curve has a 0.66 fs delay inside the gaussian envelope due to a constant phase shift.

Linear phase. Let's assume we express the phase variation as: $\Phi(\omega) = \Omega\Phi_1$. The electric field becomes:

$$E^{(+)}(t) = E_0 a(t - \Phi_1) \mathrm{e}^{-i\omega_0 t} \tag{1.28}$$

This time, we don't observe any delay between both functions but a global one (figure 1.5). The envelope and the wave are both retarded or ahead of time. Nonetheless, this term being a global delay, can be corrected by modifying the length of the optical path.

Quadratic phase. With only the quadratic term, $\Phi(\Omega) = \frac{\Omega^2}{2}\Phi_2$ the shape of the envelope is changed. Considering the case of a gaussian pulse, we have in temporal domain [Thiel 15]:

$$f(t) = \frac{1}{\sqrt[4]{2\pi}\sqrt{\gamma}} \exp\left(-\frac{t^2}{4\gamma^2}\right) \tag{1.29}$$

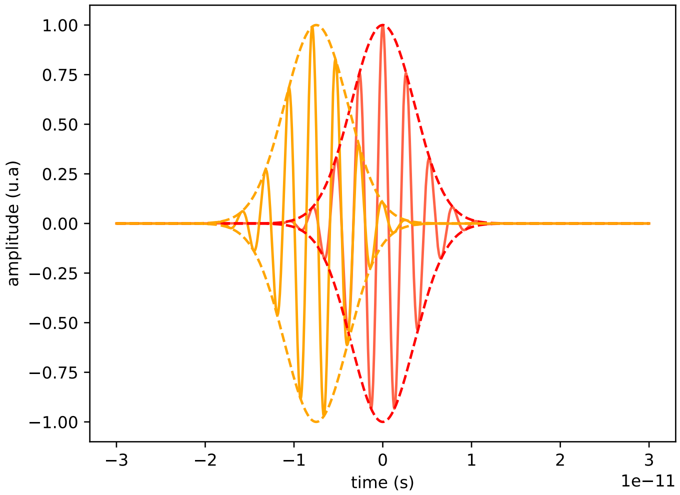

Figure 1.5 – Effect of a linear phase in the dispersion on the same pulse than 1.4. The red pulse has no temporal dispersion and the orange one is delayed from 7.5 fs because of the linear phase dispersion.

where $\gamma = \Delta t\sqrt{1 - i\frac{\Phi^2}{2\Delta t^2}}$ is complex. We can simplify the expression to exhibit a gaussian part with real argument and a part containing the information about the phase:

$$f(t) = \frac{1}{\sqrt[4]{2\pi}\sqrt{\gamma}}\exp\left(-\frac{t^2}{4\Delta t'^2}\right)\mathrm{e}^{i\phi_2} \tag{1.30}$$

$$\text{with } \Delta t' = \Delta t\sqrt{1 + \left(\frac{\Phi_2}{2\Delta t}\right)^2} \text{ and } \phi_2 = \frac{\Phi_2}{8(\Delta t'^4)} \tag{1.31}$$

When there is no quadratic dispersion, $\Delta t'$ reaches its minimum value Δt and we say the pulse is Fourier limited. In figure 1.6 is represented a superposition of two pulses, with and without dispersion effect.

The effect of quadratic dispersion is something we want to avoid. The first reason is because it changes the shape of the pulse and as we will see in chapter 3, this beam parameter is something we want to control especially for the detection. Secondly, because we seek to generate non-linear optical effects and squeezed states, we need non-linear effects which depend on the peak power of the source. Here the dispersion broadens the temporal pulse and by energy conservation the peak power is decreased from the Fourier limited situation. Another consequence of the quadratic chirp is the time delay between the different teeth modes of the spectrum. In the medium which induces the quadratic phase the higher frequency will travel faster (or lower) and will

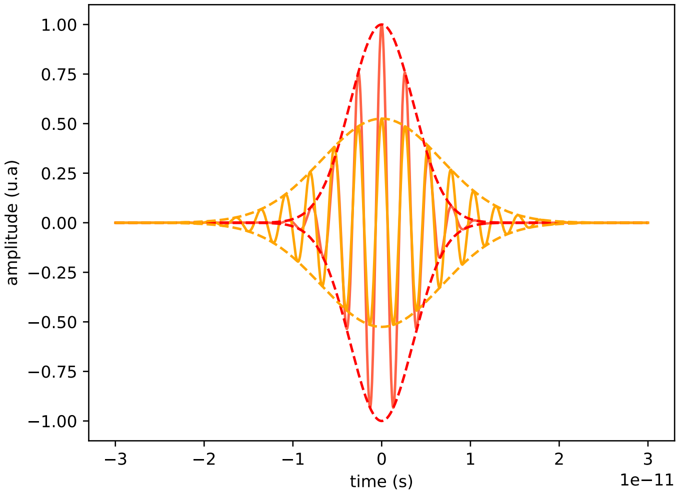

Figure 1.6 – Effect of a quadratic phase in the dispersion. The red pulse has no temporal dispersion and the orange has a quadratic dispersion of 4.5fs^2.

be at the front of the pulse (or at the back). We don't see this effect in the figure 1.6 because of the ω_0 choice. Indeed, we choose for the figure 1.4, 1.5 and 1.6 a low value for this parameter in order to show the oscillation inside the envelope. In the experimental conditions, the central frequency is around 1000 times higher.

1.1.3 Power of a pulse train beam

In this subsection, we assume the mode depends on the spatial and temporal variables. The field intensity, I, is defined by the relation:

$$I(\boldsymbol{r},t) = 2nc\epsilon_0 \left\| \boldsymbol{E}^{(+)}(\boldsymbol{r},t) \right\| \tag{1.32}$$

and it can be related to a well known quantity of the lab, the power measured by the power meter P:

$$P(z,t) = \int\int_{S_{pw}} I(\boldsymbol{r},t)\mathrm{d}^2 r \approx \int\int_{\mathbb{R}^2} I(\boldsymbol{r},t) r \mathrm{d}^r \mathrm{d}^\theta \tag{1.33}$$

where S_{pw} is the active area of the power meter and (r,θ) are the coordinates in cylindrical reference frame. The approximation is valid as long as the waist of the beam is small comparing with S_{pw}. For a pulse train, the quantity of interest is the average power defined by:

$$P_0(z) = U_{pulse}(z)\omega_r \tag{1.34}$$

where U_{pulse} is the energy of a single pulse. We can write:

$$U_{pulse}(z) = \int_{\Delta t} P(z,t)\mathrm{d}t \tag{1.35}$$

We assume that the function f which defines the mode shape, can be decomposed as $f(x,y,z,t) = s(t)u(x,y,z)$. By deriving the above equations, we get:

$$U_{pulse}(z) = 2nc\epsilon_0 E_0^2 \int_{\Delta t} |s(t)|\mathrm{d}t \int_{\mathbb{R}^2} u(x,y,z)\mathrm{d}x\mathrm{d}y \tag{1.36}$$

We denote T and S_{eff} the integrals respectively over time and space in the above equation. We deduce thus the relation between the field amplitude and the average power for a pulse train:

$$E_0 = \sqrt{\frac{P_0}{2nc\epsilon_0 S_{eff} T \omega_r}} \tag{1.37}$$

1.1.4 Cavity in optics

Cavities are key elements in optics. They can be used to enhance linear effect in optical parametric oscillators or as spatial filter for TEM modes. Here we will only focus on the case without any non-linear crystal inside in order to understand their interferential aspect.

There are several geometries for cavities. Here we present the most common one, called the Fabry Perot interferometer. It is one of the simplest type of cavity but already sufficient to show the most important physical concepts. A scheme of the interferometer is represented in figure 1.7. It's composed of two mirrors of high reflectivity. We call r and t the coefficients respectively of reflectivity and transmission. The index indicates if the coefficient is associated to the input or the output mirror.

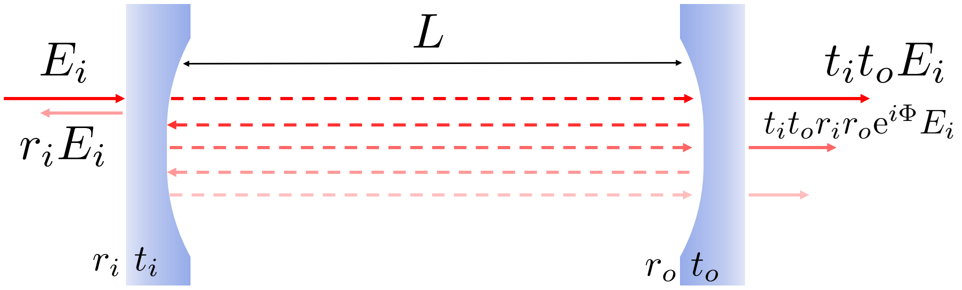

Figure 1.7 – Fabry Perot setup.

The light can do several roundtrips before exiting the cavity. We can thus express the scalar part of the output electric field as the sum below:

$$E_{out}(\omega) = \left(t_i t_o + t_i r_o \mathrm{e}^{i\Phi(\omega)} r_i t_o + t_i r_o \mathrm{e}^{i\Phi(\omega)} r_i r_o \mathrm{e}^{i\Phi(\omega)} r_i t_o + ...\right) E_{in}(\omega) \tag{1.38}$$

$$= t_i t_o \sum_{l=0}^{\infty} (r_i r_o \mathrm{e}^{i\Phi(\omega)})^l E_{in}(\omega) \tag{1.39}$$

In this expression, the phase Φ is set by the length of the cavity L that we can usually tune and lock in experiments. We recognize a geometric series where the absolute value of the argument is strictly below one, which allows us to write:

$$E_{out}(\omega) = \frac{t_i t_o E_{in}(\omega)}{1 - r_i r_o \mathrm{e}^{i\Phi(\omega)}} \tag{1.40}$$

We can also write the light intensity at the output $I(\omega) = |EE^*|$:

$$I_{out}(\omega) = \frac{T_C^2 I_{in}(\omega)}{1 + R_C^2 - 2R_C \cos(\Phi(\omega))} \tag{1.41}$$

where $T_C = t_i t_o$ and $R_C = r_i r_o$. Using the trigonometric formula $\cos(\Phi) = 1 - 2\sin^2(\Phi/2)$, we get:

$$I_{out}(\omega) = \frac{T_{max}^2 I_{in}(\omega)}{1 + m \sin^2(\Phi(\omega)/2))} \tag{1.42}$$

where $T_{max} = T_C/(1 - R_C)^2$ and $m = \frac{4R_C}{(1-R_C)^2}$. We notice the transmission of the cavity is maximal when $I_{out} = T_{max} I_{in}$ for $\Phi(\omega) = 2k\pi$ with $k \in \mathbb{N}$. When the length L is set correctly, the beams at the output of the cavity interfere constructively to reach the maximum of intensity. If we can scan the phase Φ by several number of periods by translation of one mirror, we will observe several resonance peaks. The interval between two peaks is called the free spectral range (FSR). If we assume that the peaks are not large compared with this parameter we can approximate the sin function in (1.42) around the length $L_0 = 2\pi c/\omega$ and the transmitted intensity takes a Lorentzienne form:

$$I_{out} = \frac{T_{max} I_{in}}{1 + m \left(\frac{\omega}{c}\right)^2 (L - L_0)^2} \tag{1.43}$$

Hence we can define the finesse F as the ratio between the FSR and the full half width maximum (FHWM) of the Lorentzienne function. If we consider the case where $F >> 1$, F can be approximated as:

$$F = \frac{\pi\sqrt{R_C}}{1 - R_C} \tag{1.44}$$

The demonstration above has been made in the case of a single mode electric field at frequency ω. Formulas are here linear, so, we can use them in the multimode case. For example, for a pulse train, we want to ensure that the length is set so that the cavity transmits each frequency modes of the comb. It means for all frequency ω_l of the comb we should satisfy the relation:

$$L = \frac{2\pi c}{\omega_l} K_l \quad \text{with} \quad K_l \in \mathbb{N} \tag{1.45}$$

A solution fulfilling such constraints is the one where the FSR matches the repetition rate of the pulse train. We thus have:

$$L = \frac{2\pi c}{\omega_r} \tag{1.46}$$

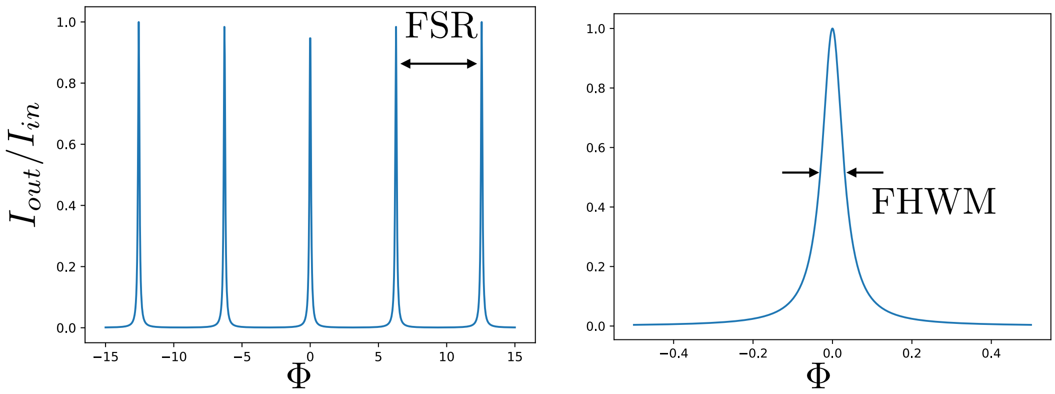

Figure 1.8 – *left*: Shape of the cavity transmission I_{out}/I_{in} as a function of the phase Φ. *right*: Zoom of the left plot on one single peak around $\Phi = 0$.

1.2 Quantum optics

1.2.1 Quantization of the field

Previous section has been dedicated to present some concepts of classical optics. These are essential in order to understand some aspects of the experimental setup presented in part II of this manuscript. However this description is not enough to get a full understanding of the involved physics. Therefore, we introduce in the following section the quantum properties of the light: how to write the field in this framework, some of the consequences and we describe some of the common states.

Quantum optics can be define through a parallelism with quantum mechanics. When in mechanics the considered operators are the position $\hat{x}$ and the momentum $\hat{p}$, in optics, we will consider the field operator $\hat{\boldsymbol{E}}$ and its conjugate. We can then say that the electric field is the sum of harmonic oscillators of frequency ω_l. Hence, again by analogy, we can define a annihilation operator $\hat{a}_l$ associated to the optical mode of frequency ω_l [Grynberg 10]. By summing all the single modes, we get the operator of the quantum electric field:

$$\hat{\boldsymbol{E}}^{(+)}(\mathbf{r},t) = \sum_l^{\infty} \mathcal{E}_l \boldsymbol{\epsilon} \hat{a}_l f_l(\mathbf{r},t) \mathrm{e}^{-i(\omega_l t - kz)} \tag{1.47}$$

with

$$\mathcal{E}_l = \sqrt{\frac{\hbar\omega_l}{2\epsilon_0 V}} \tag{1.48}$$

where $\hbar$ is the Planck constant over 2π and V is the same volume already defined in (1.3). For more details, the complete quantization of the field is derived in [Grynberg 10]. From this derivation, we find equivalent properties of quantum mechanics. The Hamiltonian of the total free field under consideration of the multimode case is:

$$\hat{H} = \sum_l \hat{H}_l = \sum_l \hbar\omega_l (\hat{a}_l^\dagger \hat{a}_l + \frac{1}{2}) \tag{1.49}$$

where $\hat{a}_l^\dagger$ is called the creation operator. With $\hat{a}_l$ they verify the following commutation relation:

$$[\hat{a}_l, \hat{a}_{l'}^\dagger] = \delta_{l,l'} \tag{1.50}$$

$$[\hat{a}_l, \hat{a}_{l'}] = 0 \tag{1.51}$$

We notice that all the information about the modes and the propagation of the wave are still present in (1.47), especially through the function f and the exponential function. Hence all the properties presented in the previous section are still valid. It's also possible to define the electric field operator in frequency domain and we can use the notations $\hat{E}^{(+)}$ and $\hat{E}^{(-)}$.

The diagonalization of $\hat{H}_l$ is the same as that of the operator $\hat{N}_l = \hat{a}_l^\dagger \hat{a}_l$. The eigenvalues of this operator are the zero or positive integers. In mechanics, it tells us how is populated the given states. In optics, we speak about number of photons.

1.2.2 The quadrature operators

The annihilation and creation operators are not hermitian, which implies they are not measurable observables. However we can build two quadrature operators that have this desired property:

$$\hat{q}_l = \hat{a}_l^\dagger + \hat{a}_l \tag{1.52}$$

$$\hat{p}_l = i(\hat{a}_l^\dagger - \hat{a}_l) \tag{1.53}$$

We can express the electric field operator in these new variables:

$$\hat{E}(\mathbf{r},t) = \sum_l \mathcal{E}_l \boldsymbol{\epsilon} f_l(\mathbf{r},t)\left(\hat{q}_l \cos(\omega_l t - k_l z) + \hat{p}_l \sin(\omega_l t - k_l z)\right) \tag{1.54}$$

It is also possible to define the quadrature operators at an arbitrary phase θ:

$$\hat{q}_{l,\theta} = \cos(\theta)\hat{q}_l + \sin(\theta)\hat{p}_l \tag{1.55}$$

$$\hat{q}_l = \mathrm{e}^{i\theta}\hat{a}_l + \mathrm{e}^{-i\theta}\hat{a}_l^\dagger \tag{1.56}$$

We denote the quantum state as $|\Psi\rangle$, which can be decomposed among many basis. One of them, the Fock basis, is used to look the state in a discrete feature:

$$|\Psi\rangle = \sum_n c_n |n\rangle \tag{1.57}$$

where $\{c_n\}_{n\in\mathbb{N}}$ are complex numbers and $|n\rangle$ are the eigenstates of the operator $\hat{N} = \hat{a}^\dagger\hat{a}$. We can also use the quadrature operators basis to represent $|\Psi\rangle$ and use their continuous properties:

$$|\Psi\rangle = \int \Psi(q)\,|q\rangle\,\mathrm{d}q = \int \tilde{\Psi}(p)\,|p\rangle\,\mathrm{d}p \tag{1.58}$$

where $|q\rangle$ and $|p\rangle$ are eigenstates of respectively $\hat{q}$ and $\hat{p}$.

1.2.3 The Wigner function

In a quantum optics experiment, we seek to generate optical quantum states, but we also need to characterize them. To do so, whatever the discrete or continuous feature we choose, we have to find the convenient way to represent the state we want to measure. Unfortunately, the notation that we have introduced above for a quantum state, $|\Psi\rangle$, is not complete especially when the state is mixed. To counterpart this limitation, we can use the density operator defined for a pure state as:

$$\hat{\rho} = |\Psi\rangle\langle\Psi| \tag{1.59}$$

This operator verifies, for a pure state, $\mathrm{Tr}(\hat{\rho}) = 1$. From this operator the purity is easily accessible by $P = \mathrm{Tr}(\hat{\rho}^2)$. For a mixed state, the density operator takes the form:

$$\hat{\rho} = \sum_i p_i |\Psi\rangle_i \langle\Psi|_i \tag{1.60}$$

It can be expressed in a given basis $\{|n\rangle\}$ of the Hilbert space as:

$$\hat{\rho} = \sum_{n,m} \rho_{nm} |n\rangle\langle m| \tag{1.61}$$

The density operator is also convenient to write the Wigner function [Wigner 32]. Indeed, since the quadrature operators do not commute, we can not represent the state using a joint spectral probability distribution. The Wigner function is a quasi-probability distribution defined in the single mode case as:

$$W_{\hat{\rho}}(q,p) = \frac{1}{2\pi}\int \left\langle q+\frac{y}{2}\middle|\,\hat{\rho}\,\middle|q-\frac{y}{2}\right\rangle \mathrm{e}^{-ipy}\mathrm{d}y \tag{1.62}$$

This function exhibits interesting properties which makes it a good representation of the state in continuous feature. Indeed we have:

$$\int_{\mathbb{R}} W_{\hat{\rho}}(q,p)\mathrm{d}p = |\Psi(q)|^2 \tag{1.63}$$

$$\int_{\mathbb{R}} W_{\hat{\rho}}(q,p)\mathrm{d}q = \left|\tilde{\Psi}(p)\right|^2 \tag{1.64}$$

For an observable $\hat{A}$, the mean value is derived from this function as:

$$\left\langle \hat{A} \right\rangle = \int_{\mathbb{R}^2} W_{\hat{\rho}}(q,p)W_{\hat{A}}(q,p)\mathrm{d}q\mathrm{d}p \tag{1.65}$$

One major difference with a usual joint probability distribution is the Wigner function can be negative [Walschaers 21a, Gottesman 01]. This singular property has already been measured for some quantum states [Ourjoumtsev 06, Ra 20].

1.2.4 The Covariance Matrix

A useful representation for our case, since it contains the correlations between modes, is the covariance matrix denoted as Γ [Ferraro 05]. We write the vector $\boldsymbol{x}$, which contains all the quadrature elements: $\boldsymbol{x} = (q_1, ...q_n, p_1, ..., p_n)$. In this context the covariance terms are defined as:

$$\Gamma_{i,j} = \frac{1}{2}\langle x_i, x_j\rangle - \langle x_i\rangle - \langle x_j\rangle \tag{1.66}$$

For multimode gaussian state, *i.e* states with gaussian Wigner functions, we can compute the purity as:

$$P = \det(\boldsymbol{\Gamma}) \tag{1.67}$$

1.2.5 Basis Change

In (1.54), the multimode quantum states is written using a sum symbol. We can also use the vectorial notation for more convenience. We introduce the vector $\hat{\boldsymbol{a}}$ whose component l corresponds to the operators $\hat{a}_l$ associated to the mode of frequency ω_l.

The equation becomes similar to the single mode case but the scalar components are replaced by vectors.

This vectorial notation is more convenient as soon as we want to do a basis change. Indeed, it is possible to change the orthonormal basis used to express field operators. If we want to move from a basis $\hat{\boldsymbol{a}} = (\hat{a}_1, ..., \hat{a}_n)$ to another one $\hat{\boldsymbol{b}} = (\hat{b}_1, ..., \hat{b}_n)$ and if $\mathbf{U}$ is the transfer matrix, we have for $0 \leqslant i, j \leqslant n$:

$$\hat{b}_i^\dagger = \sum_j U_{i,j}\hat{a}_j^\dagger \tag{1.68}$$

$$\hat{b}_i = \sum_j U_{i,j}^*\hat{a}_j \tag{1.69}$$

The matrix $\mathbf{U}$ is unitary, which implies that the Heisenberg relation is still verified in the new basis:

$$[b_l, b_{l'}^\dagger] = \delta_{l,l'} \tag{1.70}$$

This transformation affects also the vectors composed by the mode functions f_l and the normalization constants $\mathcal{E}_l$, the new vectors are noted respectively $\mathbf{g}(\mathbf{r}, t)$ and $\boldsymbol{\mathcal{G}}$ and we write the quantum electric field in the new basis as:

$$\hat{E}(\mathbf{r}, t) = \sum_l \mathcal{G}_l \boldsymbol{\epsilon}_l \hat{b}_l g(\mathbf{r}, t) \mathrm{e}^{i(\omega_l t - kz)} \tag{1.71}$$

1.2.6 Symplectic Transformation

The matrices $\mathbf{U}$ are part of the symplectic transformation group. By definition a matrix S is called symplectic if it satisfies:

$$S^T \beta S = \beta \text{ with } \beta = \begin{pmatrix} 0 & \mathbb{1} \\ -\mathbb{1} & 0 \end{pmatrix} \tag{1.72}$$

The matrix $\mathbf{U}$ is indeed symplectic because it preserves the commutation relation. An interesting property of this group, which is currently used in quantum optics, is the Bloch Messiah reduction[Bloch 62]. This theorem says that we can decompose any symplectic transformation S as:

$$S = O_1 K O_2 \tag{1.73}$$

where O_1 and O_2 are orthogonal matrices and K a diagonal matrix composed by real and positive terms. In other words, O_1 and O_2 represents a basis changes and the matrix K acts on the new basis element resulting from the O_2 basis change.

1.2.7 Usual states in quantum optics

We present here some examples of common quantum states and the way we can represent them. We will only consider the single mode case at least for the three first examples.

1.2.7.1 Fock states

The Fock states, denoted as $|n\rangle$ with $n \in \mathbb{N}$, are defined as the eigenstates of the operator $\hat{N}$. They are associated to the number of particles contained in the state, or photons in quantum optics. Indeed we have: $\hat{N}|n\rangle = n|n\rangle$ from the following properties of annihilation and creation operators:

$$\hat{a}|n\rangle = \sqrt{n}\,|n-1\rangle \tag{1.74}$$

$$\hat{a}^\dagger|n\rangle = \sqrt{n+1}\,|n+1\rangle \tag{1.75}$$

The state $|0\rangle$ with 0 photon is called vacuum state. Nonetheless, it is interesting that its standard deviation is not 0. Even for this state the Heisenberg relation is verified. For $n \neq 0$ the mean and the second moment can be expressed in terms of n:

$$\left\langle \hat{N} \right\rangle = n \tag{1.76}$$

$$\left\langle \Delta\hat{N}^2 \right\rangle = 0 \tag{1.77}$$

$$\left\langle \Delta\hat{q}^2 \right\rangle = \left\langle \Delta\hat{p}^2 \right\rangle = 2n+1 \tag{1.78}$$

We can derive the Wigner functions of Fock states as:

$$W_{|n\rangle} = \frac{1}{2\pi}(-1^n)L_n(q^2+p^2)\mathrm{e}^{-\frac{q^2+p^2}{2}} \tag{1.79}$$

where L_n are Laguerre polynomials. The Wigner function of the first Fock states are represented in the figure 1.9.

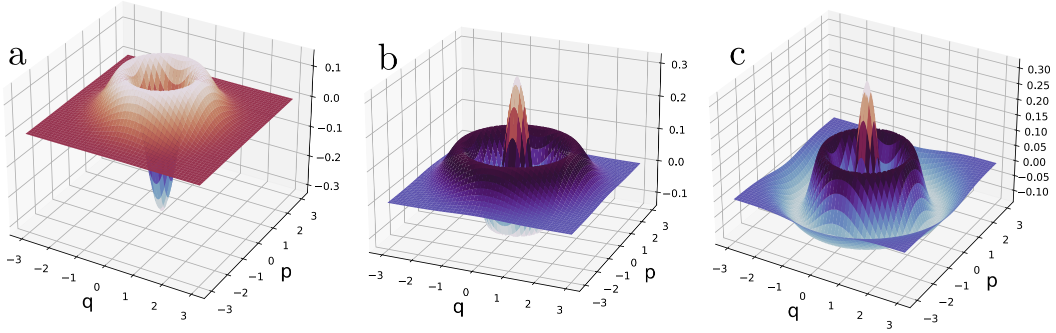

Figure 1.9 – Wigner function of the first element of the Fock states basis. a: $W_{|1\rangle}$, b: $W_{|2\rangle}$ and c: $W_{|3\rangle}$.

1.2.7.2 Coherent states

Coherent states are much easier to produce than Fock states since they are simply associated to the beam at the output of a laser. They have been originally defined by Glauber as the eigenstates of the annihilation operator [Glauber 63]. If we denote $|\alpha\rangle$ as the coherent state, we have $\hat{a}\,|\alpha\rangle = \alpha\,|\alpha\rangle$, where α is a complex number: its modulus and angle represents respectively the amplitude and the phase of the optical field associated to the state. From this definition we can easily express the coherent state as superposition of Fock states:

$$|\alpha\rangle = \mathrm{e}^{-\frac{|\alpha|^2}{2}} \sum_n \frac{(\alpha\hat{a}^\dagger)^n}{n!}\,|0\rangle \tag{1.80}$$

A second definition the coherent state is via the displacement operator: $D(\alpha) = \exp(\alpha\hat{a}^\dagger - \alpha^*\hat{a})$. We have:

$$|\alpha\rangle = D(\alpha)\,|0\rangle \tag{1.81}$$

It means that we get a coherent state by moving the vacuum state by the complex amplitude α in phase space. An example of coherent state is represented in figure 1.10. We have the following properties:

- $\langle\alpha|\,\hat{n}\,|\alpha\rangle = |\alpha|^2$
- $\langle\Delta p^2\rangle = \langle\Delta q^2\rangle = 1$

And the Wigner function is derived as:

$$W_{|\alpha\rangle} = \frac{1}{\pi}\mathrm{e}^{-\frac{(q-\mathrm{Re}(\alpha))^2+(p-\mathrm{Im}(\alpha))^2}{2}} \tag{1.82}$$

1.2.7.3 Squeezed states

Squeezed states are related to coherent states in a sense their Wigner function are obtained by squeezing along one direction the Wigner function of a coherent state [Ma 90, Walls 83]. The direction of squeezing is defined by the angle in phase space θ. The Heisenberg relation has to be verified, which implies the orthogonal direction $\theta + \pi/2$ is anti-squeezed. We speak about bright squeezing when $\alpha \neq 0$ and about vacuum squeezing when $\alpha = 0$ as shown in figure 1.11.
The squeezing operator is defined as:

$$\hat{S}(\zeta) = \mathrm{e}^{i\frac{\zeta\hat{a}^{\dagger 2} - \zeta^*\hat{a}^2}{2}} \tag{1.83}$$

where $\zeta = re^{i\theta}$ is a complex number called the squeezing parameter with $r \in \mathbb{R}^+$. For a squeezed vacuum state $|S(\zeta)\rangle = \hat{S}(\zeta)\,|0\rangle$, we have the following properties:

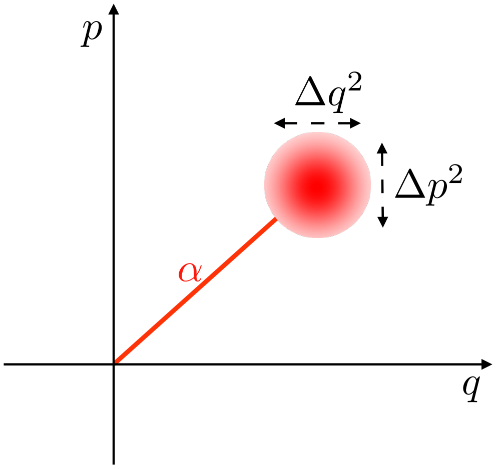

Figure 1.10 – Representation of a α amplitude coherent state in phase space

- $\langle p \rangle = \langle q \rangle = 0$
- $\langle \Delta p^2 \rangle = \mathrm{e}^{-2r} \cos^2(\theta/2) + \mathrm{e}^{2r} \sin^2(\theta/2)$
- $\langle \Delta q^2 \rangle = \mathrm{e}^{2r} \cos^2(\theta/2) + \mathrm{e}^{-2r} \sin^2(\theta/2)$

and the Wigner function for vacuum squeezed state is given by:

$$W_{|\hat{S}(\zeta)\rangle} = \frac{1}{\pi} \mathrm{e}^{-\frac{q^2}{2\langle \Delta q^2 \rangle} - \frac{p^2}{2\langle \Delta p^2 \rangle}} \tag{1.84}$$

Here, when $r > 0$, which implies $\langle \Delta q^2 \rangle \neq \langle \Delta p^2 \rangle$, the Wigner function shape is not anymore circular like for the coherent state case but ellipsoidal.

1.2.7.4 EPR states

The name EPR comes from the three physicists Einstein, Podolsky and Rosen, who have been the first to describe entanglement properties in quantum physics [Einstein 35a]. The description of what was first presented as a paradox is based on a two modes states $|\Phi\rangle = |\Phi_1(q_1), \Phi_2(q_2)\rangle$. By definition, $|\Phi\rangle$ is entangled if it is not a separable state, which means we can not write it such as $|\Phi\rangle = |\Phi_1(q_1)\rangle \otimes |\Phi_2(q_2)\rangle$.

The paradox has been identified as an important property in quantum mechanics, J. S. Bell derived a relation to test it that has been experimentally tested in several experiments [Einstein 35b, Aspect 82]. We can produce this kind of states from two squeezed vacuum states squeezed along two orthogonal direction and which interact on a balanced beam splitter (figure 1.12). When both of the squeezing parameters are $\zeta = r\mathrm{e}^{i\theta}$, the state at the output of the beam splitter can be expressed as:

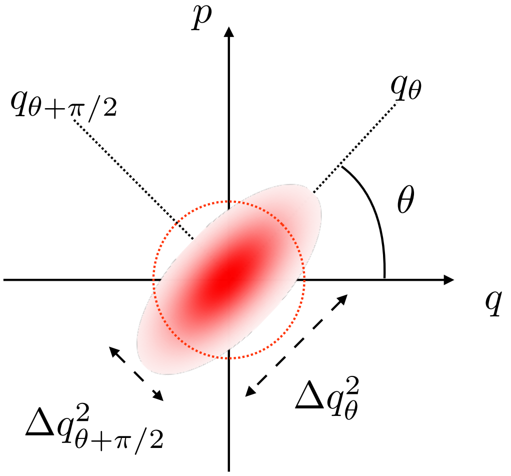

Figure 1.11 – Representation of a vacuum squeezed state in phase space. The dash line represents the unitary circle.

$$|\Phi\rangle = \exp(\frac{1}{2}[\zeta \hat{a}_1^\dagger \hat{a}_2^\dagger - \zeta^* \hat{a}_1 \hat{a}_2]) |0,0\rangle \tag{1.85}$$

$$= \frac{1}{\cosh(r)} \sum_{n=0}^{\infty} (\mathrm{e}^{i\theta} \tanh(r))^n |n,n\rangle \tag{1.86}$$

In this context, all the states involved are gaussian, and, at the output, we have correlations between $|\Phi_1\rangle$ and $|\Phi_2\rangle$ such as:

$$\left\langle (q_1 - q_2)^2 \right\rangle = \left\langle (p_1 + p_2)^2 \right\rangle = \mathrm{e}^{-2r} \tag{1.87}$$

1.2.7.5 Cluster States

In the previous paragraph, the beam splitter operate as a basis change, its unitary transformation is denoted as $\boldsymbol{U}_2$. We can also consider a quantum states composed by n modes to which we apply a unitary transformation $\boldsymbol{U}_n$. At the output we find a state that can be graphically represented by a network state where the nodes are optical modes and the links entanglement correlations as represented in figure 1.13. All the information about the connectivity between the different nodes is contained in a matrix called the adjacency matrix and denoted as $\boldsymbol{V_C} = (v_{i,j})_{0\leq i,j \leq n}$ [Ferrini 13] such as:

$$v_{i,j} = \begin{cases} 1 & \text{if } i \text{ and } j \text{ are connected} \\ 0 & \text{otherwise} \end{cases} \tag{1.88}$$

$$\begin{pmatrix} \hat{\boldsymbol{p}}_c \\ \hat{\boldsymbol{q}}_c \end{pmatrix} = \boldsymbol{U}_n \begin{pmatrix} \hat{\boldsymbol{p}}_{sqz} \\ \hat{\boldsymbol{q}}_{sqz} \end{pmatrix} \tag{1.89}$$

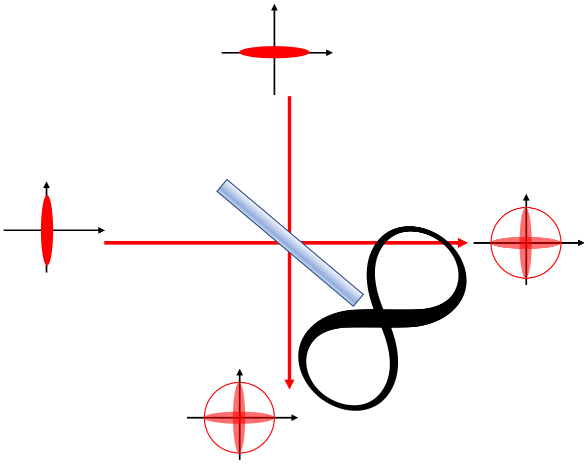

Figure 1.12 – Generation of two entangled modes from two squeezed sates.

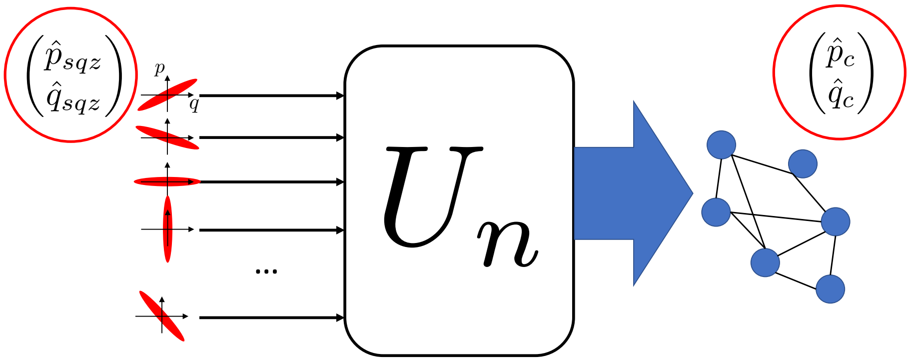

Figure 1.13 – Example of unitary transformation to form a cluster states composed by 6 modes.

The entanglement correlations are described by the nullifier operators. We define the nullifier operators as $\boldsymbol{\delta} = \hat{\boldsymbol{p}}_c - \boldsymbol{V_C}\hat{\boldsymbol{q}}_c$, which satisfy the relation $\Delta\boldsymbol{\delta} \rightarrow \boldsymbol{0}$ in the limit where the squeezing in the initial basis $(\hat{\boldsymbol{p}}_{sqz}, \hat{\boldsymbol{q}}_{sqz})^T$ tends to infinity. Because infinite squeezing is achievable only in theory, in an experiment, we expect to see that the nullifier modes are squeezed below the shot noise limit 1.14.

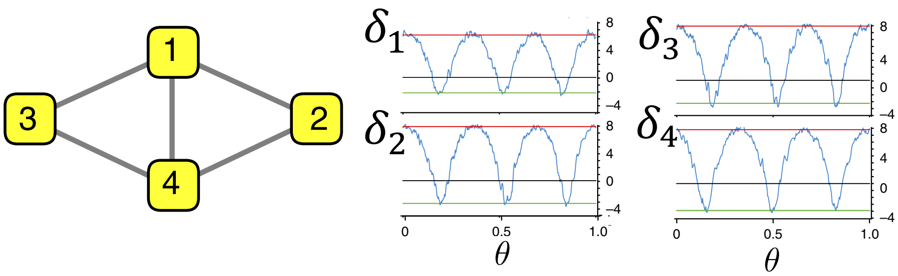

Figure 1.14 – *left*: Example of 4-modes cluster states. *center* and *right*: measurement of $\langle \Delta\delta^2 \rangle$ as a function of the phase θ (blue lines). We see for some phase intervals the curve are below shot noise limit (black lines), which witnesses of correlation between modes in the cluster basis. Taken from [Cai 17].

Part II

PRESENTATION OF THE SPOPO EXPERIMENT

Chapter 2

Preparation of multimode squeezed states

Contents

The so-called SPOPO refers to an experiment composed of an optical parametric oscillator (OPO) working with pulse trains. It is a cavity with a non-linear crystal inside, which is multimode as it fulfills the condition of equation (1.46). SPOPO stands for Synchronously Pulsed Optical Parametric Oscillator. The purpose of this cavity is to produce a collection of squeezed vacuum states on different frequency modes as defined in the first part of this thesis.
The OPO operation is explained at the end of this chapter. Before, we present all the experimental ingredients needed for the generation of the desired states starting from the laser source.

2.1 The source and preparation of the beam

A way to produce multimode squeezed states in the frequency domain is to inject a pump which is already multimode into the SPOPO cavity. As explained in the first chapter, pulsed light is a very promising candidate for producing these states due to its very large number of modes defined in the spectral domain.
The industry of pulsed lasers has continuously evolved for many years and J. Hall and T. Hänsch got Nobel prize in 2005 for their contribution to metrology based on optical frequency comb[Hall 06, Hänsch 06]. Very recently, pulses in the atto-second regime ($\Delta t \leqslant 10^{-15}$s) have been measured and stand as useful support for the study of atoms and molecules motions in chemical reactions[Krausz 09, Marinelli 20].

2.1.1 Laser source

For the SPOPO experiment, we do not need to go up to the atto-second pulses regime. The source we use is a femtosecond laser from Coherent (model MIRA 900). This is an oscillator pumped by a DPSS laser also from Coherent (model Verdi G-15). This pump laser is source of coherent light at $\lambda_p = 532$nm and its working point is at 13W. A titanium-sapphire [$\mathrm{Ti} : \mathrm{Al_2O_3}$] crystal embedded inside the MIRA allows to convert green light of the pump laser to red light around 800nm[Kerr 75, Brabec 92, Spence 91]. Then, like in the Fabry Perot, the MIRA cavity length, which is set around $L_{MIRA} \approx 4$m, selects the longitudinal modes which are resonant. However, all these modes are not able to produce lasing effect because of losses. As depicted in figure 2.1, the existence of an oscillation threshold means that the cavity also acts as a spectral filter on the frequency comb. Lasing effects still occurs for a large amount of frequencies, which oscillate all together in phase.

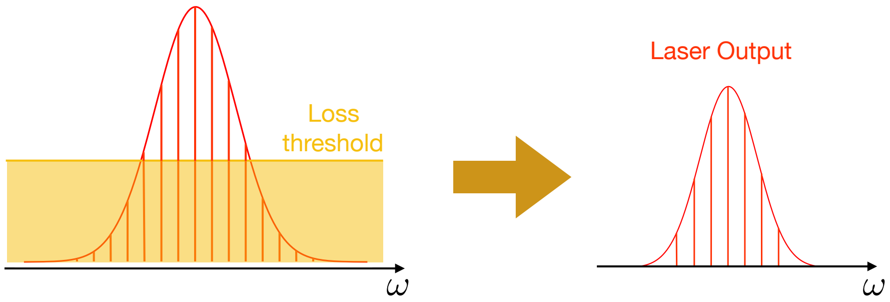

Figure 2.1 – Sketch of cavity losses on frequency comb in cavity. On the left, the Dirac peaks indicate the resonant frequency modes of the laser and on the right the modes whose amplitude is above the loss threshold and which are able to produce lasing effect.

We observe that two spatial-temporal modes can be produced at the output of the MIRA: the desired pulse train beam called mode-lock and a continuous mode, whose

diameter is larger. A tunable slit is thus inserted just before the output coupler to add extra losses on the continuous beam and to avoid any lasing from this mode. In the cavity, we also use a Lyot filter to tune the central wavelength of the comb [Lyot 33] and two prisms to correct for the temporal dispersion due to the intracavity propagation inside the MIRA.
In figure 2.2 we show the spectrum of the mode-lock beam. The shape is Gaussian as expected with a central wavelength $\lambda_0 = 795$nm and a Full Width Half Maximum $FHWM \approx 9$nm. The output power is around $1.65W$. We note that we do not see a frequency comb but only the gaussian envelope of the real spectrum, as the spectrometer resolution isn't sufficient (this measurement as well as all the spectrum measurements of this manuscript have been preformed with a HR4000 with a resolution of $\delta\lambda \approx 0.1$nm). The time duration of the pulse is around 90fs and the repetition rate is 76MHz. After the laser, some usual optics are used in order to prepare the beam for the rest of the experiment:

- An isolator to avoid any back propagation of the light into the femtosecond laser
- A $f = -3000$ mm lens to collimate the beam on a long distance
- A GLAN Thompson prism to filter the polarization. After this element, the beam has a p linear polarization.

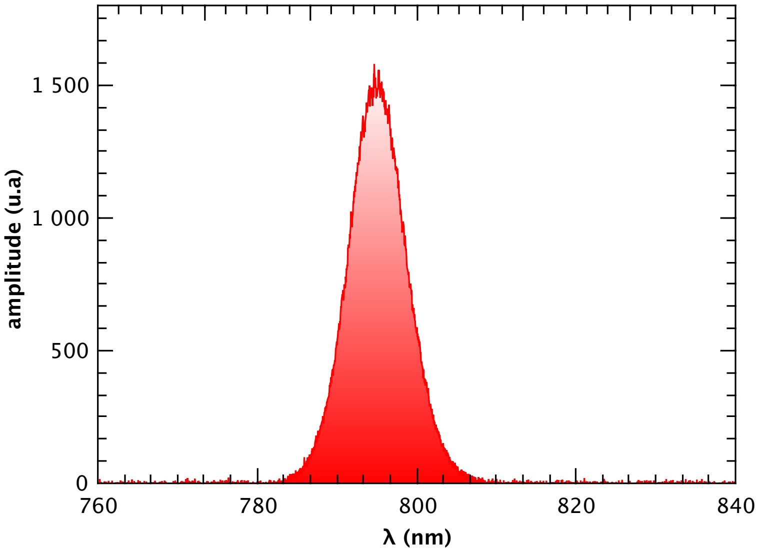

Figure 2.2 – Output spectrum of the MIRA laser.

2.1.2 The compressor

2.1.2.1 correction of the temporal chirp

As explained in the first chapter, pulse light has a significative drawback: it is sensitive to dispersion. We have to pre-compensate this effect. Indeed, as we saw, the dispersion (negative or positive) makes the pulse longer, reduces its peak power and the non-linear effect needed to produce the states we are interested in.
The dispersion is also the reason why we do not use any optical fiber in our experiment, the effect of air is negligible compared with glass, although we still need some components like polarizing beamsplitters (PBS) and non-linear crystals. They add a positive quadratic dispersion to the light, which means we can pre-compensate it knowing the path between the laser and the SPOPO cavity[Chanteloup 98].
This is the role of the compressor. As its name suggests, it can set the Φ_2 value of pulses. On the optical table, we choose the scheme composed by 2 SF10 prisms represented in figure 2.3 below[Fork 84]:

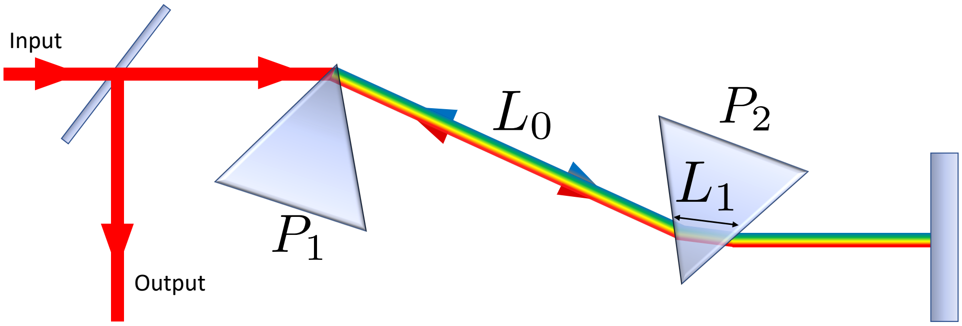

Figure 2.3 – Scheme of the compressor

If we consider the beam coming in the compressor with a spectral phase of $\phi(\omega)$, the compressor will add an extra phase Φ_2' whose expression is given by[Pinel 10]:

$$\Phi_2' = -8\frac{L_0\lambda_0^3}{2\pi c^2}(\frac{dn}{d\lambda})^2 + \frac{\lambda_0^3 L_1}{\pi c^2}\frac{d^2n}{d\lambda^2} \tag{2.1}$$

where n denotes the optical index of the propagation medium. We can make few comments about the expression of Φ_2'. The term proportional to L_0, the distance between both prisms, is negative which means the larger this distance, the more the compressor pre-compensates the positive dispersion on the table. It is the opposite for the second term, which is positive and which depends on L_1 the distance of propagation into the second prism. On the optical table, the distance L_0 is around 99 cm, we then set the position of the second prism and L_1 by optimizing on a non-linear effect described on next paragraph, the second harmonic generation (SHG) and the second order dispersion is measured with an auto-correlator. We choose the SHG and not the non-linear effect in the SPOPO itself because two different beams with different dispersions are involved in the non-linear process of the cavity while the SHG is based on only one beam as it is going to be developed later in this chapter. Besides, there are only few lenses between the SHG crystal and the crystal inside the SPOPO cavity which makes the difference of dispersion between these two positions negligible.

When both prisms are set, we can measure the dispersion at the output of the compressor using an auto-correlator. This instrument aims to measure the autocorrelation function of pulses. We call respectively $\Delta\tau_{A,0}$ and $\Delta\tau_{p,0}$ the time duration we read on the auto-correlator and the one of the pulse in the absence of any temporal chirp. We say the pulse is Fourier limited in this case. We assume the envelope of the pulse is gaussian whatever the dispersion is, we have the relation: $\Delta\tau_{A,\Phi_2'} = \sqrt{2}\Delta\tau_{p,\Phi_2'}$. Hence we deduce the pulse duration just by measuring the duration on the auto-correlator and we obtain, from the pulse duration measurement, the dispersion Φ_2' using the relation:

$$\Delta\tau_{p,\Phi_2'} = \Delta\tau_{p,0}\sqrt{1 + (\frac{\Phi_2'}{\Delta\tau_{p,0}^2})^2} \tag{2.2}$$

where $\Delta\tau_{p,\Phi_2'}$ denotes the duration of the temporally chirped pulse train. We measure before the compressor the following dispersion $\Phi'_{2,before} = 8105fs^2$ and after: $\Phi'_{2,after} = -5000fs^2$. We note the value of the chirp before the compressor is quite large. It is because of the optics used for the beam preparation.

2.1.2.2 Spatial chirp

In the compressor, we align the prisms at the Brewster angle, which means most of the beam is refracted, a slight fraction is reflected and lost. However this alignment is never optimal and by looking the light at the output of the setup, we observe angular dispersion also called spatial chirp[G. Pretzler 00, Akturk 05]. This type of dispersion is due to the coupling between the frequency and the direction of the beam. A way to evaluate this effect is to inject the light through a pinhole located on the focal plan of a lens and measure the shift of the central wavelength by translating the pinhole along the x-axis and the y-axis (when the z-axis is the direction of propagation). These both shifts evaluated in nm give us the information about the vertical and horizontal chirp. The Full Half Width Maximum of the MIRA output beam being around 10 nm, the aim is to keep the angular dispersion, in both directions, below 0.5 nm throughout the beam propagation along the experiment.

A way to eliminate the vertical chirp from the compressor is to induce a small angle on the prism P_1 to make them not parallel to the table. For the horizontal chirp, we have to "beam walk" between the front mirror of the compressor and the rotation of the first prism along the perpendicular direction to the table [Osvay 04]. The case where the spatial chirp is eliminated and the temporal chirp is pre-compensated corresponds to a case where losses are induced since the prisms are not anymore at Brewster angle. Nonetheless, the amount of lost power is negligible.

2.2 Non-linear optics

Once the temporal dispersion has been pre-compensated, we separate the beam in two paths using a PBS. One beam is dedicated for the detection, which will be the object of the next chapter and the other one is propagated in direction of the SPOPO cavity. In this part we will present some elements of non-linear optics for a better understanding of the following sections[Bloembergen 82, Boyd 07].

2.2.1 Equation of propagation in non-linear medium

Here we focus on the monochromatic case. We will deal with the train pulse on the next section. Optical non-linear phenomena appears when the optical response of the medium passed through by the light is not anymore linear. Indeed, in this kind of materials, the presence of a field can induce a mechanical response of electrons and nucleus, which implies the creation of an additional field. Let us introduce the two vectors: $\boldsymbol{D}(\boldsymbol{r},t) = \boldsymbol{E}(\boldsymbol{r},t) + \boldsymbol{P}(\boldsymbol{r},t)$ and $\boldsymbol{H}(\boldsymbol{r},t) = \frac{\boldsymbol{B}(\boldsymbol{r},t)}{\mu_0}$ where $\boldsymbol{P}$ is the density of dipole moments and is called the polarization vector. We can easily show that, in the linear regime, it is proportional to the electric field such as:

$$\boldsymbol{P}(\boldsymbol{r},\omega) = \epsilon_0 \boldsymbol{\chi}_e(\omega)\boldsymbol{E}(\boldsymbol{r},\omega) \tag{2.3}$$

$\boldsymbol{\chi}_e$ is called the electric susceptibility. It is a tensor where each component is related to a polarization direction. Here, we only treat the case where the polarization is preserved by the tensor, which is the case in the experiment. By injecting the vectors $\boldsymbol{P}$ and $\boldsymbol{H}$ in the Maxwell equations we can find a more appropriate way to write the propagation equation:

$$\Delta\mathbf{E} - \frac{1}{c^2}\frac{\partial^2\mathbf{E}}{\partial t^2} = \frac{1}{\epsilon_0 c^2}\frac{\partial^2\mathbf{P}}{\partial t^2} \tag{2.4}$$

When light power is large enough the mechanical response of the particles is not anymore linear. Hence we can express $\boldsymbol{P}$ as:

$$\boldsymbol{P} = \boldsymbol{P}_L + \boldsymbol{P}_{NL} \tag{2.5}$$

where $\boldsymbol{P}_L$ and $\boldsymbol{P}_{NL}$ stand respectively for the linear and non-linear responses of $\boldsymbol{P}$. Because of the non-linear response, equation (2.3) has to be completed by a Taylor expansion. In addition, because of polarization conservation, we can use the scalar notation. Finally, we have the relation:

$$P(\boldsymbol{r},t) = \epsilon_0 \left(\chi_e^{(1)} E(\boldsymbol{r},t) + \chi_e^{(2)} E(\boldsymbol{r},t)^2 + \chi_e^{(2)} E(\boldsymbol{r},t)^3 + ...\right) \tag{2.6}$$

with

$$P_L(\boldsymbol{r},t) = \epsilon_0 \chi_e^{(1)} E(\boldsymbol{r},t) \tag{2.7}$$

$$P_{NL}(\boldsymbol{r},t) = \epsilon_0 \sum_n \chi_e^{(n)} E^n(\boldsymbol{r},t) \tag{2.8}$$

where $\chi_e^{(n)}$ labels the electric susceptibility for n^{th} order of the non-linear response. Finally by injecting (2.5) in (2.4), we get:

$$\Delta E(\boldsymbol{r},t) - \frac{1+\chi_e^{(1)}}{c^2} \frac{\partial^2 E(\boldsymbol{r},t)}{\partial t^2} = \frac{\partial^2 P_{NL}(\boldsymbol{r},t)}{\partial t^2} \tag{2.9}$$

Using the notations introduced in the first chapter such as $E(\boldsymbol{r},t) = f(\boldsymbol{r},t)\mathrm{e}^{-i(\omega t - k(\omega)z)}$ and denoting f the mode of the electric field, we have in a Cartesian reference frame:

$$\Delta E = \left(\frac{\partial^2 f}{\partial x^2} + \frac{\partial^2 f}{\partial y^2} + \frac{\partial^2 f}{\partial z^2} + 2ik(\omega)\frac{\partial f}{\partial z} - k^2(\omega) f\right) e^{ikz} \tag{2.10}$$

The hypothesis of the slowly varying envelope compared with the variations of the wave is also valid here. We also assume, that the derivative along x and y are negligible according to the paraxial approximation. We have thus:

$$\left|\frac{\partial^2 f}{\partial z^2}\right| \ll \left|k \frac{\partial f}{\partial z}\right| \tag{2.11}$$

Hence, the equation (2.9) in the positive frequency domain is:

$$\frac{\partial f}{\partial z}(z,\omega) = \frac{i\omega}{2\epsilon_0 n c} P_{NL}^{(+)}(z,\omega) e^{-ik(\omega)z} \tag{2.12}$$

This equation is the starting point to describe several optical non-linear effects such as second harmonic generation or parametric down conversion.

2.2.2 Second harmonic generation

The second harmonic generation corresponds, in the monochromatic case, to a phenomenon where two *signal* photons of frequency ω interact together with the non-linear medium to create one *pump* photon, whose frequency is, by energy conservation, 2ω.

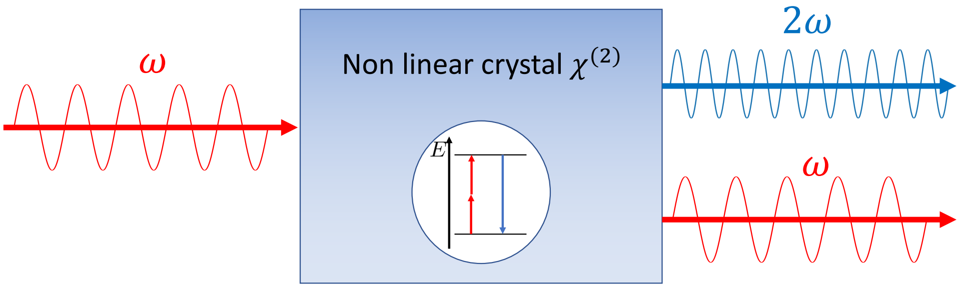

Figure 2.4 – Scheme of Second Harmonic Generation in single mode case.

To study this type of non-linear behaviour, we start from the equation (2.12) using the notation that we just have introduced:

$$\frac{\partial f_p}{\partial z}(z,\omega) = \frac{i\omega}{2\epsilon nc} P_{NL}^{(+)} e^{-ik(\omega)z} \tag{2.13}$$

with:

$$P_{NL}^{(+)} = \epsilon_0 \chi^{(2)} E_s^{(+)}(z,\omega) E_s^{(+)}(z,\omega) \tag{2.14}$$

By replacing the expression of the *signal* field, we have:

$$\frac{\partial f_p}{\partial z}(z,\omega) = \frac{i\omega}{nc} f_s^2(z,\omega) e^{-i\Delta k(\omega)z} \tag{2.15}$$

with:

$$\Delta k(\omega) = k(2\omega) - 2k(\omega) \tag{2.16}$$

We assume that the power of the *signal* beam is constant along the crystal. We can thus easily integrate the last equation over z and we obtain:

$$f_p(z,\omega) = \frac{i\omega l_c \chi^{(2)}(2\omega)}{nc} f_s^2(\omega) \mathrm{sinc}(\frac{\Delta k(\omega) l_c}{2}) \tag{2.17}$$

We note from this result that the amplitude of the pump mode is linear with the square of the signal one. Another important feature is the presence of the sinc term. Indeed, it means that there is a optimal length $l_{c,op}$ of the crystal, when $l_c > l_{c,op}$ the conversion is decreasing.

2.2.3 Parametric down convertion

The parametric down conversion (PDC) is also a non-linear process, where a photon called pump is converted into two photons, the signal and the idler. We have energy conservation: $\omega_p = \omega_i + \omega_s$ and we introduce, as for the SHG, the phase matching term: $\Delta k = k(\omega_p) - k(\omega_i) - k(\omega_s)$. There exists differents types of conversions:

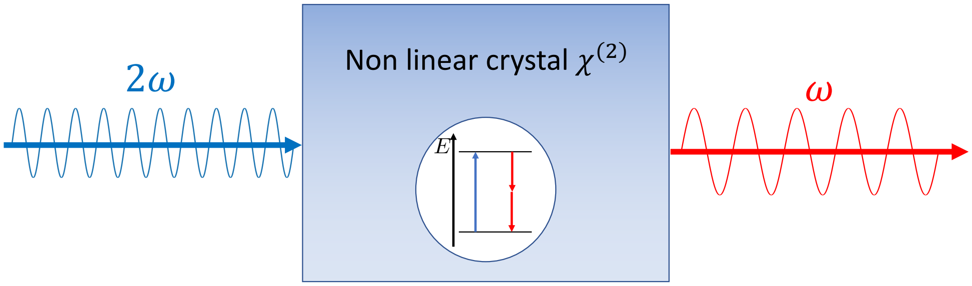

Figure 2.5 – Scheme of Paramagnetic Down Conservation in single mode case.

- Type 0: all the beams have the same polarization
- Type I: Signal and idler have identical polarizations, which is orthogonal to those of the pump.
- Type II: Signal and idler have orthogonal polarizations. One of the two beam shares its polarization with the pump.

In the degenerate case we have $\omega_i = \omega_s = \omega$ and by assuming we have conservation of the momentum, meaning $\Delta k = 0$, we derive the equation (2.12) as:

$$\frac{df_s}{dz} = \frac{i\omega\chi^{(2)}(2\omega,\omega)}{2\epsilon_0 nc} f_p(z,2\omega) f_s^*(z,\omega) \tag{2.18}$$

Taking the derivative of this equation we can find that f_s is solution of the following linear second order differential equation:

$$\frac{d^2 f_s}{dz^2} = \gamma^2 f_s(z,\omega) \tag{2.19}$$

with

$$\gamma(z) = \frac{\omega\chi^{(2)}}{2\epsilon_0 nc} \mid f_p(z,2\omega) \mid \tag{2.20}$$

We assume the pump field is constant along the non-linear crystal because there is no pump depletion, f_s is thus linear combination of exponentials whose parameters are γ and $-\gamma$, which are linear with the amplitude of f_p (the function γ does not depends anymore of z in this context). Hence, the signal field is amplified or deamplified depending on the exponential argument sign.

2.2.4 Non-linear process: the multimode case

In the precedent subsection, we have introduced the two non-linear optical effects we use in the experiment to produce quantum states. However, we simplified the derivation to the single mode case. If we consider a pulse train, it is possible to observe other frequencies combinations as show the figures 2.6 and 2.9.

2.2.4.1 Second harmonic generation in multimode case

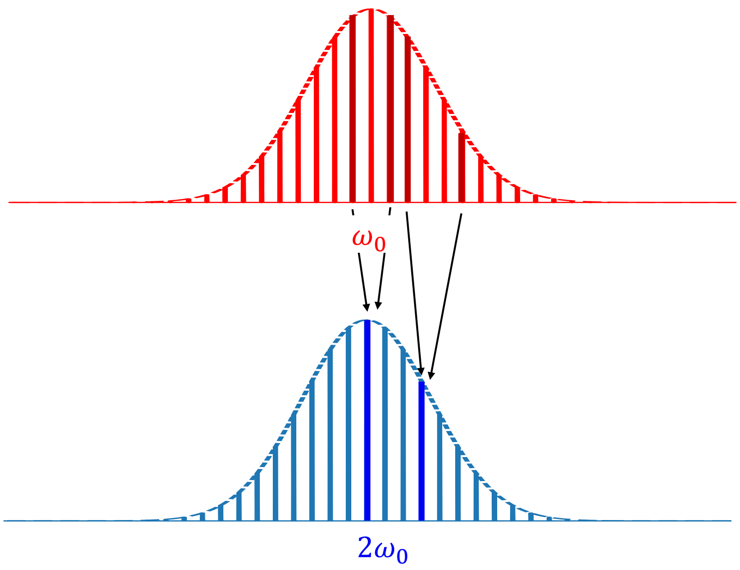

Figure 2.6 – Exemple of conversion during SHG non-linear process in frequency comb case.

Let's start with the second harmonic effect. The multi-mode version of equation 2.13 is written by adding an integral to consider all possible frequency combinations. We express thus the polarization in the frequency domain as:

$$P_{NL}^{(+,2)}(z,\omega) = \epsilon_0 \chi^{(2)} \int E_s^{(+)}(z,\omega') E_s^{(+)}(z,\omega-\omega') \frac{d\omega'}{2\pi} \tag{2.21}$$

For a frequency comb, because of the narrowband hypothesis, the frequency ω and $\omega' - \omega$ are close. We can thus assume that: $\chi^{(2)}(\omega_i,\omega_j) \approx \chi^{(2)}$ and then by injecting the new formula of P_p into the equation (2.12), we get with similar derivation:

$$f_p(z,\omega) = \frac{i\omega\chi^{(2)} l_c}{2nc} \int f_s(z,\omega') f_s(z,\omega-\omega') \Phi(\omega,\omega') \frac{d\omega'}{2\pi} \tag{2.22}$$

where $\Phi(\omega,\omega')$ is the phase matching defined as:

$$\Phi(\omega,\omega') = \operatorname{sinc}\left(\frac{\Delta k(\omega,\omega') l_c}{2}\right) \tag{2.23}$$

where

$$\Delta k(\omega,\omega') = k_p(\omega) - k_s(\omega-\omega') - k_s(\omega') \tag{2.24}$$

As we saw in the first part, in the pulse regime we have to consider the effect of dispersion. Here, since the phase matching depends on $\Delta k(\omega, \omega')$ we have to use Taylor development of both k_p and k_s around the center frequencies ω_0 and $2\omega_0$ to find the effective phase matching:

$$\Delta k(\omega, \omega') = \Delta k(2\omega_0, \omega_0) + \left(\frac{dk_s}{d\omega} - \frac{dk_p}{d\omega}(\omega - 2\omega_0\right) + \frac{1}{2}\left(\frac{dk_s^2}{d^2\omega}\right)(\omega - 2\omega_0)^2 - \frac{dk_s^2}{d^2\omega}(\omega' - \omega_0)(\omega - \omega' - \omega_0) \quad (2.25)$$

where the term $\Delta k(2\omega_0, \omega_0)$ corresponds to the mode matching term in the single mode case *i.e* $k_p(2\omega_0) = 2k_s(\omega_0)$. We can assume $\Delta k(2\omega, \omega_0) = 0$ and we keep only the first order, the relation becomes thus:

$$\Delta k(\omega, \omega') \approx \left(\frac{dk_s}{d\omega} - \frac{dk_p}{d\omega}\right)(\omega - 2\omega_0) \quad (2.26)$$

Hence, in this approximation Φ is independent of ω' and can be taken out from the integral. We can then write $f_p(z, \omega)$ as:

$$f_p(z, \omega) = \frac{i\omega\chi^{(2)} l_c}{2nc}\Phi(\omega) f_s * f_s(z, \omega) \quad (2.27)$$

We observe that f_p is linear with the auto-convolution of the function f_s at the input of the crystal, whose spectrum is a frequency comb with a gaussian envelope 2.7.

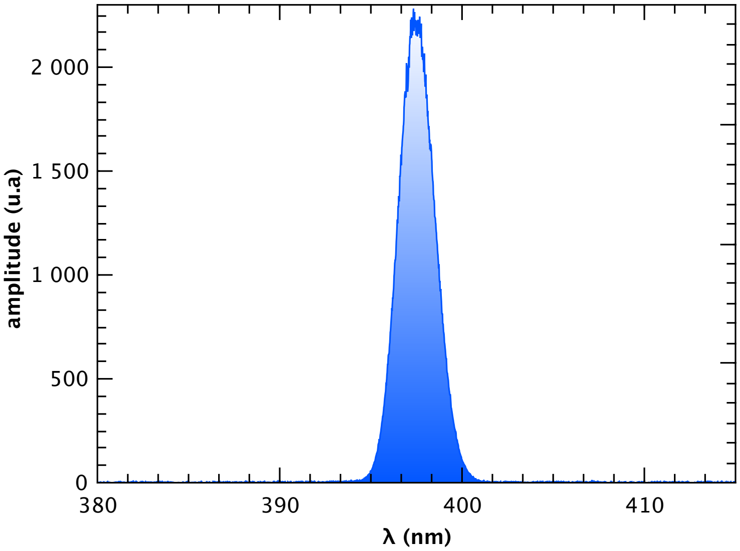

Figure 2.7 – Spectrum of blue beam at the output of the SHG.

We can then derive equation (2.27) to evaluate the power of the beam at the output of the SHG. Here we consider the field as a gaussian beam and not anymore as a plane wave, which means we can write in the frequency domain:

$$E^{(+)}(x,y,z,\omega) = E_0 u(x,y,z)\tilde{s}(\omega)e^{ik(\omega)z} \tag{2.28}$$

Then, from equation (1.33) we can express the power of the pump beam as:

$$\mathcal{P}_p = 2\epsilon_0 n_p c f_r \int_{\mathbb{R}^2} \mathrm{d}x\mathrm{d}y u_p(x,y,z) \int_{\mathbb{R}} \mathrm{d}\omega \mid E_{0,p}\tilde{s}_p(\omega) \mid^2 \tag{2.29}$$

we can replace the argument inside the integral on ω by the expression found in (2.27):

$$\mathcal{P}_p = 2\epsilon_0 n_p c f_r \int_{\mathbb{R}^2} \mathrm{d}x\mathrm{d}y u_p(x,y,z) \int_{\mathbb{R}} \mathrm{d}\omega \mid E_{0,s}^2 \frac{i\omega\chi^{(2)} l_c}{2n_s c}\Phi(\omega)\tilde{s}_s * \tilde{s}_s(\omega) \mid^2 \tag{2.30}$$

We know $E_{0,s} = \sqrt{\frac{P_s}{2n_s c\epsilon_0\omega_r S_{eff,s}}}$ where $S_{eff,s}$ is the effective section for the input beam. For the SHG beam, we can also define an equivalent surface $S_{eff,p}(z) = \int_{\mathbb{R}^2} \mathrm{d}x\mathrm{d}y\, u(x,y,z)$. If we define the integral $I = \int_{\mathbb{R}} \omega\Phi(\omega)\tilde{s}_s * \tilde{s}_s(\omega)\mathrm{d}\omega$, we find

$$\mathcal{P}_p = \frac{n_p S_{eff,p}{\chi^{(2)}}^2 l_c^2}{2n_s^2 c\epsilon_0\omega_r S_{eff,s}^2} I.\mathcal{P}_s^2 \tag{2.31}$$

From this last equation, we can deduce that the converted power from the SHG effect is quadratic with the input power. We observe the same dependency in the lab as shown in figure 2.8.

2.2.4.2 Parametric down conversion in the multimode regime

Like for the SHG case, to compute the derivation of the multimode PDC, we take inspiration from the single mode scenario. We start by rewriting P_{NL} taking into account all the frequency combinations of the non-linear process:

$$P_{NL}^{(+)}(z,\omega) = \int \chi^{(2)} E_p^{(+)}(z,\omega+\omega')E_s^{(-)}(\omega')\frac{d\omega}{2\pi} \tag{2.32}$$

By injecting this expression of the polarization into (2.12) we get:

$$\frac{\partial f_s}{\partial z}(z,\omega) = \frac{i\omega\chi^{(2)}}{2n_s c}E_{0,p}\int f_p(z,\omega+\omega')f_s^*(z,\omega')\mathrm{e}^{i\Delta k(\omega,\omega')z}\frac{\mathrm{d}\omega'}{\sqrt{2\pi}} \tag{2.33}$$

where:

$$\Delta k(\omega,\omega') = k_p(\omega+\omega') - k_s(\omega') - k_s(\omega) \tag{2.34}$$

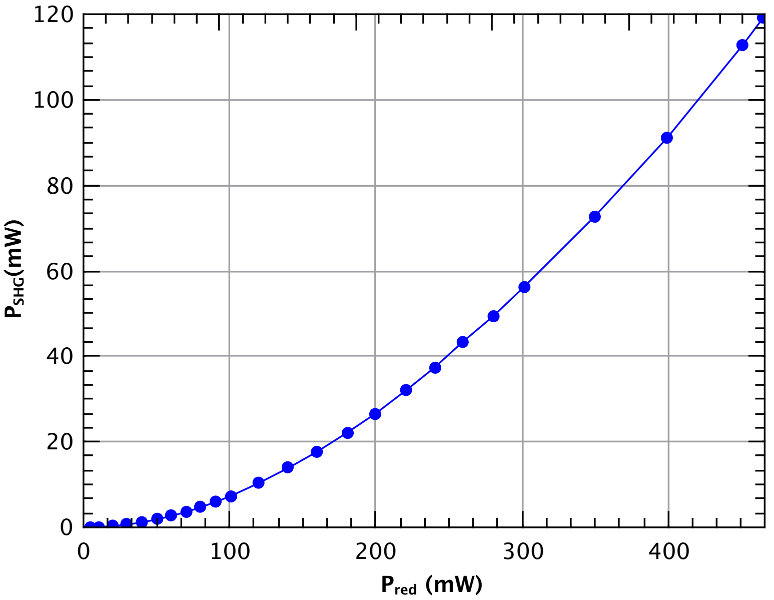

Figure 2.8 – Measurement of the power converted from SHG as a function of on the signal power injected through the crystal. Error bar are too small to be visible.

Another way to write equation (2.33) is by introducing the integral operator $\mathcal{K}$ such as:

$$\frac{\partial f_s}{\partial z}(z,\omega) = \mathcal{K}(z) f_s^*(z,\omega) \tag{2.35}$$

where $\mathcal{K}$ is an integral transform with $K(z,\omega,\omega')$ as kernel. We have for a function $h(z,\omega)$:

$$\mathcal{K}(z,\omega,\omega')h(z,\omega) := \int_{\mathbb{R}} \mathrm{d}\omega' K(z,\omega,\omega')h(z,\omega') \tag{2.36}$$

with

$$K(z,\omega,\omega') = i\frac{\omega\chi^{(2)}}{2\sqrt{2\pi}n_s c}E_{p,0}f_p(z,\omega+\omega')\mathrm{e}^{i\Delta k(\omega,\omega')z} \tag{2.37}$$

We note we can also use this formalism to express the same differential equation but this time for the complex conjugate of the signal field:

$$\frac{\partial f_s^*}{\partial z}(z,\omega) = \mathcal{K}^*(z) f_s(z,\omega) \tag{2.38}$$

Hence, If we define the two components vector:

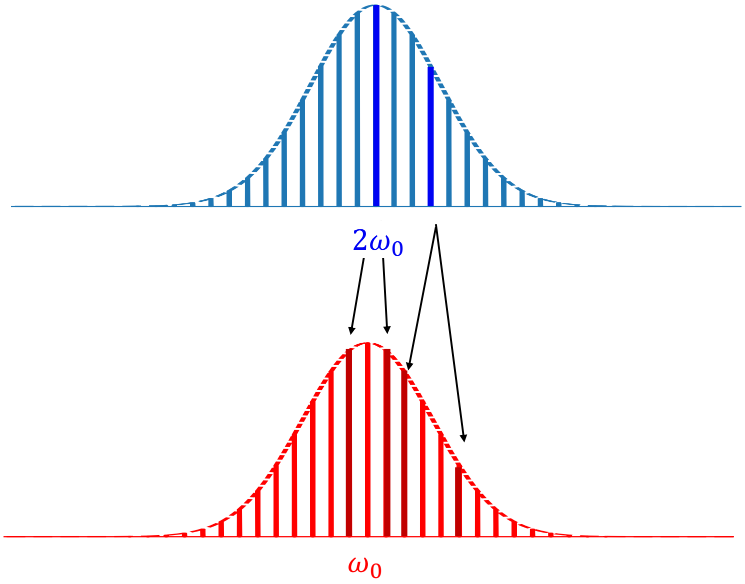

Figure 2.9 – Exemple of conversion during PDC non-linear process in frequency comb case.

$$\mathbf{f}_s = \begin{pmatrix} f_s \\ f_s^* \end{pmatrix}$$

we can write the following matrix linear differential equation:

$$\frac{\partial \mathbf{f}_s}{\partial z}(z, \omega) = \boldsymbol{\mathcal{K}}(z)\mathbf{f}_s(z, \omega) \tag{2.39}$$

with

$$\boldsymbol{\mathcal{K}}(z) = \begin{pmatrix} 0 & \mathcal{K}(z) \\ \mathcal{K}(z) & 0 \end{pmatrix}$$

We can derive this differential equation by using the Magnus expansion [Lipfert 18], which allows us to deduce the output field of crystal. We denote $\boldsymbol{f}_{s,in}$ and $\boldsymbol{f}_{s,out}$ the signal field vectors respectively for $z = z_{in}$ and $z = z_{out}$. Beside, in the limit where the pump power is weak, we assume we keep only the first order from the Magnus expansion and we get:

$$\boldsymbol{f}_{s,out} = \exp(\sum_{k=0}^{\infty} \boldsymbol{\mathcal{S}}_0)\boldsymbol{f}_{s,in} \tag{2.40}$$

where

$$\boldsymbol{\mathcal{S}}_0 = \int_{z_{in}}^{z_{out}} \mathrm{d}z \boldsymbol{\mathcal{K}}(z) \tag{2.41}$$

If we assume there is no pump depletion, which means the pump power is constant along the non-linear crystal and the integral signs can be exchanged in the derivation of the kernel of $\boldsymbol{\mathcal{S}}_0$. We also assume the bandwidth of the frequency comb is small then we finally find:

$$\boldsymbol{S}_0 = \int_{z_{in}}^{z_{out}} \mathrm{d}z \int \mathrm{d}\omega \boldsymbol{K}(z,\omega,\omega') = ig\boldsymbol{f}_p(\omega+\omega')\Phi(\omega,\omega')$$

$$\text{with} \qquad g = \frac{\omega_0\chi^{(2)} l_c E_{p,0}}{2\sqrt{2\pi}n_s c} \quad \text{and} \quad \Phi(\omega,\omega') = \operatorname{sinc}\left(\frac{\Delta k(\omega,\omega') l_c}{2}\right) \tag{2.42}$$

As for the SHG case, Φ is called the phase matching function. Let's introduce the notation:

$$\boldsymbol{L}(\omega,\omega') = \boldsymbol{f}_p(\omega+\omega')\Phi(\omega,\omega') \tag{2.43}$$

We call this function the joint spectral distribution. We can interpret it as a probability distribution to observe the conversion $\omega_p \to (\omega,\omega')$ during the PDC of the blue frequency comb as represented in figure 2.9. We make the hypothesis according to which the pump spectrum has a constant phase. Hence, if we note θ_p this phase, the vector $\boldsymbol{f}$ becomes:

$$\boldsymbol{f}_p(\omega+\omega') = \begin{pmatrix} \mathrm{e}^{i\theta_p} f_p(\omega+\omega') \\ \mathrm{e}^{-i\theta_p} f_p(\omega+\omega') \end{pmatrix} \tag{2.44}$$

where the function f_p is real. In order to make the derivation more convenient we assume $\theta_p = 0$. Hence the function $\boldsymbol{L}$ is real and symmetric. We can find an orthogonal basis of frequency modes were $\boldsymbol{L}$ is diagonal:

$$\mathbf{L} = \boldsymbol{V}\boldsymbol{\Lambda}\boldsymbol{V}^T \tag{2.45}$$

the vector composing $\boldsymbol{V}$ are the eigenvectors of the transition matrix called eigenmodes and we denote $(\Lambda_1, ..., \Lambda_n)$ as the eigenvalues. We thus write:

$$L(\omega,\omega') = \sum_k \Lambda_k s_k(\omega) s_k^*(\omega') \tag{2.46}$$

where s_k are the eigenvectors which are linear combination of modes related to the teeth of the comb. Until now, the derivation has been focused on the modes and a classical perspective. It is actually quiet easy to adapt it for a quantum version. Indeed, as we saw in chapter 1, to move from one version to another one, we just have to replace the mode s_k by corresponding creation operator $\hat{s}_k^\dagger$. We can thus write the corresponding Hamiltonian:

$$\hat{H}_{PDC} \propto \hbar g \sum_k \Lambda_k \hat{s}_k^{\dagger 2} + h.c \tag{2.47}$$

Finally, we get the unitary transformation:

$$U_T = \mathrm{e}^{\frac{i}{\hbar}\hat{H}_{PDC}t_0} = \mathrm{e}^{\frac{i}{\hbar c}\hat{H}_{PDC}l_c} \tag{2.48}$$

$$U_T = \mathrm{e}^{(\frac{g l_c}{c} \sum_k \Lambda_k \hat{s}_k^{\dagger 2} + h.c)} \tag{2.49}$$

where t_0 is the interaction time $i.e$ the propagation time through the crystal and l_c the crystal length. We actually recognize a multimode squeezing operator: each mode k is squeezed or anti-squeezed depending on the sign of Λ_k.

2.3 Optical Parametric Oscillator

An optical parametric oscillator is a cavity where a non-linear crystal amplifies or de-amplifies light according to the PDC theory introduced above in 2.2.4.2. The SPOPO is a multimode version of the OPO where each frequency mode of the comb is resonant with the cavity [Araujo 10]. In figure 2.10 a scheme of an OPO cavity is given. The SPOPO cavity, differently to the Fabry-Perot introduced in chapter 1 , is a ring cavity. Indeed, for modeling such cavity we have to add a supplementary mirror and in particular a non-linear crystals (BiBO) placed at the waist of the cavity. Nonetheless, the theories about the wave propagation and the resonance condition inside the cavity remain the same of the Fabry Perot. Here, we directly treat the quantum case in the single mode regime where the squeezing parameter is denoted as ζ, from the notation of the figure 2.10 we deduce the following relations:

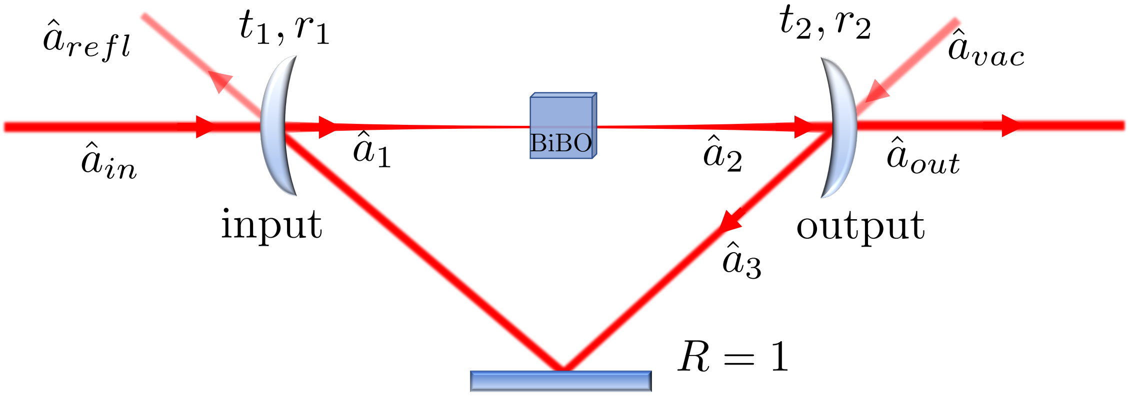

Figure 2.10 – OPO cavity scheme.

- $\hat{a}_1 = t_1 \hat{a}_{in} + r_1 \hat{a}_3$
- $\hat{a}_{refl} = t_1 \hat{a}_3 - r_1 \hat{a}_{in}$
- $\hat{a}_{out} = t_2 \hat{a}_2 - r_2 \hat{a}_{vac}$
- $\hat{a}_3 = t_2 \hat{a}_{vac} + r_2 \hat{a}_2$

- $\hat{a}_2 = \mathrm{ch}(\zeta)\hat{a}_1^\dagger - \mathrm{sh}(\zeta)\hat{a}_1$

And by computing these relations, we get:

$$\hat{q}_{out} = \frac{t_1 t_2 \mathrm{e}^{-\zeta}\hat{q}_{in} + (r_1\mathrm{e}^{-\zeta} - r_2)\hat{q}_{vac}}{1 - r_1 r_2 \mathrm{e}^{-\zeta}} \tag{2.50}$$

$$\hat{p}_{out} = \frac{t_1 t_2 \mathrm{e}^{+\zeta}\hat{p}_{in} + (r_1\mathrm{e}^{+\zeta} - r_2)\hat{p}_{vac}}{1 - r_1 r_2 \mathrm{e}^{+\zeta}} \tag{2.51}$$

We assume the input beam is the vacuum state, whose standard deviation is 1, we have then: $\langle\hat{q}_{out}\rangle = \langle\hat{p}_{out}\rangle$=0. However, the standard deviations, which contain the information on the squeezing, are not zero. Indeed we can express the variances of the output quadrature operators as:

$$\langle\Delta^2\hat{q}_{out}\rangle = \frac{t_1^2 t_2^2 \mathrm{e}^{-2\zeta} + (r_1\mathrm{e}^{-\zeta} - r_2)^2}{1 - r_1 r_2 \mathrm{e}^{-\zeta}} \tag{2.52}$$

$$\langle\Delta^2\hat{p}_{out}\rangle = \frac{t_1^2 t_2^2 \mathrm{e}^{+2\zeta} + (r_1\mathrm{e}^{+\zeta} - r_2)^2}{1 - r_1 r_2 \mathrm{e}^{+\zeta}} \tag{2.53}$$

We denote ζ_{th} the threshold of the cavity. When $\zeta \geq \zeta_{th}$ the cavity is in a regime of self oscillations. It corresponds mathematically to the case where one of the denominators of (2.52) and (2.53) is zero. We have:

$$\zeta_{th} = \ln\left(\frac{1}{r_1 r_2}\right) \tag{2.54}$$

The figure 2.11 represents the results of the calculation of (2.52) and (2.53) as a function of $\epsilon = \zeta/\zeta_{th}$. This calculation has been made for an output coupler transmission of $T_2 = 0.3$. The plot shows the effect of losses on squeezing and purity values when the SPOPO is considered as a single mode OPO.

Equation (2.47) tells us that in the right basis of modes, the SPOPO acts like a collection of squeezer operators where Λ_k are the squeezing parameters. These eigenvalues and their corresponding eigenvectors have been derived in C. Jacquard thesis [Jacquard 17]. The eigenvalues are alternately positive and negative. Hence, since the sign indicates the squeezing direction, if the even modes are squeezed along the q quadrature, the odd ones will be squeezed on the orthogonal direction, along the p quadrature (figure 2.12)

2.4 The SPOPO cavity

2.4.1 Description of the experimental setup

Here, we describe the main piece of the experiment, the SPOPO. As we know, the cavity length has to match the one of the laser source, $L \approx 3.92$ m. On the optical

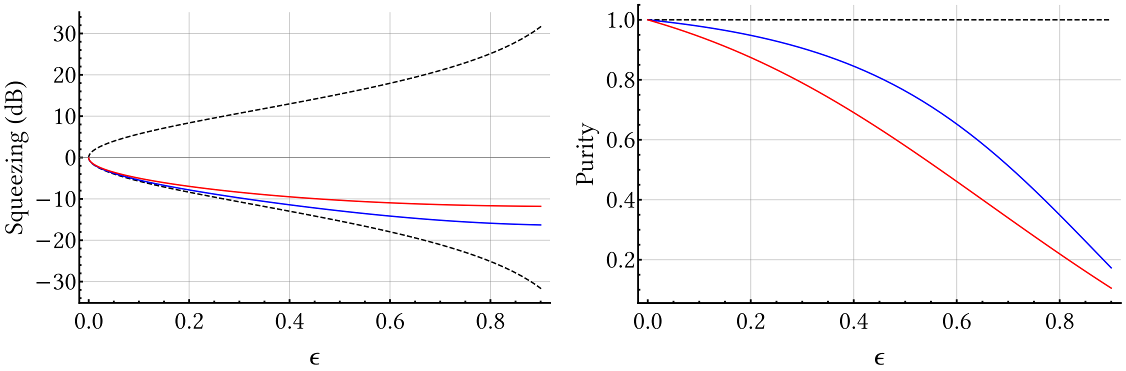

Figure 2.11 – *left*: Calculation of squeezing values as a function of ϵ for different values of r_1: black dash line (along with anti-squeezing): $r_1 = 1$; blue line: $\sqrt{r_1} = 0.99$; red line: $\sqrt{r_1} = 0.97$ *right*: Purity of the states with respect to ϵ. The figure is taken from [Jacquard 17].

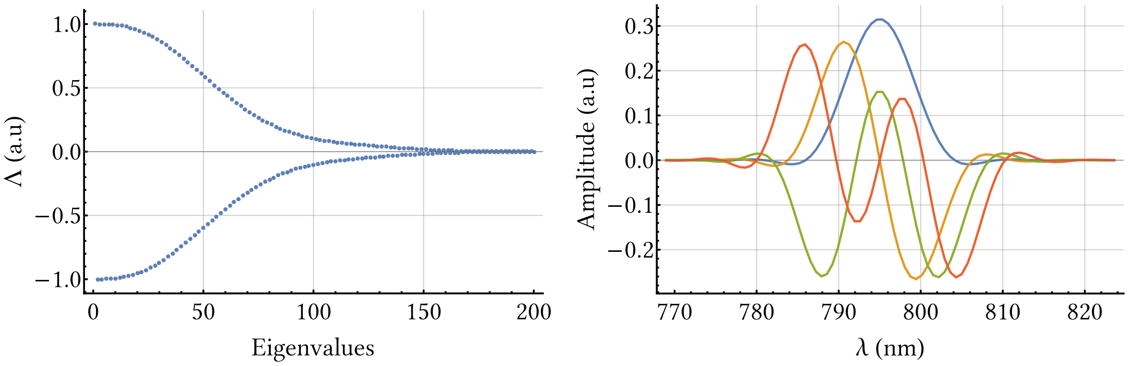

Figure 2.12 – *left* Calculation of Λ_k/Λ_0 as a function of the supermodes when the nonlinear crystal is a 2mm BiBO. *right*: Spectrum of the four first supermodes. The figure is taken from [Jacquard 17].

table, we reach this length by folding the path using 13 mirrors as shown in figure 2.13. Some of these optics are also added to ensure control specific parameters:

- M1 is the input coupler with a reflectivity $R = 99.85\%$ and M10 is the output coupler. For this beam splitter we have three optional transmissivity $T = 20; 30; 50\%$. All along my PhD, we used the 20% one.

- M2 and M13 are spherical mirrors with a curvature radius $R = 250$ mm. M4 and M11 are also concave mirrors but with a larger radius: $R = 6$ m. They aim to control the size of the beam width and make the waist of the beam 38 μm in the non-linear crystal.

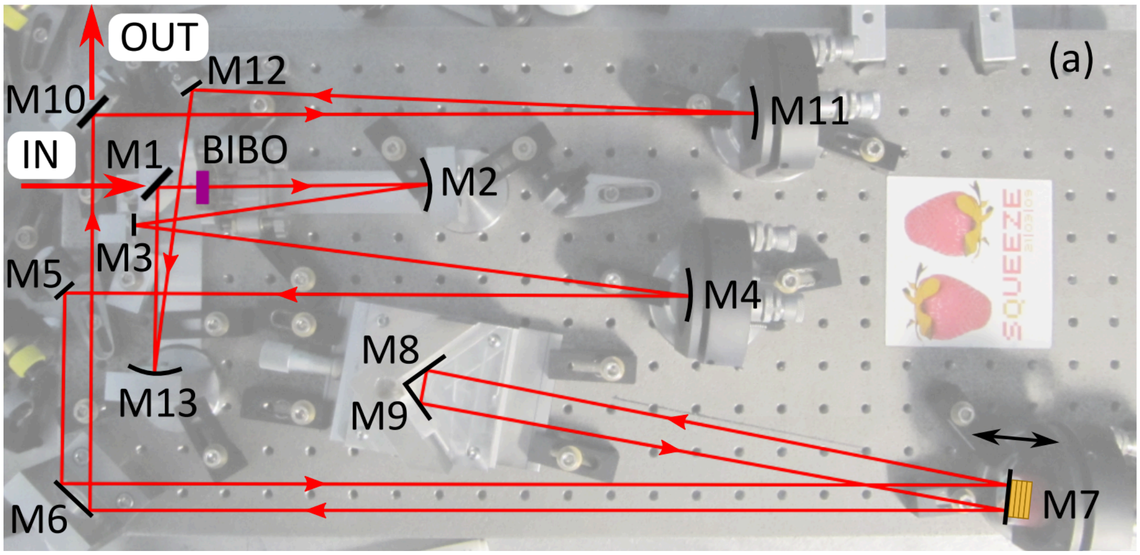

Figure 2.13 – Picture of the SPOPO on the optical table

- M3 and M7 have a special coating to compensate 150 fs^2 of the dispersion from the propagation inside the SPOPO.
- The non-linear crystal is a 2mm BiBO crystal which is just after the input coupler.

2.4.2 Beam propagating through the SPOPO

Three different beams are propagated through the cavity. The one used to pump the SPOPO directly comes from the SHG converted light. It is a blue beam whose spectrum is represented in figure 2.7
Two other beams, taken from the compressor output and whose spectrum is centered on $\lambda_0 = 795$ nm are also injected into the cavity. First, the lock beam. As the name suggests, it is used to lock one cavity parameter: the length. To do so, we use the Pound Drever Hall method [Drever 83]. The lock field, modulated with a EOM, counterpropagats through the SPOPO, then the light after the output coupler is collected by a photodiode. The demodulated signal is sent to a PID, which generates an error signal and the ouput signal, which is amplified and sent to the piezo-electric crystal. This is mounted on the mirror M7 in order to correct the cavity-length fluctuations.
Secondly, the seed beam ensures the good alignment of the cavity and it is a reference since it takes the same path than the squeezed beam. Hence, when the pump beam matches spatially and temporally the seed we optimize the amplification or deamplification of the seed depending on the phase between the two beams as predicted by equation (2.19). Accordingly to this remarks, by scanning the pump phase, we measure a sinusoidal signal using a photodiode placed on the seed path. The contrast of

this function, denoted as V_{PDC}, tell us about the strength of the non-linear effect in the cavity 2.15. Nonetheless, the relation between this contrast and the squeezing level, when the seed beam is blocked, is not straightforward. It is because of the difference of temporal dispersions between the seed and the squeezed vacuum beam.

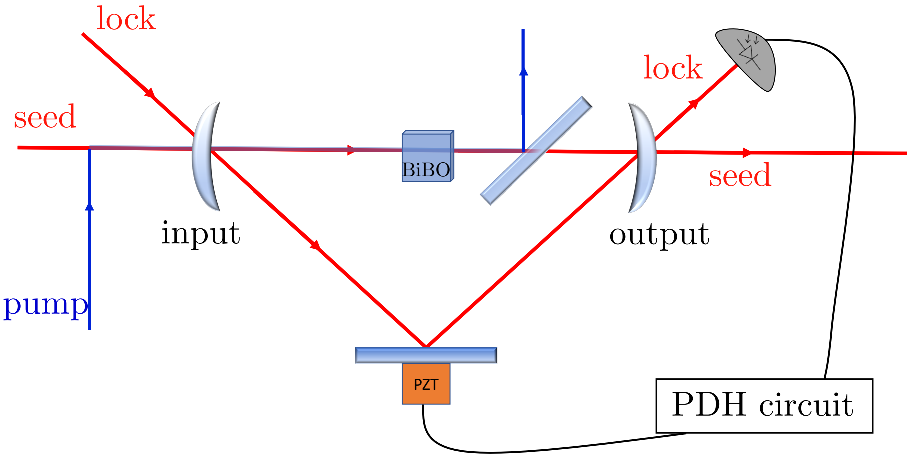

Figure 2.14 – Scheme of the OPO setup with the three different beam injected.

When the seed is blocked, we should observe multimode squeezed vacuum at the output of the cavity as long as the pump power is weak. If the pump power exceed the threshold $P_{p,th}$, we observe self oscillations of the cavity. With a $T = 20\%$ output coupler the finesse is $F = 27$ and the bandwidth of the cavity is around 3MHz. In these conditions, we measure a threshold of $P_{p,th} = 101\text{mW}$

2.5 summary

In this chapter, we have investigated the role of non-linear optics effects in the experiment in addition of the femtosecond laser functionality. First the SHG enables to convert red light into blue light which corresponds to a frequency doubling of the beam coming from the laser source. This blue beam is called the pump. We have seen that this effect is highly dependent of the input beam power with a efficiency proportional to P_{red}. The pump power is a key ingredient on the optical table since it is used, as its name suggests, to pump the OPO cavity. The non-linear effect in this cavity is called the parametric down conversion. Inside the non-linear crystal, blue photons are converted into two red photons by preserving the energy conservation. Hence this cavity is the squeezing source and we have seen that the advantage of the cavity which have been designed lies in the multimode aspect since the state is a superposition of squeezed vacuum states. In the next chapter, are reviewed the last element of the optical table to get a full understanding of the experiment.

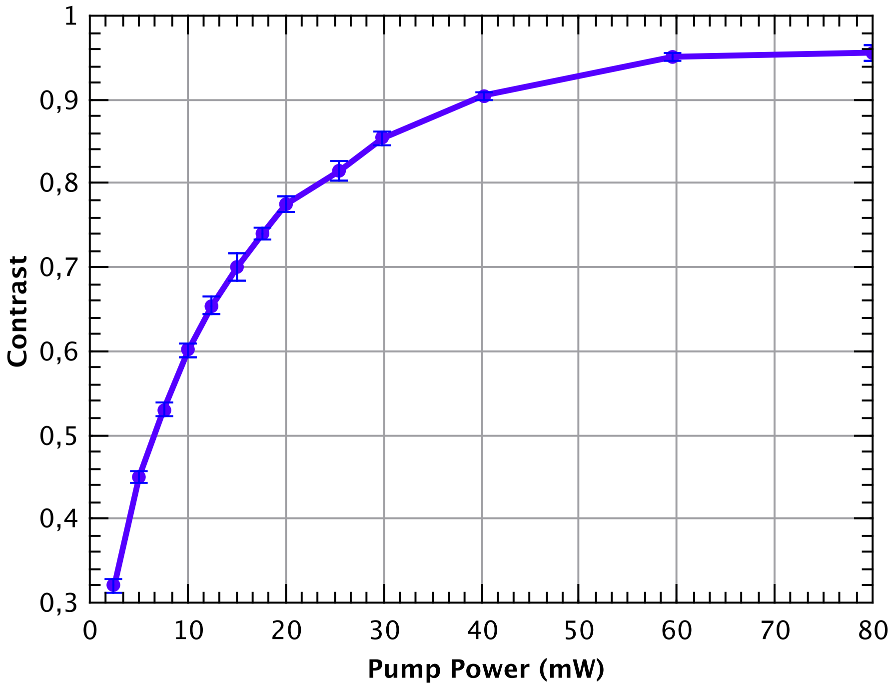

Figure 2.15 – Contrast of the PDC signal as a function of the pump power.

Chapter 3

Description of the measurement setup

Contents

In this second chapter, we investigate the part of the experiment dedicated to the detection. The main piece is the homodyne detection. However, since we deal with multimode optics, the pulse shaper is also a key element in this process. Its optical elements must be chosen carefully in order to maximize the number of degrees of freedom within the limit of the space requirement due to optical components
Hence, in this chapter, we first describe the homodyne detection from a general point of view and then its implementation in the SPOPO experiment. In a second section, we present the pulse shaper and finally, in a last section, we explain the use of a photonic crystal fiber which improves the number of degree of freedom for the detection.

3.1 Homodyne detection

3.1.1 Principle of the homodyne detection

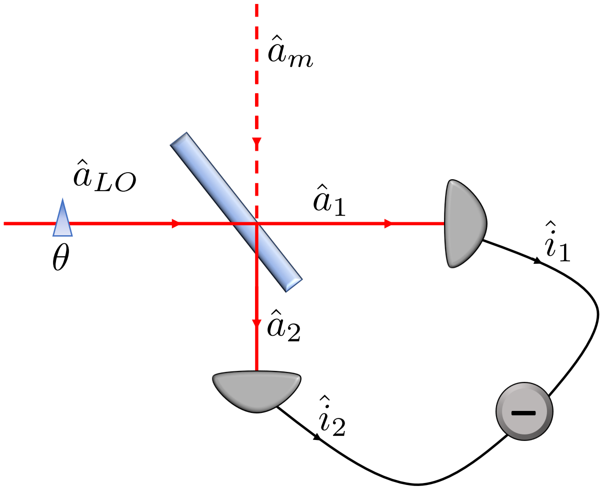

Figure 3.1 – Homodyne detection scheme.

The homodyne detection is a common used method for measuring noise fluctuations (figure 3.1) [Yuen 83, Abbas 83]. The state that we want to characterize, defined by the annihilation operator $\hat{a}_m$, is mixed on a 50:50 beam splitter with a bright coherent state of amplitude α_{LO} called the local oscillator . We denote θ the phase of this beam.

We can write at the outputs the annihilation operators as:

$$\hat{a}_1 = \frac{1}{\sqrt{2}}(\hat{a}_{LO} + \hat{a}_m) \tag{3.1}$$

$$\hat{a}_2 = \frac{1}{\sqrt{2}}(\hat{a}_{LO} - \hat{a}_m) \tag{3.2}$$

Then, two photodiodes collect the light and convert the energy of the field into photocurrent. This current is proportional to the number of photons $\hat{i} = K\hat{n}$. We have:

$$\hat{n}_1 = \frac{1}{2}\left(\hat{a}^\dagger_{LO}\hat{a}_{LO} + \hat{a}^\dagger_{LO}\hat{a}_m + \hat{a}^\dagger_m\hat{a}_{LO} + \hat{a}^\dagger_m\hat{a}_m\right) \tag{3.3}$$

$$\hat{n}_2 = \frac{1}{2}\left(\hat{a}^\dagger_{LO}\hat{a}_{LO} - \hat{a}^\dagger_{LO}\hat{a}_m - \hat{a}^\dagger_m\hat{a}_{LO} + \hat{a}^\dagger_m\hat{a}_m\right) \tag{3.4}$$

We are interested in the difference of the two currents: $\hat{i}_- = \hat{i}_1 - \hat{i}_2 = K(\hat{n}_1 - \hat{n}_2)$:

$$\hat{i}_- = K(\hat{a}^\dagger_{LO}\hat{a}_m + \hat{a}^\dagger_m\hat{a}_{LO}) \tag{3.5}$$

Because the local oscillator is bright, its amplitude is large compared to the beam m. At first order, by replacing the annihilation operator with the amplitude of the LO beam we obtain:

$$\hat{i}_- = K\alpha_{LO}\left(\mathrm{e}^{i\theta}\hat{a}_m + \mathrm{e}^{-i\theta}\hat{a}_m^\dagger\right), \quad \text{with } \alpha \in \mathbb{R} \tag{3.6}$$

We recognize the quadrature operator rotated by an angle θ: $\hat{i} = K\alpha_{LO}\hat{q}_\theta$. Hence, measuring the photocurrent difference, we get information on the quadrature q_θ in the direction θ. In our context, when we work with squeezed vacuum states, we are interested in the second moment of the measured data, meaning we want to get access to $\langle\Delta\hat{i}_-^2\rangle = K^2\alpha_{LO}^2\langle\Delta\hat{q}_\theta^2\rangle$. Indeed the mean value of the quadrature operators are zero for these states. A common mathematical tool for noise analysis is the auto-correlation function defined as:

$$C_i(t,t') = \overline{i(t)i(t')} - \overline{i(t)}\,\overline{i(t')} \tag{3.7}$$

In the stationary regime, C depends only on the variable $\gamma = t - t'$ [Reynaud 97]. We then introduce the noise spectral density $S_i(\Omega)$ defined as:

$$S_i(\Omega) = \int_{\mathbf{R}} C_i(\gamma)\mathrm{e}^{-i\Omega\tau}\mathrm{d}\tau \tag{3.8}$$

and expressed in A^2/Hz. $S_i(\Omega)$ is actually the Fourier transform of $C_i(\gamma)$ and we have:

$$\left\langle\Delta i^2\right\rangle = C_i(\tau = 0) = \int_{-\infty}^{+\infty} S_i(\Omega)\frac{\mathrm{d}\Omega}{2\pi} \tag{3.9}$$

All the information about the noise is contained in the noise spectral density. If we are interested in the noise of a specific bandwidth, which is the case of our experiment since the bandwidth of the SPOPO cavity is around 3MHz, we can select, via a filter, the region we want. In the experiment, this is the role of the spectrum analyzer.

3.1.2 A projective measurement in the multimode case

In the multimode case, as we saw previously , the light we study can be decomposed on an orthogonal mode basis. For example, the state at the output of the SPOPO cavity is a superposition of squeezed vacuum states where each state is related to a mode, which can be approximated by a Hermite-Gaussian mode. In the experiment, especially for covariance matrix measurements, we will also consider the frequency band mode basis which is also orthogonal. In the context of multimode optics, homodyne detection has the advantage of being projective. To understand this aspect, we need to consider the complete field notation and not only the annihilation operators as previously. We have in the frequency domain:

$$\hat{E}_{LO}^{(+)} = \mathcal{E}_{LO}\hat{a}_{LO}(\omega)f_{LO}(\omega) \tag{3.10}$$

$$\hat{E}_m^{(+)} = \frac{1}{\sqrt{N_m}} \sum_l \mathcal{E}_l \hat{a}_l(\omega) f_l(\omega) \tag{3.11}$$

where N_m is the number of optical modes which compose the beam that we want to measure. The mode m is decomposed among an orthogonal basis. We assume that the coefficients of the balanced beam splitter remain the same for all the modes: $r = t = \frac{1}{\sqrt{2}}$. Equation (3.6) then becomes

$$\hat{i}_- \propto \int \mathrm{d}\omega \left(\hat{E}_{LO}^{(-)} \hat{E}_m^{(+)} + \hat{E}_m^{(+)} \hat{E}_{LO}^{(-)} \right) \tag{3.12}$$

Replacing $\hat{E}_m$ and $\hat{E}_{LO}$ by their expression (3.11)(3.10) and we obtain at first order:

$$\hat{i}_- \propto \alpha_{LO} \int \mathrm{d}\omega \sum_l \left(\hat{a}_m \mathrm{e}^{i\theta} f_{LO}(\omega) f_l^*(\omega) - \hat{a}_m^\dagger \mathrm{e}^{-i\theta} f_{LO}^*(\omega) f_l(\omega) \right) \tag{3.13}$$

Hence, the terms in the sum are non zero if and only if the mode functions f_l are not orthogonal to f_{LO}. In this sense the measurement is indeed projective in the frequency domain. We notice that this demonstration can be adapted to other types of mode basis such as spatial modes or temporal modes as introduced in chapter 1.

3.1.3 Effect of losses in a homodyne detection setup

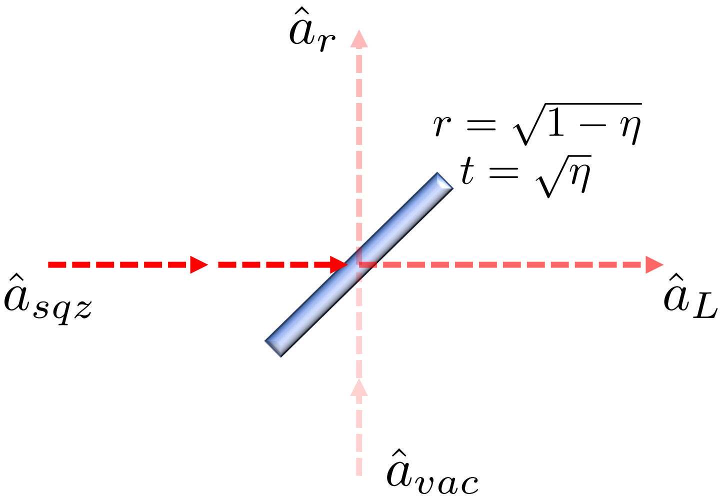

Figure 3.2 – Model of losses on the detection.

Unfortunately, every state we want to measure is sensitive to losses and not necessarily pure. A way to model this effect is to assume that it is equivalent to a variable beam splitter with a transmission $T_L = \eta$ (figure 3.2). This quantity characterizes the amount of losses we have in the full experiment from the cavity to the detection.

The effect of losses is directly observed in the Wigner function, which becomes [Leonhardt 97]:

$$W_L(q,p) = \frac{1}{\pi\eta(1-\eta)} \int\int W(\frac{q'}{\sqrt{\eta}}, \frac{p'}{\sqrt{\eta}}) \mathrm{e}^{\frac{-(q-q')^2-(p-p')^2}{1-\eta}} \mathrm{d}q'\mathrm{d}p' \tag{3.14}$$

where W and W_L denote respectively the Wigner functions before and after the beam splitter. Equation (3.14) is the convolution of the initial Wigner function with a Gaussian function of width $\sqrt{1-\eta}$, which smooths the Wigner function W. The effect of losses on the Wigner function of squeezed states is shown in figure 3.3. For the calculation, the state without loss is squeezed along the p direction with a squeezing parameter of $\zeta = 0.3$, as defined in chapter 1. We observe that the smaller η, the better the fit of the Wigner function with a vacuum state Wigner function. In figure 3.4 are represented the same Wigner functions for $q = 0$ and $p = 0$ in order to bring more perspective to the precedent plot. Indeed, the effects of losses are more visible on the standard deviations of the Gaussian distribution. As losses increase, Δp^2 decreases and Δq^2 increases, *i.e* the squeezing vanishes.

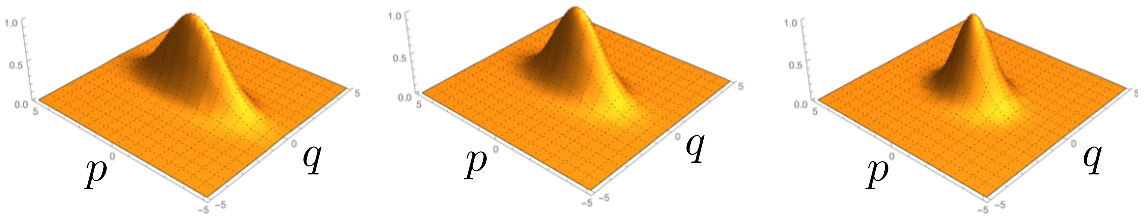

no loss $\eta = 0.6$ $\eta = 0.2$

Figure 3.3 – Wigner function of a squeezed vacuum state with $\zeta = 0.3$ in the absence of loss (*left*) and with $\eta = 0.6$ (*center*) and $\eta = 0.2$ (*right*).

There are several sources of noise impacting the experiment:

- **Optical losses**: it contains all the losses related to the imperfection of the optical components. For example, the reflectivity of the mirror we use is close but not equal to 1. We denote these losses as η_{opt}
- **Multimode losses**: these losses corresponds to a partial overlap between the LO mode and the target state mode in the homodyne detection. It is denoted as

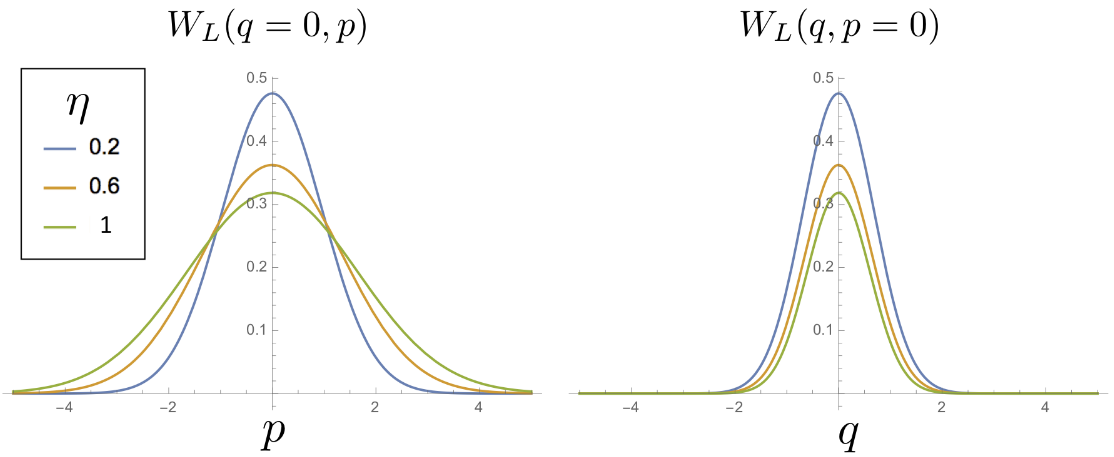

Figure 3.4 – Result of the Wigner function calculation for $q = 0$ (*left*) and $p = 0$ (*right*) when the states is affected by losses.

η_{rec} and by considering the modes as respectively f_{LO} and f_m, we have:

$$\eta_{rec} = \langle f_{LO}, f_m \rangle \tag{3.15}$$

where $\langle ., . \rangle$ is the scalar product of two functions. The overlap can be interpreted in different ways. Indeed, since the modes are functions of the variables $(\omega, t, \boldsymbol{r})$, they have to be set to maximize η_{rec}. Therefore, we have to ensure that both pulses arrive at the same time at the beam splitter, the beams must be superposed spatially in the transverse plan and finally they also must have the same spectrum.

- **detection losses**: they are due to photodiode imperfections. Indeed, until now we assumed that the quantum efficiency was equal to 1, *i.e* all the photons were converted into electrons by the photodiodes. Unfortunately, this value is physically unfeasible. We denote this type of losses as η_q and we have

$$\eta_q = \frac{N_e}{N_p} \tag{3.16}$$

where N_e and N_p are respectively the number of electrons and photons involved in the conversion during the detection.

- **electrical noise**: this last type of noise is denoted as η_{elec}. It is due to the imperfections of the electrical circuit which comes after the photodiodes. If $i(t)$ is the photocurrent, A the amplification factor of the circuit and $u_e(t)$ the electronic noise, we can express the signal amplitude at the output of the circuit as [Kumar 12, Appel 07]:

$$u(t) = Ai(t) + u_e(t) \tag{3.17}$$

We denote S_e and S the spectral densities related to the electronic noise and the photocurrent signal respectively. The losses are given by

$$\eta_{elec} = 1 - \frac{S_e}{S} \tag{3.18}$$

We can define the clearance, C, from the electronic noise. This quantity is defined in dB as :

$$C = 10\log_{10}(\eta_{elec} - 1) \tag{3.19}$$

Finally, η_{tot} is denoted as the global loss. We can express it as the product of all the losses presented above:

$$\eta_{tot} = \eta_{opt}\, \eta_{rec}\, \eta_q\, \eta_{elec} \tag{3.20}$$

3.1.4 Description of the measurement setup

A picture of the homodyne detection we use is presented in figure 3.5. The LO and signal beams interfere at the beam splitter and the output beams are directed to the grey box which contains the photodiodes and the amplification circuit (figure 3.6). The pulses from the local oscillator and the target state must arrive at the same time at the beam splitter to interfere together. However, the distances between the beam splitter and each photodiode can be different because the photodiode can not resolve temporally the pulse duration. Here, the difference between the two distances is around 10 cm which is equivalent to $3.10^{-11}s$ of light propagation duration while the time distance between two pulses of the laser is around $10^{-8}s$. The photodiodes that we use in our electrical circuit are not able to resolve this.

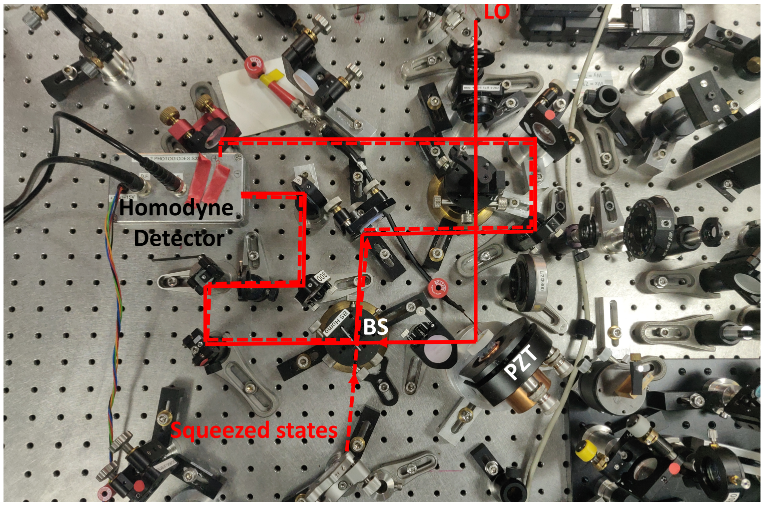

Figure 3.5 – Picture of the homodyne detection setup.

The mirror depicted by the notation “PZT” in the picture is mounted on a piezo-electrical resonator plugged to a low frequency generator set on a “triangular signal” setting. We can thus scan the phase of the local oscillator by monitoring the amplitude voltage of the piezo and induce a longitudinal translation movement on the mirror.

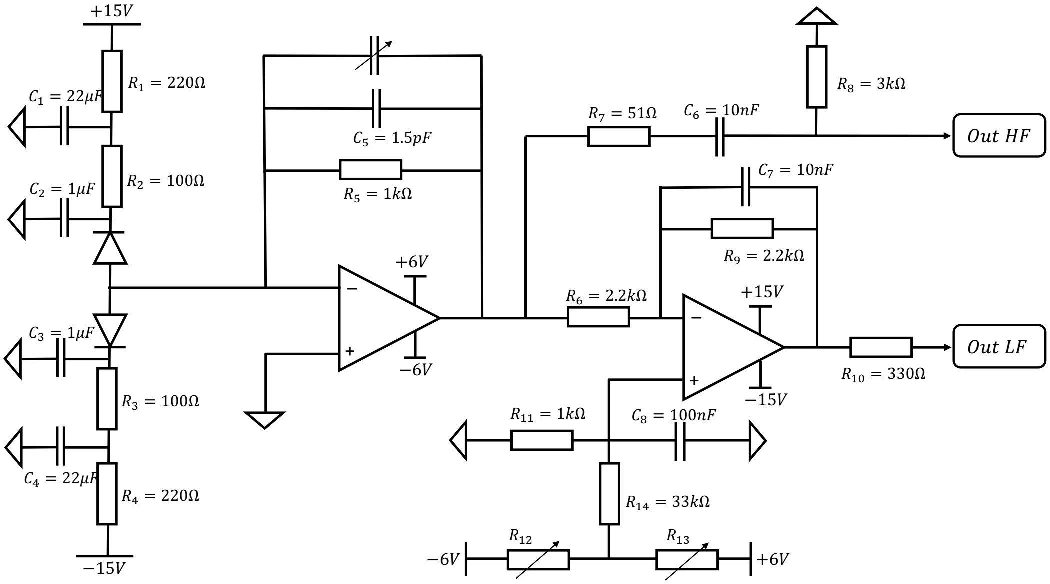

Figure 3.6 – Homodyne circuit scheme.

The electrical scheme of the homodyne detector is presented in figure 3.6. The circuit is divided in two parts. The first one is the transimpedance circuit, which aims to convert photocurrent to voltage and amplify the signal. The second part is the amplification scheme. There are two outputs of this circuit: one for the DC component and the other one for the AC. The DC output is used for alignment. Indeed, a way to check the good overlap between the local oscillator and the signal beams is to measure the interference visibility between the LO and the seed beam propagating along the signal path. Usually, for the SPOPO experiment, this quantity is around 95%. To be sure that this value is not affected by a wrong spectral overlap we use a 1nm spectral filter centered on 795nm. The second output, the AC one, that we plug to the spectrum analyzer to carry out measurement on the target state [Kouadou 21].
Usually, for the measurement, we set the frequency of the piezo at 5Hz. The spectrum analyzer, which measures the noise spectral density at a given frequency, works on the zero span mode with the following parameters:

- central frequency: 1MHz.
- frequency resolution: 100kHz.

- video bandwith: 500Hz.
- time duration for 1000 data points: 0.09s.

We define the clearance as the ratio between the shot noise level (level of the noise when only the local oscillator is sent into the detector) and the electronic noise level (level of the noise without any light). It is usually expressed in dB. This value has to be as high as possible in order to maximize η_{elec}. Indeed, we want to measure squeezing and anti-squeezing of the signal noise, which means for some phase θ of local oscillator, we will observe a noise level below the shot noise. We have to make sure this noise is not contaminated by the inherent noise of the electronic circuit we use.

Two electrical supplies are needed for the circuit. The first one is a ±15V, which is used for the operational amplifier. The second one is a variable bias voltage for the photodiode, which can supply between ±10V and ±70V. This value influences the clearance as we can see in the figure 3.7. For each curve we observe a saturation of the clearance. Nonetheless, the lower the supply voltage, the higher the saturation threshold. In the rest of this manuscript, the measurements are performed with the $\pm 10V$ voltage.

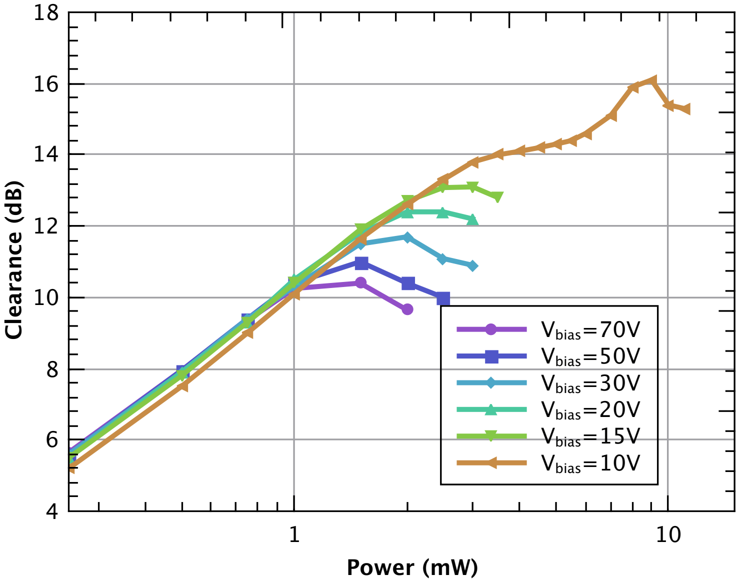

Figure 3.7 – Measured clearance measurement dependance of the LO power for different bias voltages of the photodiodes.

3.2 Pulse shaper

3.2.1 Description of the pulse shaper

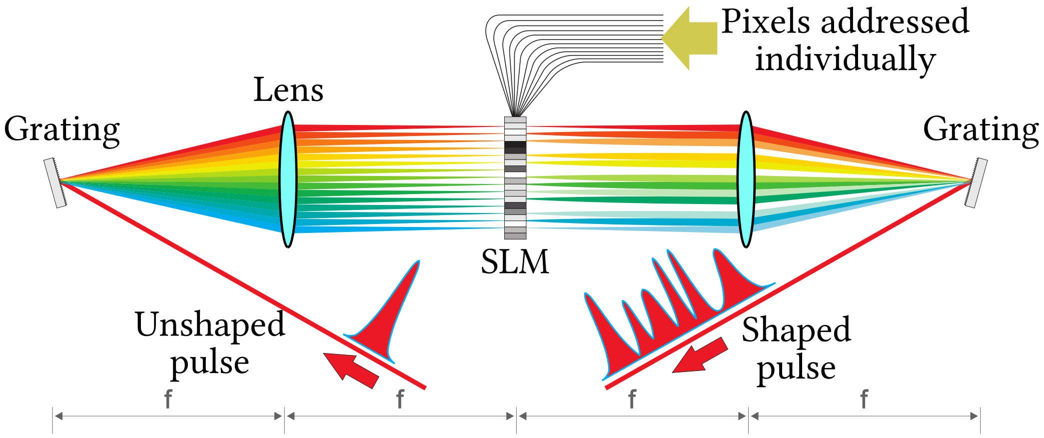

Figure 3.8 – Pulse shaper scheme.

In the precedent part, we presented the homodyne detection as a projective measurement. In the context of our experiment, if the optical mode of the target state is defined by a spectral function $f(\omega)$, which can exhibit complex values, we need to shape the local oscillator spectrum with the same function. The setup to shape the optical mode has to be adjustable since we want to measure a large of number modes for data acquisitions.
Regarding the Fourier theorem, we have two options to shape the mode f:

- temporal shaping
- spectral shaping

Considering the first option, the time duration of one pulse is too short. There exists no optical instrument for complex amplitude shaping with a resolution around 10fs. We have then to consider to shape the pulse in the spectral domain. To do so, we use the pulse shaping approach described in [Monmayrant 05, Monmayrant 10, Weiner 11] and represented in figure 3.8. It requires a 4-f line composed by two gratings, two lenses and one SLM (Spatial Light Modulator) [M. Danailov 89]. In our setup, we use a SLM in reflexion, which allows us to use only one grating and one lens. The grating diffracts the light in the parallel direction of the table, then the lens is used to image the diffraction figure on the screen of the SLM. The lens we use is actually a cylindrical mirror to focus the light only in the horizontal direction. Then, the light interacts on the SLM screen which is an array of pixels each composed by liquid crystal cells. Applying a controlled voltage on the border of the cell, as shown in figure 3.9, the configuration of the crystals changes and at the same time their interaction with the incident light. We can thus control the phase modulation of every spatial repartitions of the diffracted beam interacting on the screen.

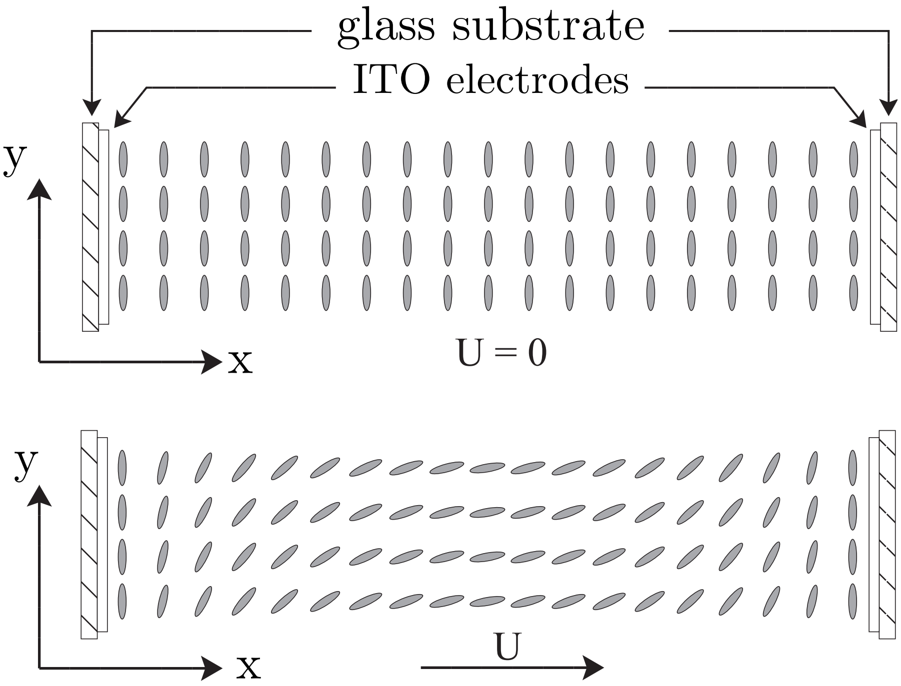

Figure 3.9 – Orientation of the liquid crystal in one SLM cell when the voltage between electrodes is zero and when it is positive, taken from [Monmayrant 05].

In figure 3.10, is represented the type of mask which is applied on the SLM screen to shape the spectrum of the local oscillator. The sawtooth profile allows to separate spatially the incident beam from the shaped one by a small angle between both beams. The vertical position of the sawtooth function controls the phase of the reflected beam and the depth of the teeth controls the amplitude. Thus each vertical line of the SLM can control the complex value of the optical mode of the local oscillator. For more detail see 3.2.3.

In the optical setup, we use a sawtooth grating from the Spectrogon with 1500 grooves per mm optimized to diffract the light around 800nm. The cylindrical mirror has a 200mm focal lens. The SLM we use is the model LCOS-SLM X10468 from Hamamatsu

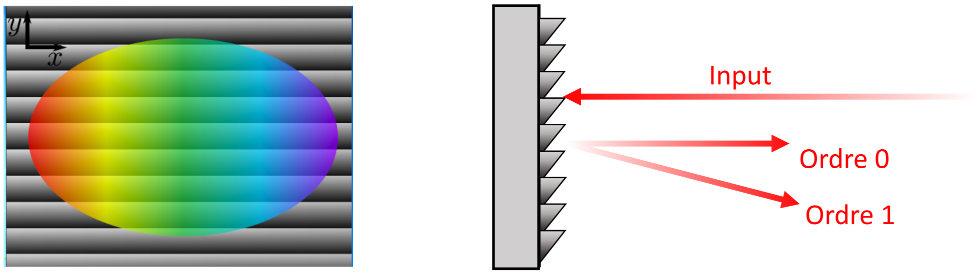

Figure 3.10 – Figure applied on the SLM mask and profile of the mask.

with 792 pixels in the horizontal and 600 in vertical direction. The size of the screen is $15.8 \times 12mm$. The choice of all these elements is important because it defines the resolution of the setup to shape the spectral mode we want (figure 3.11).

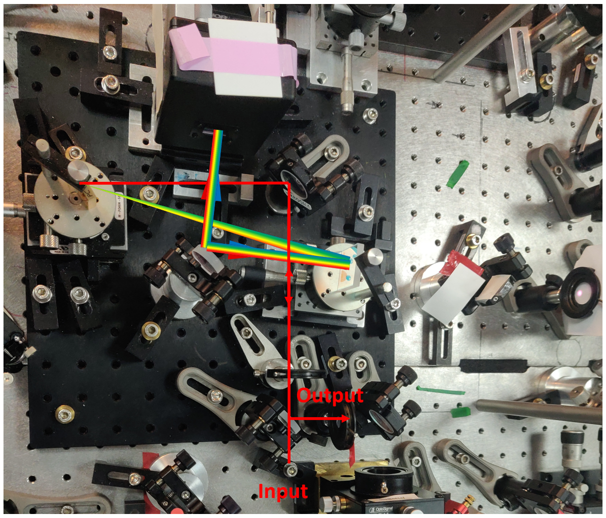

Figure 3.11 – Picture of the pulse shaper setup on the optical table.

3.2.2 Complexity

The quantity we use to determine the resolution of the pulse shaper is the complexity, which can be interpreted as the number of degrees of freedom in the frequency domain. There are two ways to define this term: the optical complexity and the pixel complexity. We show below how do we determine them.

3.2.2.1 Pixel complexity

The pixel complexity is defined by the following expression:

$$\mathcal{N}_{px} := \frac{\Delta\lambda}{\delta\lambda_{px}} \tag{3.21}$$

where $\Delta\lambda$ is the spectral width of the incident beam and $\delta\lambda_{px}$ the wavelength resolution imposed by the pixels size. The derivation of the resolution term can be found in [Michel 21], we have:

$$\mathcal{N}_{px} = \frac{f\Delta\lambda}{d\delta x_{px}\cos\theta_d} \tag{3.22}$$

where f is the focal length of the cylindrical mirror, d the distance between each groove of the grating, δx_{px} the pixel size and θ_d the angle between the incident and the diffracted beams. We can make few comments about this formula:

- The pixel complexity is linear with the focal length f. We can interpret this observation as follows: the larger f, the broader the diffracted beam is spread on the SLM screen and better the resolution. So it is in our interest to choose f as large as possible while respecting the screen size of the SLM.

- Another way to spread the beam is to play with the grating by increasing the groove density $a = 1/d$.

In our optical setup we have $f = 19$cm, $a = 1500$gr/mm, $\theta_d = 8°$ and $\delta x_{px} = 0.0199$ mm. We deduce the value of the pixel complexity: $\mathcal{N}_{px} \approx 136$, which is larger than the values calculated for the second pulse shaper set on the optical table and which is described in next chapter 4.

3.2.2.2 Optical complexity

In the precedent section, to derive $\mathcal{N}_{px}$ we assumed that the input beam was a plane wave. Considering a Gaussian beam, another limitation appears in terms of resolution. We call this complexity the optical complexity and it is defined as

$$\mathcal{N}_{opt} := \frac{\Delta\lambda}{\delta\lambda_{opt}} \tag{3.23}$$

Here $\delta\lambda$ represents the wavelength resolution of the system composed by the grating and the cylindrical mirror. This expression has also been derived in [Michel 21] and we can write:

$$\mathcal{N}_{opt} = \frac{\pi w_i a\Delta\lambda}{2\cos\theta_i\lambda_0} \tag{3.24}$$

This expression introduces two new elements in comparison with formula (3.22): θ_i is the incident angle of the beam on the grating and w_i is the waist of the beam before the pulse shaper. We notice that this complexity expression is independent of the focal length f. $\mathcal{N}_{opt}$ is linear with the size of the beam which is not surprising. Indeed, the larger the waist, the smaller the image of the beam on the SLM screen. We can also improve this complexity by increasing the density of grooves of the grating.
At the input of the pulse shaper, the beam has a size of $w_i = 2$mm and the incident angle is $\theta_i = 8°$. Hence we have an optical complexity of $\mathcal{N}_{opt} \approx 60$. This number is much smaller than the precedent. A way to improve it could by increasing the size of the beam till the limit imposed by the screen size of the SLM.

3.2.3 SLM mask

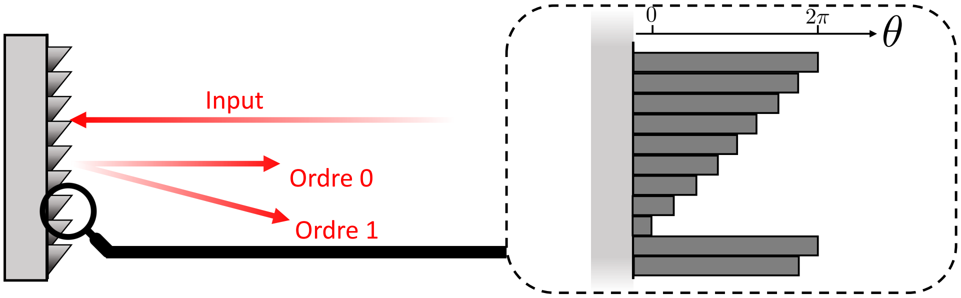

Figure 3.12 – Real mask applied on the SLM.

Previously, evoking the use of a SLM, it has been seen that a sawtooth mask was applied to separate spatially the input and the output beam in the pulse. However, moving from theory to practice, building a continuous function from a limited number of pixels looks wobbly (figure 3.12). Here we justify the approximation by showing that the number of pixels dedicated to build a phase ramp on the SLM mask is enough.
In appendix B is explained how is derived the diffraction figure in the far field, when the beam is diffracted by a grating composed by the repetition of several transmission pattern defined by the function $\mathcal{T}$. Here, the mask printed on the SLM screen is the cause of the diffraction. The function $\mathcal{T}$ depends on two variables: ω represents the frequency related to the horizontal position x on the screen and y is the vertical position. The SLM acts only on the phase of the beam, we have thus:

$$\mathcal{T}(y, \omega) = e^{-iM(y,\omega)} \tag{3.25}$$

with:

$$M(y, \omega) = 2\pi \left(\frac{1}{2} + A(\omega) \sum_{n=0}^{N_{\mathcal{T}}} t(y - nL) \right) \tag{3.26}$$

where $N_{\mathcal{T}}$ is the number of $\mathcal{T}$ repetitions printed on the screen, $A(\omega)$ is the depth of the printed grating for each frequency, L the length of an individual transmission pattern and t is the ramp function which can be continuous in the theoretical case or discrete in the practical one. We assume that we need $2M+1$ pixels to build an individual ramp where the pixels pitch is still denoted as δx_{px}. In appendix B, the field in far field after interacting on the SLM mask has been derived in both cases, discrete and continuous. Here, considering that we can vary the amplitude of the sawtooth function with the factor $A(\omega)$, we have used equation in appendix B and have obtained:

$$E_{th}(k_y,\omega) = KE_0 e^{-i\frac{(N_{\mathcal{T}}-1)k_y L}{2}} \frac{\sin(N_{\mathcal{T}} k_y L/2)}{N_{\mathcal{T}}\sin(k_y L/2)} \frac{L}{2} \operatorname{sinc}(k_y L/2 + A(\omega)\pi) \tag{3.27}$$

$$E_{exp}(k_y,\omega) = KE_0 e^{-i\frac{(N_{\mathcal{T}}-1)k_y L}{2}} \frac{\sin(N_{\mathcal{T}} k_y L/2)}{N_{\mathcal{T}}\sin(k_y L/2)} \frac{\delta x_{px}}{2} \operatorname{sinc}(k_y \delta x_{px}/2) \sum_{l=-M}^{M} e^{i\left(k_y\delta x_{px} + A(\omega)\frac{\pi}{M}\right)l} \tag{3.28}$$

where k_y is the component of the wave vector $\boldsymbol{k}$ on the y axis and we introduced the notation $\alpha_M := k_y\delta x_{px} + A(\omega)\frac{\pi}{M}$. We note that the electric fields are expressed as a function of k_y, which is related to the beam angle, instead of the position y. It is a convenient choice for the calculation and both variables are easily related in the small angle approximation in the far field: $k_y \approx \frac{2\pi\sin(y/f)}{\lambda_0}$. The labels th and exp are related respectively to the field diffracted by the continuous mask and the discretized one. We note that for both cases the terms coming from the grating structure are the same. The difference between both equations is the presence of a sinc function to describe the diffraction by a ramp in E_{th}. In E_{exp}, this term becomes a sum multiplied by the term $\frac{\delta x_{px}}{2}\operatorname{sinc}(k_y\delta x_{px}/2)$. This last term comes from the diffraction by individual pixels. In spite of the variation in the expressions that we have just pointed out, assuming that M is large enough and that the angles are tiny, we have:

$$\sum_{l=-M}^{M} e^{i\alpha_M l} = \frac{e^{-iM\alpha_M} - e^{i(M+1)\alpha_M}}{1-e^{i\alpha_M}} \approx 2M\operatorname{sinc}(M\alpha_M) \tag{3.29}$$

We know that we have $L=(2M+1)\delta x_{px}$. Hence, we can express the experimental field as:

$$E_{exp}(k_y,\omega) \approx KE_0 e^{-i\frac{(N_{\mathcal{T}}-1)k_y L}{2}} \frac{\sin(N_{\mathcal{T}} k_y L/2)}{N_{\mathcal{T}}\sin(k_y L/2)} \frac{L}{2} \operatorname{sinc}(k_y\delta_x/2)\operatorname{sinc}(k_y\delta_x M + A(\omega)\pi) \tag{3.30}$$

Both expression are now similar. Only the term from the diffraction due to the individual pixels is still remaining. In the experiment, the number of ramp repetitions is $N_{\mathcal{T}} = 19$, each composed by $M = \left(\frac{600}{N_{\mathcal{T}}} - 1\right)/2 \approx 15$ pixels. the two numerical applications are in agreement with the approximations made above. In figure 3.13 is represented the analytical calculation of the intensity derived for both cases (3.27)(3.30) as a function of the angle of reflection on the SLM denoted as θ. In both curves, the maximum appears around $\theta = -0.0013$rad. It is the angle between order 0 and order 1 which allows to separate beams represented in figure 3.10. The maxima of the two peaks are not the same. Although $M \neq L/2$, it is difficult to distinguish the position of the two maxima. The losses in the real mask are mainly due to the pixel diffraction but this loss remain acceptable comparing with the grating and the SLM itself (the losses due to the total setup is around 50%). Another information that brings the plot is that most of the energy is transferred to the first order. Indeed, the ratio of the peak amplitudes of the two diffraction order is 0.0028. Less than 1% of the intensity is remaining in the order 0.

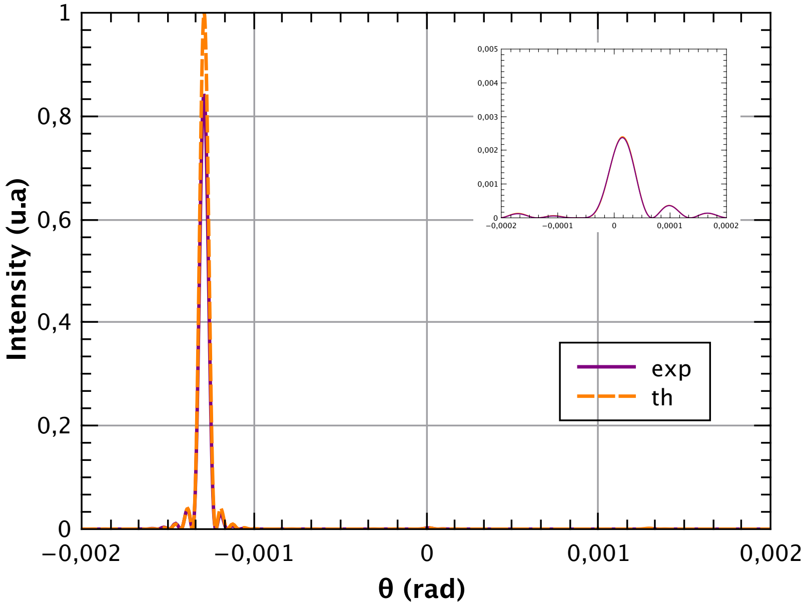

Figure 3.13 – Intensity as a function of the angle θ normalized to the maximum of $I_{th} = |E_{th}|^2$ for $A = 1$. Inset: Intensity around $\theta = 0$.

Finally, in figure 3.14, we show the intensity measured at the output of the pulse shaper as a function of the sawtooth depth A. We observe that this efficiency of the SLM is not linear but follows a sinc as expected from the equations (3.30), (3.27). We use this measurement to calibrate the amplitude shaping, *i.e* to know which depth we have to use to imprint a set amplitude.

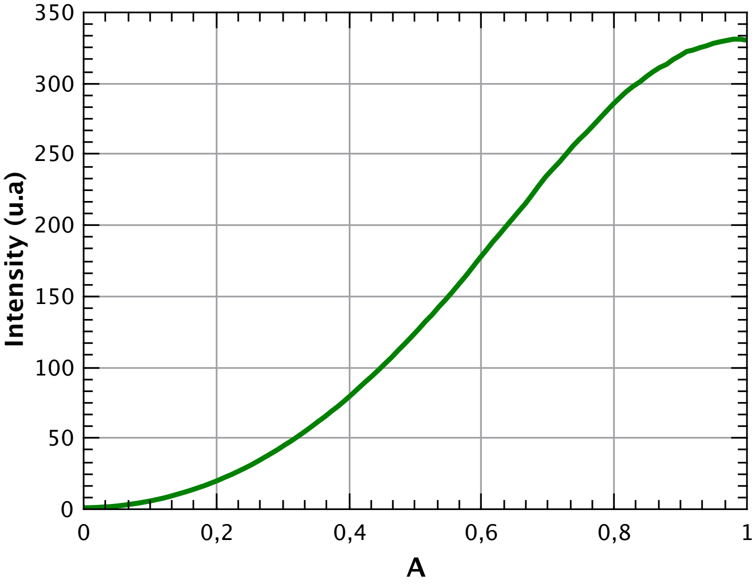

Figure 3.14 – Measured intensity at the output of the pulse shaper as a function of the depth A of the sawtooth printed on the SLM screen.

3.2.4 Alignment details of the pulse shaper

Once we have chosen the correct optics to build the pulse shaper, we have to set them on the table, which may be more difficult than expected since we want to see at the output of the pulse shaper a beam with the same spatial form than at the input but spectrally shaped. Besides, we have also to take care of not to adding temporal or spatial chirps due to by misalignment (details can be found in [Monmayrant 05, Weiner 00]).

3.2.4.1 Spatial chirp

As we saw previously spatial chirp or angular dispersion appears along the vertical and horizontal directions. Two different misalignments are at the origin of these dispersions. For the vertical one, there exists two different reasons: the orientation of the gratings and the cylindrical mirror. If the grating is not well oriented, the beam will be diffracted in the wrong direction. The effect is double since the beam is recombined on the same grating. The recombination will be wrong and some vertical chirp will appear. For the same orientation issue, the cylindrical mirror can induce vertical chirp.

The origin of the horizontal dispersion is different. It appears when the distance between the SLM screen and the lens is different to the focal distance. In this case, the beam propagates on a longer or shorter distance and different parts of the frequency comb arrive at the SLM screen with different incident angles. Therefore, an additional symptom of the horizontal chirp is the ellipticity of the beam after recombination on

the grating.
A way to measure the effect of spatial dispersion is to measure the spectrum of the beam at the output of a pinhole setup, which acts as a spectral filter if there is spatial dispersion. If we eliminate the dispersion, we will measure the same spectral bandwidth before and after the pinhole.

3.2.4.2 Temporal dispersion

Because we diffracted the beam to shape the spectral amplitude and phase, temporal dispersion can be introduced by misalignment. Indeed, this dispersion appears as soon as the frequencies which compose the pulse train do not propagate along the same distance in the pulse shaper. In our configuration, the temporal dispersion is given by [Michel 21]:

$$\phi^{(2)} = \frac{\delta\lambda_0^3 a^2}{\pi c^2 \cos^2(\theta_d)} 2\left(L_1 - f\right) \tag{3.31}$$

where L_1 is the distance between the grating and the parabolic mirror. The quadratic dispersion in this configuration is linear with the difference between L_1 and the focal length.

3.3 How to make the spectrum broader

As we just saw in previous sections, the homodyne detection is a projective measurement and the pulse shaper is the tool that we use to tailor the local oscillator as the mode of the target state. However, since the shaping is made in the spectral domain, we are limited by the bandwidth of the input beam spectrum. On one side, the spectrum at the output of the femtosecond laser source is Gaussian which means the energy is mainly concentrated in the center of the spectrum. And on the other side, as we saw in chapter 2, the eigenmodes of the SPOPO have Hermite-Gaussian shapes. For modes with an index above 4 the energy is distributed more to the sides than to the centre of the spectrum. In addition, the effective bandwidth increases with the index n. Hence, an important part of the energy of the LO will be lost if we want to shape higher order Hermite-Gaussian modes, which becomes a problem when the mode is too large in comparison with the LO because we will not measure the expected mode on the homodyne detector. Another problem is that we need a certain amount of power to perform the detection, otherwise the clearance and the transmission of the detector η_{elec} will drop. Hence, we would prefer ideally an input beam whose FHWM is as large as possible and whose spectrum is as flat as possible in order to minimize the electrical losses and to increase the number of measurable modes. To do so, we resort to a photonic crystal fiber (PCF), that widens the spectrum by means of a non-linear effect.

3.3.1 Description of the PCF

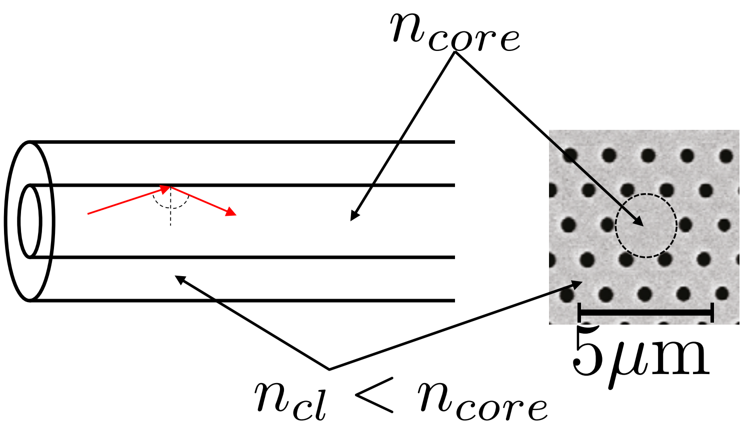

Figure 3.15 – Longitudinal structure of the PCF (*left*), transverse picture of the PCF (*right*).

The PCF has been designed and fabricated by Nicolas Joly and his team from the Max Planck Institute based in Erlangen for our purpose [Hammer 16, Joly 12]. It is called ANDi fiber for "All-Normal Dispersion". Its honeycomb structure is represented in figure 3.15. The core is the part where the beam propagates. Its diameter is around 1.3 μm. This type of optical fiber exhibits several advantages for the experiment including a wide range of transmission and a good resistivity to damage due to high optical intensity. The broadening of the spectrum is due to a non-linear phase self-modulation effect [Hammer 16, Dudley 10].

3.3.2 Implementation of the fiber in the experiment

On the optical table, the PCF setup is mounted just before the pulse shaper on an auxiliary path for the local oscillator. We use lenses of short focal length to ensure the waist of the input beam matchs the width of the fiber core. The length of the fiber is around 2 cm. The longer the fiber the borader the the spectrum. Nonetheless, our goal is to find a compromise between obtaining a flat spectrum and having enough power for the homodyne detection equally distributed among the spectrum. The transmission of the fiber is around 60%. In figure 3.16, is represented a measurement of the spectrum at the output of the fiber as a function of the LO power injected. We see that the working point is around $P = 100$ mW. Below this value, the spectrum is Gaussian and above, it is not flat anymore, a hole appears at the centre of the spectrum. We want to avoid the appearance of this hole since the goal here is to spread the power over the spectrum as wide as possible. A cut in figure 3.16 left with the desired effect. Nonetheless, the use of this fiber has a drawback: its lifetime. Indeed, we always observed a drop in its efficiency and broadening of the spectrum after few weeks of use. We designed a cap to protect it from dust, which increased its lifespan by 2 or 3 weeks.

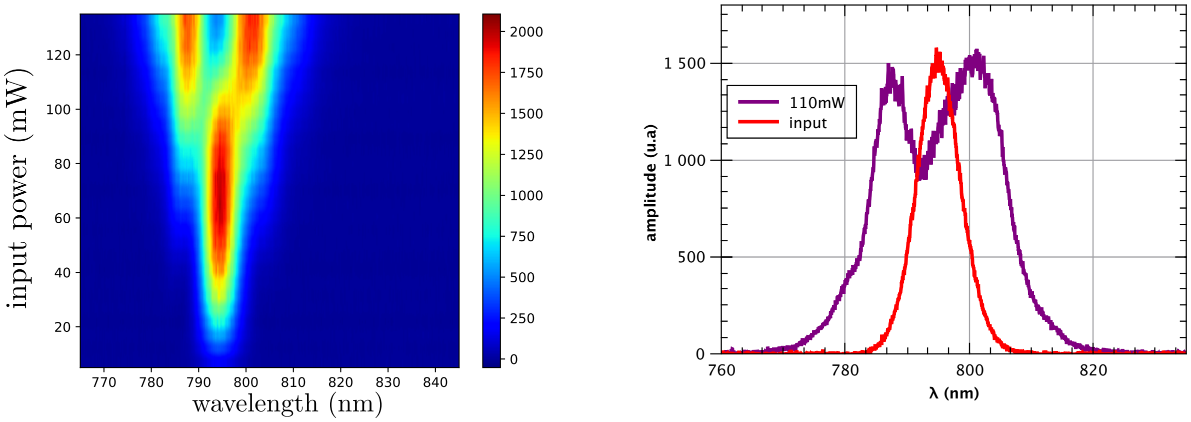

Figure 3.16 – *left*: Measurement of the spectrum at the output of the PCF as a function of the red power injected. *right*: Spectrum of $P_{in} = 110mW$ and the input beam.

3.3.3 Detection with a broader local oscillator

The last point we have to investigate about the PCF is the detection itself. We wonder if the PCF does add extra noise, which would affect the squeezing measurements. The answer is no. In figure 3.17, we show the measurements of quadrature variances versus LO phase for the first supermodes of the SPOPO. The measurements are made with the two different local oscillators. The difference between them is only the fact of using the PCF or not. Both optical paths share the same pulse shaper and then the same path through the homodyne detection. We measured the same spatial overlap between these beams and the seed (the visibility is around 95%). We observe that there is no significant difference between the two types of measurements in terms of signal noise ratio. Thus, the use of the PCF does not have any effect on these modes. However the improvement is substantial in terms of the number of HG modes accessible. In figure 3.17, the plots are very similar between the case with the PCF and the case without.

3.4 Summary

In this chapter, we have investigated the part of the experiment dedicated to the measurement of the SPOPO quantum state. The measurement setup is based on a homodyne detection which has the advantage to be projective and enables to measure

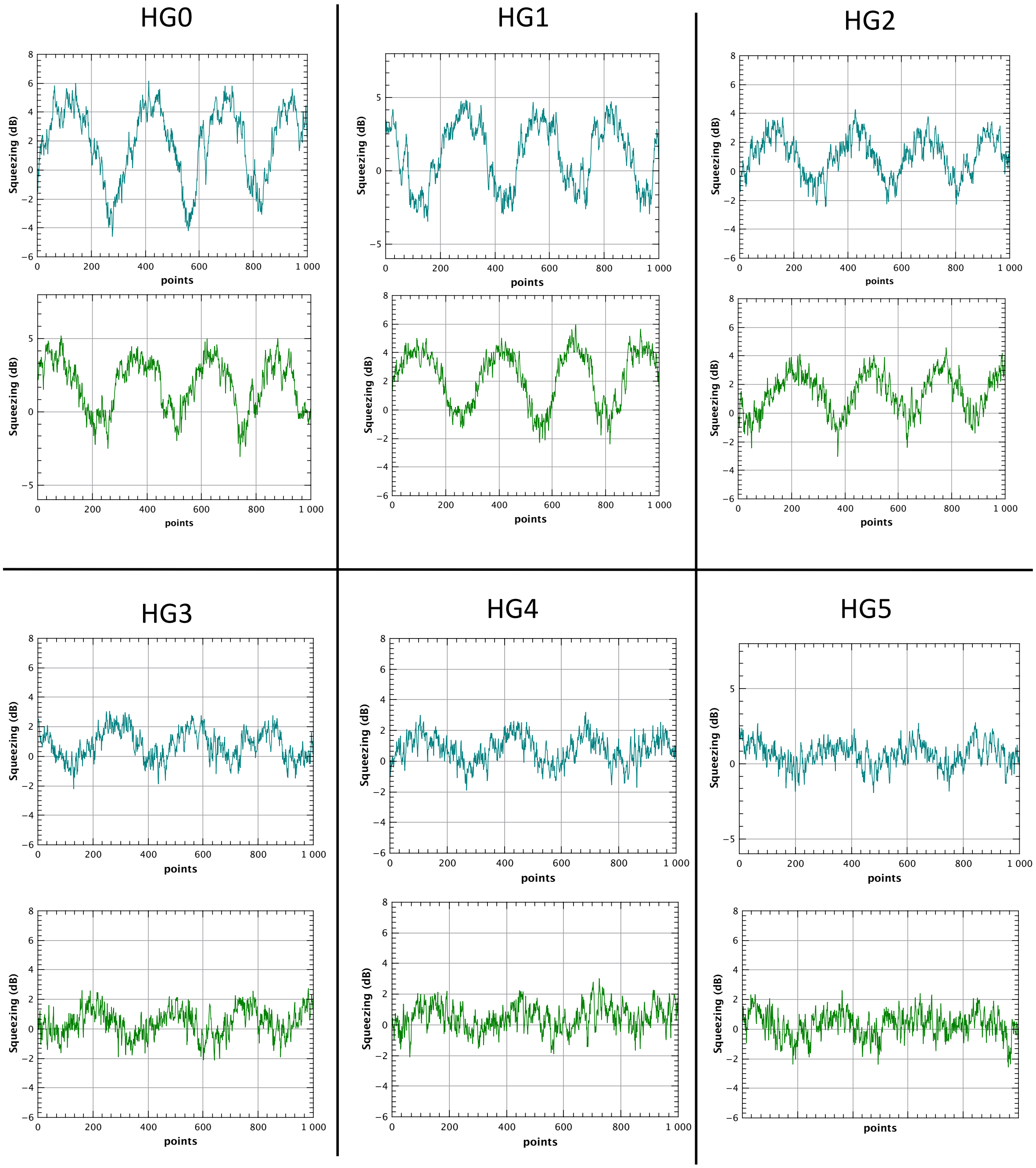

Figure 3.17 – Measurements of quadrature variance as a function of the LO phase for the different HG modes using the PCF (blue curves) or not (green curves).

individually the states related to the supermodes of the SPOPO calculated in the previous chapter. The choice of the modes is done via a pulse shaper, whose the functioning is recalled here. In addition we have seen the use of a PCF designed and made by N. Joly's team in Max Planck institute in Erlangen. This fiber enables to broaden the spectrum of the laser source. At the end, it allows us to measure more modes although it doesn't show more squeezing in the measurement.

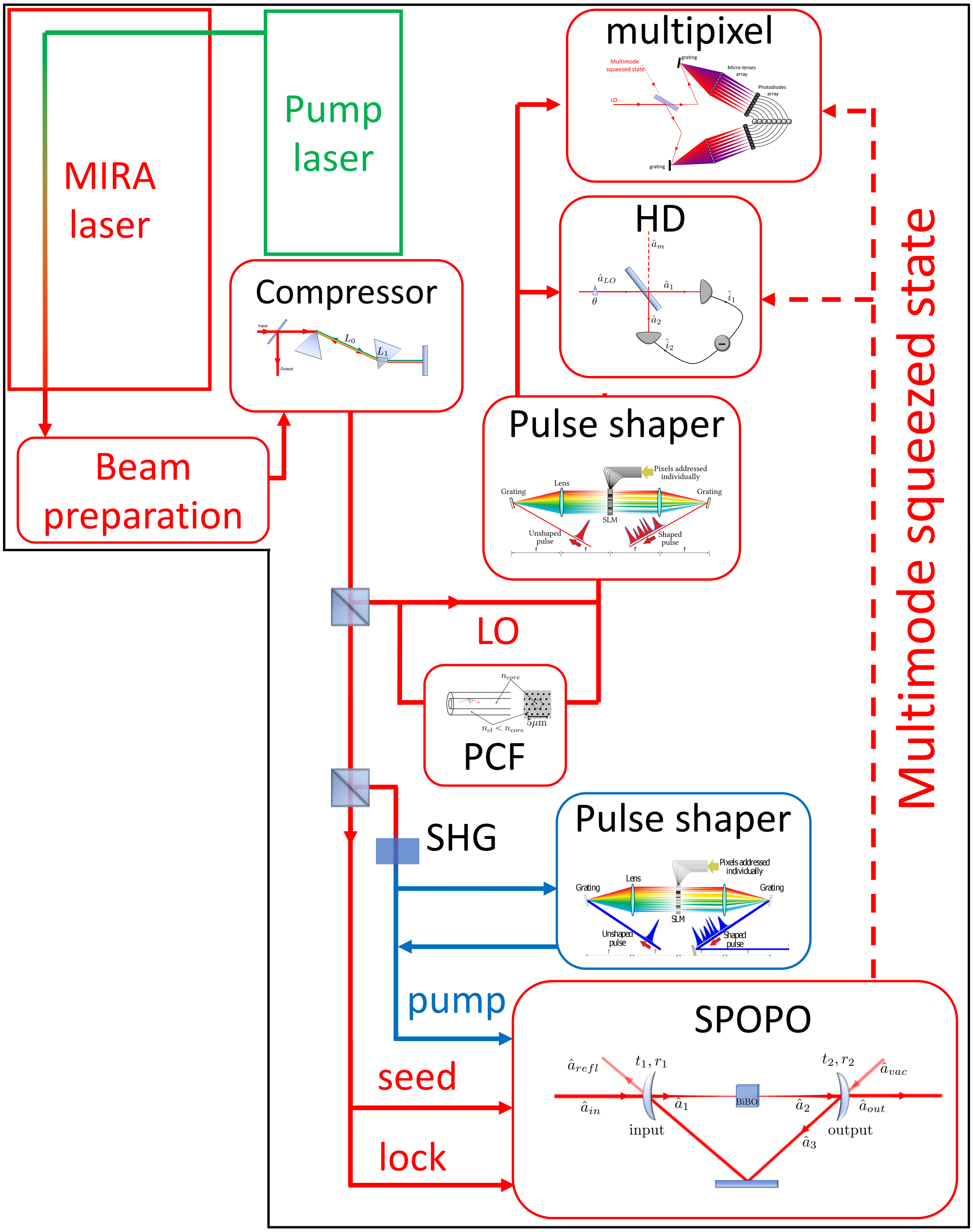

Figure 3.18 – Scheme of the whole experiment. The pulse shaper for the blue beam and the multipixel are described on next chapter. HD stands for homodyne detection.

Chapter 4

Multimode squeezed state measurements

Contents

The questions about the generation and the characterization of multimode squeezed states have been previously evoked theoretically and experimentally, let us now show the results of the measurements. This is the purpose of this chapter. First of all, we discuss on which basis of modes to choose for the covariance matrix reconstruction and we expose the way to extract informations from raw data. Secondly, we show covariance matrices and squeezing measurements. Finally, we present a variant for the detection scheme based on homodyne detections performed in parallel. We call this setup the multipixels homodyne detection.

4.1 Reconstruction of the covariance matrix

4.1.1 The basis choice

We saw in chapter 3, that depending on the mode basis choice for the local oscillator mode, we will measure correlations between optical modes or superposition of squeezed states. We also know that the transformation of the SPOPO, denoted as U_{SPOPO}, is symplectic, which means we can decompose it as follows [Cai 17]:

$$U_{SPOPO} = O_1 \Delta O_2^T \tag{4.1}$$

where O_1 and O_2 are orthogonal matrices and Δ is a diagonal matrix. The following interpretation is coming out: if we write the transformation in a given basis of modes, we will always find a transition matrix to write the transformation for another orthogonal basis where the transformation is diagonal. In other words, as long as the chosen basis to measure the covariance terms is orthogonal, we will find the supermodes which compose the vectors of the transition matrix given by the diagonalization of the covariance matrix. In this new basis, we optimize the squeezing quantity that we can measure.

4.1.2 The frequency band basis

The most natural choice for an orthogonal basis is the one composed by all the teeth of the frequency comb. However, as we saw in chapter 3, the complexity of the pulse shaper is much lower in comparison with the number of modes calculated in chapter 1. For this reason, our basis choice is reduced to the frequency band elements of the spectrum which are represented in figure 4.1. Two constraints are imposed for the proper execution of the acquisitions:

- We must ensure that there is no overlap between the modes to make sure the basis is effectively orthogonal. To guarantee this condition, the frexels are spaced 3 pixels apart on the SLM.

- We choose the width of the frexels to ensure to have enough elements in the basis. This number is important because it impacts the resolution on the determination of the supermodes after diagonalization. However, we can't reduce the width as much as we want in order to get enough power for each band and ensure a good transmission of the detector. N_b is the total number of frequency bands

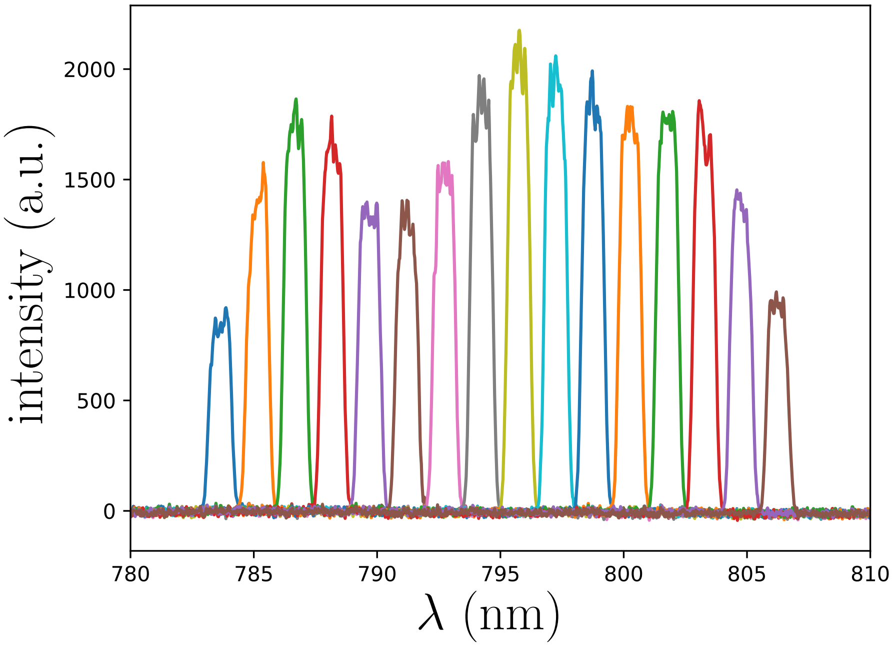

Figure 4.1 – Intensity of the different frexel modes. The beam in input of the spectrometer is here coming from the PCF, which explains the global shape of the bundled frexels.

From the derivation of the interaction Hamiltonian of the SPOPO described in chapter 2, we saw that if the phase among the pump spectrum is constant, the covariance terms $\langle \Delta q_i p_j \rangle$ and $\langle \Delta p_i q_j \rangle$ are zero for $0 \leq i, j \leq N_b$. Hence, to reconstruct the covariance matrix, we restrict ourself to measure $\langle \Delta q_i, q_j \rangle$ and $\langle \Delta p_i, p_j \rangle$ values.
During the measurement, the local oscillator is shaped as the frequency bands or as a linear combination of frequency bands and the phase of the beam is scanned. Hence, we expect to observe oscillations of the noise level on the spectrum analyzer. Starting from equation (3.6), we write the signal at the output of the homodyne detector as:

$$s_i(\theta) = \alpha_i(\cos(\theta)q_i + \sin(\theta)p_i) \tag{4.2}$$

where i is the frequency band label and θ depicts the LO phase. On the screen of the spectrum analyzer, we observe the variance of the signal versus time but since we apply a triangular signal on the piezo and we assume that the voltage is low enough to be in the linear regime, the time variable is replaced by θ in the equation (4.2). α_i is the LO power. We then deduce the variance of the signal which is the quantity measured by the spectrum analyzer:

$$\left\langle s_i^2(\theta) \right\rangle = \alpha_i^2 \left\langle q_i^2 \cos^2(\theta) + p_i^2 \sin^2(\theta) + (q_i p_i + p_i q_i) \cos(\theta) \sin(\theta) \right\rangle \tag{4.3}$$

Because $\langle q_i p_i \rangle = \langle p_i q_i \rangle = 0$, we have:

$$\frac{\langle s_i^2(\theta) \rangle}{\alpha_i^2} = \left\langle q_i^2 \cos^2(\theta) + p_i^2 \sin^2(\theta) \right\rangle \tag{4.4}$$

Then using trigonometric formulas $\cos^2(\theta) = \frac{1+cos(2\theta)}{2}$ and $\sin^2(\theta) = \frac{1-\cos(2\theta)}{2}$ we get:

$$\frac{\langle s_i^2(\theta) \rangle}{\alpha_i^2} = \frac{1}{2}(\left\langle q_i^2 \right\rangle + \left\langle p_i^2 \right\rangle) + \frac{1}{2}(\left\langle q_i^2 \right\rangle - \left\langle p_i^2 \right\rangle)\cos(2\theta) \tag{4.5}$$

The variance of the signal is thus of the form $f(\theta) = A + B\cos(2\theta)$ with $(A, B) \in \mathbb{R}^2$. Hence, just by extracting the mean and the amplitude of the signal from the spectrum analizer, we get $\langle q_i^2 \rangle$ and $\langle p_i^2 \rangle$ values thanks to the relations:

$$\left\langle q_i^2 \right\rangle = A + B \tag{4.6}$$

$$\left\langle q_i^2 \right\rangle = A - B \tag{4.7}$$

Now, let us consider the case where two frexels i and j are printed on the SLM. The signal can be expressed as:

$$s_{i,j} = \frac{\alpha_{i,j}}{\sqrt{2}}[(q_i + q_j)\cos(\theta) + (p_i + p_j)\sin(\theta)] \tag{4.8}$$

where $\alpha_{i,j}$ is the LO power when the two frequency band i and j are turned on on the SLM screen. We assume that the power repartition between the two modes is balanced. Then, the variance is expressed as:

$$\begin{aligned}\frac{\left\langle s_{i,j}^2 \right\rangle}{\alpha_{i,j}^2} &= \frac{1}{2}\left[\frac{\langle q_i^2 \rangle + \left\langle q_j^2 \right\rangle + \langle p_i^2 \rangle + \left\langle p_j^2 \right\rangle}{2} + \langle q_i q_j \rangle + \langle p_i p_j \rangle\right] \\ &\quad + \frac{1}{2}\left[\frac{\langle q_i^2 \rangle + \left\langle q_j^2 \right\rangle - \langle p_i^2 \rangle - \left\langle p_j^2 \right\rangle}{2} + \langle q_i q_j \rangle - \langle p_i p_j \rangle\right]\cos(2\theta)\end{aligned} \tag{4.9}$$

$\left\langle s_{i,j}^2 \right\rangle / \alpha_{i,j}^2$ has the same form than in (4.5). By using the same notation we have introduced above for the amplitude and the mean, we have:

$$\langle q_i q_j \rangle = A + B - \frac{\langle q_i^2 \rangle + \left\langle q_j^2 \right\rangle}{2} \tag{4.10}$$

$$\langle p_i p_j \rangle = A - B - \frac{\langle p_i^2 \rangle + \left\langle p_j^2 \right\rangle}{2} \tag{4.11}$$

A remark comes here: in order to find $< q_i q_j >$ and $< p_i p_j >$, it is not enough to just interpret the data related to the SLM mask composed by the frexels i and j, it is also needed to know the diagonal terms of the covariance matrix.

4.1.3 Extraction of the covariance terms

Just by knowing the amplitude and the mean of one signal, it is possible to determine one term of the covariance matrix or two because of the symmetry property. However, with N_b frequency bands, at least $N_b(N_b - 1)/2$ shots of measurement are needed for the full reconstruction, which forces us to automate the data process. We wrote thus a python code to extract the mean and the amplitude for all the measured curves. How the code works is described below.

4.1.3.1 The mean value extraction

We first start by extracting the mean value. The given signal s has a sine function form composed of M points. s can be discretize and it becomes:

$$\mathfrak{S}(k) = A + B\cos(f_k k + \phi), \text{ with } k \in \mathbb{N} \tag{4.12}$$

where ϕ and f_k are respectively the phase and the frequency of this discretized function. Because $\mathfrak{S}$ is a sin function, to extract A, we can directly average the discretize function. Nonetheless, the average is done over the M acquired points and not over a fixed number of periods. If, we introduce the function:

$$l(k) = \frac{1}{k}\sum_{j=0}^{k} s(j) \tag{4.13}$$

and we can easily show that:

$$\lim_{k\to\infty} l(k) = A \tag{4.14}$$

However, because we do not acquire an infinite number of points, we have:

$$l(M) \approx A \tag{4.15}$$

This equation is an approximation. On the code we take the mean of the last 100 points as limit of the function l.

In order to check wether this method is consistent with experimental data, we generate a sine function where noise on the different parameters (frequency, phase, amplitude, mean) is added and we verify that this method can recover the original values of A for different noise levels. The added noise is created by a random function of python. In figure 4.2 below, the plots represent the errors of the method for different types of noise. The noise level is defined as the ratio between the amplitude of the noise and the value of the parameter to which the noise has been added. We see in figure 4.2 that in the three noise frameworks, the code is still able to recover the right mean values. When the noise level is above 1, the relative error may exceed 10%. Nonetheless, this is not a problem since we meet this amount of noise during the acquisition when the squeezing is close to zero.

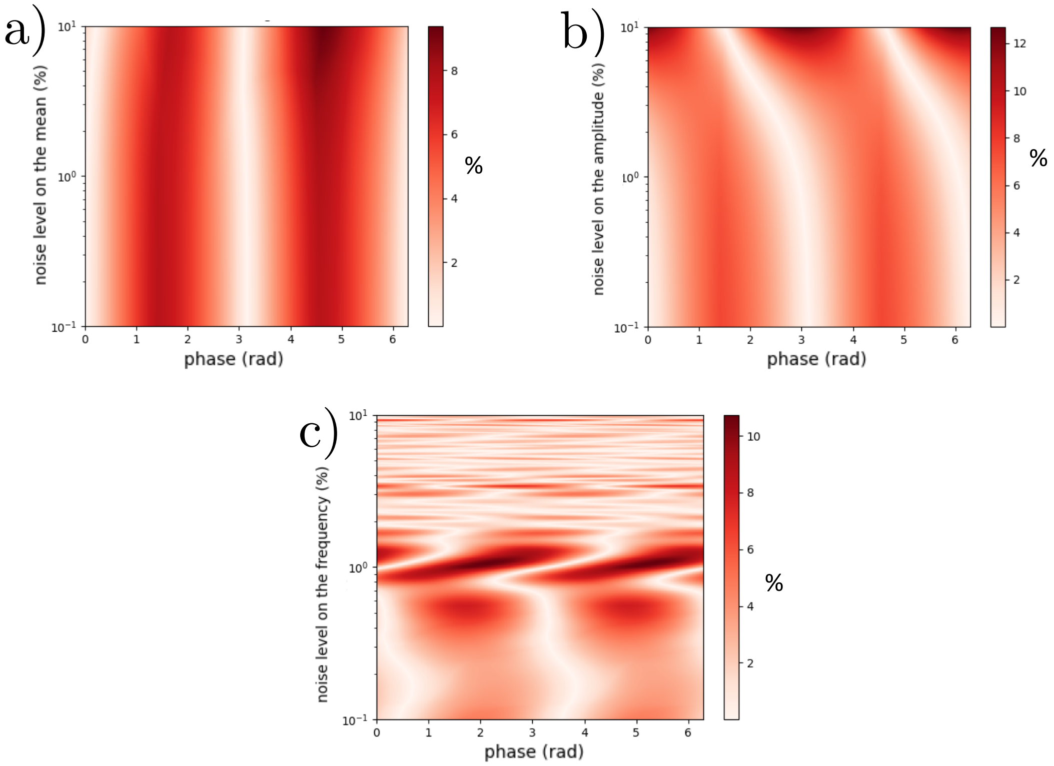

Figure 4.2 – Relative errors on the determination of the signal mean in % of the mean as a function of the phase of the signal ϕ and the noise level for different types of noise: (a) noise on the mean; (b) noise on the amplitude; (c) noise on the frequency

4.1.3.2 The amplitude determination

The second value that we have to extract from all the data sets is the amplitudes value. To do so, the first step is to deduce the frequency of the given signal thanks to a Discrete Fourier Transform (DFT). Then, we multiply the discrete signal by a cosine function such as:

$$\mathcal{O}_\psi(k) = s(k) \times \cos(f_{DFT}k + \psi) \tag{4.16}$$

where f_{DFT} is the frequency determined by the DFT. We assume $f_{DFT} = f_k$ and we obtain:

$$\mathcal{O}_\psi(k) = A\cos(f_k k + \psi) + B\left[\cos(\phi - \psi) + \cos(2fk + \phi + \psi)\right] \tag{4.17}$$

The average of this function is $B\cos(\phi - \psi)$. Hence, we find the amplitude of s as:

$$B = \max_{\psi} \langle \mathcal{O}_\psi(k) \rangle \tag{4.18}$$

The robustness of the code against noises is checked. Indeed, the same verification than for the mean value determination is done. In figure 4.3 below is represented the error plot when the data are corrupted by fluctuations on the mean and the amplitude.

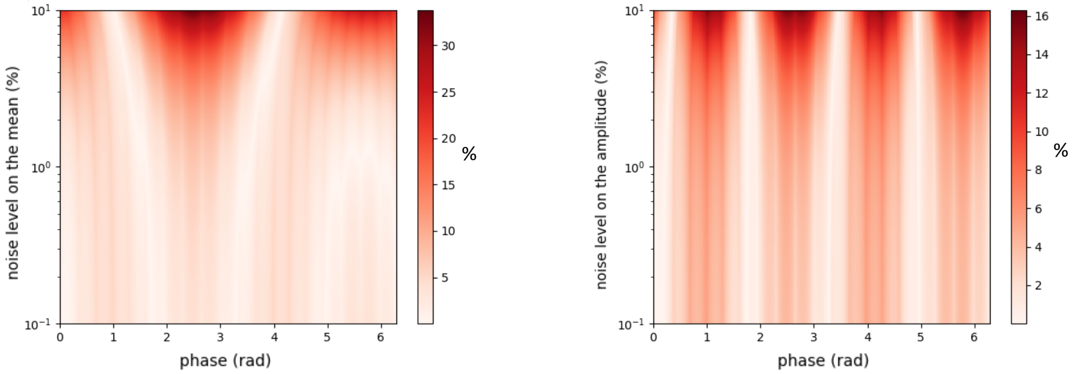

Figure 4.3 – Relative errors on the determination of the signal amplitude in % of the amplitude as a function of the phase of the signal and the noise level for different types of noise: (*left*): noise on the mean; (*right*): noise on the amplitude.

We can make the same remark than for the mean recovery. The relative error is important when the noise level exceed 1, which have not massive consequence in the interpretation of the experimental data, and which makes this method is acceptable for our use.

4.1.4 $\langle Q^2 \rangle$ and $\langle P^2 \rangle$ matrices measurements

For the measurement, we choose $N_b = 16$ frexels, which means we need 120 shots of measurement for a complete reconstruction of the covariance matrix. The piezo-electric component is set at 5Hz. We use a spectrum analyzer (Agilant Technologies, modelMXA Signal Analyzer N9020A 20Hz-2,6Ghz) in the 0 span mode where the frequency is fixed at 1MHz with a resolution bandwidth $\Delta = 100kHz$ and a video bandwidth of $\Delta_v = 500Hz$. Besides, this instrument is triggered on the triangular signal of the piezo in order to reduce phase fluctuations in the data acquisitions. For one shot, we take 1000 data points in 0,09s. Hence, when we take several acquisitions, saving the full data set last around 20 minutes which is compatible with the experiment stability.
In figure 4.4, we show the $\langle P^2 \rangle$ and $\langle Q^2 \rangle$ matrices. Each square in the matrices corresponds to the average of the 10 covariance terms obtained from the code presented before. For this measurement the pump power is 40mW.

From both of these matrices we can find the supermodes of the SPOPO. It has been shown in [Williamson 36, Ikramov 18] that any positive definite matrix $\mathbf{\Gamma}$, which is the

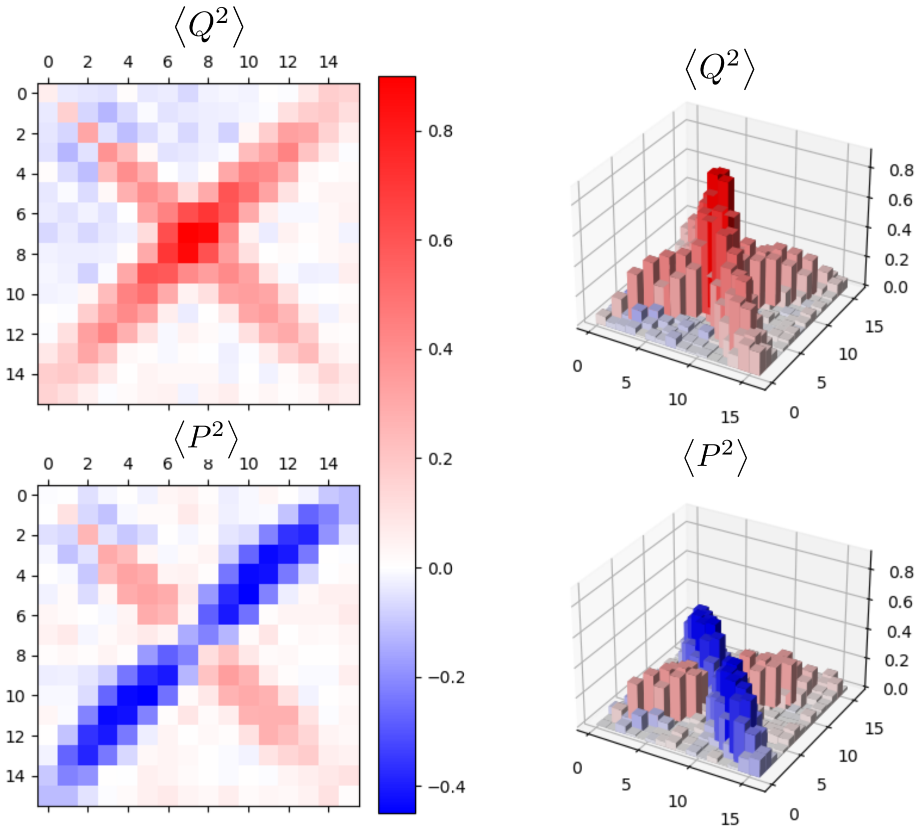

Figure 4.4 – $\langle Q^2 \rangle$ and $\langle P^2 \rangle$ matrices measured for a pump power $P = 40mW$. The 3D plots represent the absolute values.

Modes	λ_0 (nm)	FHWM (nm)
0	794.98	9.61
1	795	7.94
2	795.02	6.34
3	795.07	6.67
4	794.96	5.88
5	795.20	5.74
6	794.90	6.07
7	795.46	5.19
8	795.24	4.60

Table 4.1 – λ_0 and $FHWM$ values obtained from the fit of the eigenmodes with Hermite-Gaussian function

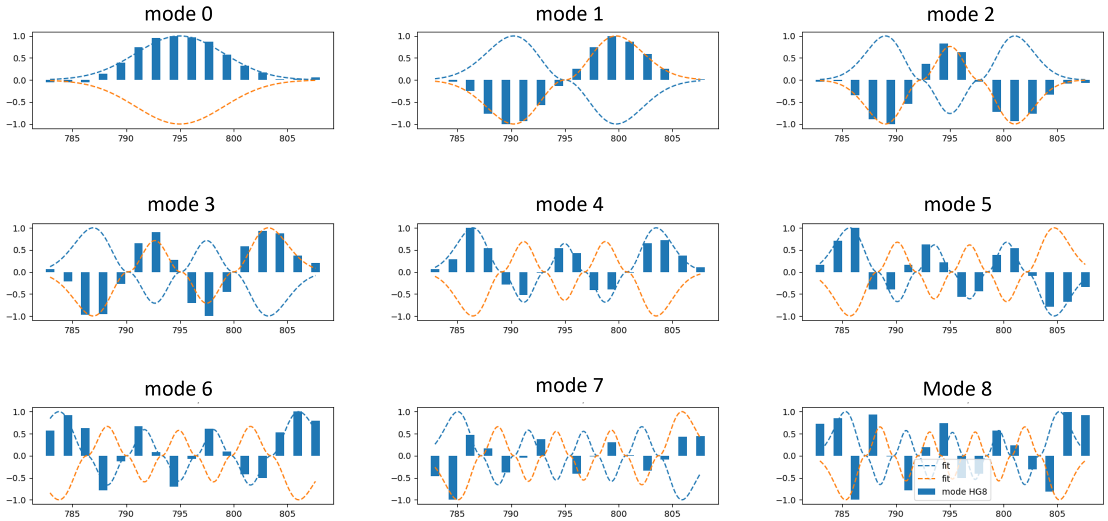

Figure 4.5 – Representation of the supermodes found by Grahm Schmidt process applied on the eigenvectors of the matrices represented in 4.4.

case of a covariance matrix, can be decomposed as:

$$\mathbf{\Gamma} = \boldsymbol{S}\mathbf{\Gamma}_W\boldsymbol{S}^T \tag{4.19}$$

where $\mathbf{\Gamma}_W = \text{diag}(v_1, ..., v_n)$ is diagonal with $v_i \geq 0$ and $\boldsymbol{S}$ is symplectic. Then, the Bloch Messiah decomposition can be applied and we get:

$$\mathbf{\Gamma} = \boldsymbol{O}_1\boldsymbol{K}\boldsymbol{O}_2\mathbf{\Gamma}_W\boldsymbol{O}_2^T\boldsymbol{K}\boldsymbol{O}_1^T \tag{4.20}$$

where $\boldsymbol{K}$ is also diagonal and $\boldsymbol{O}_1$, $\boldsymbol{O}_2$ are orthogonal. The total decomposition can be interpreted as follows: $\mathbf{\Gamma}_W$ is the covariance matrix containing the classical correlations, $\boldsymbol{O}_2$ is is the operation which consists in changing the basis for the SPOPO eigenmodes. $\boldsymbol{K}$ is the squeezer of the eigenmodes and finally $\boldsymbol{O}_1$ is the last basis change corresponding in the experiment to the measurement. If there is no classical noise, $\mathbf{\Gamma}_W$ is the identity and the decomposition can be written as:

$$\mathbf{\Gamma} = \boldsymbol{O}_1\boldsymbol{K}^2\boldsymbol{O}_1^T \tag{4.21}$$

When losses are taken into account, the covariance matrix is not anymore unitary and we have to consider (4.20). In other words, the transformation $\boldsymbol{O}_2^{-1}\mathbf{\Gamma}_W\boldsymbol{O}_2$ is not necessary diagonal. Nonetheless, as long as the classical correlations are small, we assume we can find a basis of eigenmodes where each element is close to be independant from the others.

In practice, after the acquisition of $\langle\Delta q^2\rangle$ and $\langle\Delta p^2\rangle$ matrices (the terms $\langle q_i p_j\rangle$ are zero), we diagonalize it and we build an orthogonal basis from the two sets of eigenvectors using Gram Schmidt process 4.5. From this characterization, we also measure the squeezing when the Hermite-Gaussian fits are implemented on the pulse shaper. The results of this measurement is shown in figure 4.6. We see that the first modes are the most squeezed but also the less pure.

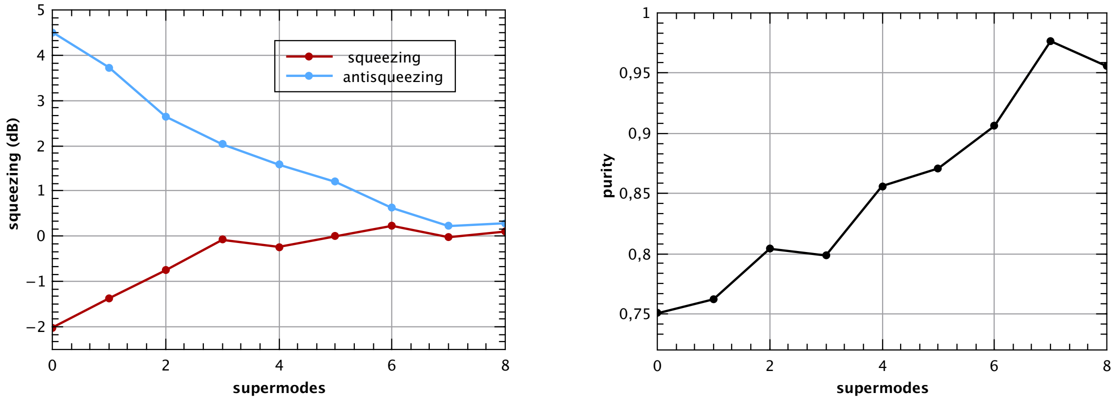

Figure 4.6 – *left*: Squeezing and anti-squeezing levels in dB as a function of the supermodes. *right*: Purity of the supermodes. The purity is obtained via the formula (1.67)

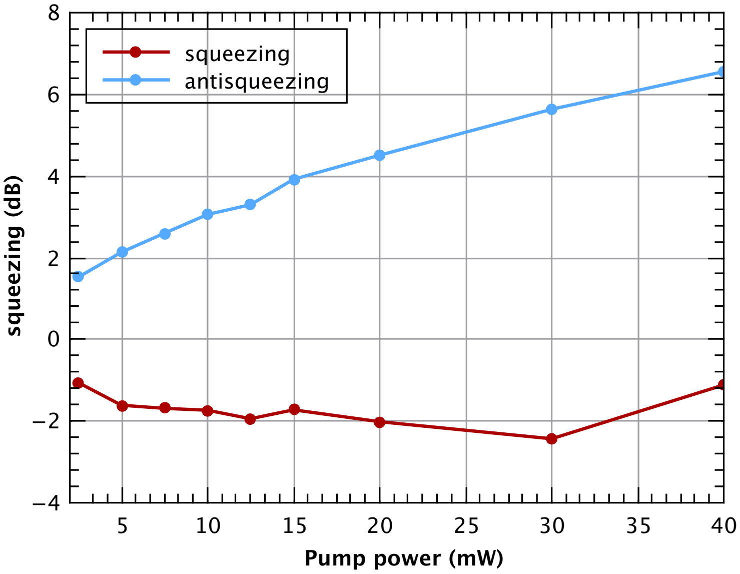

Figure 4.7 – Squeezing of the supermode 0 as a function of the pump power.

The figure 4.7 represents the squeezing of the first supermode as a function of the pump power. We observe that the curve follows the shapes predicted by the theory in chapter 2. We also performed this measurement for the second and the third supermodes, the results are shown in appendix C.

4.2 The multipixel homodyne detection

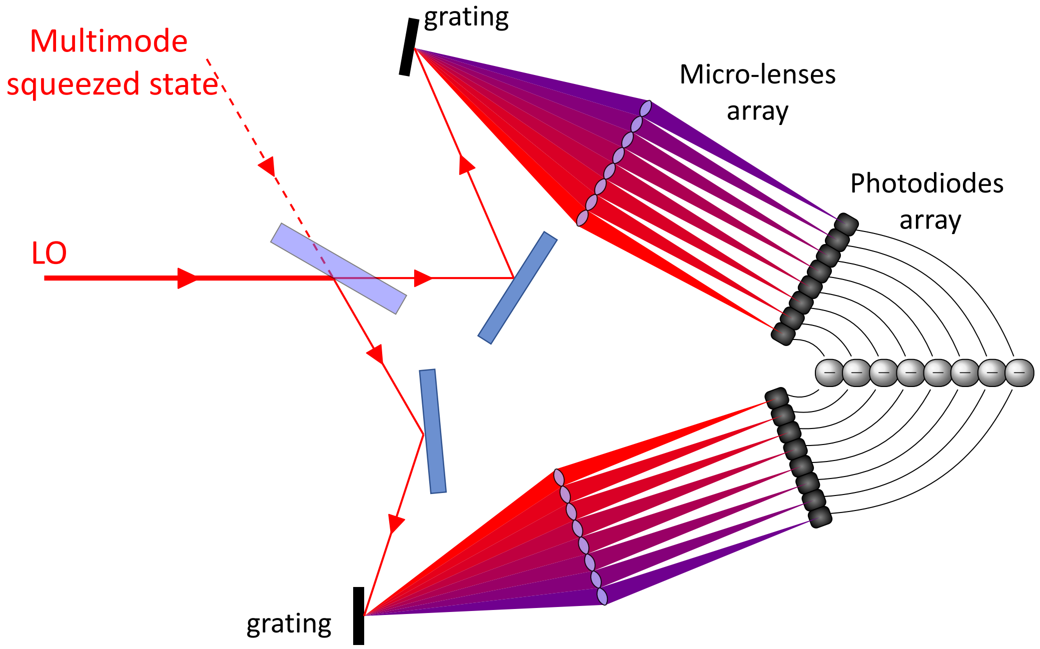

Figure 4.8 – Scheme of the Multipixel homodyne detection.

4.2.1 Limitation of the homodyne detection

For the precedents results, we have restricted ourself to the reconstruction of the $(\langle Q_i, Q_j \rangle)_{0 \leq i,j \leq M}$ and $(\langle P_i, P_j \rangle)_{0 \leq i,j \leq M}$ matrices according to the hypothesis that the phase among the pump spectrum is flat. Hence, if this assumption does not stand anymore, we have to determine the remaining terms, not accessible by using the setup of homodyne detection previously shown. In this part we present another scheme for the detection which consists to several homodyne detections set in parallel called multipixel homodyne detection (MHD).

4.2.2 The mutipixel homodyne detection

A scheme of the MHD is shown in the figure 4.8. After the balanced beam splitter, the light is diffracted and focused on two photodiodes arrays, which allows us to perform measurements on several frequency bands of the LO spectrum at the same time. One of the interest of this new setup is to improve the speed of the acquisitions but mainly to get access to the extra terms of the covariance matrix and reconstruct the full matrix.

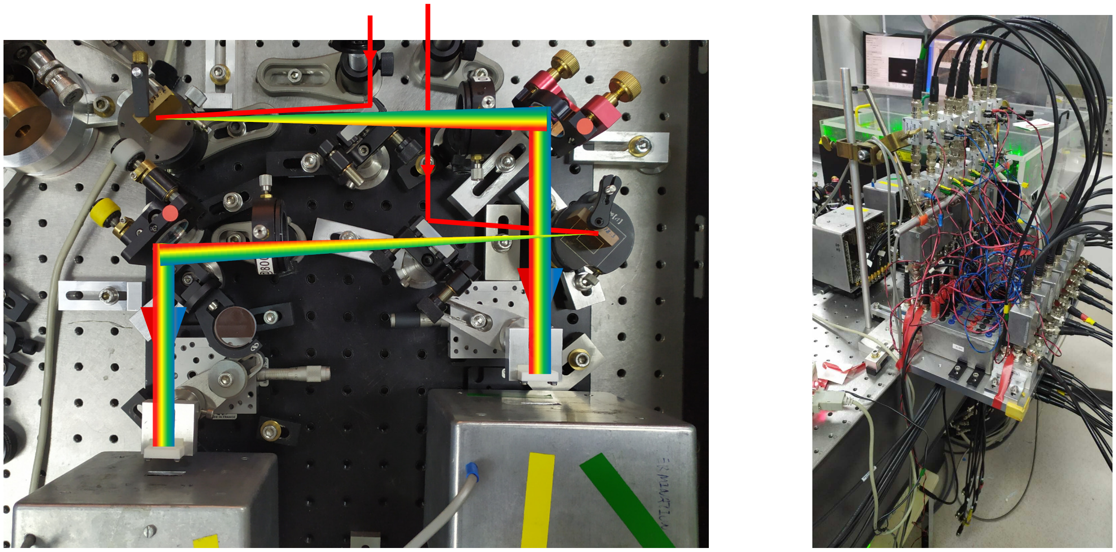

Figure 4.9 – Picture of the experimental setup of the MHD: *left*: optical part and *right*: electronic part.

A picture of the implementation on the optical table is represented in figure 4.9. A system gratings - lens - micro-lenses array is placed on each side of the beam splitter. We use gratings of 1800 gr/mm and lenses with focal length of 175mm. These optics are chosen in order to match the LO spectrum with the detection array. For more details about this choice see [Michel 21, Dufour 18]. However the efficient area of photodiodes are slightly spaced between them. To counterpart any loss of light, a micro lens array is mounted in front of the detection box to focus and collect light in the centre of each photodiode.

The array is composed of 8 photodiodes (Hamamatsu, model S4111) with a quantum efficiency of 80%. Then, for each channel, an electric setup is installed in order to process the signals. The electronic part is composed as follows:

- The first stage of the scheme is a homemade amplifier design by C. Yin and J. Roslund, printed on a electronic card and implemented in the box as shown on the left in figure 4.9

- The current difference is performed using power splitter from mini circuit (model ZSC-2-1+).
- We use electronic filters to only keep the relative signal: a 5MHz low pass filter (model BLP 5+ from minicircuit) and a 25kHz homemade high pass filter.
- The signal is mixed with a signal at 1MHz using a ZAD 3+ from minicircuit.
- The demodulated signal is filtered by a 100kHz low pass filter
- The signal is amplified using two amplifiers from minicircuit (model ZFL-500LN-BNC+)

Finally, the signal is collected by an acquisition card from National Instrument (model NI-PSXI-5105). All these stages of electronics play the role of the 8 spectrum analyzers in the 0 span mode set at $f = 1$MHz with a resolution bandwidth of $\Delta_v = 100$kHz.

4.2.3 Reconstruction of the full covariance matrix

The derivation, to recover the covariance terms, is slightly different than the method presented above. In this paragraph, we show the main part of the calculation but more details can be found in the thesis of T. Michel[Michel 21].
In the experimental setup, each channel i of the MHD is acquiring a signal s_i such as:

$$s_i(\theta_i) = \alpha_i \left(\cos(\theta_i) q_i + \sin(\theta_i) p_i\right) + e_i \tag{4.22}$$

where α_i is the LO powers, e_i is the electronic noise and θ_i is the phase of the LO beam related to the channel i. This phase is monitorable via a vertical shift of the sawtooth grating printed on related area of the SLM screen in the pulse shaper. We are interested by the covariance of two signal i and j, $C_{i,j}(\theta_i, \theta_j) = \mathrm{Cov}\left(s_i(\theta_i), s_j(\theta_j)\right)$. This covariance function is derived as

$$\begin{aligned} C_{i,j}(\theta_i, \theta_j) = \alpha_i \alpha_j (&\cos(\theta_i)\cos(\theta_j)\langle q_i q_j\rangle + \sin(\theta_i)\sin(\theta_j)\langle p_i p_j\rangle \\ &+ \cos(\theta_i)\sin(\theta_j)\langle q_i p_j\rangle + \sin(\theta_i)\sin(\theta_j)\langle p_i q_j\rangle) \end{aligned} \tag{4.23}$$

We assume here that the electrical noise is negligible. The expression can be normalized such as:

$$\tilde{C}_{i,j}(\theta_i, \theta_j) := \frac{C_{i,j}(\theta_i, \theta_j)}{\alpha_i \alpha_j} \tag{4.24}$$

and the expression of the covariance terms are thus rewritten as:

$$
\begin{aligned}
\tilde{C}_{i,j}(\theta_i, \theta_j) = \frac{1}{2}[&(\cos(\theta_i - \theta_j) + \cos(\theta_i + \theta_j)) \langle q_i q_j \rangle \\
&+ (\cos(\theta_i - \theta_j) - \cos(\theta_i + \theta_j)) \langle p_i p_j \rangle \\
&+ (\sin(\theta_i - \theta_j) - \sin(\theta_i - \theta_j)) \langle q_i p_j \rangle \\
&+ (\sin(\theta_i + \theta_j) + \sin(\theta_i - \theta_j)) \langle p_i q_j \rangle]
\end{aligned} \tag{4.25}
$$

In order to extract the term of the covariance matrix in position (i, j), we need two measurements:

- one where the two frexel modes are in phase: $\theta_i = \theta_j$
- one where there is $\pi/2$ phase shift: $\theta_i = \theta_j + \pi/2$

All the channel are doing the acquisition in parallel. Hence, by crossing all the data, we can recover the full covariance matrix using only four SLM masks with the following relative phases:

- $\begin{pmatrix} 0 & 0 & 0 & 0 & 0 & 0 & 0 & 0 \end{pmatrix}$
- $\begin{pmatrix} \frac{\pi}{2} & \frac{\pi}{2} & \frac{\pi}{2} & \frac{\pi}{2} & 0 & 0 & 0 & 0 \end{pmatrix}$
- $\begin{pmatrix} \frac{\pi}{2} & \frac{\pi}{2} & 0 & 0 & \frac{\pi}{2} & \frac{\pi}{2} & 0 & 0 \end{pmatrix}$
- $\begin{pmatrix} \frac{\pi}{2} & 0 & \frac{\pi}{2} & 0 & \frac{\pi}{2} & 0 & \frac{\pi}{2} & 0 \end{pmatrix}$

For more details about the calculation to extract $\langle p_i, q_j \rangle$, $\langle q_i, q_j \rangle$, $\langle p_i, p_j \rangle$ terms, see [Michel 21]. Results of full covariance matrices reconstructions are shown in the following of this section.

4.3 Pump shaping

4.3.1 How to change the output state of the SPOPO

Once we have performed homodyne detection and we are able to recover all the terms of the covariance matrix, a question comes out: is it possible to change the output state of the SPOPO and to measure it. To answer to this question, let's consider the joint spectral distribution formula defined in chapter 2. Indeed, this function, which theoretically describes the interaction Hamiltonian in the SPOPO influences the eigenstates and eigenvalues of the system. It is the product of two terms:

- $f_p(\omega + \omega')$ the function that describes the mode of the pump in the frequency domain.
- $\Phi(\omega, \omega')$, the phase matching within the crystal inside the cavity.

It seems hard to change the non-linear crystal from the cavity especially if we hope to always recover the phase matching and to be consistent in all measurements. Hence it excludes any change on the phase matching term. Nonetheless, modifying the shape and the phase of the function f_p is accessible using a setup that we have already introduced in chapter 3: a pulse shaper.

4.3.2 The pulse shaper of the pump beam

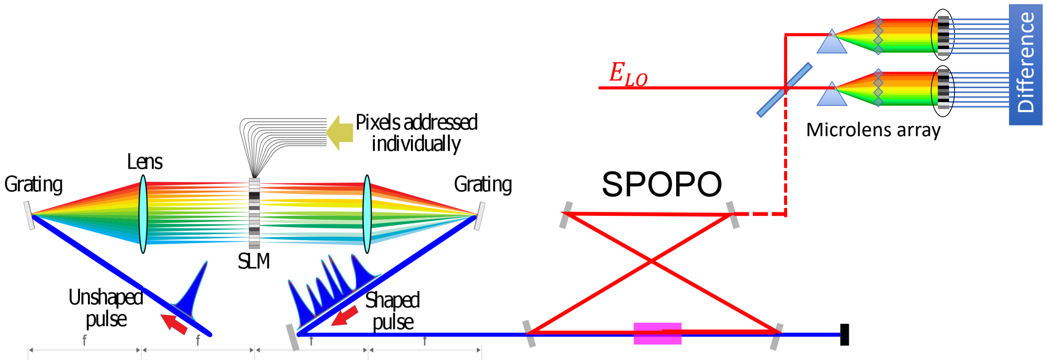

Figure 4.10 – Pulse shaper scheme dedicated to the pump beam.

An auxiliary path for the pump had been created to implement the pulse shaper 4.10. In order to match temporally pump pulses with the ones from the seed we have to ensure that the total length of the new path is $L = 3,92m$, the same than the MIRA laser cavity. The pulse shaper has the same design than the one used for the LO. We use a grating with a density of 2400 gr/mm with $\theta_d = 28.5°$. The focal length of the cylindrical mirror is $f = 250$ mm and the SLM is from the brand hamamatsu (model X10468-05) with 792×600 pixels. The spectrum of the beam is also a frequency comb but centered in $\lambda_0 = 397.5$ nm, with a bandwidth of $\Delta\lambda = 1.3$ nm and spatially the waist is $\omega_0 = 3$ mm. From these parameters, we compute the complexities:

$$\eta_{pxl} = 44.4 \tag{4.26}$$

$$\eta_{opt} = 42.1 \tag{4.27}$$

Finally we add a pinhole on the path to filter spatially the beam and remove order 0. For a pump power of 20 mW, the contrast of the amplified deamplified signal of the seed due to PDC is $V_{PDC} = 78\%$, which is close to the value found in chapter 2 for the usual pump beam. The complexities are lower compared to the LO pulse shaper but they are sufficient for the different masks that we present below. The efficiency of the extra path is around 30% and is mainly due to the pulse shaper losses (50%). There is also more losses from the pinhole, which comes after the pulse shaper, than usual because of the beam spatial shape which is less gaussian than the one at the output of the LO pulse shaper. This amount of efficiency forces us to inject a lot of power into the SHG to be able to achieve pump power levels comparable to those without going through the auxiliary path.

4.3.3 Results

In figure 4.11 is shown the full measurement of covariance matrices in two cases. The first one is without any pump shaping. We see that we retrieve the same form that has been found with the single pixel homodyne detection and that the $\langle q_i p_j \rangle$ and $\langle p_i q_j \rangle$ terms are effectively negligible in comparison with $\langle q_i q_j \rangle$ and $\langle p_i p_j \rangle$ values. This observation confirms the hypothesis which has been made in the derivation of the parametric down conversion of the SPOPO in chapter 2. However, in the second case, this is not anymore valid. Indeed, for this measurement, a phase shift of $\pi/2$ has been applied on the right part of the spectrum. We observe that some non zero values of $\langle p_i q_j \rangle$ and $\langle q_i p_j \rangle$ appear. Hence, in this case, we observe that to characterize the output state of the SPOPO a full recovery of the covariance terms using the MHD is needed. Here, we do not diagonalize the covariance matrices, which will be done for the matrices of the following section.

4.4 Optimization of the SPOPO output state via machine learning

4.4.1 A brief introduction to the problem

In this last part is shown results of the optimization of the SPOPO output states using machine learning algorithms. This project, initiated by T. Michel [Michel 21], follows the work of F. Arzani [Arzani 18] who also studied this optimization question. The goal here is to highlight some of the main results in order to give an example of the advantage of the pump shaping.

Machine learning is a domain of mathematics and informatics which aims to improve resolution or classification problems. Today and for about ten years now, machine learning has experienced tremendous growth and has proven useful in many fields, both industrial and academic[Lecun 89, Lecun 15]. Physics, and in particular optics, are not lacking [Carleo 19].

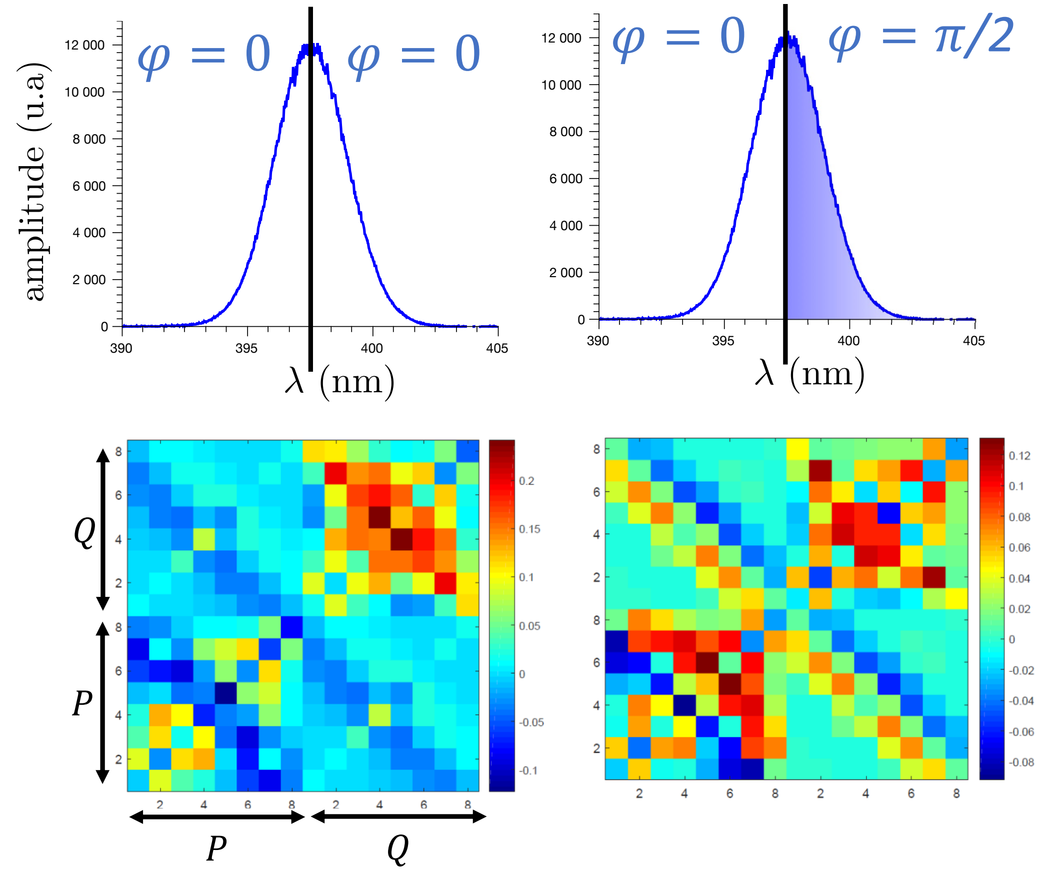

Figure 4.11 – Results of covariance matrix measured with the MHD. The plots on the top represent the pump spectrum injected into the SPOPO and on the bottom the respective covariance matrices. On the left, where there is no pump shaping and on the right there is a phase shift of $\pi/2$ between the two sides of the spectrum.

Here we show how we can optimize via Machine learning the SPOPO output states using 2 types of algorithms:

- a reenforcement one based on projective simulation method (PS)
- a deep learning one based on neural network (ANN)

We first show how the algorithms work and then the results of both processes.

4.4.2 Optimization of the SPOPO output state

Two objectives of optimizations have been studied:

- (1) the degenerate squeezing or in other words the case where the eigenmodes are steadily squeezed.
- (2) the maximization of the squeezing on the first eigenmode

To do so, cost functions are evaluated during the compilation of the codes and the goal is to find the best input in order to maximize them. The cost function chosen corresponding to the two options are:

$$f_1(\boldsymbol{u}) = \frac{1}{\Lambda_1(\boldsymbol{u})} \sum_{j=1}^{100} \Lambda_j \tag{4.28}$$

$$f_2(\boldsymbol{u}) = \frac{\Lambda_1(\boldsymbol{u})}{\Lambda_2(\boldsymbol{u})} \tag{4.29}$$

where Λ_j are the eigenvalues coming from diagonalization of the joint spectral distribution, which have been already introduced in chapter 2. The vector $\boldsymbol{u}$ contains the parameters of the blue pulse shaper.

This type of optimization is a continuation of the work of F. Arzani who studied how to improve output states by using an algorithm which mimics Darwinian evolution to explore the different input parameters [Arzani 18]. In this work, the loss due to the variation of power in the exploration of the spectrum shapes is compensated by modifying the cost functions such as:

$$\bar{f}_1 = f_1 - \frac{3}{(5w(\boldsymbol{u}))^6} \tag{4.30}$$

$$\bar{f}_2 = f_2 - \frac{1}{(5w(\boldsymbol{u}))^6} \tag{4.31}$$

where $w(\boldsymbol{u})$ is the power ratio between the gaussian pump and the shaped one. The results of the two improvements are presented in figure 4.12 The plot of the eigenvalues as a function of the modes number shows the expected results. The dots resulting from $\bar{f}_1$ optimization demonstrate a longer plateau than for the gaussian pump. Regarding $\bar{f}_2$ results, there is a clear difference between the first eigenvalues and the next ones. Nonetheless, the resulted pump shape requires a high level of details and are not suitable for a low complexity pulse shaper.

In the code compiled by T. Michel, the cost function $\bar{f}_2$ contains also a term to compensate the loss from the shaping but they are slightly different with the version of F. Arzani:

$$\bar{f}_2 = \Lambda_1 \tag{4.32}$$

Indeed the normalization to Λ_2 is absent. The penalty of pump power is already included in the cost.

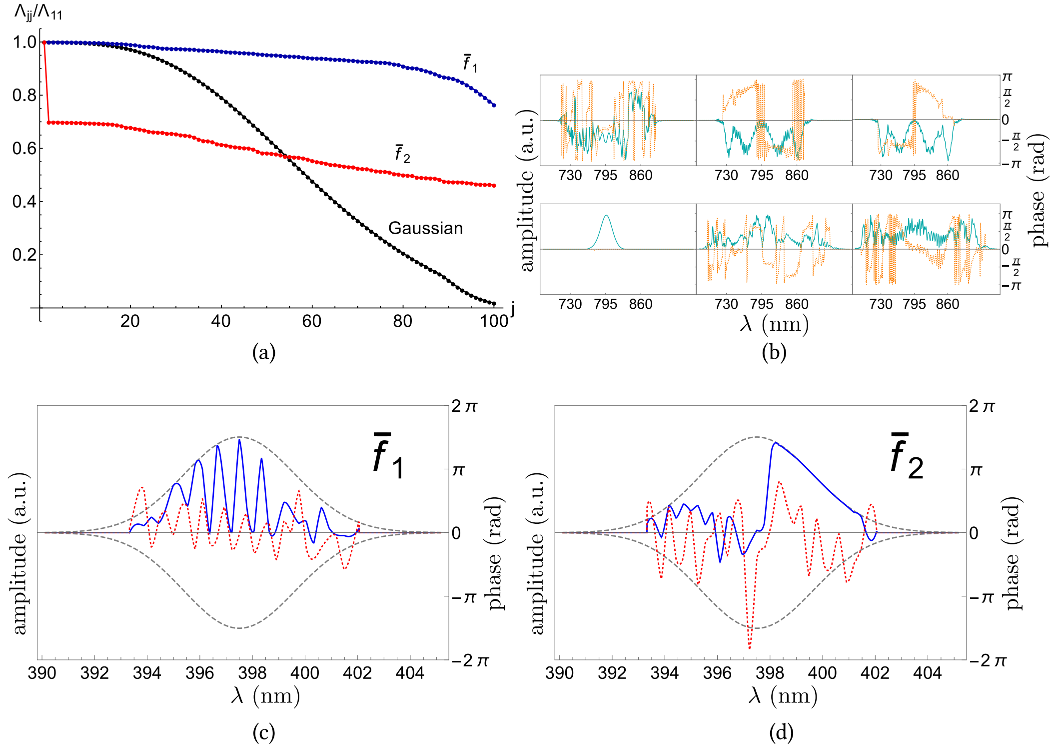

Figure 4.12 – Results of the optimization via genetic algorithm. (a): Calculated eigenvalues for a gaussian pump and the two functions $\bar{f}_1$ and $\bar{f}_2$. (b): Firsts eigenmodes calculated from the $\bar{f}_1$ optimization. Orange line represents the phase and green line the amplitude. (c) and (d): Shapes of the pump to be implemented in the pulse shaper corresponding to the two different optimizations. (taken from [Arzani 18])

4.4.3 Presentation of the algorithms

4.4.3.1 Projective simulation

The figure 4.13 depicts the operations of the algorithm based on projective simulation. We see that an agent acts, via an action denoted as a, on an environment, the system of interest, whose parameters are to be tuned. The environment response to the agent action is monitored, the resulted state is called percept and is denoted as p. The interpretation of the percept will be source of reward or not for the agent, which will influence the agent's next action. Indeed, at each given time, the action is the results of a choice influenced by a probability distribution we can denote $P^{(t)}(a|p)$. We do not go into the details of the calculation here, for more details see [Michel 21].
For the experiment, we use a algorithm developed A. Melnikov and K. Ried and designed for quantum experiments [Melnikov 17, Melnikov 18].

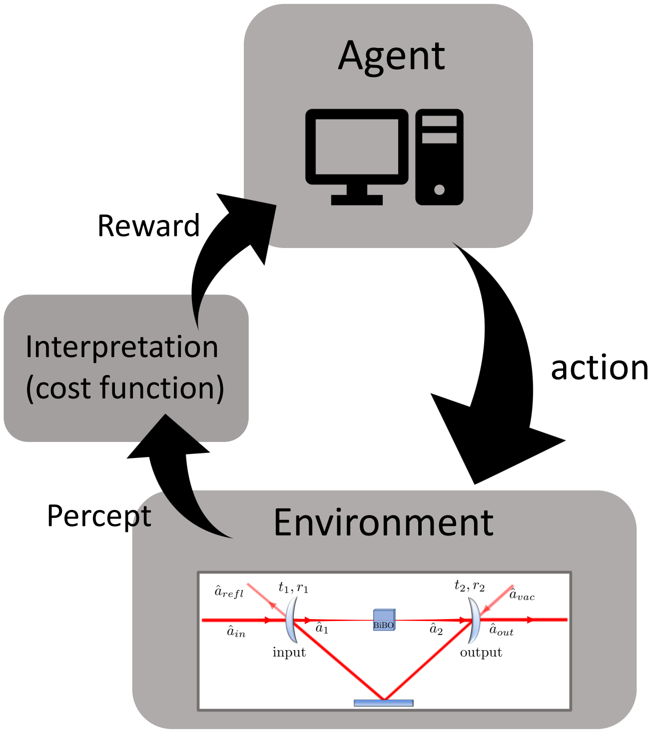

Figure 4.13 – Scheme of the projective simulation algorithm principle.

4.4.3.2 Artificial neural network

The way this algorithm works gets inspiration of neural networks we find in brain as represented in figure 4.14. It explains the given name. Neurons are interconnected with each other via dendrites, which allows the communication of electronic signals from one layer to the next one in nature and which indicates links between nodes in the informatics version. In the figure 4.14, $x_1, ...x_n$ represent the input values and y is the output at the end of the network that is optimized. In the hidden layer, the neurons values are determined by the ones of the neurons present in the precedent layer and by using the formulas from the figure 4.14

A training data set is used, as its name suggests, to train the network and determine the good parameters $w_{i,j}$ and $b_{i,j}$ which characterize the given network. In our case, the neural network considered is composed by 5 hidden layers with 64 neurons each. The algorithm has been developed by Tranter and Slatyer [Tranter 18].

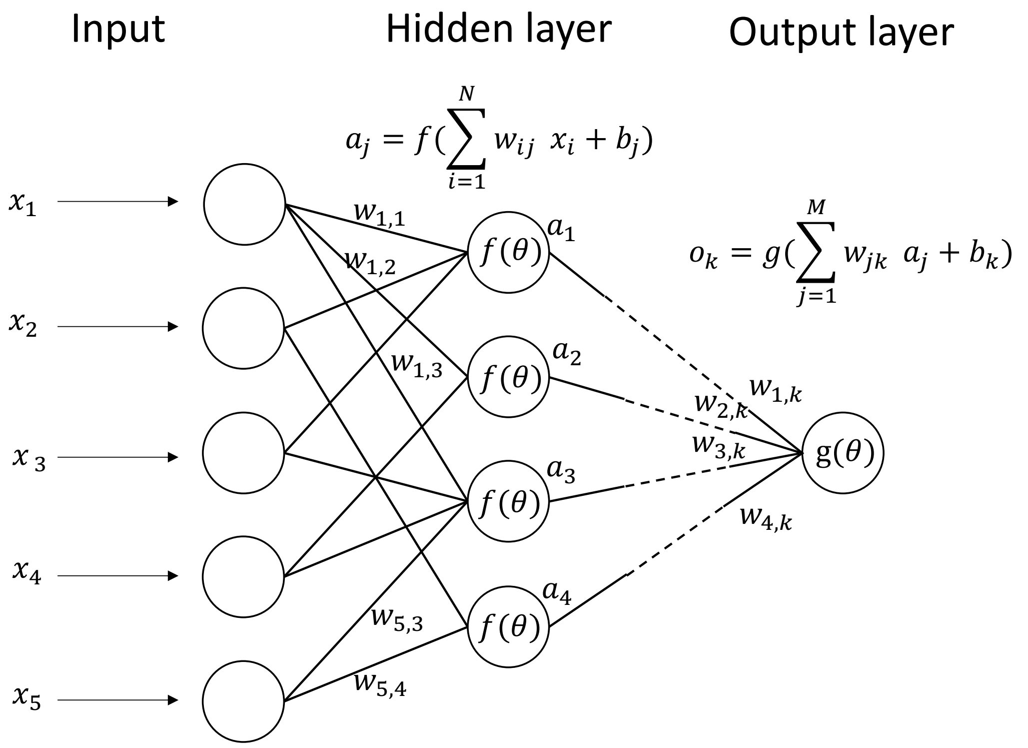

Figure 4.14 – Scheme of an artificial neural network used for machine learning algorithm.

4.4.4 Results

4.4.4.1 External condition

For both codes, the pump beam has a gaussian spectrum with $FHWM = 3,54$ nm and a centre wavelength $\lambda_0 = 397,5$ nm. The spectrum is divided into n frequency bands such that the total is 9 nm wide. On each part labelled k, is applied a factor $a_k e^{i\theta_k}$ with $k \in [1, n]$. It is possible to process the optimization by only shaping the amplitude, only the phase or both. Considering the projective simulation algorithm, the values taken by the shaping factor are discretized such as:

$$a_k \in \left\{0, \frac{1}{m-1}, ..., 1\right\} \tag{4.33}$$

$$\theta_k \in \left\{0, \frac{2\pi}{m-1}, ..., 2\pi\right\} \tag{4.34}$$

For each action from the agent, amplitude or phase values are increased from an increment and when the maximum is reached the initial situation is restored. During

one run, there is several trials whose goal is to beat a threshold of the cost function in order to be rewarded, otherwise the trial keeps going with a new action. After a certain number of unsuccessful steps, the trial is stopped in order to avoid to be stuck in an area far from the optimal point. The threshold undergoes also some updates along the compilation (every 5 times it is beaten) to refine the result.
For the artificial neural network code, unlike the projective simulation one, the values of the shaping factor are taken in a continuous range:

$$a_k \in (0, 1) \tag{4.35}$$

$$\theta_k = (0, 2\pi) \tag{4.36}$$

4.4.4.2 Calculation of the optimal pump spectrum shape

Optimization by shaping the amplitude or the phase has been investigated with different sharing of the blue spectrum. However, we here restrict ourself in this manuscript to the amplitude shaping where $n = 8$ and the optimized cost function is f_2. The rest of the results can be found in the manuscript of T. Michel [Michel 21].
In figure 4.15 is shown the spectrum shape of the pump after maximization of the cost function for the projective simulation and the artificial neural network algorithms. We notice a similarity in the structure of these plots although a slightly lack of symmetry on the graph (b) hinders a perfect matching.

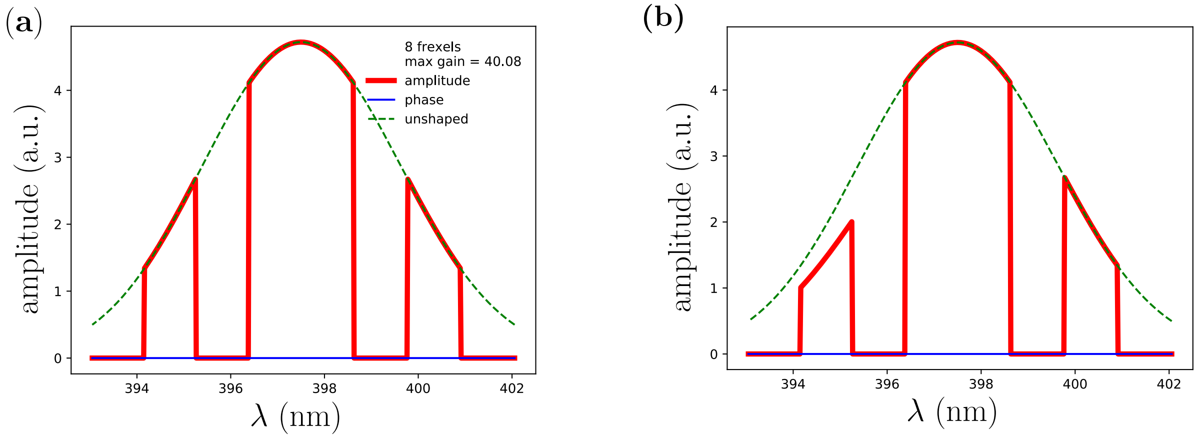

Figure 4.15 – Results of the $\bar{f}_2$ optimization using the PS (b) and the ANN (a) algorithms. Taken from [Michel 21]

.

To verify that the optimization is working well, we implement the calculated pump shape on the blue pulse shaper and we measure the covariance matrix using the MHD and the single pixel one. Both spectrums from the figure 4.15 are similar but we choose to try the measurement only for the artificial neural network one because it is symmetric. The results of the MHD covariance measurements for the optimized and the non-optimized are presented in figure 4.16. We see that, as expected, because the phase is flat for both spectrum, the $\langle Q, P\rangle$ terms are negligible comparing with the $\langle \Delta P^2\rangle$ and the $\langle \Delta Q^2\rangle$ terms. Both measurements have been made with a $P = 20mW$ pump power and for the gaussian pump, the beam follows the path of the pulse shaper. The measurement made with the single pixel homodyne detection are presented in figures 4.17 and 4.18. These measurement are also made with a pump power of $P = 20\text{mW}$. The higher number of pixels gives to this measurement a better resolution. We extract the eigenvalues of the diagonalization of these matrices. The results are shown in figure 4.19. We see that for the eigenvalues obtained from the optimized pump, the first eigenvalue is higher than the rest of the values. We determine the ratio $r = \Lambda_0/\Lambda_1$ for both cases. For the optimized pump $r = 3.0$ against $r = 1.19$ for the gaussian one, which show that the optimization is working well.

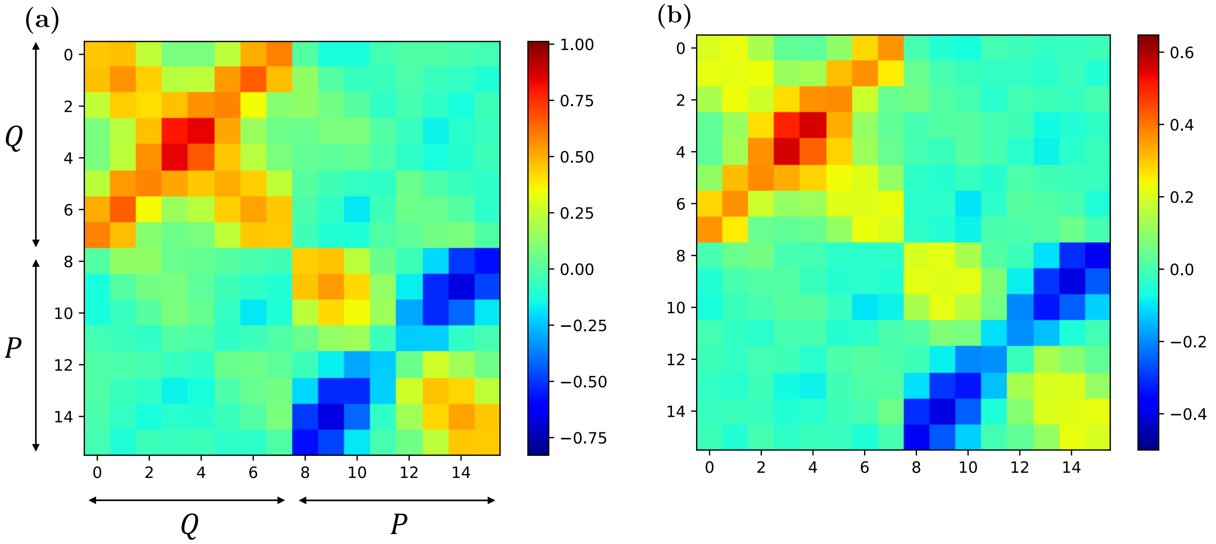

Figure 4.16 – Full covariance matrix reconstruction using (a) optimized pump and (b) gaussian pump. (taken from [Michel 21]

4.5 Summary

In this part, we have seen some covariance matrices measurement and how machine learning can improve the squeezing of the different modes. First is shown the way the covariance terms are extracted from the measured data. Then the PP and QQ

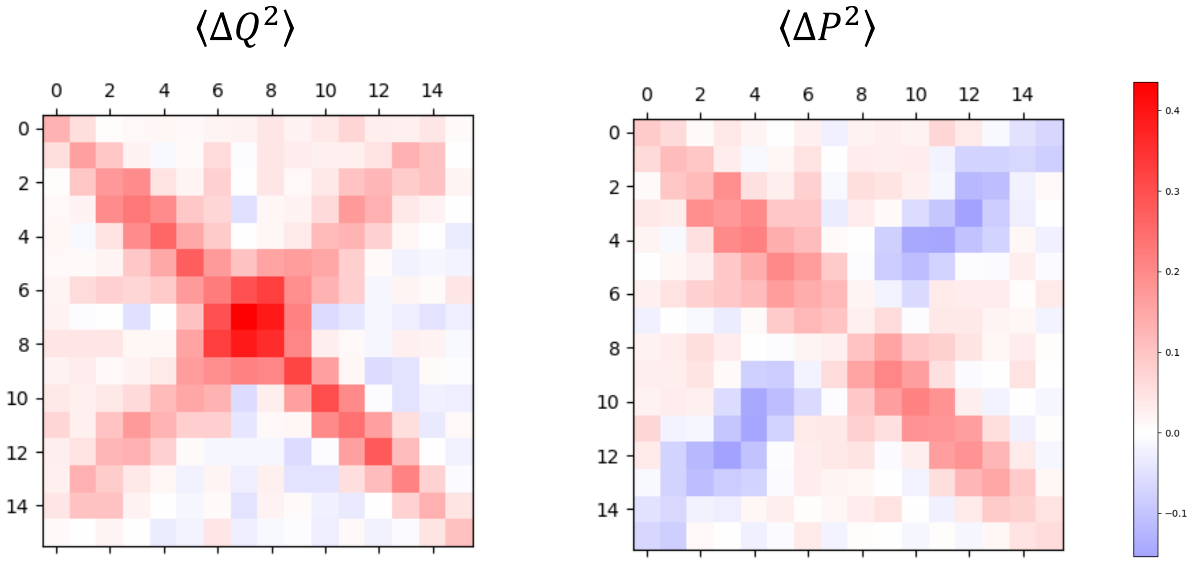

Figure 4.17 – $\langle P^2 \rangle$ and $\langle Q^2 \rangle$ matrices measured with gaussian pump spectrum.

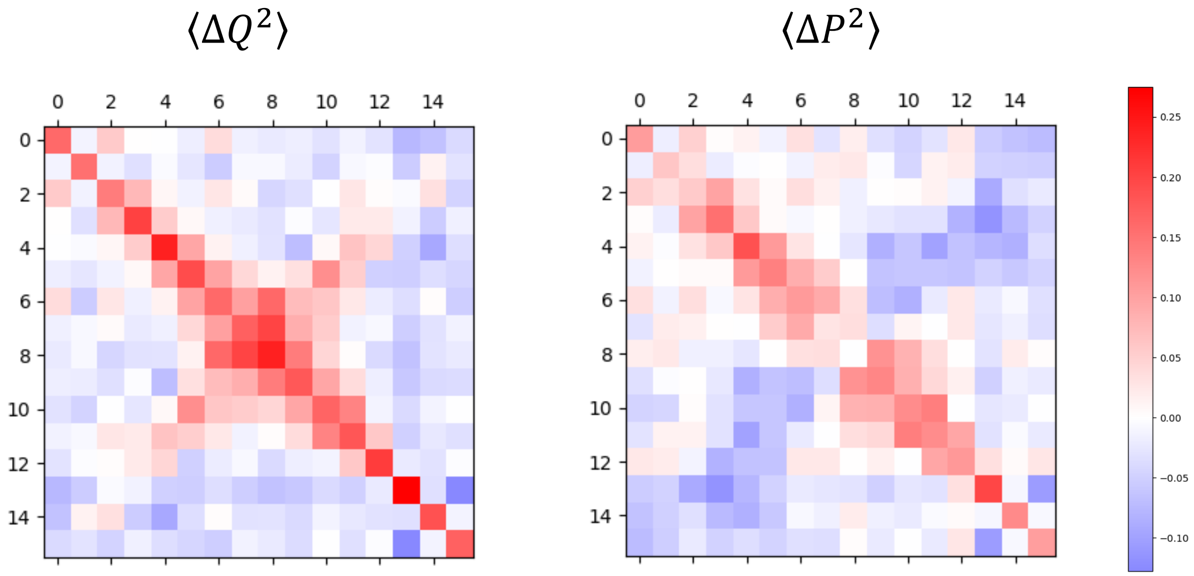

Figure 4.18 – $\langle P^2 \rangle$ and $\langle Q^2 \rangle$ matrices measured with the optimized pump spectrum.

covariance submatrices have been plotted. As we have seen, from the two submatrices we can, via a diagonalisation and a Gram Shmidt decomposition, find the supermodes of the SPOPO. The related squeezing for a 20mW pump power has also been plotted. In this chapter, we also have shown some result of optimization using machine learning algorithms. Two process have been considered here: the artificial neural network and

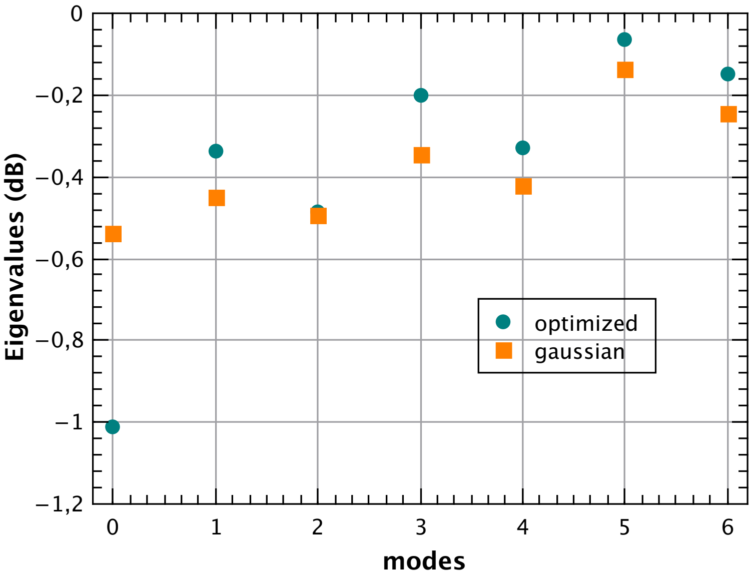

Figure 4.19 – Eigenvalues calculated from the diagonalization of the matrices presented in figures 4.18 and 4.17.

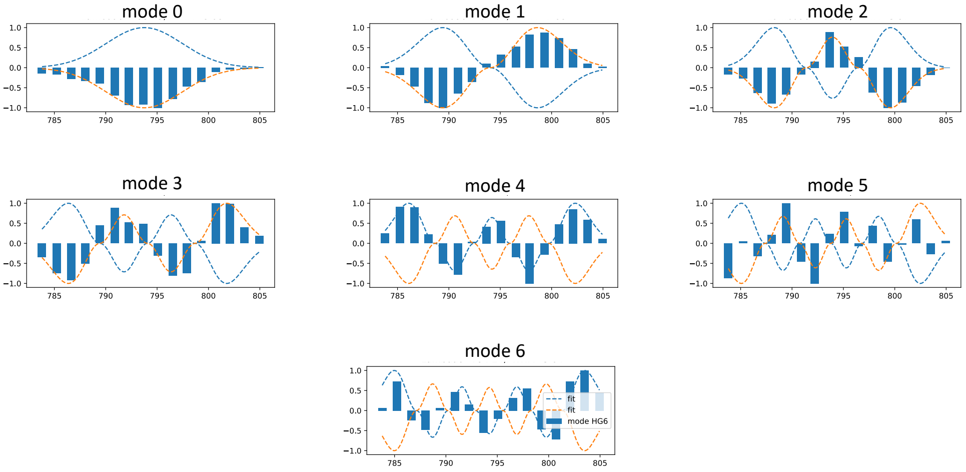

Figure 4.20 – Supermodes obtained from the diagonalization of the matrices represented in 4.17

the projective simulation algorithms. These two methods have been computed in order to optimize the squeezing in the first supermode. The diagonalization of the covariance submatrix with the shaped pump have shown a higher value of the squeezing on the first mode than with the original pump spectrum but at the expense of the other modes.

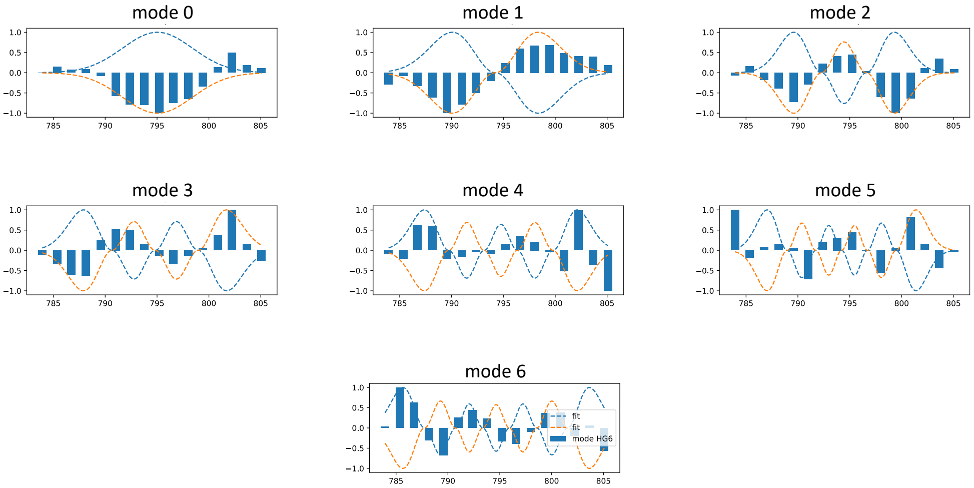

Figure 4.21 – Supermodes obtained from the diagonalization of the matrices represented in 4.18

	optimized		gaussian	
Modes	λ_0 (nm)	FHWM (nm)	λ_0 (nm)	FHWM (nm)
0	795.04	7.94	793.75	8.68
1	794.21	6.91	794.01	7.68
2	794.44	5.11	793.93	5.97
3	794.82	5.65	794.07	6.31
4	794.75	5.08	794.19	5.58
5	794.22	4.34	793.78	5.26
6	794.65	4.89	794.24	5.04

Table 4.2 – λ_0 and $FHWM$ values obtained from the fit of the eigenmodes with Hermite-Gaussian function when the pump is gaussian or optimized

Part III

Study of network properties via squeezing measurements

Chapter 5

Study of quantum network dynamic

Contents

In the two last chapters of this manuscript, we investigate how multimode quantum optics is a fruitful tool to study quantum networks and more specifically open quantum systems. This first chapter is dedicated to the characterization of the spectral density function of environmental coupling.
We first briefly introduce the quantum complex network and the quantum open system topics as well as the different ways to characterize energy exchanges, experimentally and

theoretically, inside the total system. Then we explain which protocol of measurement we use to finally show some measurements of spectral density functions for different types of network.

5.1 Open quantum system

5.1.1 Definitions and notations

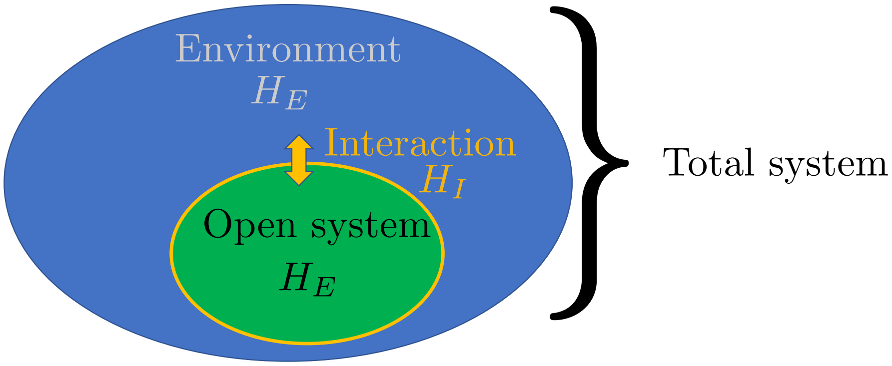

Figure 5.1 – Scheme of an open quantum system coupled to an environment.

Open quantum system is the study of a quantum system coupled with an external environment. It makes the quantum physics more realistic in the sense that isolated systems, quantum or not, do not exist in nature. We briefly introduce here the main concepts and the notations in this paragraph. However, this introduction does not intend to be complete. This field is well detailed in many articles and books especially in [Weiss 12, Gardiner 99]
One frequently used approach in open quantum system is the one where we consider a two components system composed by the subsystem of interest labelled S and the other one called the bath or environment labelled E. Both are defined in two Hilbert subspaces $\mathcal{H}_S$ and $\mathcal{H}_E$ and the hilbert space of the total system is $\mathcal{H} = \mathcal{H}_S \bigotimes \mathcal{H}_E$ (figure 5.1). The density operator of the total system is denoted as ρ and ρ_S, ρ_E denote the reduced operator for respectively the open quantum system and the environment. The system is recovered as ρ_S is given by the partial trace of ρ with respect of E:

$$\rho_S = \mathrm{Tr}_E(\rho) \tag{5.1}$$

The Hamiltonian of the total system is written:

$$H = H_S + H_E + H_I \tag{5.2}$$

where H_S and H_E are respectively the Hamiltonians related to the open system and to the bath. In this equation, H_I denotes the Hamiltonian of interaction. It is the Hamiltonian which allows energy exchanges between the two sub systems.

5.1.2 Dynamics of an open quantum system

The object of this chapter is restricted to the study of the dynamic of an open quantum systems coupled with an environment modeled by engineered networks and more specifically to the question: how do we characterize the energy exchanges in the global system?

The main motivation of this work lies in the new way we see the interactions between an open quantum system with its environment. Indeed, for several years now, the perception on the role of environments has changed: it had been shown that, if the interaction between both subsystems are suitably tailored, the presence of an environment will not be source of decoherence but, on the contrary, would act as a shield to protect the quantum resource [Barreiro 02, Verstraete 09, Biercuk 09].

There is two common used equations to study the dynamic of an open quantum system. The choice of one or the other equation depends on the picture in which we place ourself for our study: either the Schödinger or the Heisenberg pictures.

5.1.2.1 The GKSL equation

In the Schrödinger picture, the time master equation of the system is the following [Weiss 12]:

$$\frac{\mathrm{d}\rho_S(t)}{\mathrm{d}t} = -i\left[H_S, \rho_S(t)\right] + \sum_k \left(\left[C_k\rho_S(t), C_k^\dagger\right] + \left[C_k, \rho_S(t)C_k^\dagger\right]\right) \tag{5.3}$$

where we assume that $\hbar = 1$ and C_k are called jump operators. They describe the effect of the environment on the system in Born Markov approximation. The first term represents the reversible dynamic of the system S. This equation is called the Gorini-Kossakowski-Sudarshian-Linblad (GKSL) equation[Gorini 76, Linblad 76]. It is a well known equation and its demonstration can be found in a large number of books like [Weiss 12, Gardiner 99]. The evolution of $\rho_S(t)$ can be described by a map, $\Phi_{t,0}$, such as:

$$\rho_S(t) = \Phi_{t,0}\rho_S(0) = \mathrm{Tr}_E[U(t)\rho_S(0) \otimes \rho_E(0)U^\dagger(t)] \tag{5.4}$$

where $U(t)$ is the time evolution operator related to the Hamiltonian of the total system H. An interesting property of the map is its positivity, which will be developed and discussed in the next chapter about quantum non Markovianity.

5.1.2.2 The Langevin equation

In the Heisenberg picture, the most common way to resolve the dynamics of the system is to use the generalized Langevin equation ([Senitzky 60, Ford 65a, Ford 65b]). In this model, the considered system has a mass m_S and is moving in a potential $V(q_S)$. It is coupled to N harmonic oscillators of mass m_i and frequency ω_i. We assume the interaction are linear in the bath coordinate. A common way of writing H_I is [Nokkala 18a, Vasile 14]

$$H_I = \sum_{i=1}^{N} g_i q_s q_i \tag{5.5}$$

where g_i are the coupling strength between the system and the different oscillators of the environment. More details about this equation with a more general expression of H_I can be found in [Weiss 12]. The total Hamiltonian can be express as:

$$H = \frac{p_S^2}{2m_S} + V(q_S) + \sum_{i=1}^{N} \frac{p_i^2}{2m_i} + \frac{1}{2} m_i \omega_i^2 q_i^2 + \sum_{i=1}^{N} g_i q_s q_i \tag{5.6}$$

The evolution of the subsystem of interest can also be derived and depends on the expression of the potential V. From this derivation, we can define a friction term equivalent to the jump operator of equation (5.3). Because our work is based on environments of finite size composed by harmonic oscillators, this model is most appropriate for our use. Beside, due to its ability to produce cluster states with different structures, the SPOPO seems perfectly suitable to the study of engineered environments effects on an open quantum system.

5.2 Environment based on network

As we will see more in detail further in this chapter, environments are defined as networks composed by optical modes. A way to engineer them is to change their characteristics and their structure from ordered to random. We take inspiration of different models, which already exist in complex network theory. In this part we briefly introduce the complex network field and we present the different model that we use further in this chapter. More details on complex network field can be found in [Barabási 16, Strogatz 01]

5.2.1 Definition of complex network

Complex network is the study of properties and statistics of a system composed by a large number of entities interconnected with each others. Networks study, based on the graph theory in mathematics, finds its origin in the XVIII century and the demonstration of Euler that no one can walk across the seven bridges in Königsberg city without crossing one twice (figure 5.2) [Euler 41](in latin) [Alexanderson]. In literature, network and graph terms are both used to depict the same object. When a network is composed by nodes with links between them, we speak for graphs about vertices and edges respectively.

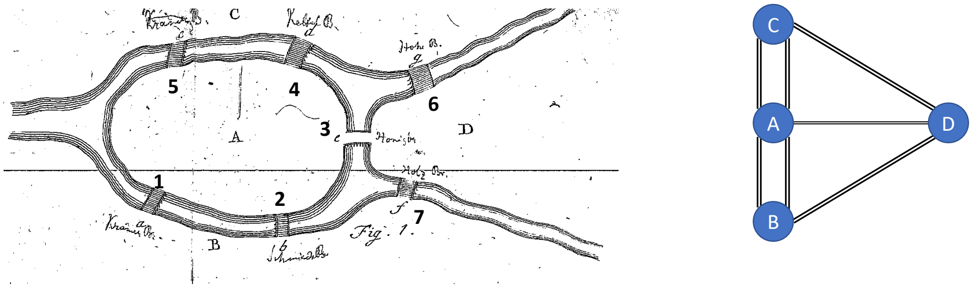

Figure 5.2 – *left*: Scheme of the Königsberg's bridge configuration by Euler [Euler 41]. *right*: Corresponding graph of the problem.

In a given network, N is the number of nodes and L the total number of links. The connection can be directed or undirected and balanced by different weights. For many years now, the field has experienced real growth in term of publications and applications. For certain examples, defining a graph is fairly straightforward. Let's take the example of N cities in a geographic area linked by roads, we can easily imagine that this ensemble forms a graph. We can find also this mathematical object in many other domains like health [Barabási 99], World Wide Web [Albert 99], genetics [AL. Barabási 04] or even cinema with the Kevin Bacon game (see https://oracleofbacon.org/) (figure 5.3).
In the following subsections are presented structures of network, which are currently used to describe complex systems.

5.2.2 Example of networks considered in this work

5.2.2.1 Random network

For large systems, the number of nodes explodes, that's why we speak about complex networks. Futhermore, the structures often lack of regularity. Thus, studying random graphs seems to be, at first glance, a way to characterize properties of networks we can find in real life.
Rál Erdős and Alfred Rényi were not the first working on random networks but they produced high impact discoveries for the field by merging probability and combinatorial with graph theory [Erdös 59, Erdös 61a, Erdös 61b].
There are two ways to define random networks:

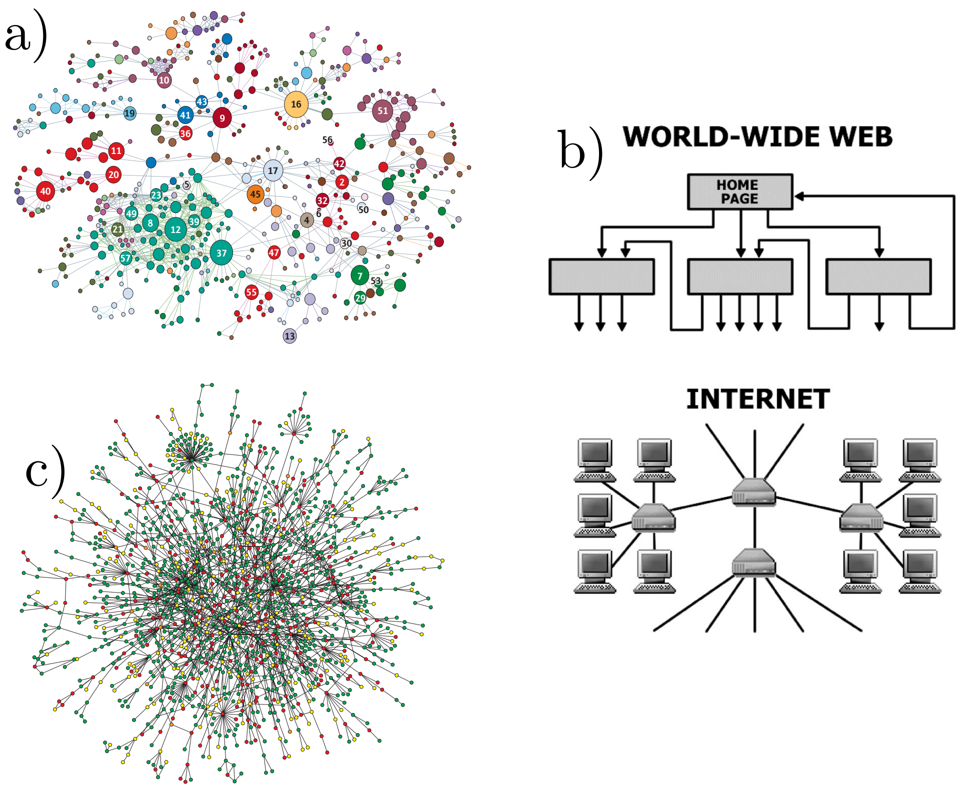

Figure 5.3 – Example of complex network structures; a) Network of human diseases, each number is a disease and the nodes connections are made by the similarity of the genotype (taken from [Barabási 99]). b) Structures of the World Wide Web showing the way the web pages are linked and internet networks with the connection between computers and routers (taken from [Albert 02]). c) Map of proteins interactions in *Saccharomyces cerevisiae*: each node is a protein and they are connected with each other through their physical and chemical interactions (taken from [AL. Barabási 04]).

- $G(N, L)$ is a graph composed by N nodes with L links placed randomly.
- $G(N, p)$ is a graph composed by N nodes connected with each other with the probability p.

In a graph, k_i is denoted as the degree of connection of the node i. It is the number of connections of the node, we keep this definition for the next paragraphs . For a given network all the nodes do not have necessary the same degree, we define thus a degree distribution, p_k. The works of R. Erdős and A. Rényi have shown that p_k follows Poisson distribution. However, observations showed that it is not the case of real networks. Hence, the randomness of networks encountered in nature is not as random as we think. This diagnosis prompted the community to define new graph families while retaining a certain degree of randomness.

5.2.2.2 Barabasi Albert networks

This model of network is named from of Réka Albert and Albert László Barabasi, who were the first to describe it in their publication of 1999 [Barabási 99]. It is a type of graph that we can find in real life like in internet for example[Albert 99]. It is build from the preferred attachment rule in network growth. In other words, if we consider a network under construction, the higher the number of connections of an individual node, the higher the probability to be linked to a new node. This model exhibits the appearance of hubs, which is a property we can find in many networks based on real data.

Hence, Barabasi Albert's networks are builded step by step and at each step a new node is created and is linked to m other nodes of the pre-existing network. At a given time, the probability for the new node to be connected to the node i depends on the degree k_i, defined above. The probability is expressed as:

$$P(i) = \frac{k_i}{\sum_l k_l} \tag{5.7}$$

We have $k_i > m$. Although the probability keeps a part of randomness in the network fashion, the way P is defined promotes the emergence of hubs. In figure 5.4 is represented different networks build through Barabasi Albert process for different m parameters. For $m = 1$, the network adopts a tree structure. Besides, we observe that the larger m, the more random the network structure.

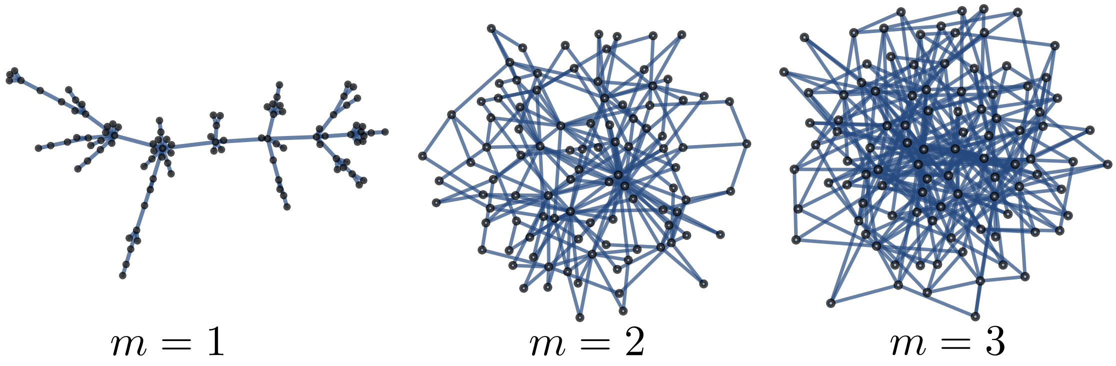

Figure 5.4 – Examples networks based on Barabasi Albert process with different values of m and with $n = 100$.

5.2.2.3 Watts Strogatz

The Watts Strogatz (WS) model of networks is also neither completely regular nor random. They have been defined by Duncan J. Watts and Steven H. Stogatz in 1998 [Watts 98]. At this time they were not called by the name of their finders but as *small world* networks because of one of their properties also observed in networks within society: there often exists 6 or less social links between two persons randomly chosen in the world. Although the assertion is difficult to prove rigorously, scientific work has been done to identify this surprising property of our society's networks[Milgram 67, Travers 69]. Moreover, in the digital age, the maximum number of connections between two people has even decreased by studying the connections within the Facebook network[Ugander 11].

To build a WS graph composed by N vertices and L edges, the starting point is a ring lattice network composed by N nodes with the same degree k. Then each node is rewired with the probability β and we get the desired graph. The rewiring is random. Indeed, let's take the example of the connection (i, j) between nodes i and j, it is cut to be replaced by the new one (i, l) with the probability β when l is randomly chosen among the ensemble $[0, N]/\{i, j\}$. Example of WS graphs are shown in the figure 5.5 below for different values of rewiring probability. We observe that when β tend to be 0, the graph is almost regular and when β gets closer to 1, the structure looks more random.

5.2.3 Building a quantum network from Multimode squeezed states

We have seen previously that the network science can be used in large and broad number of domains. It is also possible to build graph structures based on physical systems where the nodes are composed by harmonic oscillators and the links are the coupling strengths denoted as g_{ij} between the different resonators labelled i and j as pictured in figure 5.6. This model can be used to describe many physical systems like springs, atoms but also optical modes networks as it is the case in this work.
We assume the mass is equal to 1 and the frequency of the nodes are denoted as ω_i. The Hamiltonian of the total system is expressed as:

$$\boldsymbol{H} = \boldsymbol{p}^T \boldsymbol{\Delta}_{\omega} \boldsymbol{p} + \boldsymbol{q}^T \sqrt{\boldsymbol{\Delta}_{\omega}^{-1}} \boldsymbol{A} \sqrt{\boldsymbol{\Delta}_{\omega}^{-1}} \boldsymbol{q} \tag{5.8}$$

where $\boldsymbol{\Delta}_\omega = diag(\omega_1, ..., \omega_n)$, $\boldsymbol{p}$ and $\boldsymbol{q}$ are the vectors composed by the quadrature operators of the nodes and $\boldsymbol{A}$ is the adjacency matrix defined by:

$$A_{i,j} = \frac{\delta_{ij}\omega_i^2}{2} - \frac{(1 - \delta ij)g_{ij}}{2} \tag{5.9}$$

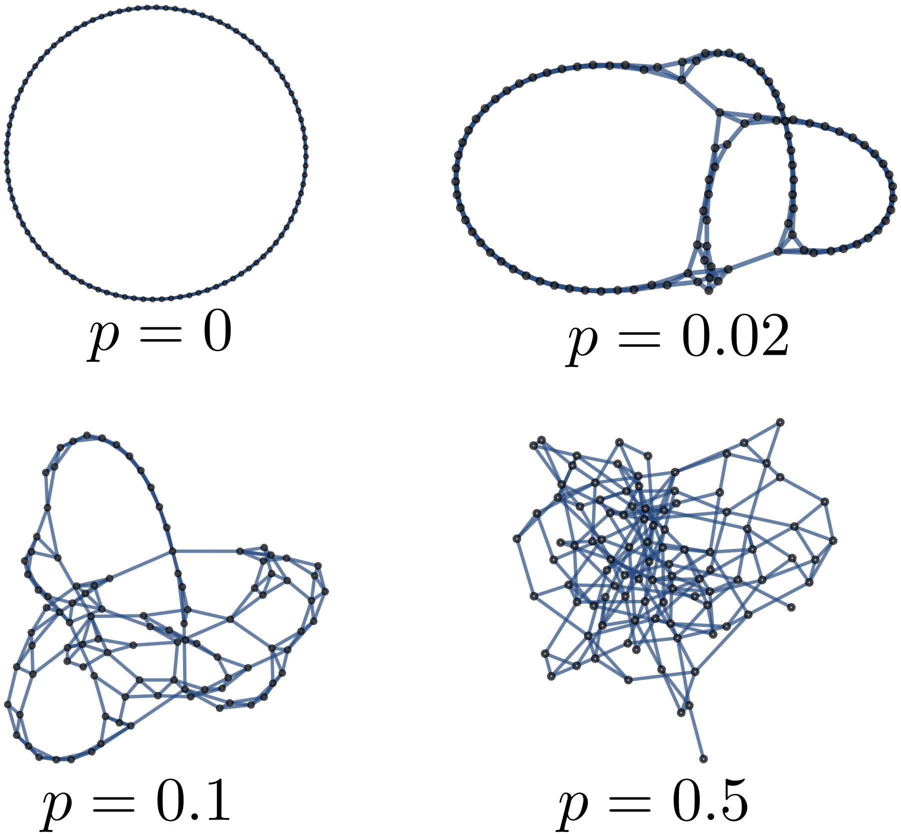

$p = 0$ $p = 0.02$

$p = 0.1$ $p = 0.5$

Figure 5.5 – Example of Watts Stogatz graphs with $n = 100$ nodes for different rewiring probabilities p

Regarding the parameters $g_{i,j}$, although they are called "strength", they are homogeneous to the square of a frequency. This remarks tells us when g_{ij} is low, it means the energy takes a long time to flow between two nodes of the network and, on the other hand, if it is high, this time will be shorter. $\boldsymbol{A}$ is a symmetric and real matrix, which implies we can diagonalize it:

$$\boldsymbol{A} = \boldsymbol{K}^T \boldsymbol{\Delta}_\Omega \boldsymbol{K} \tag{5.10}$$

where $\boldsymbol{K}$ is an orthogonal matrix and $\boldsymbol{\Delta}_\Omega = diag(\Omega_1, ..., \Omega_n)$ with Ω_i the frequencies of the total system resulting from the diagonalization. In this new basis, the anti diagonal terms of the adjacency matrix reflecting the coupling between the nodes are zero. In other words, applying the basis change $\boldsymbol{p}' = \boldsymbol{K}\boldsymbol{p}$, $\boldsymbol{q}' = \boldsymbol{K}\boldsymbol{q}$, we obtain an ensemble of oscillators defined by the frequencies $\Omega_1, ..., \Omega_n$ independent from each other. We can go further by defining the quadrature operators with the same dimensionality:

$$\boldsymbol{\mathcal{P}} = \sqrt{\boldsymbol{\Delta}_\Omega}^{-1} \boldsymbol{K}^T \sqrt{\boldsymbol{\Delta}_\omega} \boldsymbol{p} \tag{5.11}$$

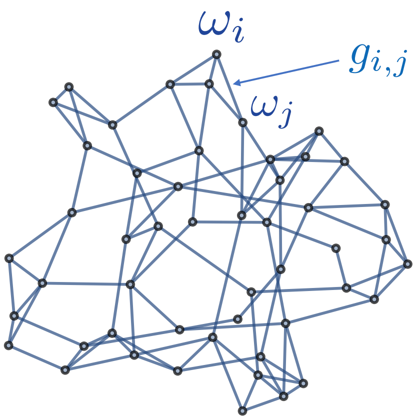

Figure 5.6 – Exemple of network composed by harmonic oscillators.

$$\boldsymbol{\mathcal{Q}} = \sqrt{\boldsymbol{\Delta}_\Omega}\boldsymbol{K}^T\sqrt{\boldsymbol{\Delta}_\omega^{-1}}\boldsymbol{q} \tag{5.12}$$

In this basis, the Hamiltonian becomes:

$$\boldsymbol{H} = \frac{1}{2}\left(\boldsymbol{\mathcal{P}}^T\boldsymbol{\Delta}_\Omega\boldsymbol{\mathcal{P}} + \boldsymbol{\mathcal{Q}}^T\boldsymbol{\Delta}_\Omega\boldsymbol{\mathcal{Q}}\right) \tag{5.13}$$

5.3 The spectral density of environmental coupling

5.3.1 Dynamics of a quantum complex network

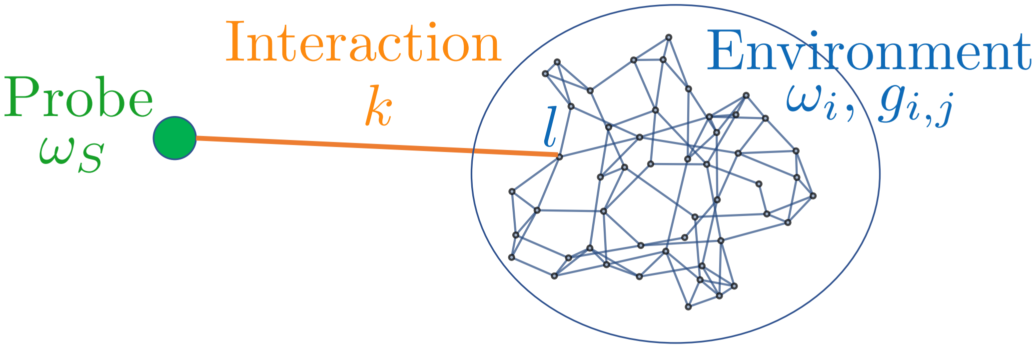

Figure 5.7 – Open quantum system with a network of bosonic harmonic oscillators as environment.

Let's consider now the total system represented in figure 5.7 where a open quantum system called the probe and labelled S is coupled to an environment E. According to the generalized Langevin equation, it is composed by a network of N harmonic oscillators such as:

$$\boldsymbol{H}_E = \boldsymbol{p}^T \boldsymbol{\Delta}_{\boldsymbol{\omega}} \boldsymbol{p} + \boldsymbol{q}^T \sqrt{\boldsymbol{\Delta}_{\boldsymbol{\omega}}^{-1}} \boldsymbol{A}_E \sqrt{\boldsymbol{\Delta}_{\boldsymbol{\omega}}^{-1}} \boldsymbol{q} \tag{5.14}$$

where $\boldsymbol{A}_E$ is the corresponding adjacency matrix of the environment. For its part, the Hamiltonian of the probe is:

$$H_S = \frac{p^2}{2} + \frac{\omega_s^2 q^2}{2} \tag{5.15}$$

where ω_S is the frequency of the probe. We assume the connection between the probe and the environment is established only through one link to the node l. Hence, the Hamiltonian of interaction between both objects can be written as:

$$H_I = \sum_i^N g_{s,i} q_s q_i = k q_s q_l \tag{5.16}$$

where k is the coupling strength between the probe and the node l, $k = g_{s,l}$. In the uncorrelated picture, we have:

$$q_l = \sum_{i=0}^N \boldsymbol{K}_{(l,i)}^T Q_i = \sum_{i=0}^N \boldsymbol{K}_{(i,l)} Q_i \tag{5.17}$$

We denote $\boldsymbol{h}$ the vector corresponding to the column l of $\boldsymbol{K}$. We have thus

$$H_I = k \sum_i h_i q_s Q_i \tag{5.18}$$

As mentioned above 5.1.2.2, the reduced dynamics is described by the generalized Langevin equation. From this derivation (details in [Weiss 12, Mascherpa 20]), we define a time dependent damping kernel function γ, which can be expressed as:

$$\gamma(t) = \sum_{j=1}^N \frac{k^2 h_j^2}{\Omega_j^2} \cos(\Omega_j t) \tag{5.19}$$

The damping kernel is a function which characterizes the energy exchange between both subsystems in time domain. In the frequency domain, we look another function, the spectral density, defined as:

$$J(\omega) = \frac{\pi}{2} \sum_i \frac{k^2 h_i^2}{\Omega_i} \delta(\omega - \Omega_i) \tag{5.20}$$

In the limit where Ω_i tends to be a continuum,

$$J(\omega) = \omega \int_0^{t_{max}} \gamma(t)\cos(\omega t)\mathrm{d}t \tag{5.21}$$

where t_{max} is the interaction time between the probe and the environment. The spectral density can be interpreted as follows: when this function is non zero it means there is energy exchanges between the open system and the environment. The function $J(\omega)$ tells us the frequency ranges where the energy exchanges are promoted. However, the function $J(\omega)$ is not the Fourier transform of the damping kernel, despite similar information. This function have been built because, as explained in next paragraph, it is more accessible from an experimental point of view.

5.3.2 Probing the spectral density

We can get access to the spectral density measuring the level of energy in the probe. This technique called probing enable also to find the structure of a unknown environment [Nokkala 16]. Nonetheless, we focus here and in the rest of this chapter only on the recovery of the function J. By assuming the coupling strength between the probe and the environment is small in comparison with $g_{i,j}$, we can express at a given time t the mean excitation number of the probe, proportional to the energy level, as [Nokkala 16]:

$$\langle n(t)\rangle = e^{-\Gamma t}\langle n(0)\rangle + N(\omega_s)(1-e^{-\Gamma t}) \tag{5.22}$$

with $\Gamma = \frac{J(\omega_s)}{\omega_s}$ and N is the thermal average excitation number in the environment with $N(\omega_s) = (e^{\omega_s/T}-1)^{-1}$ where T is the temperature of the subsystem in unit of the Boltzmann constant. From this formula we deduce the expression of J:

$$J(\omega_s) = \frac{\omega_s}{t_{max}}\ln\left(\frac{N(\omega_s)-\langle n(0)\rangle}{N(\omega_s)-\langle n(t)\rangle}\right) \tag{5.23}$$

The values of t_{max} is fixed as well as the value $N(\omega_S)$ by the initial conditions (see 5.4.3). Hence, we can deduce the value of $J(\omega_s)$ for a given probe frequency just by knowing the average excitation number in the probe at $t=0$ and $t=t_{max}$.

5.4 Simulation of an open quantum system with a multimode squeezed state

5.4.1 Bloch Messiah decomposition of the global network

Let's consider the total system introduced above (figure 5.7) where the oscillators frequencies are $(\omega_s, \omega_1, ..., \omega_N)$ and the quadrature vector $\boldsymbol{x} = (q_S, \boldsymbol{q}^T, p_S, \boldsymbol{p}^T)^T$. This vector can also be written in uncoupled picture $\boldsymbol{\mathcal{X}} = (\mathcal{Q}_S, \boldsymbol{\mathcal{Q}}^T, \mathcal{P}_S, \boldsymbol{\mathcal{P}}^T)^T$. The frequencies of the uncoupled oscillators are $(\Omega_S, \Omega_1, ..., \Omega_N)$. We use the same notations than in section 5.2.3 in spite of the addition of the probe in the system. In both picture, the evolution of the quadrature vectors can be computed such as:

$$\boldsymbol{x}(t) = \begin{pmatrix} \boldsymbol{T}_1 \boldsymbol{D}^{\Omega}_{cos}(t) \boldsymbol{T}_1^{-1} & \boldsymbol{T}_1 \boldsymbol{D}^{\Omega}_{sin}(t) \boldsymbol{T}_2^{-2} \\ -\boldsymbol{T}_2 \boldsymbol{D}^{\Omega}_{sin}(t) \boldsymbol{T}_1^{-1} & \boldsymbol{T}_2 \boldsymbol{D}^{\Omega}_{cos}(t) \boldsymbol{T}_2^{-1} \end{pmatrix} \boldsymbol{x}(t=0) = \boldsymbol{S}(t)\boldsymbol{x}(0) \tag{5.24}$$

where $\boldsymbol{D}^{\Omega}_{cos}(t)$ and $\boldsymbol{D}^{\Omega}_{sin}(t)$ are diagonal matrices such as $\boldsymbol{D}^{\Omega}_{cos}(t) = diag(\cos(\Omega_s t), ..., \cos(\Omega_N t))$ and $\boldsymbol{D}^{\Omega}_{sin}(t) = diag(\sin(\Omega_s t), ..., \sin(\Omega_N t))$. We also have $\boldsymbol{T}_1 = \sqrt{\boldsymbol{\Delta}_{\boldsymbol{\omega}}} \boldsymbol{K} \sqrt{\boldsymbol{\Delta}_{\Omega}^{-1}}$ and $\boldsymbol{T}_2 = \sqrt{\boldsymbol{\Delta}_{\boldsymbol{\omega}}^{-1}} \boldsymbol{K} \sqrt{\boldsymbol{\Delta}_{\Omega}}$. The matrix $\boldsymbol{S}$ is symplectic. It means that for any probe frequency ω_s and at any time t, we can write a transformation of Bloch Messiah:

$$\boldsymbol{x}(t) = \boldsymbol{R}_1(t) \boldsymbol{\Delta}_{sq}(t) \boldsymbol{R}_2(t) \boldsymbol{x}(0) \tag{5.25}$$

where $\boldsymbol{R}_1$ and $\boldsymbol{R}_2$ are orthogonal and $\boldsymbol{\Delta}_{sq}$ diagonal.

We assume $\boldsymbol{x}(0)$ is a superposition of vacuum states, we can initialize the system adding energy in some modes, we have to multiply $\boldsymbol{S}$ by a diagonal matrix $\boldsymbol{\Delta}'_{sq}$. We denote the effective evolution matrix $\boldsymbol{S}_{eff}$, such as $\boldsymbol{S}_{eff} = \boldsymbol{S}\boldsymbol{\Delta}'_{sq}$. $\boldsymbol{S}_{eff}$ is also symplectic and we have $\boldsymbol{S}_{eff} = \boldsymbol{R}''_1 \boldsymbol{\Delta}''_{sq} \boldsymbol{R}''_2$. Because $\boldsymbol{x}(0)$ is a collection of vacuum states, $\boldsymbol{R}''_2$ is discarded and $\boldsymbol{S}_{eff} = \boldsymbol{R}''_1 \boldsymbol{\Delta}''_{sq}$. As we saw in chapter 4, the Bloch Messiah transformation is also used for the determination of the supermodes of the SPOPO cavity. We have:

$$\boldsymbol{x}(t) = \boldsymbol{R}_{SPOPO}(t) \boldsymbol{\Delta}_{SPOPO} \boldsymbol{x}(0) \tag{5.26}$$

Hence the experiment described in part II of this thesis appears as a correct platform for the simulation of the evolution of such networks presented above.
If the orthogonal basis is easily monitorable on the experiment using the pulse shaper, that is not the case for the squeezing. We are enable to choose what node is squeezed and what node is not by implementing some supermodes which are squeezed or not. However it is more difficult to have control on the squeezing level spectrum since we have only one degree of freedom in the experiment for this setting, the pump power. Nonetheless, as we will see further, in spite of these limitations, the mapping can work

We stress here that, although we want to simulate an ensemble of resonators with optical modes, the frequencies of the nodes are not optical frequencies. They are parameters of the network as described in sections 5.4.2 and 5.4.3 below. The different network parameters and their equivalent for the experimental implementation are gathered in the table 5.1 below. More details about the decomposition of the network evolution can be found in [Nokkala 18b].

Network component	Quantum network	experimental implementation
Node	Quantum harmonic oscillator	Optical mode
Link	Coupling strength	entanglement
t	Interaction time	parameter for S
Decoupled mode	Normal mode of the network	Supermode
Addressing a node	Local measurement	Pulse shaping and projective measurement

Table 5.1 – Mapping of experimental implementation for the quantum network for open quantum system.

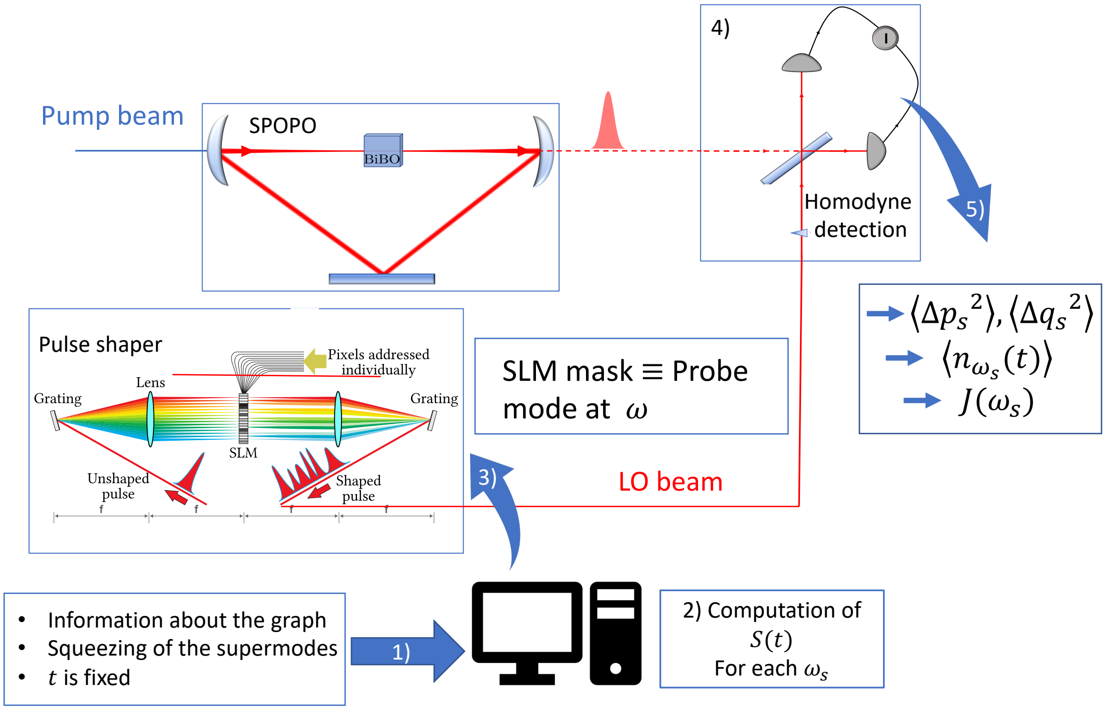

Figure 5.8 – Steps for the J recovery measurement.

5.4.2 Measurement protocole

A scheme to illustrate the measurement protocol is shown in 5.8. This protocol follows the steps described below:

- 1) The informations about the graph of the total system (structure, frequencies, coupling strengths...) and the interaction time are entered in a mathematica code along with informations about the squeezing and the supermodes of the SPOPO.

- 2) The code computes the evolution matrix $\boldsymbol{S}$ and the Bloch Messiah decomposition for a given probe frequency ω_S in order to extract the vector related to the probe mode given by $\boldsymbol{O}_1(t)$.

- 3) In the experiment, the LO mode is shaped as the evolved probe mode at t.
- 4) Measurement of the quadrature variance by varying the LO phase.
- 5) Extraction of the $\langle q_S^2(t)\rangle$ and $\langle p_S^2(t)\rangle$ values. From these, we deduce the average number of photons in the probe mode for the given frequency ω_S via the formula:

  $$\langle n_{\omega_s}(t)\rangle = \frac{1}{2}\left[\langle q_S^2(t)\rangle + \langle p_S^2(t)\rangle - 1\right] \tag{5.27}$$

  We can do the same for $t = 0$ and measure $\langle n_{\omega_s}(0)\rangle$ in order to deduce the value of $J(\omega_S)$.

We repeat the process for all the probe frequencies which allows us to recover the spectral density function.

5.4.3 Experimental conditions

For sake of simplicity, we set the frequencies of all environment node to be the same $\omega_i = \omega_0$. The probe frequency is not fixed because it is the variable of the function J. Regarding the rest of the parameters which define the environment, we have to adequately choose as explained below:

- In order to have some energy exchange in the environment, the coupling strength $g_{i,j}$ has to be of the same order of magnitude at ω_0^2.
- Another coupling strength which is fixed is k. As well as the parameter $g_{i,j}$, the value has to be entered in the mathematica code. The role of the probe is to interact weakly with the environment to not disrupt its dynamics too much. However if k is too small, the global system will look like two independent subsystems, which is something we want to avoid. For the total system we show in the rest of this manuscript, k is chosen such as: $0.1g_{ij} < k < 0.5g_{ij}$
- The interaction time is determined by the form of the damping kernel. Indeed, this parameter is chosen in an range where $\gamma(t)$ is flat and low in comparison with $\gamma(t = 0)$. It means that in an interval of time around t_{max}, the spectral density is stable and independent of time.
- In the expression (5.23) of the spectral density, we observe the presence of the parameter N. For reasons of simplicity, we prefer to set it to 0. Setting this parameter means that, at the initial time, all the energy is concentrated in the probe

and we are looking then only at the transfer from the probe to the environment during the time evolution of the total system. This initial conditions are consistent with the previous equations (5.24), (5.25), (5.26). In order to have $N = 0$, we ensure the supermodes of the SPOPO which are implemented as normal modes of the environment are not squeezed. In figure 5.9, we see the squeezing measurements for different supermodes for a pump power of $P_p = 6,5mW$. For the first one, we can observe oscillations of the noise level, this is the normal mode related to the probe. Then, we can distinguish some weak fluctuations on supermode 4 but not anymore from supermode 5. This indicates us the supermodes we can use and implement into the environment network. Beside, because we know the squeezing parameter is decreasing with respect of the mode number, we interpolate the squeezing value to 0 for the normal modes above 5.

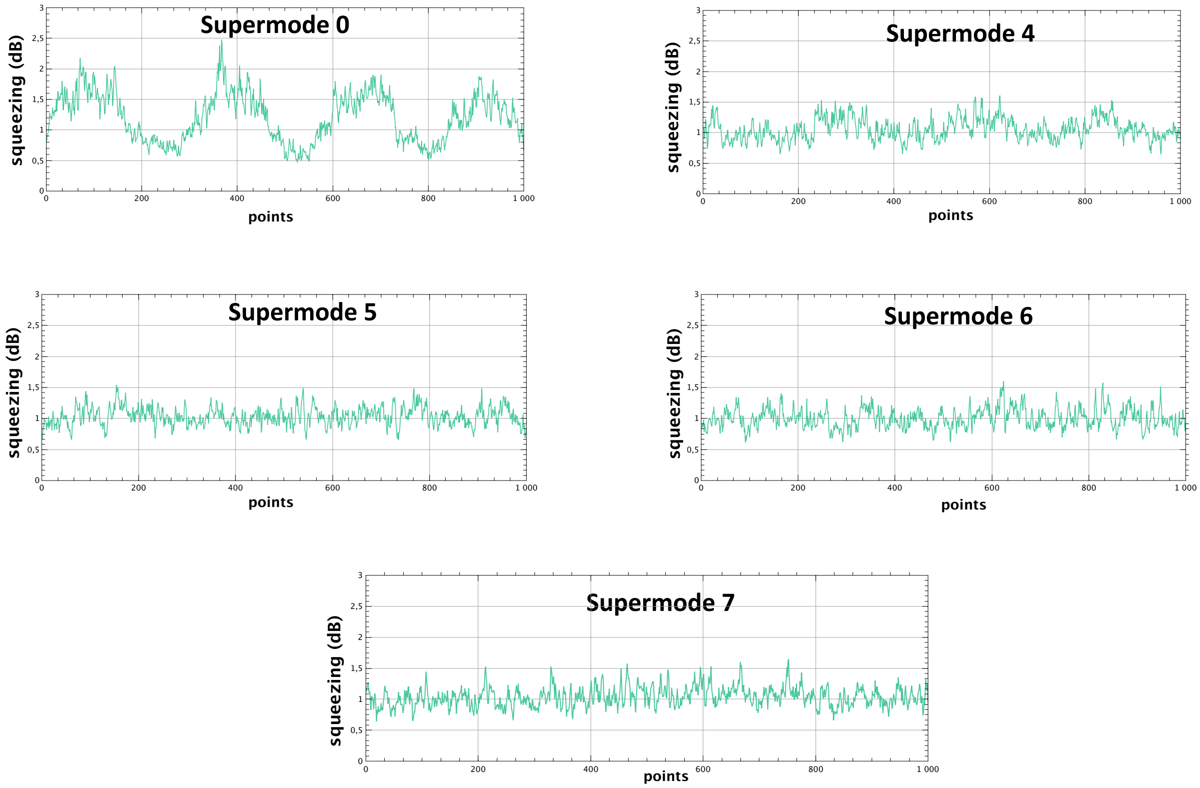

Figure 5.9 – Squeezing curves for different supermodes for a pump power of $P_p = 6,5mW$.

During the acquisition, the LO is passing through the PCF fiber in order to optimize the width of the beam spectrum and shape modes as broad as possible. The power of the input beam injected to the fiber is around 100mW.

During the acquisition, we do not measure only squeezing, we also save the optical spectrum related to the computed probe modes in order to compare them to the theoretical ones. We want to compare the theory and the experimental curves to ensure we measure squeezing on the correct mode. To verify that the matching is correct we look at the relative error rate function, Π defined as:

$$\Pi(\text{probe}) = \frac{\int d\lambda (\tilde{f}_{th}(\lambda) - \tilde{f}_{exp}(\lambda))^2}{\int d\lambda \tilde{f}_{th}(\lambda)^2} \tag{5.28}$$

where $\tilde{f}$ are the spectrum functions. Unfortunately, we can only measure and compare the intensity of the modes without any information about the phase.
Another parameter which is checked on the measurement is the clearance defined in chapter 2. Indeed, we must ensure that the electronic transmission of the detector is roughly the same for all LO modes. When we measure a non zero values for J, it means that the probe dissipates its energy into the environment during the interaction duration. We have to check, thus, a non zero value of $J(\omega_s)$ is not due to measurement losses.

5.5 Spectral density measurements

5.5.1 Linear networks

In this section, we show results of spectral density recoveries. We restrict ourself to the case where the environment is a linear network composed by $n = 16$ nodes of frequency $\omega_0 = 0.25$ (figure 5.10). Although the structure is fixed, we can play with the coupling strengths values. We study 3 networks with periodic values of g_{ij}:

Figure 5.10 – Scheme of the linear network plugged to the probe.

- network 1: $g_{1,2} = 0.1 - g_{2,3} = 0.05 - g_{3,4} = 0.1 - ...$
- network 2: $g_{1,2} = 0.1 - g_{2,3} = 0.1 - g_{3,4} = 0.05 - g_{4,5} = 0.1 - ...$
- network 3: $g_{1,2} = 0.1 - g_{2,3} = 0.05 - g_{3,4} = 0.025 - g_{4,5} = 0.1 - ...$

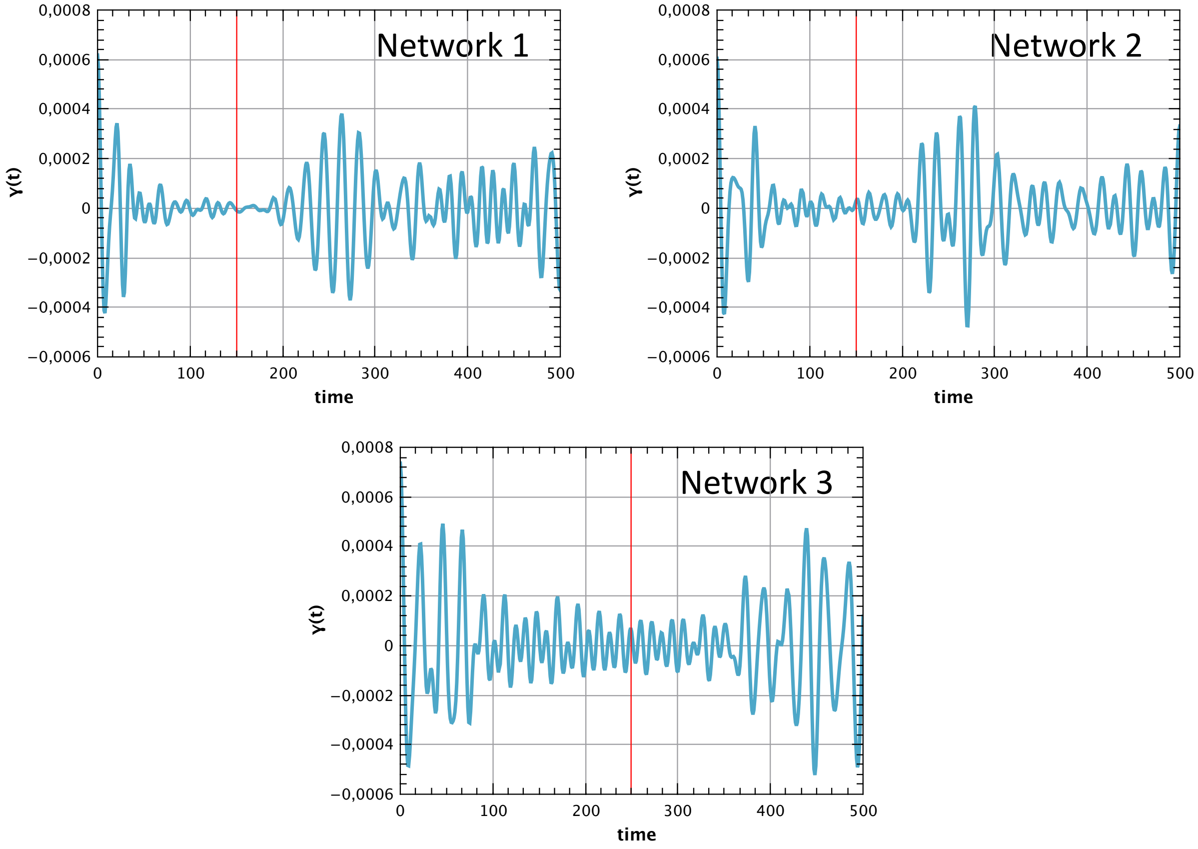

Figure 5.11 – Analytical simulation of the $\gamma(t)$ for the three linear networks. The vertical red line represents the values of t_{max}.

The values of k is the same for the three cases: $k = 0.01$. For the pump power, we choose the same than the one used in the case of the figure 5.9: $P_p = 6.5mW$. In figure 5.11 is represented the damping kernel of the networks calculated from the equation (5.19). We see, that in the three case scenario, the function $\gamma(t)$ has the same structure: first a decay of the oscillations and then γ becomes flat for a relatively long time. We set the interaction time, $t_{max,i}$, for the calculation of J in this interval. We have for the three networks:

- $t_{max,1} = 150$
- $t_{max,2} = 150$
- $t_{max,3} = 250$

For the three networks, we study the spectral density between $\omega_s = 0.2$ and $\omega_s = 0.7$ with a resolution of $\delta\omega_s = 0.0042$ (120 points). The results of the measurements are shown in the figures 5.12,5.13,5.14. The theoretical lines have been obtained using formula (5.21). On the experimental curves, the dots are averages on 20 acquisitions and the error bars are determined from the standard deviations. Regarding the experimental conditions, the visibility of the interference fringes on the homodyne detector is $V_h = 95\%$.

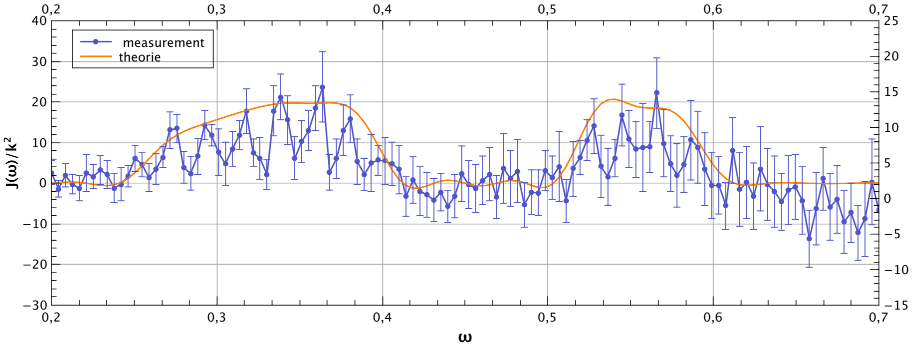

Figure 5.12 – Results of the J measurement for the network 1.

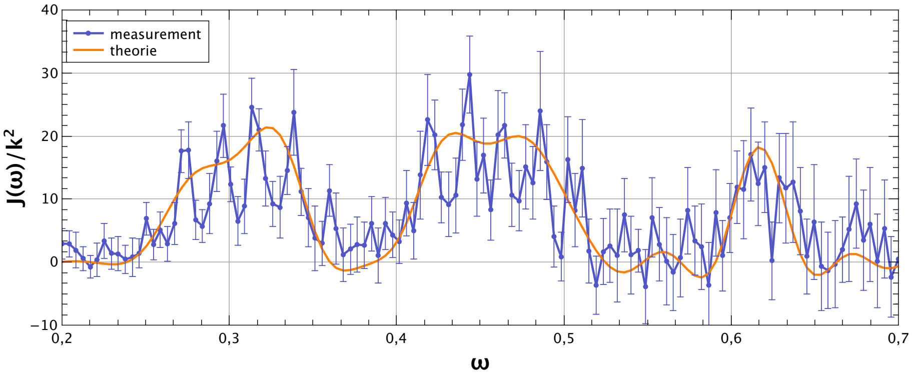

Figure 5.13 – Results of the J measurement for the network 2.

We observe on these plots that the matching between experimental and theoretical curves are not optimal. It is possible to distinguish on the experimental curves the frequency range where there are energy exchanges between the probe and the environment. Although the experimental curves follow the theoretical ones, we also observe oscillations inside the global peaks which are not present in the theory. Unfortunately, we can not explain so far the origin of this deviation from the theory

In figure 5.16, we show the ratio Π versus the probe frequency for the different environments. We see that the ratio is below 5% for all the modes which indicates no failure

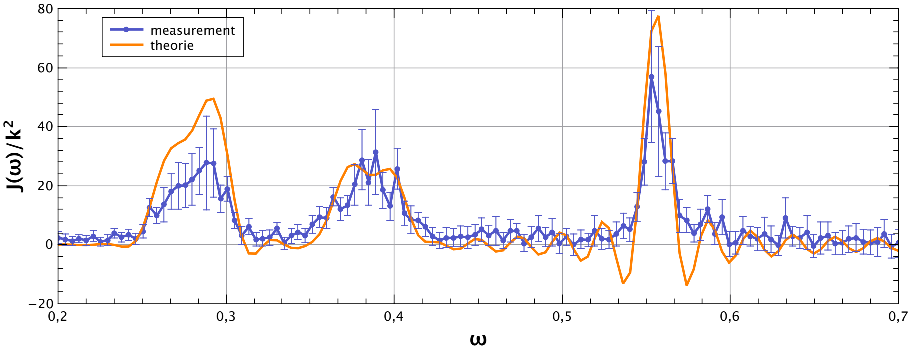

Figure 5.14 – Results of the J measurement for the network 3.

of the pulse shaper.
In figure 5.15, we show the clearance as a function of the probe frequency mode. We observe that for the three networks, the clearance is close to 8dB for most of the probe modes. Nonetheless, we also see for networks 1 and 2 oscillations in phase with the ones present on the spectral density plots. For the network 3, we see drops of the clearance on frequency ranges where the density spectral exhibits peaks. These observations show that the fluctuation of the detector transmission could affect the density spectral measurement. It is not. Indeed, in appendix D is plotted the J functions corrected from the electronic losses, which show a good superposition with the non corrected presented here. Hence these two last figures tell us about the accuracy of the measurements. When we measure a drop of the squeezing during the acquisition and consequently a drop of the average photon number, which results in the appearance of a peak in the J function, this is neither due to a bad spectral shaping nor to a drop of the detection transmission. The understanding of the fluctuations on the experimental determination of J will requires further investigation.

5.5.2 Networks from complex network models

After the first try on regular and linear networks as environment, the next step is to measure J for random structures. Here, we show the measurements for two networks based on Watts Strogatz and Barabasi Albert models and composed each by $n = 50$ nodes. The structure of both environments have been determined randomly with a mathematica code and they are pictured in figure 5.17. The parameters chosen to build the two networks are listed in the table 5.2 below.

Here, the coupling strengths inside the environment are the same for all the vertices contrary to the linear networks. The calculated damping kernels are represented in figure 5.18. We observe, in both cases a decline of the function $\gamma(t)$. However the flat region is not as clear as for the networks 1, 2 and 3. From these figures, we set the

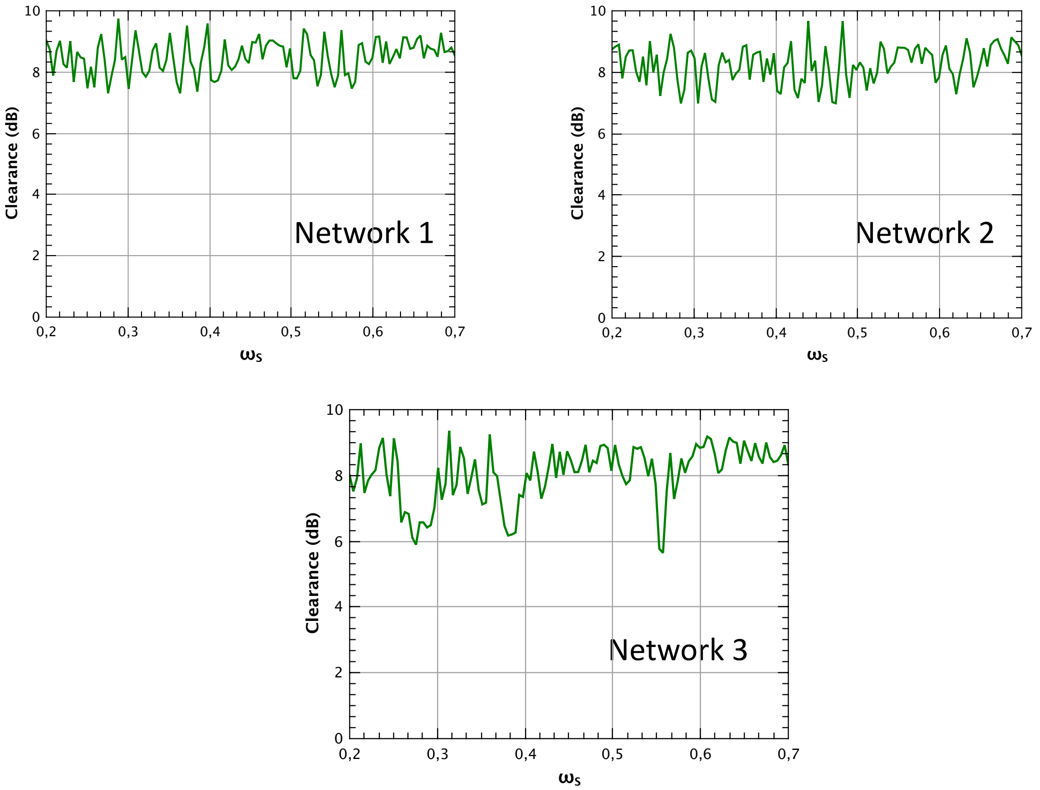

Figure 5.15 – Clearance measurements as a function of the probe mode frequency for the different linear networks.

Network	label	g_{ij}	k	ω_0	ω	Number of points
Watts Strogatz	WS	0,08	0,02	0,25	[0,1;1,1]	100 points
Barabasi Albert	BA	0,02	0,004	0,25	[0,5;0,8]	100 points

Table 5.2 – Parameters for the networks 4 and 5.

interaction times as follows:

- $t_{max,WS} = 90$
- $t_{max,BA} = 250$

As for the precedent measurements, the experimental conditions are identical. The results of spectral densities are shown in figure 5.19 and 5.20. We observe that the experimental data are more noisy than for the regular environments. The matchings between lines are just acceptable, although it still possible to recognize the peaks of J. For Barabasi Albert environment, the expected peak is hard to distinguish from the

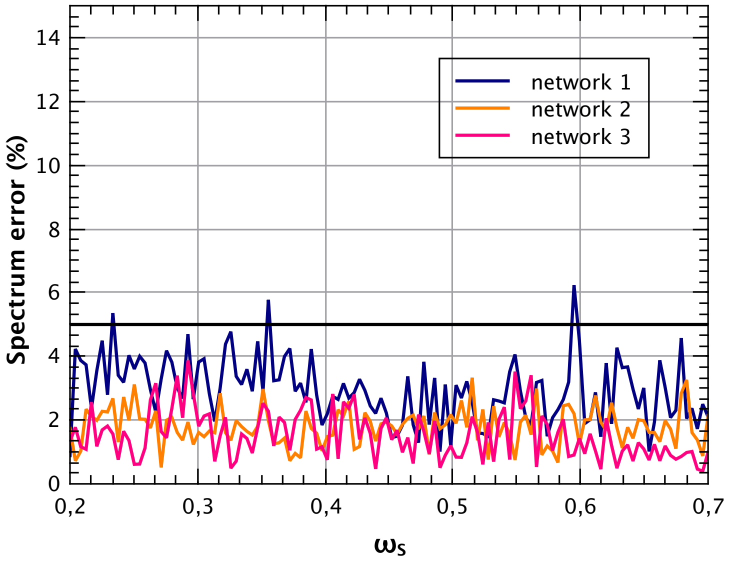

Figure 5.16 – Shaping errors of the probe's spectrum as a function of the frequency for the different linear networks. The black horizontal line delimits the 5% error threshold.

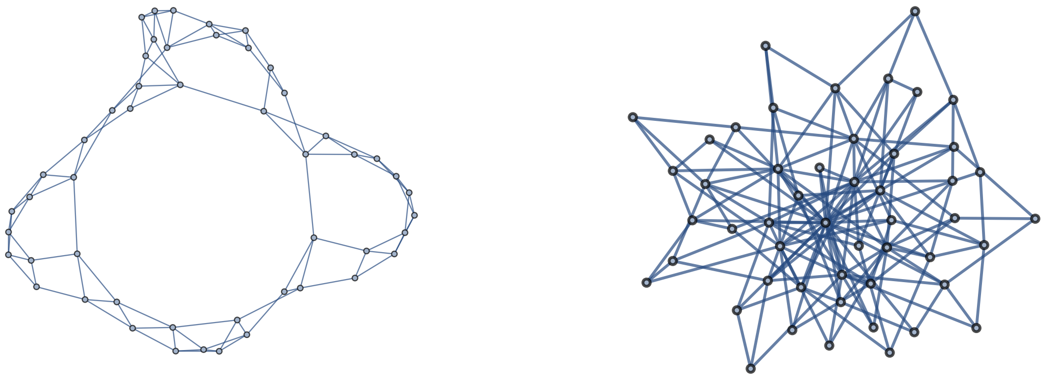

Figure 5.17 – Graph of the two environments based on Watts Strogatz (*left*) and Barabasi Albert (*right*) structures

noise.

The ratio Π and the clearances versus ω_S are plotted respectively in figure 5.22 and 5.21. We see that Π has the same order of magnitude than the precedent ones, it is for all modes below 5%. Regarding the clearance, values fluctuate around 10dB and 8dB. Nonetheless, there is no particular drop and the amplitudes of the oscillations are of the same order of magnitude than previously.

The quality of the results for the first measures are mitigated. On one hand, the

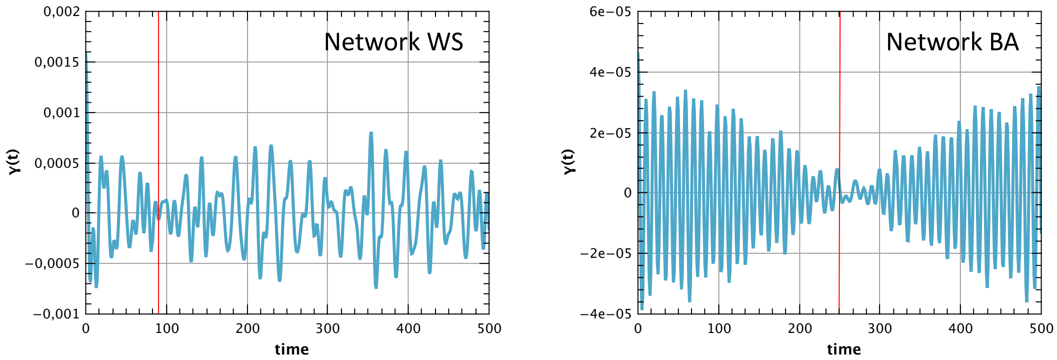

Figure 5.18 – Calculation of the $\gamma(t)$ for network WS (*left*) and network BA (*right*)

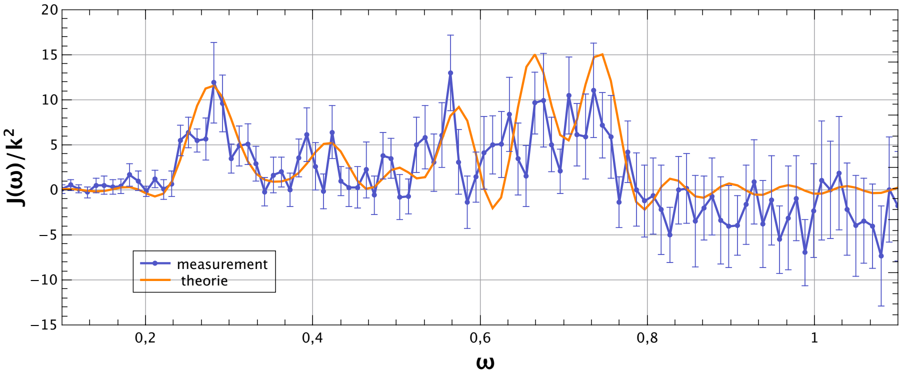

Figure 5.19 – Results of the J measurement for the network WS.

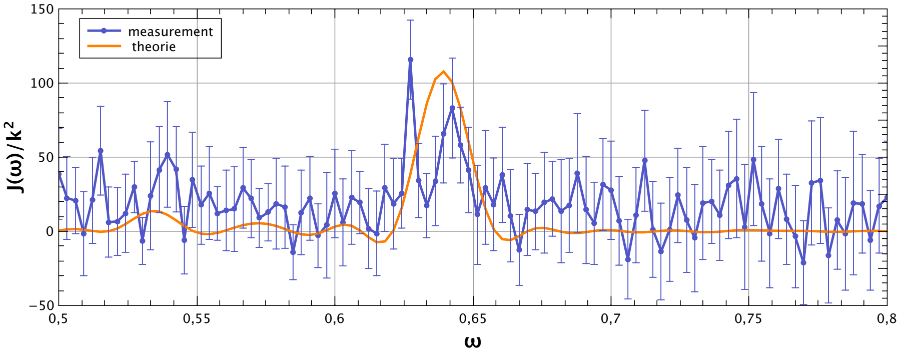

Figure 5.20 – Results of the J measurement for the network BA.

expected J shape is found, but on the other hand the overlaps with theoretical curves are less satisfactory than for the regular networks.

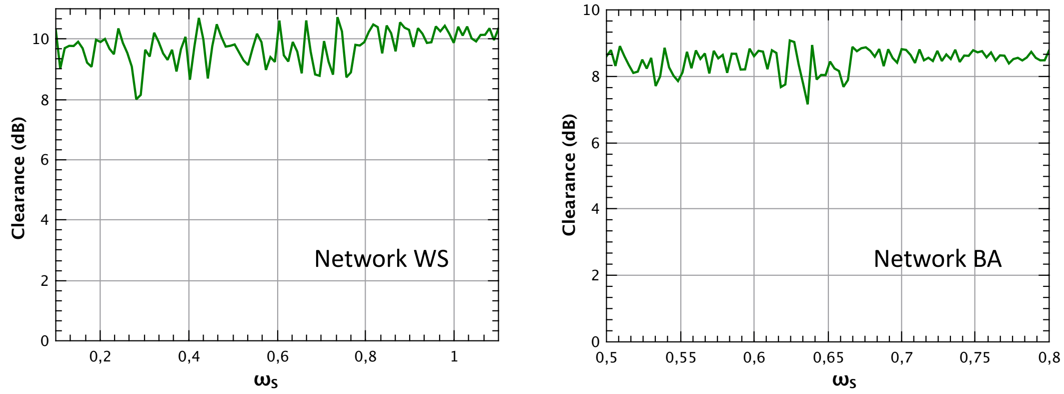

Figure 5.21 – Clearance as a function of the probe frequency for network WS (*left*) and network BA (*right*).

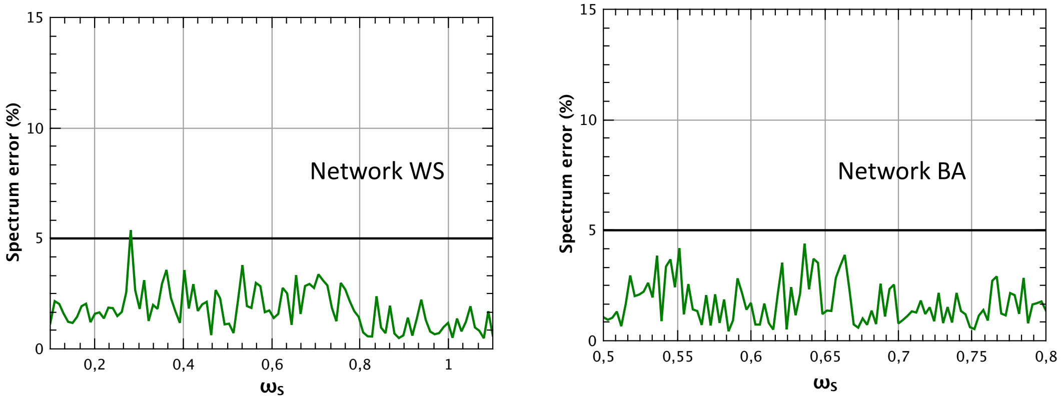

Figure 5.22 – Spectrum errors as a function of the probe frequency for the WS and BA networks.

5.5.3 Measurement with other normal modes

The results presented above show that the simulation via the SPOPO experiment enables to recover the J function for a given environment. The matching with theoretical curves are promising for the linear networks. However, the results obtained with the complex networks encouraged us to improve our measurements. We thus tried new measurements by implementing different normal modes in the networks. This time, instead of the supermodes determined in chapter 4, we choose Hermite-Gaussian modes with the same spectral bandwidth. The choice to fix the spectral width for all supermodes is motivated by probing J with an orthogonal basis. We set $FHWM = 6.5$nm, which correspond to the value calculated analytically by C. Jacquard in his thesis [Jacquard 17]. We repeated the spectral density measurement of the five networks presented above in this new configuration.

Although the graph parameters remain the same, some experimental conditions change. Indeed, because we do not work with the supermodes anymore the threshold of pump power to observe squeezing in the environment components have driffted. For the following measurement the pump power was set to $P_p = 7,5$mW. The number of acquisitions is the same than previously, 20.

The results for J are shown in figure 5.23. We see that in comparison with previously, the experimental data are more consistant and less noisy and it is easier to distinguish the different shapes of the peaks expected from the theory. The improvement is most visible for the BA network where we clearly resolve the peak which follows the theoretical line, which was not the case on measurements using supermodes. We also notice the presence of oscillations for some spectral densities, but their amplitudes are weaker than before.

The spectral shaping errors are plotted in figure 5.24. The result of this acquisition remains good because the matching error for the 5 networks and for most of the frequencies is below 5%.

In figure 5.25 are shown the different plots of the clearance related to the environments. We observe that although the presence of tiny oscillations, the clearance are flatter than previously especially for high values of the frequency. Except for the network WS, there is no particular drop of the electronic transmission, which enhances the relevance of the observed peaks in 5.23.

To go further in the comparison of the measurements with different normal modes, we calculate the relative error between the experimental data with the ones from the theory. To do so, we use the same function Π introduced in 5.28 but this time the variable is the network label. The results are gathered in the table 5.3 below.

Network	1	2	3	WS	BA
FHWM=6.5mn	0,15	0,16	0,17	0,29	0,43
Supermodes	0,37	0,25	0,23	0,49	1,04

Table 5.3 – Calculation of Π for the different networks in the case where the normal modes are the supermodes of the SPOPO and in the case where they have a fixed spectral bandwidth.

The results of this calculation is in favor of the protocol using the fixed spectral bandwidth: for each network the error of recovery is lower for this measurement. We also observe that for the networks based on complex structures the quality of the measurements is lower than for the linear one. For the Barabasi Albert one, the number is larger ($\Pi = 0.43$) in comparison with the other. A reasonable explanation is the low SNR of the experimental data which cancel the good matching between both line we can see by eyes (figure 5.23).

5.6 Summary

In this chapter, we have shown the first part of the results related to the emulation of complex network dynamic. First quantum system ands complex network topic have been introduced in addition of the different definition of network which are used in this last part. Then the mapping of the network with the experiment described in part 2 are also detailed. Finally some measurements of spectral density for a given environments are plotted. The recovery between then theory and the experimental data are satisfactory especially when the supermode basis is chosen as the the theoretical one highlighted in chapter 2.

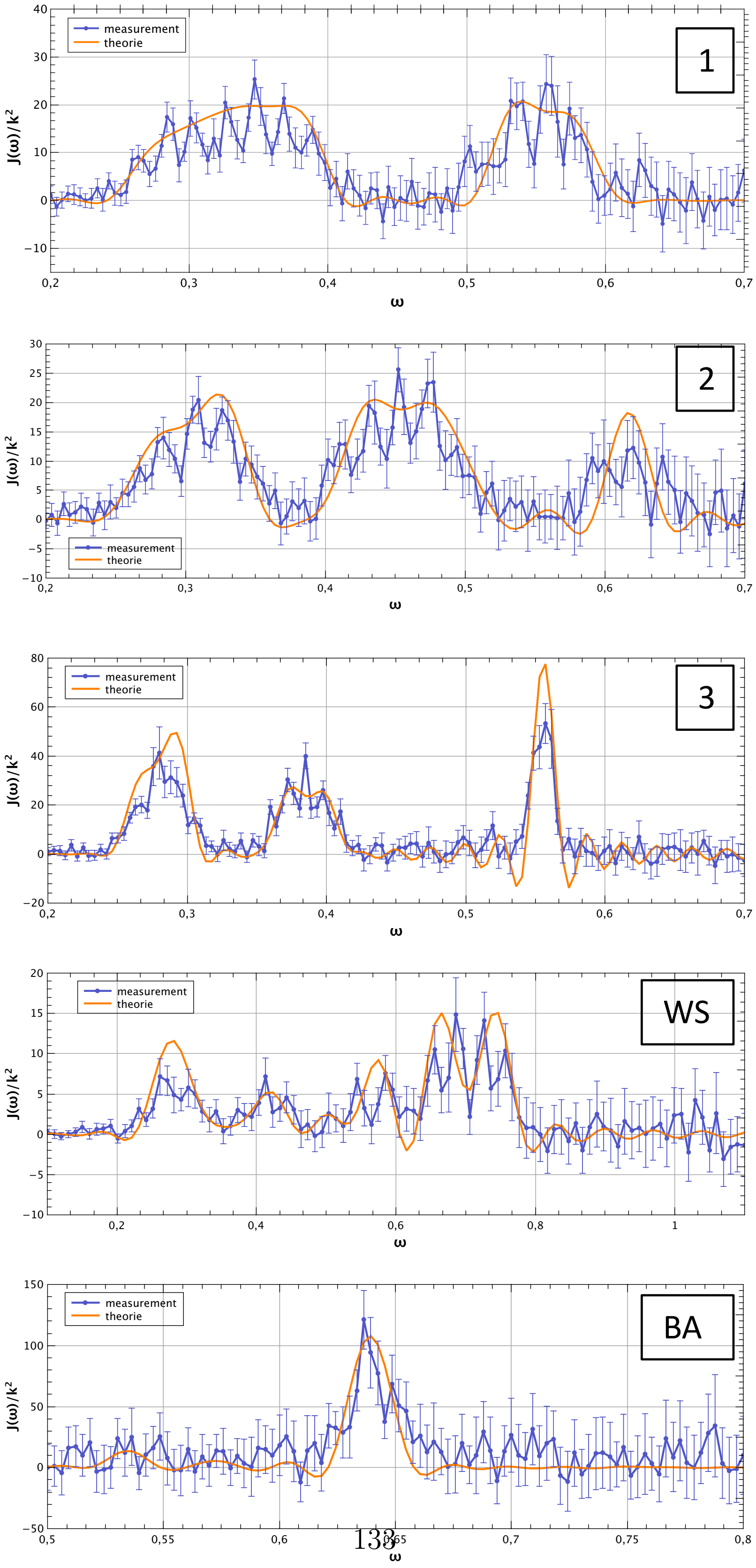

Figure 5.23 – Results of J measurements with fixed FHWM normal modes.

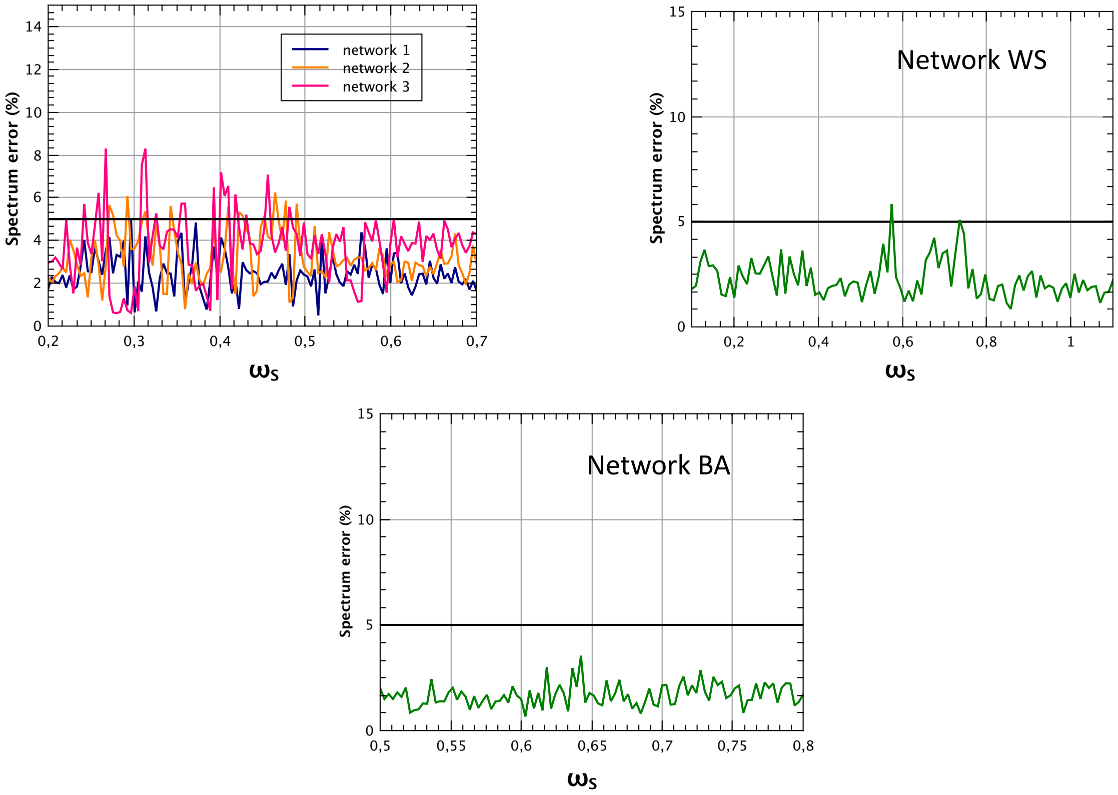

Figure 5.24 – Spectrum errors as a function of the probe frequency for the different networks when the normal mode have a fixed FHWM.

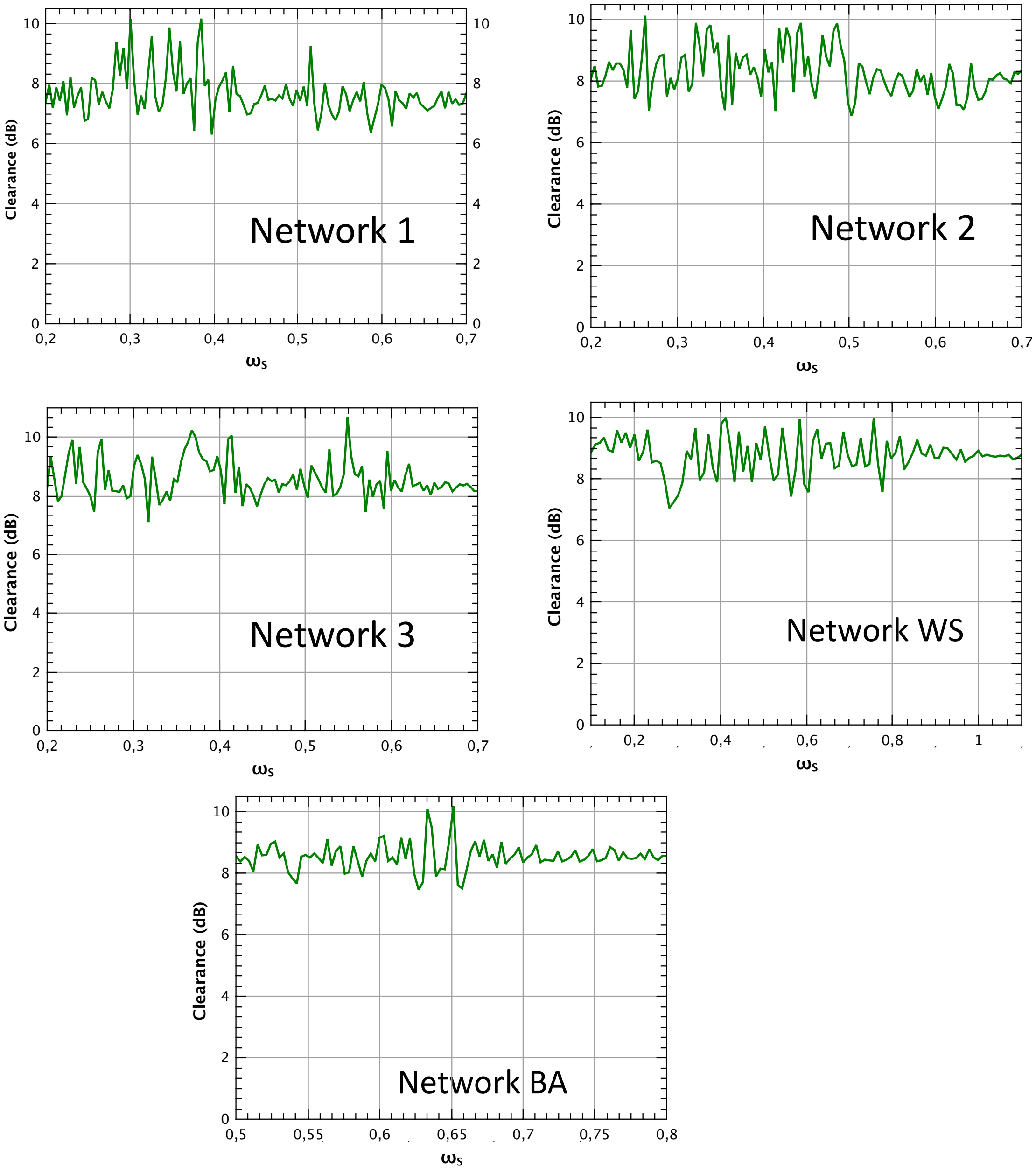

Figure 5.25 – Clearance as a function of the probe frequency for the different networks when the normal mode have a fixed FHWM.

Chapter 6

Quantum non Markovianity in quantum networks

Contents

In the last chapter of this manuscript, we investigate the appearance or not of non-Markovian behaviour when we simulate an open quantum system coupled to an environment modeled by a network. Here the networks are the same as those introduced in chapter 5: they are composed by an ensemble of bosonic harmonic oscillators, one

is the probe while the others compose the nodes of the environment. The definition of non Markovianity in the quantum regime is not straightforward, we will restrict ourself here to the definition based on the variation of the distance between two states and more specifically to the Bures distance.
This chapter is organised as follows: first a classical definition of non-Markovianity is given and then its quantum version. Then the way in which this effect can be characterized is explained. Finally, we present measures for different networks

6.1 Classical Markovian process

6.1.1 Notations and definitions

Markovian behaviour is an expression we found originally in probability field. It is named after the Russian mathematician A. Markov (1856-1922), who is considered as a pioneer in the study of the stochastic processes [Basharin 04]. In order to define this term, let's consider a probability distribution X, which takes its values x in a vectorial space denoted as $\mathcal{K}$. In the context of a discrete stochastic process, X takes n successive values at given times $\{t_1, ..., t_n\} \in I^n$ with $I \subset \mathbb{R}$. The values are labelled according to those of the corresponding times such as $X(t = t_i) = x_i$, for $i \in [\![1; n]\!]$. The probability to observe all the values $x_1, ..., x_n$ at the time $t_1, ..., t_n$ is denoted as follows [G. R. Grimmett 02]:

$$\mathcal{P}\left((x_n, t_n); (x_{n-1}, t_{n-1}); ...; (x_1, t_1)\right) \tag{6.1}$$

For this definition and the following of this introduction about Markovian concept, we use the notation of [Rivas 14]. Then, the joined probability to observe x_n at $t = t_n$ when we already know the past events $X(t = t_i) = x_i$ for $i < n$, is denoted as:

$$\mathcal{P}\left((x_n, t_n)|(x_{n-1}, t_{n-1}); ...; (x_1, t_1)\right) \tag{6.2}$$

We say that the stochastic process is Markovian if the probability at $t = t_n$ is only affected by the previous event at $t = t_{n-1}$. We can write in this case:

$$\mathcal{P}\left((x_n, t_n)|(x_{n-1}, t_{n-1}); ...; (x_1, t_1)\right) = \mathcal{P}\left((x_n, t_n)|(x_{n-1}, t_{n-1})\right) \tag{6.3}$$

In other words, a Markovian process does not have any memory of the past events of X. This definition has direct impacts on the expected values and the standard deviation of the probability distribution. Beside, it exhibits other properties which will be useful in the definition of the markovianity in quantum regime.
Indeed let's consider three events at $t = t_1, t_2, t_3$. We have for any distribution:

$$\mathcal{P}\left((x_3, t_3); (x_2, t_2); (x_1, t_1)\right) = \mathcal{P}\left((x_3, t_3)|(x_2, t_2); (x_1, t_1)\right) \times \mathcal{P}\left((x_2, t_2)|(x_1, t_1)\right) \times \mathcal{P}\left((x_1, t_1)\right) \tag{6.4}$$

In the case of a Markovian stochastic process, we can write:

$$\mathcal{P}\left((x_3,t_3)|(x_1,t_1)\right) = \sum_{x_2\in\mathcal{K}} \mathcal{P}\left((x_3,t_3)|(x_2,t_2)\right)\mathcal{P}\left((x_2,t_2)|(x_1,t_1)\right) \tag{6.5}$$

This is the Chapman-Kolgomorov equation. This property is used to introduce the concept of divisibility of the stochastic matrices developed in the next paragraph.

6.1.2 The stochastic matrix

Let's introduce the transition matrix T. It is a linear map whose goal is to connect the values $\{x_i\}_{i\in\mathbb{N}}$ taken successively by X between them. For time t_1 to t_2, we have:

$$\mathcal{P}\left(x_2,t_2\right) = \sum_{x_1\in\mathcal{K}} T\left((x_2,t_2)|(x_1,t_1)\right)\mathcal{P}(x_1,t_1) \tag{6.6}$$

The matrix T is called stochastic matrix if it respects the two following rules:

$$\sum_{x_2\in\mathcal{K}} T((x_2,t_2)|(x_1,t_1)) = 1 \tag{6.7}$$

$$T((x_2,t_2)|(x_1,t_1)) \geqslant 0 \tag{6.8}$$

In the case of two events $t_2 > t_1$, the stochastic matrix is the joint probability:

$$T((x_2,t_2)|(x_1,t_1)) = \mathcal{P}((x_2,t_2)|(x_1,t_1)) \tag{6.9}$$

For 3 or more events, this equality is not straightforward and we can meet some cases where the equality is broken. Nonetheless, in [Rivas 14], it is shown that if the process is Markovian, then for any couple of time $(t_i,t_j)\in I^2$ with $t_j > t_i$ and for all $(x_i,x_j)\in\mathcal{K}^2$:

$$T((x_j,t_j)|(x_i,t_i)) = \mathcal{P}((x_j,t_j)|(x_i,t_i)) \tag{6.10}$$

A consequence of this property is, considering three events:

$$\sum_{x_3\in\mathcal{K}} T((x_2,t_2)|(x_1,t_1)) = 1 \tag{6.11}$$

$$T((x_2,t_2)|(x_1,t_1)) \geqslant 0 \tag{6.12}$$

$$T((x_3,t_3)|(x_1,t_1)) = \sum_{x_2\in\mathcal{K}} T((x_3,t_3)|(x_2,t_2))T((x_2,t_2)|(x_1,t_1)) \tag{6.13}$$

These three last equations are another way to define a Markovian process, especially the last one. Indeed we say a process is divisible when the equation (6.13) is verified. It is a direct consequence of the markovian memoryless effect.

6.2 Markovianity in the quantum regime

In this part, we develop the idea behind quantum Markovianity, which aims to transcribe the concept of memoryless presented above in the quantum regime.

6.2.1 Memoryless effect in of quantum state

At first glance, it seems straightforward to associate quantum physics and Markovianity since the quantum physics is based on statistics. However, it quickly becomes challenging to build a quantum version of Markovianity from the memoryless property. Indeed, quantum theory is also based on no commutative algebra, which gives rise to a problem: the system of interest is disturbed by the sampling and not only by its own time evolution. Hence, let's consider a quantum system and $\{x_i\}_{i\in[\![1;n]\!]}$ the results of n successive measurements. The probability to perform a new measurement and to get the value of x_{n+1} is depending on the value of $x_1, ..., x_n$ and not only x_n because all the measurements are projective.

Hence, the memoryless property does not look like the most straighforward one to build the concept of quantum Markovianity. Nonetheless, for many years, several definitions have been proposed for the transcription of this concept to the quantum regime. These definitions are based on different properties such as quantum white noise [Hudson 84, Gardiner 85], factorization approximation [Wangsness 53, Argyres 64, Lax 64], divisibility, the GSKL master equation[Hall 14]. They are not equivalent and some are the consequence of others. A hierarchy between all the proposed definitions can be found in [Li 18]. Here on this manuscript, we will use the definition based on the back flow of information proposed by Breuer et al in 2009 [Breuer 09]. In this paper, they define a process as non Markovian if its time evolution exhibits back-flow of information from the environment to the system of interest.

6.2.2 P- and CP-divisible map and quantum Markovianity

Before going exploring some consequences of this definition, let's introduce two other definitions about the divisibility of map. We say that a quantum system subject to time evolution associated to a linear map Φ is P-divisible if for any time t_1 and t_2, $\Phi_{(t_1,t_2)}$ is a positive map, which implies that for any positive semi-definite matrix $\boldsymbol{A}$:

$$\Phi_{(t_1,t_2)}\boldsymbol{A} \geqslant 0 \tag{6.14}$$

Furthermore, if for any positive definite matrix $\boldsymbol{A}$, $\Phi_{(t_1,t_2)}\boldsymbol{A} > 0$, then we say Φ is a completely positive (CP) divisible map.

In [Breuer 16], a quantum process is said to be Markovian if the associated map is P-divisible. As soon as there exists an interval of time $I' \subset I$, where the map is not

P-divisible then the process is quantum non Markovian. In figure 6.2 is represented a scheme showing the region where the quantum process is associated to divisible or not map in order to indicate the Markovian property. In this figure, $\mathcal{N}_{BLP}$ denotes a witness function that we will define in section 6.3.

6.2.3 Interpretation in term of distinguishability

An interesting property of quantum Markovianity concerns the distinguishability of quantum states, where a way to evaluate this parameter between two states is the distance between them. To study quantum non Markovian behaviour, several distance functions can be considered. We can cite for example the Bures distance or the one defined through the trace. It has been shown that for a P-divisible map Λ[Ruskai 94]:

$$\forall \rho_1, \rho_2 \quad D(\Lambda\rho_1, \Lambda\rho_2) \leqslant D(\rho_1, \rho_2) \tag{6.15}$$

In other words, for a Markovian process, when the quantum system evolves, the distinguishability between two different states decreases. As soon as the inequality (6.15) is broken as shown in figure 6.1, the evolution is said quantum non Markovian. This consequence allows us to translate into equations the initial definition based on the backflow of information.

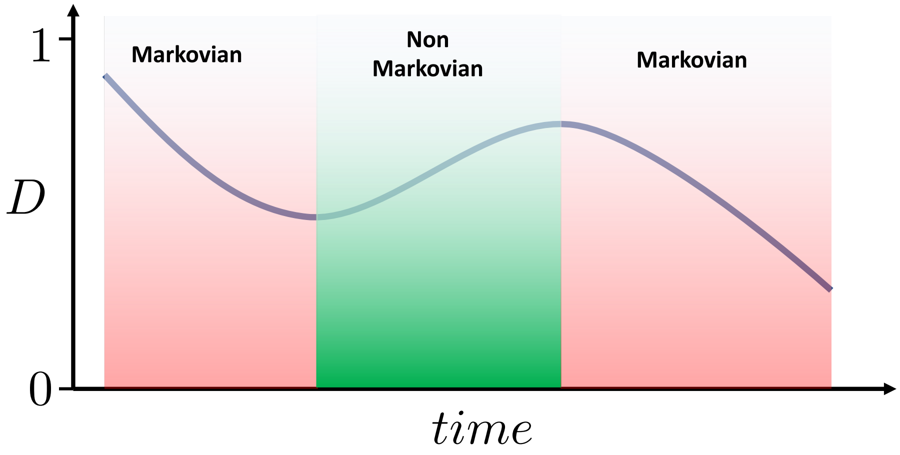

Figure 6.1 – Example of trace distance function of two states against time. The curve is expected to show an increasing part over a time interval wether the stochastic process admit quantum non Markovian behaviour. For the trace distance $D = 1$ means the states are orthogonal and non zero and $D = 0$ if they are the same

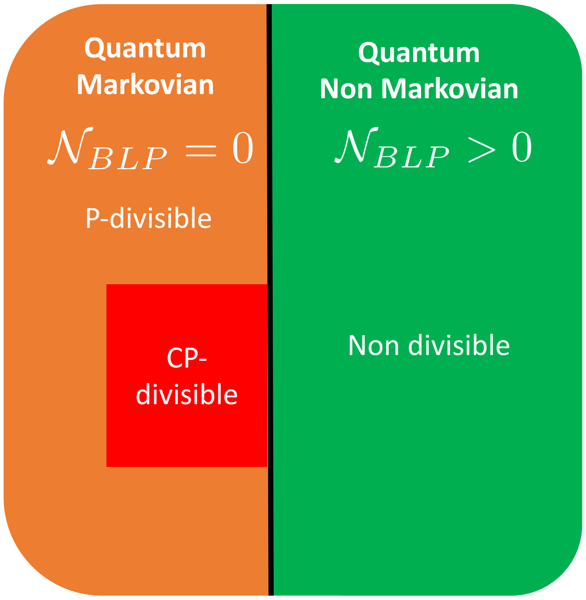

Figure 6.2 – Mapping for quantum Markovian or non Markovian behaviour as a function of the positivity of the associated dynamical map.

6.3 Witness of non Markovianity

6.3.1 The BLP Witness

Since the quantum non Markovianity is related to a back flow of information for the time evolution of the system of interest, we are looking for the characterization of the transition from Markovian to non Markovian and the assessing of the strength of the information back flow.

For the last ten years, many witnesses have been build to respond to the study of this phenomenon. Most of them are inspired by two publications that appeared at the same time [Breuer 09, Rivas 10]. The work of Á. Rivas *et al* [Rivas 10] is based on the study of the evolution of a maximally entangled state composed by the system of interest and an ancilla. They look wether the entanglement measure behaves non monotonically in time which implies non Markovianity properties. Here we only introduce the work by PH. Breuer *et al* [Breuer 09, Laine 10] since the witness used on the following of this manuscript is inspired by the results of their article. The witness they have developed is named as their name initial and is denoted as $\mathcal{N}_{BLP}$. It is based on the distance between two states and is expressed as:

$$\mathcal{N}_{BLP} = \max_{\rho_1,\rho_2} \left[\int_{\dot{D}(t)>0} \mathrm{d}t \dot{D}(t) \right] \tag{6.16}$$

where for any time t, $D(t) = D(\rho_1(t), \rho_2(t))$. The maximized quantity is the integral of a time derivative, it is thus the subtraction of two distances at different times which delimits an interval where $\dot{D}(t) > 0$ and the system exhibits back flow of information. Hence, by definition, we have for any open quantum system evolution:

$$\mathcal{N}_{BLP} \geqslant 0 \tag{6.17}$$

Indeed, if the process is quantum Markovian, we have at any time t, $\dot{D}(t) < 0$ and thus $\mathcal{N}_{BLP} = 0$ because the interval of integration is zero. On the other hand, if the process is quantum non Markovian, there exists an interval of time I' such as $I' \subset I$ where $\forall t \in I'$, $\dot{D}(t) > 0$. We have then:

$$\mathcal{N}_{BLP} \geqslant \max_{\rho_1,\rho_2} \left[\int_{I'} \mathrm{d}t \dot{D}(t) \right] > 0 \tag{6.18}$$

Hence the BLP witness presents the benefit to draw a clear boarder between quantum Markovianity and non Markovianity. Then the positive values tells about the level of quantum non Markovianity.

6.3.2 Derivation of the BLP witness

Some experimental works about the measurement of non Markovianity in open quantum system has already been made [Liu 11]. Nonetheless, sometimes this witness must be adapted to experimental constrains for a better fit with measurement data. Indeed, the quantum Fisher information [Lu 10], the sign of the damping kernel [Hall 14], correlation [Luo 12] or quantum interferometric power [Dahr 15, Guarnieri 16] can be used as witnesses of non Markovianity. Beside, other functions than the trace distance can be considered for the witness as soon they are contractive with P-divisible and trace preserving dynamical map. We can for example quote the quantum mutual information or the relative entropy [Rivas 10, He 17] .

In our case of quantum system based on continuous variable, the witness we will use is based on the Bures distance D_B. The theoritcal work on this witness is developed in [Vasile 11]. The Bures distance, D_B, is defined as follows [Bures 16]:

$$D_B(\rho_1, \rho_2) = \arccos\left(\sqrt{F(\rho_1, \rho_2)}\right) \tag{6.19}$$

This distance function has the benefit to work as witness and furthermore there is another way to express it as a function of the fidelity:

$$D_B(\rho_1, \rho_2) = \sqrt{2 - 2\sqrt{F(\rho_1, \rho_2)}} \tag{6.20}$$

and we can deduce the relation between both time derivatives:

$$\frac{\mathrm{d}D_B(t)}{\mathrm{d}t} = -\frac{2}{\sqrt{1 - F(t)}\sqrt{F(t)}} \frac{\partial F}{\partial t} \tag{6.21}$$

Actually both Bures distance and fidelity can be used as witness[Vasile 11]. Nonetheless, the time derivatives have opposite signs. The integration must be done thus on the interval where the derivative of the fidelity is negative:

$$\mathcal{N}_{BLP} = \max_{\rho_1,\rho_2} \left[- \int_{\dot{F}(t)<0} \mathrm{d}t \dot{F}(t) \right] \qquad (6.22)$$

6.4 Measurement protocol

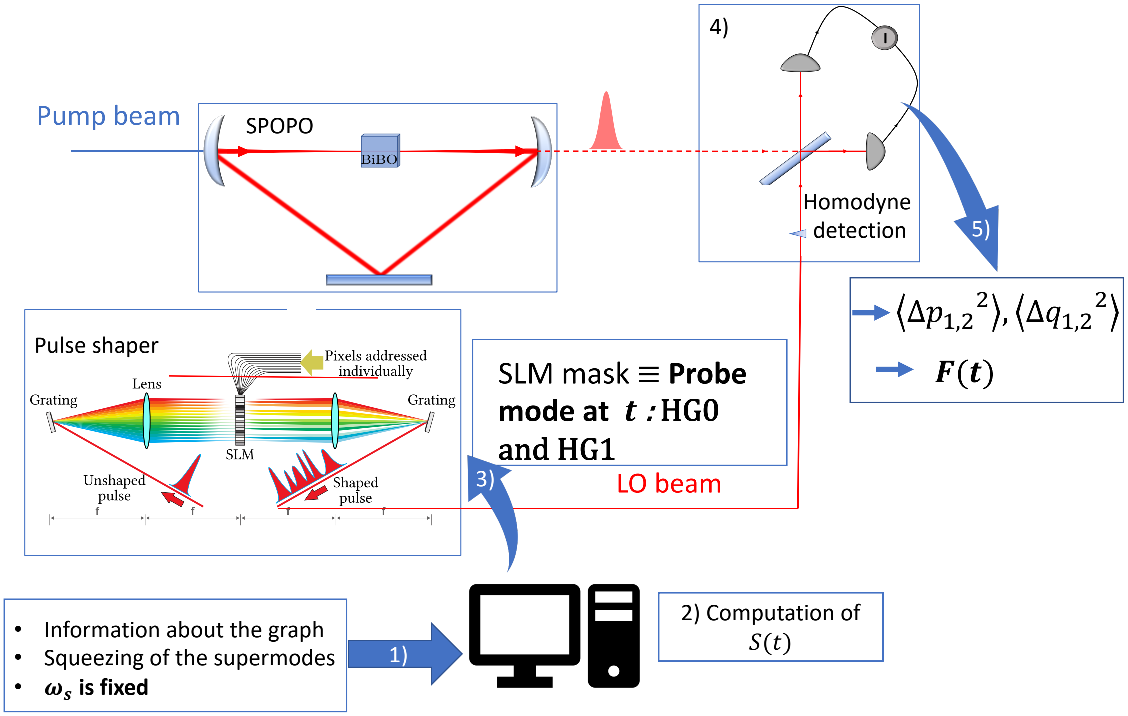

Figure 6.3 – Protocol for the measurement of quantum non Markovian behaviour for a given environment and at a given probe frequency.

6.4.1 Simulation of open quantum system and quantum non Markovianity

In the rest of this chapter, we investigate the presence or not of quantum non Markovianity in simulated networks. We consider the same model than introduced in chapter 5 *i.e* the system of interest is a probe of frequency ω_S connected through a coupling strength k to an environment. This environment is an engineered network of bosonic harmonic oscillators of frequency ω_0. The goal, here is to simulate, via the SPOPO experiment, wether, for a given network as environment and a given probe frequency, we can observe a back flow of information, that we detect by using the fidelity measurement between two states and as a function of the time t to determine the witness.

6.4.2 Non Markovianity measurement protocol

The protocol used to measure the time evolution of the fidelity of the probe with its environment is very similar to the previous one used for the spectral density recovery. Nonetheless there are slight changes as shown in figure 6.3. Indeed, if we still send the informations related to the network and the output states of the SPOPO in a mathematica code, this time, the frequency ω_S is fixed and the interaction time of the total system is the variable. The code computes the matrix $\boldsymbol{S}$ introduced in chapter 5 for each time t. The first vector of the matrix related to a time t gives us the shape of the probe mode at this same time. Once we have computed the shapes for all the times t we want, we start a measurement sequence where we measure, for each SLM mask related to a given time t, the quadrature variance versus the LO phase in order to extract the values $\langle\Delta^2 q_s\rangle$, $\langle\Delta^2 p_s\rangle$ and deduce the value of the fidelity $F(t)$. The fidelity of two quantum states ρ_1 and ρ_2 is given by the Uhlmann formula [Jozsa 94]:

$$F(\rho_1,\rho_2) = \left(\mathrm{Tr}\left(\sqrt{\sqrt{\rho_1}\rho_2\sqrt{\rho_1}}\right)\right)^2 \tag{6.23}$$

In the case of two gaussian states with zero mean the fidelity is derived as follows:

$$F(\rho_1,\rho_2) = \frac{2}{\sqrt{\Delta + T} - \sqrt{T}} \tag{6.24}$$

with:

$$\Delta = \det\left(C_1 + C_2\right) \tag{6.25}$$

$$T = \left(\det\left(C_1 - \mathbb{I}\right)\det\left(C_2 - \mathbb{I}\right)\right) \tag{6.26}$$

where C_i is the covariance matrix of states i for $i = 1, 2$. They are 2×2 symmetric matrices with in the diagonal the squeezing and anti-squeezing terms and in the anti-diagonale position $\langle\Delta qp\rangle = 0$. They are thus both diagonal. To find the fidelity $F(t)$, it is sufficient to determine the squeezing from the mask related to both quantum states to then deduce the witness determined by the equation (6.22). In theory, the witness is calculated by a maximization over all the possible couples of states. Unfortunately, this is not achievable via the SPOPO experiment. Hence, the quantity we measure in this chapter is a witness related to a network representing an environment for a given couple of states as well as it was done in [Liu 11]. We still have to choose a couple of state which maximize the witness. As suggested by [Wissmann 12], the states have to be orthogonal. In the context, of continuous variable gaussian state, this assertion amounts to consider two states squeezed along orthogonal direction.

6.4.3 Differents types of quantum non Markovianity

We comment in this paragraph the fact that the full system is composed by harmonic oscillators which makes it has inherent non markovian characteristics. Therefore, considering the matrix $\boldsymbol{S}$ from (5.24) that we have introduced in the chapter 5, the probe mode is a linear combination of cosine and sine functions at any time t. Hence, we will observe oscillations of the squeezing and the fidelity against time as showed in figure 6.4. In this graph, is plotted the result of simulations of the fidelity of the two states related to the probe for different frequencies ω_S where the environment is a network randomly chosen and composed by $n = 20$ nodes. We observe oscillations for each curve related to a ω_S frequency. The frequencies of the oscillations are not exactly equal to ω_S. The frequencies $(\Omega_1, ...\Omega_n)$ are different from $(\omega_1, ...\omega_n)$ in equations (5.24) because of the recombination due to the diagonalization operation. However, we can see a trend: the oscillations frequency increase with ω_S and they are of the same order of magnitude. On the rest of this chapter we restrict ourself to the study of quantum non Markovianity due to slower oscillations of the fidelity. The goal here is to find non Markovian behaviour which does not come from the model we choose to simulate the network. We are seeking effect where the energy has sailed through several nodes in the environment before returning to the probe.

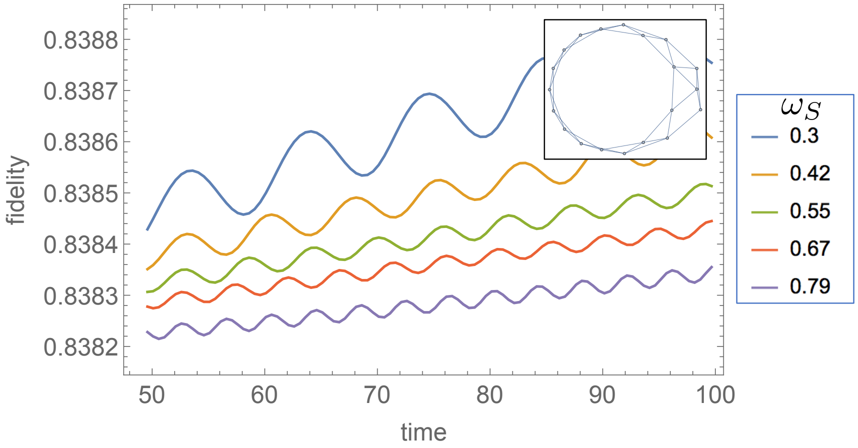

Figure 6.4 – Simulation of the Fidelity against time for different probe frequencies. *inset:* Structure of the environment. For this simulation the network parameters are: $\omega_0 = 0,25$, $g = 0,02$ and $k = 0,02$

6.5 Results of quantum non Markovianity measurements

6.5.1 Experimental conditions

In this section, we show results of Fidelity measurements, which witness quantum non Markovian or not behaviours. The measurements have been performed for two networks: a linear and a complex network. Their structure have already been presented in chapter 5 as it concerns networks 3 and the Watts Strogatz one. In both case scenario, the matrix $\boldsymbol{S}$ is computed from $t_i = 0$ to $t_e = 498$ with 250 points which gives a time step of $\Delta t = 2$. Because we have here to measure two states the number of acquisitions drops in comparison to the spectral density reconstructions in order to keeps the same measurement time which is allowed by the stability of the experiment. The total number of acquisitions is then 5.

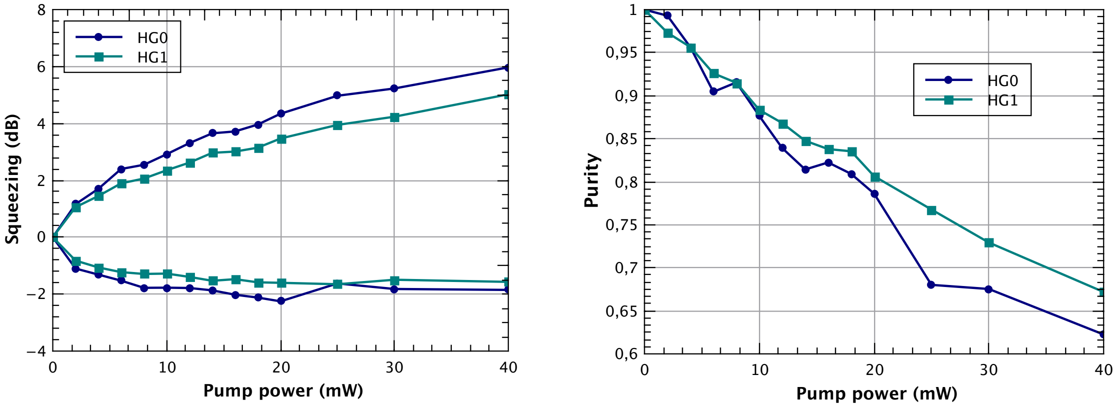

Figure 6.5 – *left*: Squeezing and anti-squeezing versus pump power for the two first Hermite-Gaussian modes. *right:* Purity as a function of the pump power

The conditions on the detection scheme are similar to previous measurements: the visibility of the interference fringes on the homodyne detector is $V_h = 95\%$. The normal modes of the full network are composed by the Hermite-Gaussian modes with a fixed spectral bandwidth (FHWM=6,5nm for the first mode). We use as probes for the non-Markovianity the two first Hermite-Gaussian modes that are naturally occupied by orthogonally squeezed states. So the initial fidelity between the two modes is minimal. The environment is composed by the Hermite-Gaussian modes with index larger or equal to 5.

The choice of the pump power injected into the SPOPO is no more limited by the fact to have a depopulated environment ($N = 0$). We can then adjust it via a compromise between having enough squeezing and having a good purity for the measured states. In

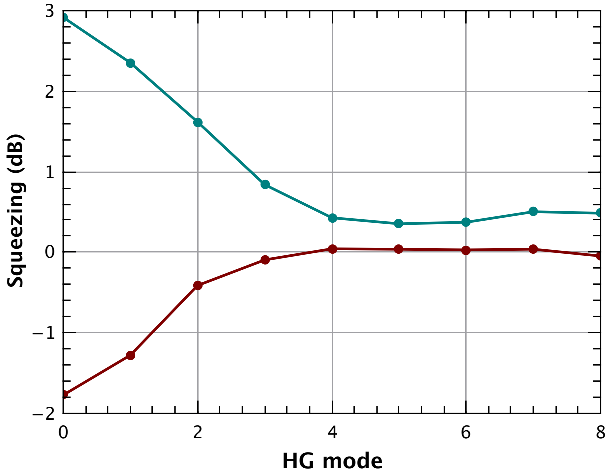

Figure 6.6 – Squeezing and anti-squeezing against mode number for $P_p = 10mW$ as pump power.

figure 6.5 we show the squeezing of the Hermite-Gaussian modes 0 and 1 as a function of the pump power and the purity. From these plots, we choose a pump power of $P_p = 10mW$. In figure 6.6 is shown the squeezing and anti-squeezing values in the case of $10mW$ pump power versus the mode number. However, in this plot the squeezing is calculated from the code presented in chapter 4 and we see that from mode 4 the SNR is too low to extract the correct values. The squeezing and anti-squeezing are actually zero after mode 5. The squeezing and anti-squeezing values are then used in the mathetimatica code dedicated to the computation of $\boldsymbol{S}$. In the different computations, the HG modes which were not measured in the figure 6.6 are interpolated to 1.

6.5.2 Linear networks

The environment chosen for the linear structure is the network 3 presented in chapter 5. The result of the fidelity measurement is shown in figure 6.7 for two different frequencies: $\omega_S = 0.58$ and $\omega_S = 0.70$. We observe a back flow of the information for the first frequency while for the second the fidelity remains stable. Hence there is quantum non Markovianity only for $\omega_S = 0.58$. This difference of behaviour could have been anticipated since, for $\omega_S = 0.7$, the spectral density measured in chapter 5 doesn't show any sign of coupling between the system and the environment. Indeed, this frequency is far from any peak exhibited by J differently from the case $\omega = 0.58$. Hence, it is not not possible to see for the selected time-window a sign of information return while the amount of exchanged energy is low. Regarding the time step, it is selected as depending of the total acquisition duration but also in order to avoid to see the inherent oscillations due the presence of harmonic oscillators in the composition of the total system (figure

6.4). Indeed, $\Delta t = 2$ when this type of fluctuation will oscillate at a pulsation close to the values of ω_S. Hence, the resolution set by Δt makes these oscillations are not resolved. In figure 6.8 is shown the error ratio on the shaping of the LO spectrum calculated with the formula (5.28). We determine this quantity for the two quantum states versus the time variable of the simulation. The relative error remains always below 5% which tells us that the shaping of the modes works at any time t. In figure 6.9 is represented the clearance against time for the two probe states. As we can see for $\omega = 0.70$ there is no issue, the clearance is stable around 9 dB for both modes. For $\omega_S = 0.58$, the clearance remains flat between 7 and 9 dB but there is more fluctuations on the plot mainly due to the presence of more information exchanges between the probe and the environment. Indeed, before the acquisition, we set the LO power using the gaussian mode as a reference. For an acquisition where the exchange are low, the spectrum of the probe is weakly affected as is the LO power and the clearance. On the contrary, when the information flux are more important, the fluctuation on the LO spectral shape have a direct impact on the LO. Nevertheless, in spite of the fluctuations, the clearance remains above 5 dB for all the time, which confirms the performance of the homodyne detection for each measured points.

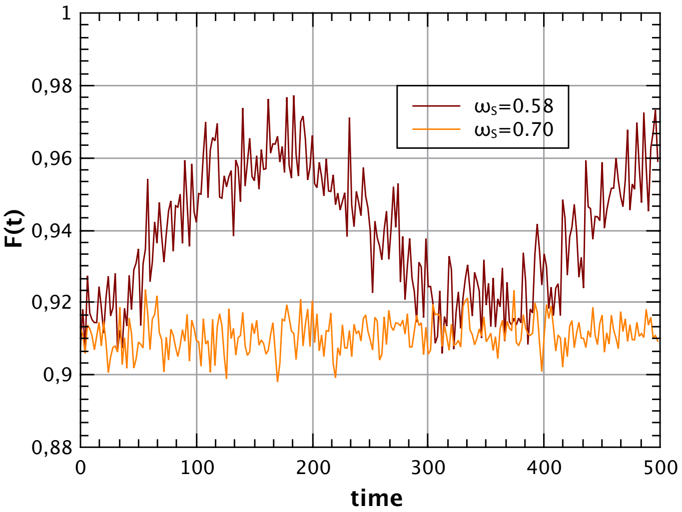

Figure 6.7 – Fidelity as a function of time when the environment is the linear network 3 for two frequency: $\omega_S = 0.58$ and $\omega_S = 0.70$

In addition of these first measurements of Fidelity, we can also check that we recover Non Markovian behaviour at a lower time scale as predicted by the results of the analytical simulation in figure 6.4. The plots in 6.10 show two fidelity measurements when the time windows is reduced to $t_e - t_i = 50$ with a time step of $\Delta t = 0.25$ for the frequency $\omega_S = 0.58$. We observe evident oscillations of $F(t)$. For this time scale, we conclude that the resolution of the inherent probes oscillations is possible for both

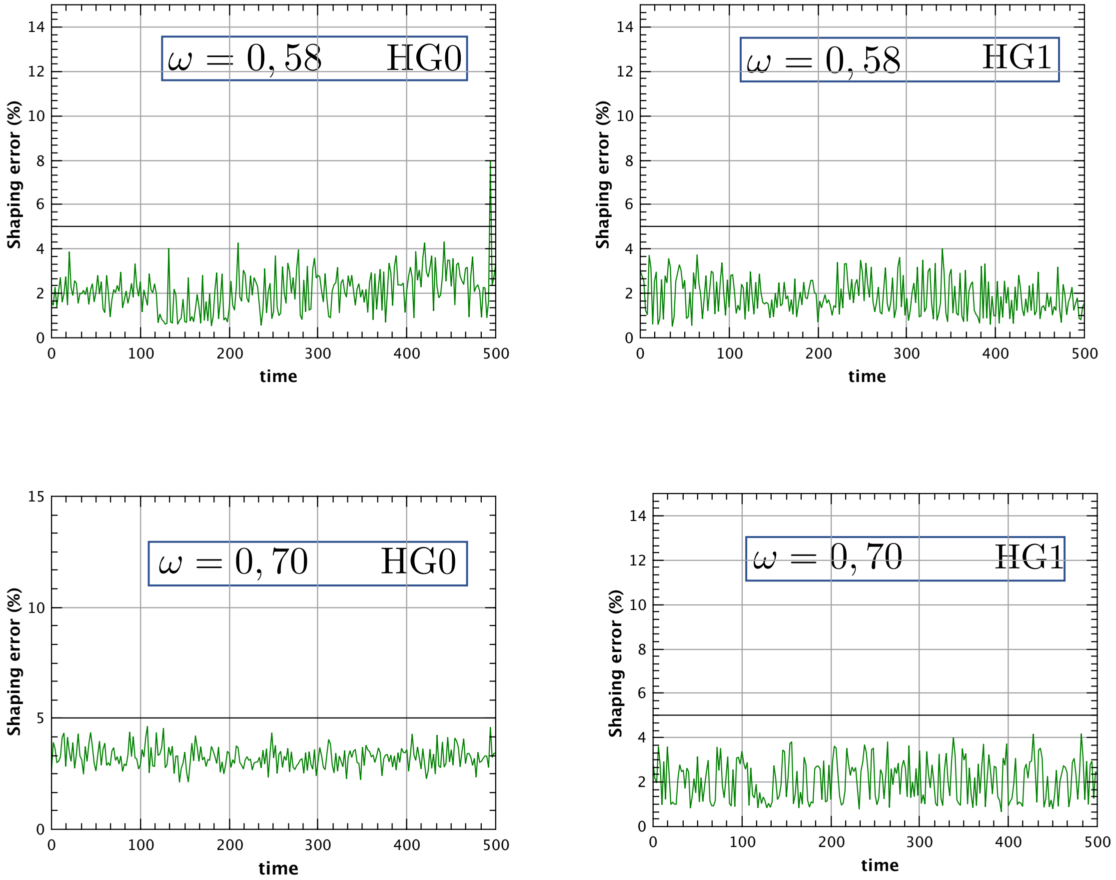

Figure 6.8 – Spectrum error against time in the case of the linear network for the different ω_s and the Hermite-Gaussian modes (HG).

of these time windows. We also retrieve the general behaviour of the fidelity on both curves: for the plot with the following time window $t \in [50, ..100]$, the successive peaks are increasing when for the second interval they are decreasing.

6.5.3 Complex networks

For the random network, the environment takes the structure of the network WS based on Watts Strogatz structure presented in chapter 5. The fidelity $F(t)$ is measured for three probe frequencies: $\omega_S = 0.40$; $\omega_S = 0.75$; $\omega_S = 0.9$. We see the same oscillation than the one observed for the linear network which highlights quantum non Markovian behaviour. For the highest frequency the coupling is low and the Fidelity remains constant and for $\omega_S = 0.40$ there is first an increase of the fidelity which indicates a transfer of the energy from the probe to the environment and a slight decline of the

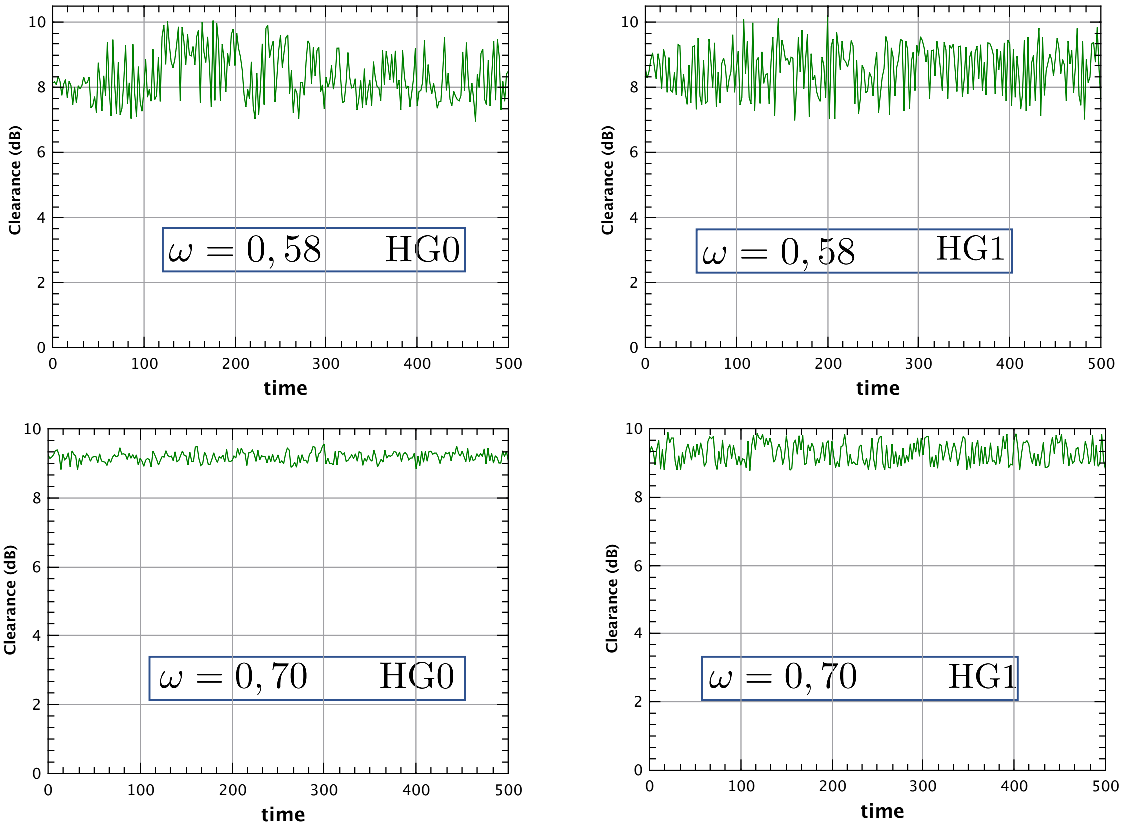

Figure 6.9 – Clearance against time in the case of the linear network for the different ω_s and the Hermite-Gaussian modes (HG).

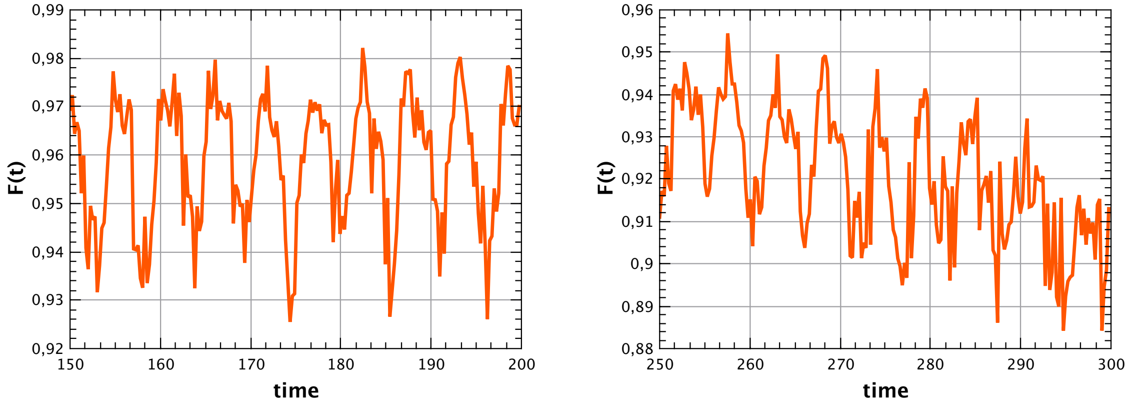

Figure 6.10 – Measurement of the Fidelity against time in the case of the linear network as environment for shorter time periods with a time step of $\Delta t = 0.25$.

fidelity. We see here that we have quantum non Markovianity but the effect is less strong than for $\omega_S = 0.75$. The different errors of shaping against time are plotted in figure 6.12 and the clearance in figure 6.13. We observe that for each frequency and each mode, the error on the shaping of the local oscillator is below 5% as for the precedent measurements. Nonetheless, we also notice a peak of the relative error for the mode HG1 at $\omega_S = 0.9$, which reaches 16%. These peak on the error rate is surprising although there is no consequence on the clearance. As we observe the fidelity curve there is no particular drop for this time interval.

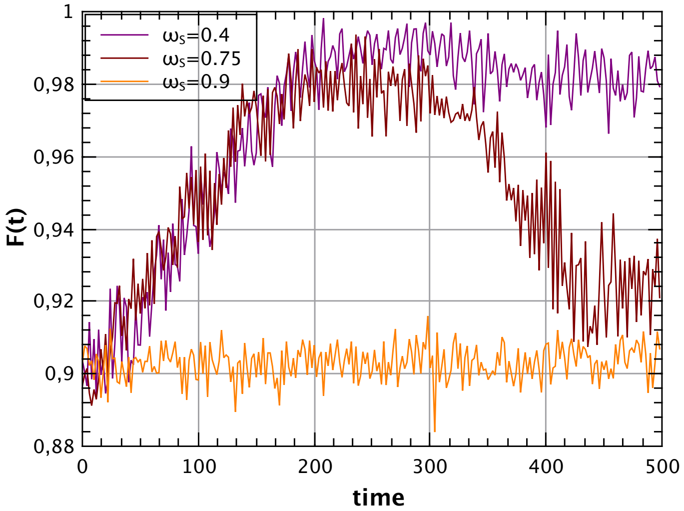

Figure 6.11 – Fidelity as a function of time when the environment is the random network WS for three frequency: $\omega_S = 0,40$, $\omega_S = 0,75$ and $\omega_S = 0,90$

The clearance gives similar results than for the linear network. The quantity remains flat and there is more fluctuations of the clearance where we observe energy exchanges between the probe and the environment. However, the plot of the clearance versus time for $\omega_S = 0.4$ does not validate completely the measurement. Indeed, we can notice a correlation of the clearance with the Fidelity: when we observe the thermalization of the states and an increase of the fidelity, the clearance reaches its minimum and then the revival of quantum information is correlated to an increase of the clearance. Nonetheless, the clearance remains above 6 dB which should be sufficient to resolve the squeezing we need to measure when the states are close to be thermalized.

Finally, we measure the BLP witnesses using the formula based on the Bures distance. The results are gathered in the tables 6.1. We notice the witness calculated using the Bures distance gives higher results. Nonetheless, the expected trends is observed in both cases: the lower values are obtained for the frequencies where no back flow of information were observed in 6.7 and 6.11. On the other hand, the maximum values are reached for the frequencies where an oscillation was exhibited.

	BLP from fidelity		BLP from Bures distance	
frequency	linear network	WS network	linear network	WS network
0.4		0.92		3.11
0.58	1.15		2.49	
0.7	0.65		1.13	
0.75		1.41		3.57
0.9		0.74		1.24

Table 6.1 – BLP witnesses calculated from the Bures distance and the fidelity for both simulated networks and for the different frequencies.

6.6 Summary

In this final chapter, we have investigated the appearance or not of quantum non Markovianity for two environments, the network 3 and 4. First, a definition of this behavior is given. Here we assume that a total system is quantum non Markovian when the dynamic exhibits a back-flow of energy into the probe mode. In opposition of the measurement of $J(\omega)$, we look the dynamic of the probe as a function of the interaction time and we use a witness of non Markovianity based on the fidelity of two states of the probe. We found that for both environments considered, non Markovian behavior appeared for different frequency. The choice of the probe frequency is very important since, if it is to far from the region where the J function exhibits peak, we wont see any energy exchange between the two subsystems.

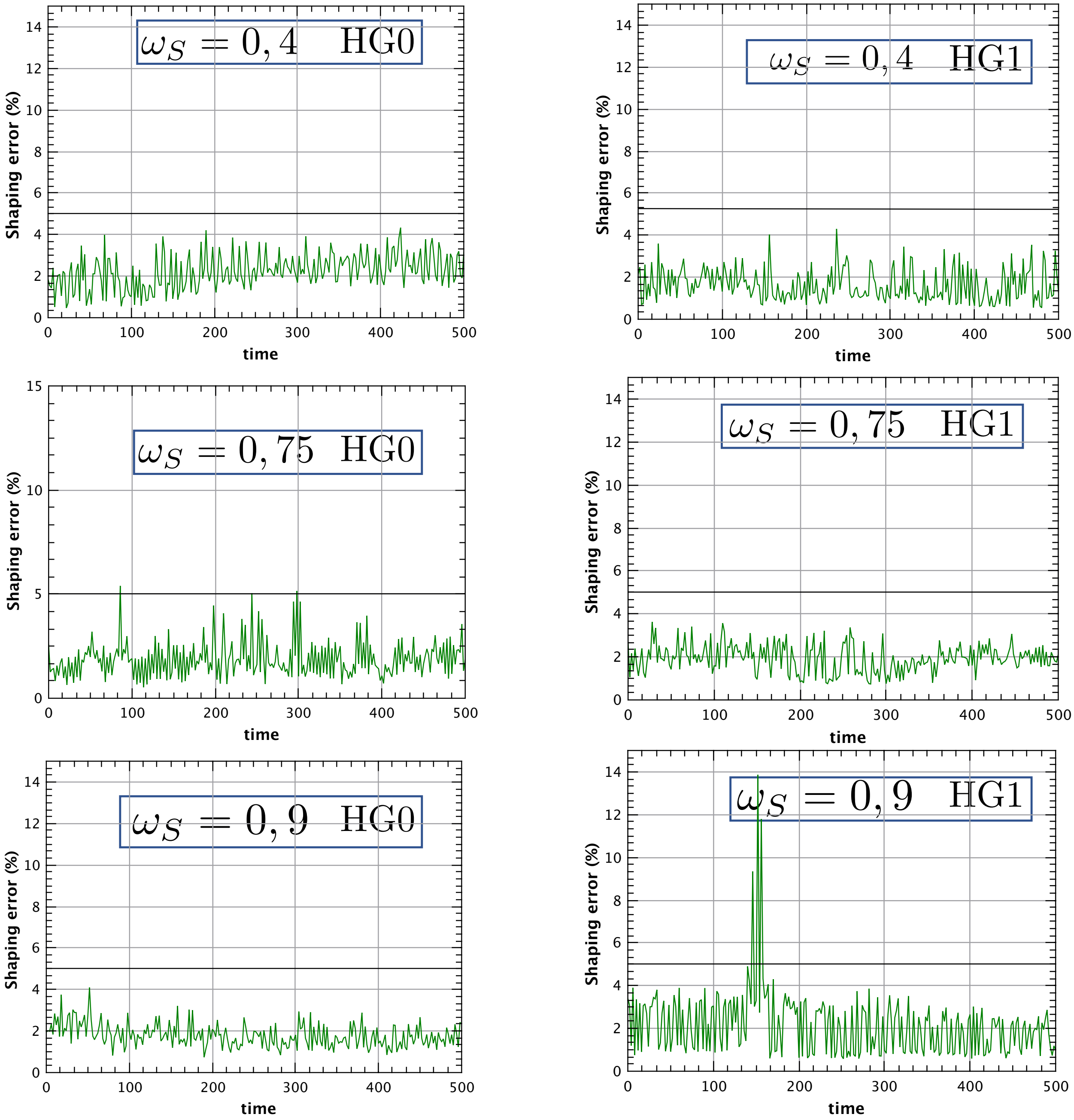

Figure 6.12 – Spectrum error against time in the case of the random network for the different ω_s and the Hermite-Gaussian modes (HG).

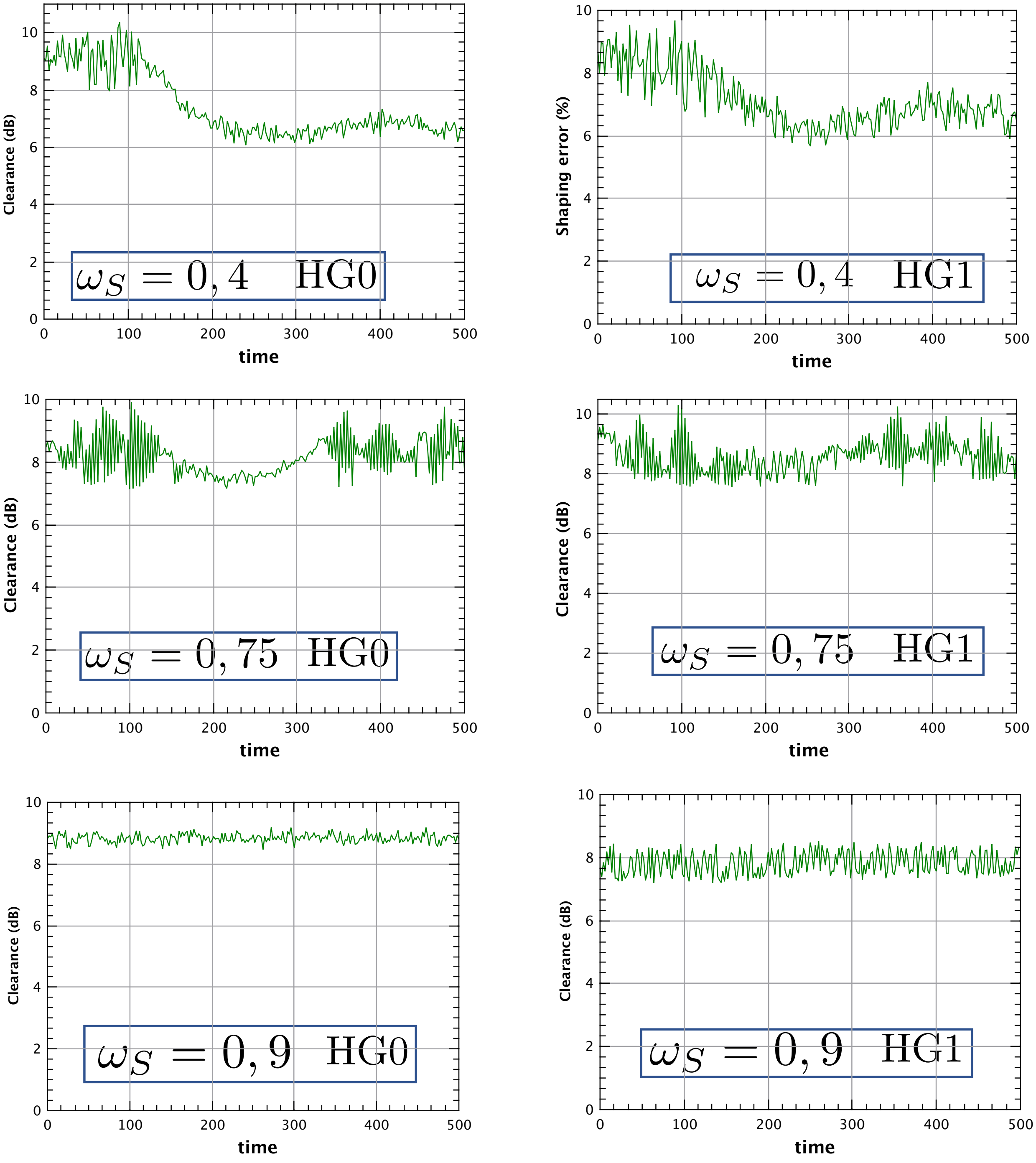

Figure 6.13 – Clearance against time in the case of the random network for the different ω_s and the Hermite-Gaussian modes (HG).

Conclusion and outlook

In the course of this thesis, we investigated the characterization of energy exchanges between an open quantum system and its environment via graph states simulations. This work contains two significant advances. We first recovered the spectral density function for a given environment. Secondly, we highlighted non Markovian behaviour for some of the simulated networks.

In order to carry out the simulations of large cluster states, some improvements have been achieved in the SPOPO experiment. First, on the generation of the multimode squeezed states. A method for tayloring the output states of the SPOPO cavity consits in using a pulse shaper on the pump path. Although the relations between the pump spectral shape and these states are not trivial, we can monitor them using machine learning algorithms. This work follows the results of F. Arzani on the optimization of the pump spectral shape using genomic algorithms. On the work conducted by T. Michel, we showed that artificial neural network and projective simulation methods give similar results and the diagonalization of the covariance matrix highlights the expected effects on the eigenvalues. The limitation on this experimental optimization remains in the resolution of the pulse shaper. We only used 8 frequency bands to shape the pump spectrum. Increasing the complexity of the pulse shaper would enable to check if the machine learning optimization give the same results than the one obtained from genomic algorithms.

On the detection part, we implemented a Photonic Crystal Fiber (PCF) in order to widen the LO spectrum and measure squeezing on a larger number of supermodes. The PCF made by N. Joly and its team in Erlangen has found its full use while making the spectrum flatter which improved the covariance matrix characterization.

To simulate quantum open system coupled to an environment we restricted ourself to network of small size composed by $N \leq 50$ nodes and we implemented graph structures inspired by complex network model. We tried two ways of recovering the spectral density function J associated to a given environment. The first one is done implementing the supermodes obtained form the diagonalization of the $\langle \Delta^2 Q \rangle$ and $\langle \Delta^2 P \rangle$

matrices in chapter 4 as normal modes of the full networks. The second one is done by using the theoretical supermodes with a fixed spectral bandwidth as normal modes. The best results are given by the second method in spite of the presence of fluctuations in the measured J function.
Quantum non Markovianity, which witnesses energy back-flow into the open quantum system has also been measured. First with a regular network and then on an random network based on Watts Strogatz structure. We showed that the total system exhibits quantum non Markovianity when the probe frequency is suitably chosen.

These different measurements proved that the SPOPO experiment is an adequate platform to simulate the dynamics of an open quantum system. One way of improving these measurements would be to reduce the acquisition time while increasing the number of acquisitions to be averaged. To do so, a solution is to lock the mirror used to scan the LO phase in order to measure the noise variance only on the q and p quadrature.
In this project, we didn't use the pump optimization for the network simulation. It would be interesting to increase the squeezing on the first mode and try to recover the J function and compare with the measurements we have done without any optimization. Beside the experimental improvements, it would be interesting to study further some points of this project like the SPOPO limitations problems and answer to the question what is the maximum network size the experiment can map. Is it the same limited size for random and regular network? Another experimental aspect, which would be interesting to bring, is the the non gaussianity via photon subtraction [Walschaers 21b]. Some properties of non gaussian states in network of small and large size have already been studied theoretically.

Appendices

Appendix A

Hermite Gaussian modes

In this thesis, I often refer to Hermite gaussian modes. I define below orthogonal basis of function below.

A.1 Hermite polynomials

The Hermite polynomials, denoted H_n are defined as follows:

$$H_n(x) = (-1)^n \mathrm{e}^{x^2} \frac{\mathrm{d}^n}{\mathrm{d}x^n} \mathrm{e}^{-x^2} \tag{A.1}$$

where n is a positive integer. We can also express them under polynomial form:

$$H_n(x) = \sum_{k=0}^{\lfloor n/2 \rfloor} (-1)^k \frac{n!}{k!(n-2k)!} (2x)^{n-2k} \tag{A.2}$$

They compose an orthogonal basis such as:

$$\int_{-\infty}^{+\infty} H_n(x) H_m(x) \mathrm{e}^{-x^2/2} \mathrm{d}x = n! \sqrt{2\pi} \delta_{n,m} \tag{A.3}$$

A.2 Hermite Gaussian functions

The Hermite gaussian function we use to fit the supermodes in the thesis are defined from the Hermite polynomials:

$$\psi_n(x) = \frac{1}{\sqrt{2^n n! \sqrt{\pi}}} H_n(x) \mathrm{e}^{-x^2/2} \tag{A.4}$$

Some of these modes are plotted in A.2.

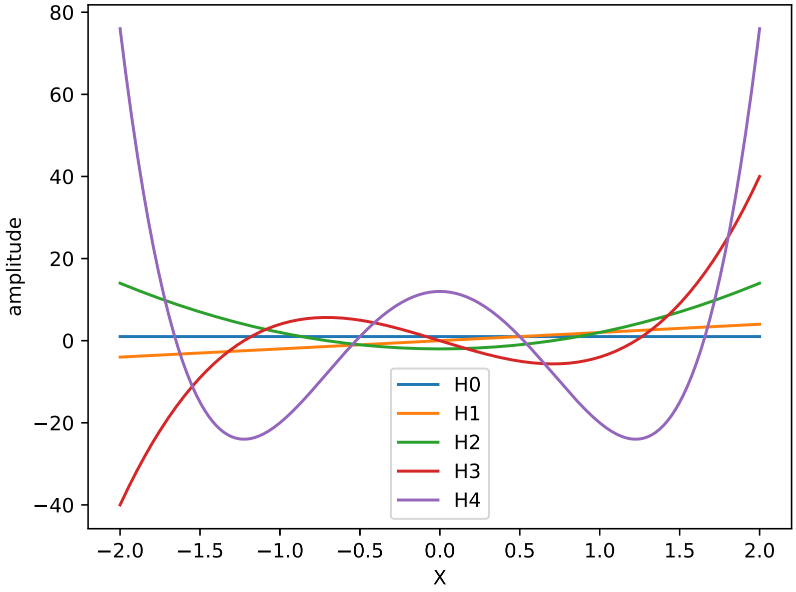

Figure A.1 – Plot of the 5 first Hermite polynomials

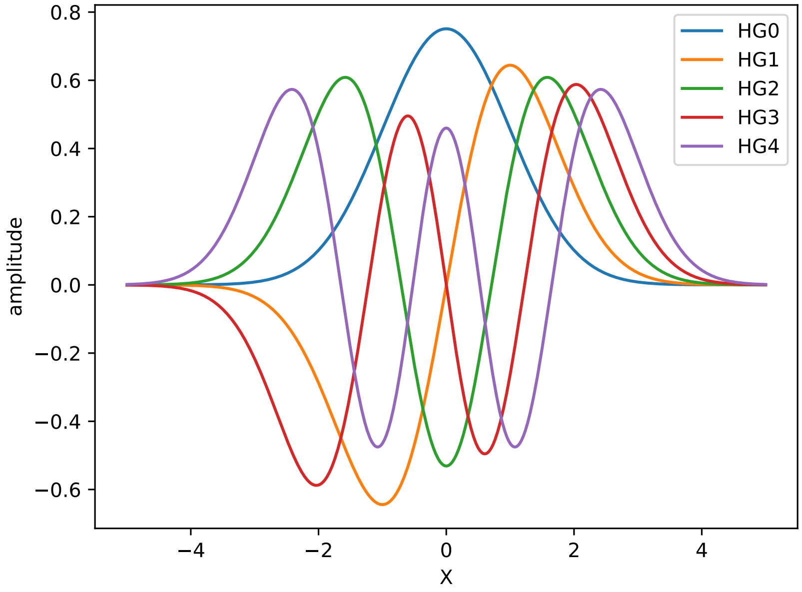

Figure A.2 – Plot of the five first Hermite Gaussian functions

Appendix B

Diffraction of the SLM mask

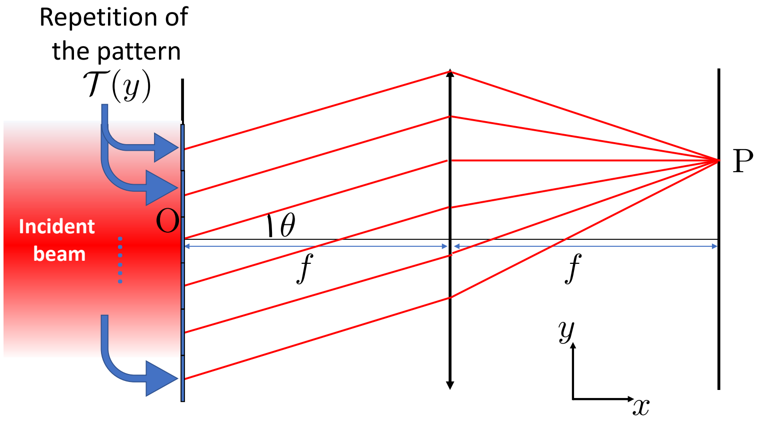

Figure B.1 – Scheme of the diffraction produced by repetition of a transmission pattern

Here we derive the diffraction formula presented in chapter 3. We consider the case of a beam with a normal incidence on a grating composed by several patterns of transmission $\mathcal{T}(y)$ as represented in the figure above. The variable k_y is the component on the y axis of the wave vector $\boldsymbol{k}$. It is known that for a grating of N individual secondary sources, spaced by a length L, the electric field can be expressed in far field by the relation:

$$E(k_y) = KE(O)e^{-iN\phi}\frac{\sin(N\phi/2)}{N\sin(\phi/2)} \tag{B.1}$$

where $E(O)$ is the field in point O and $\phi = \frac{2\pi L\sin(\theta)}{\lambda} = k_y L$. Now, by analogy to these this, the case field in far field as represented on figure B.1 can be expressed as:

$$E(k_y) = KE(O)e^{-iN\phi}\frac{\sin(N\phi/2)}{N\sin(\phi/2)}.\int_{-L/2}^{L/2}\mathcal{T}(y)e^{-ik_y y}\frac{\mathrm{d}y}{\sqrt{2}\pi} \tag{B.2}$$

Let us inject in $\mathcal{T}$ a ramp function on the phase such as:

$$\mathcal{T}(y) = \begin{cases} e^{-i\frac{2\pi}{L}y} & \text{if } y \in [-L/2, L/2] \\ 0 & \text{otherwise} \end{cases} \tag{B.3}$$

We inject this function in (B.2) and we get:

$$E_{ramp}(k_y) = KE(O)e^{-iN\phi}\frac{\sin(N\phi/2)}{N\sin(\phi/2)}.\int_{-L/2}^{L/2}e^{-i(\frac{2\pi}{L}+k_y)y}\frac{\mathrm{d}y}{\sqrt{2}\pi} \tag{B.4}$$

We can easily integrate the exponential between the two terminals and we find

$$E_{ramp}(k_y) = KE(O)e^{-iNk_yL}\frac{\sin(Nk_yL/2)}{N\sin(\phi/2)}.\frac{L}{2}\operatorname{sinc}(\frac{k_yL}{2}+\pi) \tag{B.5}$$

Now, let's consider the case where the ramp is discretize. The ramp is then more comparable to a staircase composed by M steps such as:

$$\mathcal{T}(y) = \begin{cases} e^{-i\psi_l(y)} & \text{if } l \in [\![-M, M]\!] \\ 0 & \text{otherwise} \end{cases} \tag{B.6}$$

with :

$$\psi_l(y) = \pi l/M \quad \text{if } \; l.d < y < (l+1).d \tag{B.7}$$

is the discretize ramp function. We inject this new function in (B.2) and we find:

$$E_{step}(k_y) = KE(O)e^{-iNk_yL}\frac{\sin(Nk_yL/2)}{N\sin(\phi/2)}.\frac{d}{2}\operatorname{sinc}(k_yd/2)\sum_{l=-M}^{M}e^{i(k_yd+\pi/M)l} \tag{B.8}$$

where d is the width of one step.

Appendix C

Extra squeezing measurements

In chapter 4 of the thesis is shown several measurements for the characterization of the SPOPO cavity, especially the supermode shapes and the squeezing of the first mode as a function of the pump power. On the figures below, we show the same squeezing measurement but for the supermodes 1 and 2.

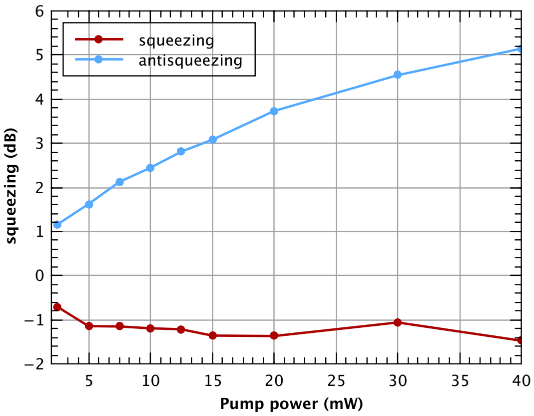

Figure C.1 – Squeezing as a function of the pump power for the supermode 1

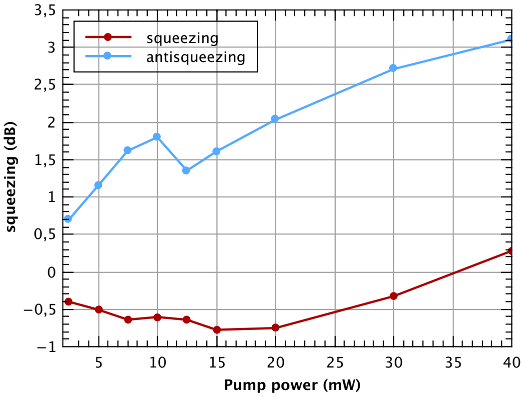

Figure C.2 – Squeezing as a function of the pump power for the supermode 2

Appendix D

Corrected spectral densities

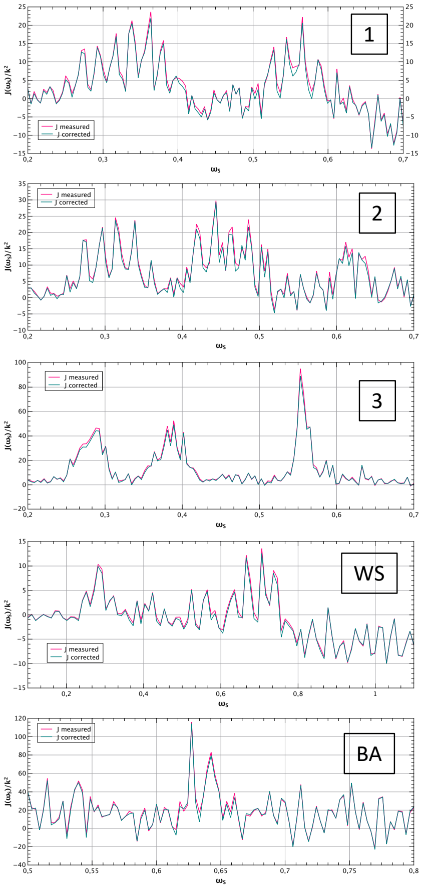

Figure D.1 – Measurement of the spectral densities for the different environment and the corrected function as a function of ω_s, when the normal modes are composed by the SPOPO supermodes.

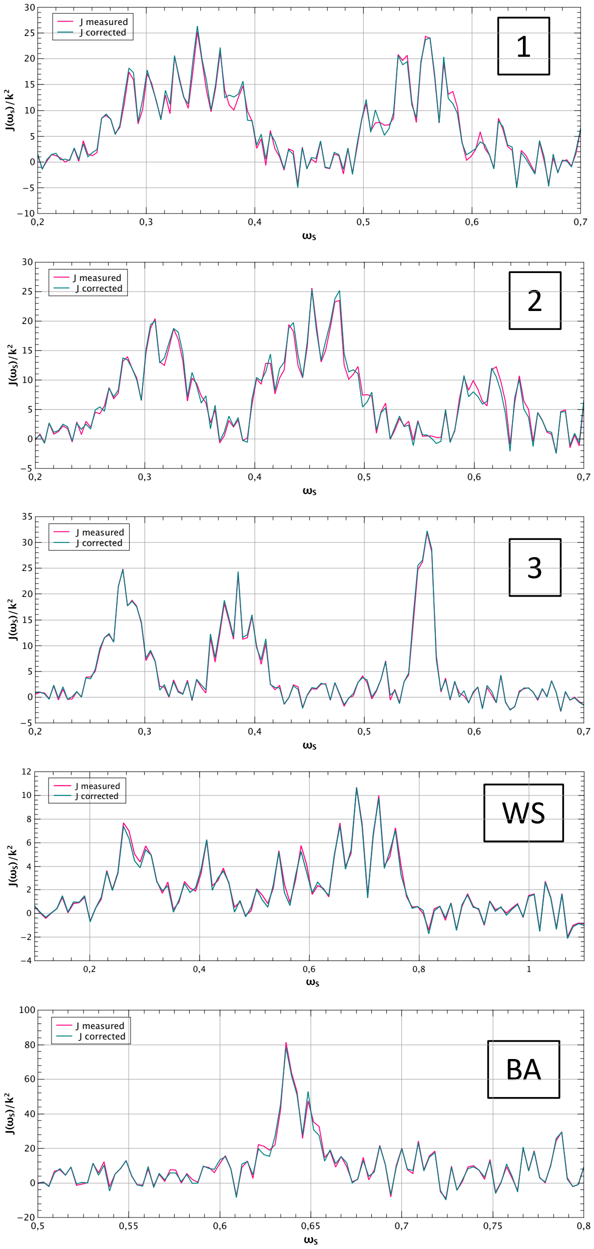

Figure D.2 – Measurement of the spectral densities for the different environment and the corrected function as a function of ω_s, when the normal mode of the total system have a fixed spectral bandwidth ($FHWM = 6.5nm$).

Bibliography

[Abbas 83] G. L. Abbas, V. W. S. Chan & T. K. Yee. *Local-oscillator excess-noise suppression for homodyne and heterodyne detection.* Optics letters, vol. 8, 1983, (Cited on page 56.)

[Akturk 05] S. Akturk, X. Gu, P. Gabolde & R. Trebino. *The general theory of first-order spatio-temporal distortions of Gaussian pulses and beams.* Optics Express, vol. 13, no. 21, 2005, (Cited on page 37.)

[AL. Barabási 04] Z. N Oltvai AL. Barabási. *Network biology: understanding the cell's functional organization.* Nature Reviews Genetics, vol. 5, 2004, (Cited on pages 111 and 112.)

[Albert 99] R. Albert, H. Jeong & AL Barabási. *Diameter of the World-Wide Web.* Nature, vol. 401, 1999, (Cited on pages 111 and 113.)

[Albert 02] R. Albert & AL. Barabási. *Statistical mechanics of complex networks.* Rev. Mod. Phys., vol. 74, no. 47, 2002, (Cited on page 112.)

[Alexanderson] G. Alexanderson. *Euler and Königsberg's bridges: a historical view.* Bulletin of the American Mathematical Society., vol. 43, (Cited on page 111.)

[Anderson 58] P. W. Anderson. *Absence of diffusion in certain random lattices.* Phys. Rev., vol. 109, 1958, (Cited on page 1.)

[Appel 07] J. Appel, D. Hoffman, E. Figueroa & A.I. Lvovsky. *Electronic noise in optical homodyne tomography.* Phys. Rev. A, vol. 75, no. 035802, 2007, (Cited on page 60.)

[Araujo 10] R. C. Medeiros De Araujo. *Génération et manipulation de peignes de fréquences quantiques multimodes.* PhD thesis, Université Pierre et Marie Curie, 2010. (Cited on page 48.)

[Argyres 64] P. N. Argyres & P. L. Kelley. *Theory of spin resonance and relaxation.* Phys. Rev., vol. 134, no. A98-A111, 1964, (Cited on page 140.)

[Arzani 18] F. Arzani. *Measurement Based Quantum Information with Optical Frequency Combs.* PhD thesis, Sorbonne Université, 2018. (Cited on pages 94, 96, and 97.)

[Aspect 82] A. Aspect, J. Dalibard & G. Roger. *Experimental test of Bell's inequalities using time-varying analyzers.* Phys. Rev. Lett., vol. 49, no. 1804, 1982, (Cited on pages 1 and 26.)

[Barabási 99] AL. Barabási & R. Albert. *Emergence of scaling in random networks.* Science, vol. 286, no. 5439, 1999, (Cited on pages 111, 112, and 113.)

[Barabási 16] AL. Barabási. Network science. Cambridge University Press, 2016. ISBN: 978-1-1070-7626-6. (Cited on page 110.)

[Bardeen 57] J. Bardeen, L. N. Cooper & J. R. Schrieffer. *Theory of Superconductivity.* Phys. Rev., vol. 108, no. 1175, 1957, (Cited on page 1.)

[Barreiro 02] J. T. Barreiro, P. Schindler, O. Gühne, T. Monz, M. Chwalla, C. F. Roos, M. Hennrich & R. Blatt. *Experimental multiparticle entanglement dynamics induced by decoherence.* Nature Phys., vol. 6, no. 943, 2002, (Cited on pages 3 and 109.)

[Bartlett 02] S. D. Bartlett, B. C. Sanders, S. L. Braunstein & K. Nemoto. *Efficient Classical Simulation of Continuous Variable Quantum Information Processes.* Phys. Rev. Lett., vol. 88, no. 097904, 2002, (Cited on page 2.)

[Basharin 04] G. P. Basharin, A. N. Langville & V. A. Naumov. *The life and work of A.A. Markov.* Linear Algebra Appl, vol. 386, 2004, (Cited on page 138.)

[Biercuk 09] M. J. Biercuk, H. Uys, A. P. VanDevender, N. Shiga, W. M. Itano & J. J. Bollinger. *Optimized dynamical decoupling in a model quantum memory.* Nature, vol. 458, no. 996, 2009, (Cited on pages 3 and 109.)

[Blatt 12] R. Blatt & C. F. Roos. *Quantum simulation with trapped ions.* Nature physics, vol. 8, 2012, (Cited on page 2.)

[Bloch 62] C. Bloch & A. Messiah. *The canonical form of an antisymmetric tensor and its application to the theory of superconductivity.* Nuclear Physics, vol. 39, 1962, (Cited on page 23.)

[Bloch 12] I. Bloch, J. Dalibard & S. Nascimbène. *Quantum simulations with ultracold quantum gases.* Nature Physics, vol. 8, 2012, (Cited on page 2.)

[Bloembergen 82] N. Bloembergen. *Nonlinear optics and spectroscopy.* Rev. Mod. Phys., vol. 54, no. 685, 1982, (Cited on page 38.)

[Born 23] M. Born & W. Heisenberg. *Die Elektronenbahnen im angregten Heliumatom.* Z.Physik, vol. 16, 1923, (Cited on page 1.)

[Bourassa 21] J.E. Bourassa, N. Quesada, I. Tzitrin, A. Szàva, T. Isacsson, J. Izaac, K. Kumar Sabapathy, G. Dauphinais & I. Dhand. *Fast Simulation of Bosonic Qubits via Gaussian Functions in Phase Space.* PRX Quantum, vol. 2, no. 040315, 2021, (Cited on page 2.)

[Boyd 07] R. W. Boyd. Nonlinear optics, third edition. Academic Press, 2007. ISBN: 978-0-12-369470-6. (Cited on page 38.)

[Brabec 92] T. Brabec, Ch. Spielmann, P. F. Curley & F. Krausz. *Kerr lens mode locking.* Optics Letter, vol. 17, no. 18, 1992, (Cited on page 34.)

[Braunstein 05] SL. Braunstein & P. Van Loock. *Quantum information with continuous variables.* Rev. Mod. Phys., vol. 77, no. 513, 2005, (Cited on page 2.)

[Breuer 09] HP. Breuer, EM. Laine & J. Piilo. *Measure for the degree of non-Markovian behavior of quantum processes in open systems.* Phys. Rev. Lett., vol. 103, no. 210401, 2009, (Cited on pages 140 and 142.)

[Breuer 16] HP. Breuer, EM. Laine, J. Piilo & B. Vacchini. *Colloquium: Non-Markovian dynamics in open quantum systems.* Rev. Mod. Phys., vol. 88, no. 021002, 2016, (Cited on page 140.)

[Bures 16] D. Bures. *An extension of Kakutani's theorem on infinite product measures to the tensor product of semifinite ω^*-algebras.* Trans. Amer. Math. Soc., vol. 135, 2016, (Cited on page 143.)

[Cai 17] Y. Cai, J. Roslund, G. Ferrini, F. Arzani, X. Xu, C. Fabre & N. Treps. *Multimode entanglement in reconfigurable graph states using optical frequency combs.* Nat. Commun., vol. 8, no. 15645, 2017, (Cited on pages 2, 29, and 80.)

[Carleo 19] G. Carleo, I. Cirac, K. Cranmer, L. Daudet, M. Schuld, N. Tishby, L. Vogt-Maranto & L. Zdeborová. *Machine learning and the physical sciences.* Review modern of physics, vol. 91, no. 4 045002, 2019, (Cited on page 94.)

[Chanteloup 98] J. C. Chanteloup. *Contrôle et mise en forme des fronts de phase et d'énergie d'impulsions brèves ultra-intenses.* PhD thesis, École Polytechnique, 1998. (Cited on page 36.)

[Chen 14] M. Chen, N. C. Menicucci & O. Pfister. *Experimental Realization of Multipartite Entanglement of 60 Modes of a Quantum Optical Frequency Comb.* Phys. Rev. Lett., vol. 112, no. 120505, 2014, (Cited on page 2.)

[.Childress 13] L .Childress & R. Hanson. *Diamond NV centers for quantum computing and quantum networks.* MRS Bulletin Cambridge University Press, 2013, (Cited on page 2.)

[Church 69] D. A. Church. *Storage-Ring Ion Trap Derived from the Linear Quadrupole-Radio Frequency Mass Filter.* Journal of Applied Physics, vol. 40, no. 3127, 1969, (Cited on page 2.)

[Dahr 15] H. S. Dahr, M. N. Bera & G. Adesso. *Characterizing non-Markovianity via quantum interferometric power.* Phys. Rev. A., vol. 91, no. 03215, 2015, (Cited on page 143.)

[de Broglie 24] L. de Broglie. *Recherches sur la théorie des quanta.* 1924, (Cited on page 1.)

[Devoret 13] M. H. Devoret & R. J. Schoelkopf. *Superconducting circuits for quantum information: an outlook.* Science, vol. 339, no. 6124, 2013, (Cited on page 2.)

[Dirac 25] P. A. M. Dirac. *The fundamental equations of quantum mechanics.* Proc.Roy.Soc., vol. A109, 1925, (Cited on page 1.)

[Drever 83] R. W. P. Drever, J. L. Hall, F. V. Kowalski, J. Hough, G. M. Ford, A. J. Munley & H. Ward. *Laser phase and frequency stabilization using an optical resonator.* Applied Physics B, vol. 31, 1983, (Cited on page 51.)

[Dudley 10] J. M. Dudley & J. R. Taylor. Supercontinuum generation in optical fibers. Cambridge University Press, 2010. ISBN: 9780511750465. (Cited on page 73.)

[Dufour 18] A. Dufour. *Ingénierie d'états quantiques multimodes avec des impulsions femtosecondes*. PhD thesis, Sorbonne Université, 2018. (Cited on page 90.)

[Einstein 35a] A. Einstein, B. Podolsky & N. Rosen. *Can Quantum-Mechanical Description of Physical Reality Be Considered Complete?* Physical review, 1935, (Cited on pages 1 and 26.)

[Einstein 35b] A. Einstein, B. Podolsky & N. Rosen. *On the Einstein Podolsky Rosen Paradox*. Physics, vol. 1, no. 3, 1935, (Cited on pages 1 and 26.)

[Erdös 59] P. Erdös & A. Rényi. *On random graphs, I*. Publicationes Mathematicae (Debrecen), vol. 5, 1959, (Cited on page 111.)

[Erdös 61a] P. Erdös & A. Rényi. *On the evolution of random graphs*. Publ. Math. Inst. Hung. Acad. Sci., vol. 38, no. 4, 1961, (Cited on page 111.)

[Erdös 61b] P. Erdös & A. Rényi. *On the Strength of Connectedness of a Random Graph*. Acta Math. Acad. Sci. Hungary., vol. 12, no. 1, 1961, (Cited on page 111.)

[Euler 41] L. Euler. *Solutio Problemat is ad Geometriam Situs Pertinentis*. Commentarii Academiae Scientiarum Imperialis Petropolitanae, vol. 8, 1741, (Cited on page 111.)

[Fabre 20] C. Fabre & N. Treps. *Modes and states in quantum optics*. Rev. Mod. Phys., vol. 92, no. 3, 2020, (Cited on page 8.)

[Ferraro 05] A. Ferraro, S. Olivares & M. G. A. Paris. *Gaussian states in continuous variable quantum information*. arXiv preprint quant-ph/0503237, 2005, (Cited on page 22.)

[Ferrini 13] G. Ferrini, J. P. Gazau, T. Coudreau, C. Fabre & N. Treps. *Compact Gaussian quantum computation by multi-pixel homodyne detection*. New J. Phys., vol. 15, no. 093015, 2013, (Cited on page 27.)

[Feynman 86] RP Feynman. *Quantum mechanical computers*. Foundations of physics., 1986, (Cited on page 2.)

[Feynman 96] RP Feynman, T Hey & RW Allen. Feynman lectures on computation. taylorfrancis.com, 1996. ISBN: 978-0738202969. (Cited on page 2.)

[Ford 65a] G. W. Ford, M. Kac & P. Mazur. *Statistical Mechanics of Assemblies of Coupled Oscillators.* J. Maths. Phys., vol. 6, no. 504, 1965, (Cited on page 110.)

[Ford 65b] G. W. Ford, M. Kac & P. Mazur. *Transport, Collective Motion, and Brownian Motion.* Prog. Theor. Phys., vol. 33, no. 423, 1965, (Cited on page 110.)

[Fork 84] R. L. Fork, O. E. Martinez & J.P. Gordon. *Negative dispersion using pairs of prisms.* Opt. Lett., vol. 9, no. 5, 1984, (Cited on page 36.)

[Furusawa 98] A. Furusawa, J. L. Sorensen andS. L. Braunstein andC. A. Fuchs andH. J. Kimble & E. S. Polzik. *Unconditional quantum teleportation.* Science, vol. 282, no. 5389, 1998, (Cited on page 2.)

[G. Pretzler 00] K.J Witte G. Pretzler A. Kasper. *Angular chirp and tilted light pulses in CPA lasers.* Applied Physics B, vol. 70, 2000, (Cited on page 37.)

[G. R. Grimmett 02] D. R. Stirzzaker G. R. Grimmett. Probability and random processes 3rd edition. Oxford University Press, 2002. ISBN: 978-0-19-884760-1. (Cited on page 138.)

[Gardiner 85] C. W. Gardiner & M. J. Collett. *Input and output in damped quantum systems: quantum stochastic differential equations and the master equation.* Phys. Rev. A, vol. 31, no. 3761, 1985, (Cited on page 140.)

[Gardiner 99] C. W. Gardiner & P. Zoller. Quantum noise: a handbook of markovian and non-markovian quantum stochastic methods with applications to quantum optics. Springer, 1999. ISBN: 978-3-642-06094-6. (Cited on pages 108 and 109.)

[Glauber 63] R. J. Glauber. *The quantum theory of optical coherence.* Physical Review, vol. 130, no. 6, 1963, (Cited on page 25.)

[Gorini 76] V. Gorini & A. Kossakowski. *Completely positive dynamical semigroups of N level systems.* J. Math. Phys, vol. 17, no. 821, 1976, (Cited on page 109.)

[Gottesman 01] D. Gottesman, A. Kitaev & J. Preskill. *Encoding a qubit in an oscillator.* Phys. Rev. A, vol. 64, no. 012310, 2001, (Cited on pages 2 and 22.)

[Grynberg 10] G. Grynberg, A. Aspect & C. Fabre. Introduction to quantum optics: From the semi-classical approach to quantized light. Cambridge University Press, 2010. ISBN: 978-0-5215-5112-0. (Cited on pages 8 and 20.)

[Guarnieri 16] G. Guarnieri, J. Nokkala, R. Schmidt, S. Maniscalco & B. Vacchini. *Energy backflow in strongly coupled non-Markovian continuous-variable systems*. Phys. Rev. A., vol. 94, no. 062101, 2016, (Cited on page 143.)

[Hall 06] J. L. Hall. *Nobel Lecture: Defining and measuring optical frequencies*. Rev. Mod. Phys., vol. 78, no. 1279, 2006, (Cited on page 34.)

[Hall 14] M. J. W. Hall, J. D. Cresser & E. Andersson L. Li. *Canonical form of master equations and characterization of non-Markovianity*. Phys. Rev. A, vol. 89, no. 42120, 2014, (Cited on pages 140 and 143.)

[Hammer 16] J. Hammer. *Spectral Wavelet Interferometry via Dispersive Fourier Transformation*. Master Thesis Friedrich-Alexander-Universität Erlangern-Nürnberg, 2016, (Cited on page 73.)

[Hänsch 06] T. W. Hänsch. *Nobel Lecture: Passion for precision*. Rev. Mod. Phys., vol. 78, no. 1297, 2006, (Cited on page 34.)

[He 17] Z. He, H.-S. Zeng, Y. Li, Q. Wang, & C. Yao. *Non-Markovianity measure based on the relative entropy of coherence in an extended space*. Phys. Rev. A., vol. 96, no. 022106, 2017, (Cited on page 143.)

[Heisenberg 25] W. Heisenberg. *Über quantentheoretische Umdeutung kinematischer und mechanischer Beziehungen*. Z.Physik, vol. 33, 1925, (Cited on page 1.)

[Horstmeyer 15] R. Horstmeyer, H. Ruan & C. Yang. *Guidestar-assisted wavefront-shaping methods for focusing light into biological tissue*. Nature Photonics., vol. 9, 2015, (Cited on page 1.)

[Hudson 84] R. L. Hudson & K. R. Parthasarathy. *Quantum Ito's formula and stochastic evolutions*. Comm. Math. Phys, vol. 93, 1984, (Cited on page 140.)

[Ikramov 18] K. D. Ikramov. *On the Symplectic Eigenvalues of Positive Definite Matrices*. Moscow University Computational Mathematics and Cybernetics, vol. 42, 2018, (Cited on page 85.)

[Jacquard 17] C. Jacquard. *A single-photon subtractor for spectrally multimode quantum states.* PhD thesis, Université Pierre et Marie Curie, 2017. (Cited on pages 49, 50, and 130.)

[John 84] S. John. *Electromagnetic absorption in a disordered medium near a photon mobility edge.* Phys. Rev. Lett., vol. 53, no. 2169, 1984, (Cited on page 1.)

[Joly 12] N. Joly. *Contribution à l'élaboration de sources spectralement étendues par propagation d'impulsions dans les fibres microstructurées.* Habilitation à diriger des recherches (HDR). Ecole normale supérieure de Cachan, 2012, (Cited on page 73.)

[Jozsa 94] R. Jozsa. *Fidelity for Mixed Quantum States.* J. Mode. Opt., vol. 41, 1994, (Cited on page 145.)

[Kerr 75] J. Kerr. *A new relation between electricity and light: Dielectrified media birefringent.* The London, Edinburgh, and Dublin Philosophical Magazine and Journal of Science, vol. 50, 1875, (Cited on page 34.)

[Knill 10] E. Knill. *Quantum computing.* Nature, vol. 463, 2010, (Cited on page 2.)

[Kouadou 21] T. Kouadou. *Single-Pass Generation and Detection of Ultrafast Multimode Squeezed Light.* PhD thesis, Sorbonne University, 2021. (Cited on page 62.)

[Krausz 09] F. Krausz & M. Ivanov. *Attosecond physics.* Rev. Mod. Phys., vol. 81, no. 163, 2009, (Cited on page 34.)

[Kumar 12] R. Kumar, E. Barrios, A. MacRae, E. Cairns, E.H. Huntington & A.I. Lvovsky. *Versatile wideband balanced detector for quantum optical homodyne tomography.* Optics Communications., vol. 285, no. 24, 2012, (Cited on page 60.)

[Laine 10] EM. Laine, J. Piilo & HP. Breuer. *Measure for the non-Markovianity of quantum processes.* Phys. Rev. A., vol. 6, no. 062115, 2010, (Cited on page 142.)

[Lax 64] M. Lax. *Formal theory of quantum fluctuations from a driven state.* Phys. Rev., vol. 129, no. 2342, 1964, (Cited on page 140.)

[Lecun 89] Y. Lecun, B. Boser, J. S. Denker, D. Henderson, R. E. Howard, W. Hubbard & L.D. Jackel. *Backpropagation applied to handwritten zip code recognition.* Neural computation, vol. 1, no. 4, 1989, (Cited on page 94.)

[Lecun 15] Y. Lecun, Y. Bengio & G. Hinto. *Deep learning.* Nature, vol. 521, no. 7553, 2015, (Cited on page 94.)

[Leibfried 03] D. Leibfried, R. Blatt, C. Monroe & D. Wineland. *Quantum dynamics of single trapped ions.* Rev. Mod. Phys, vol. 75, no. 281, 2003, (Cited on page 2.)

[Leonhardt 97] U. Leonhardt. Measuring the quantum state of light. Cambridge Studies in Modern Optics, 1997. ISBN: 978-0-5214-9730-5. (Cited on page 59.)

[Li 18] L. Li, M. J. W. Hall & H. M. Wiseman. *Concepts of quantum non-Markovianity: a hierarchy.* Physcis Reports, vol. 759, 2018, (Cited on page 140.)

[Linblad 76] G. Linblad. *On the generators of quantum dynamical semigroups.* Communication in Mathematical Physics, vol. 48, no. 2, 1976, (Cited on page 109.)

[Lipfert 18] T. Lipfert, D. Horoshko, G. Patera & M. Kolobov. *Bloch-Messiah decomposition and Magnus expansion for parametric down-conversion with monochromatic pump.* Phys. Rev. A, vol. 98, no. 013815, 2018, (Cited on page 46.)

[Liu 11] BH. Liu, L. Li, YF. Huang, CH. Li, GC. Guo, EM. Laine, HP. Breuer & J. Piilo. *Experimental control of the transition from Markovian to non-Markovian dynamics of open quantum systems.* Nature Phys, vol. 7, 2011, (Cited on pages 143 and 145.)

[Lu 10] X.-M. Lu, X. Wang & C. P. Sun. *Quantum fisher information flow and non-Markovian processes of open systems.* Phys. Rev. A., vol. 82, no. 042103, 2010, (Cited on page 143.)

[Luo 12] S. Luo, S. Fu & H. Song. *Quantifying non-Markovianity via correlations.* Phys. Rev. A., vol. 86, no. 044101, 2012, (Cited on page 143.)

[Lvovsky 09] A. I. Lvovsky & M. G. Raymer. *Continuous-variable optical quantum-state tomography.* Rev. Mod. Phys., vol. 81, no. 299, 2009, (Cited on page 2.)

[Lyot 33] B. Lyot. *Optical apparatus with wide field using interference of polarized light.* Acad. Sci. Paris, vol. 197, no. 1593, 1933, (Cited on page 35.)

[M. Danailov 89] I. Christov M. Danailov. *Time-space Shaping of Light Pulses by Fourier Optical Processing.* Journal of Modern Optics, vol. 36, 1989, (Cited on page 64.)

[Ma 90] X. Ma & W. Rhodes. *Multimode squeeze operators and squeezed states.* Physical Review A, vol. 41, 1990, (Cited on pages 2 and 25.)

[Maiman 60] T. H. Maiman. *Stimulated Optical Radiation in Ruby.* Nature, vol. 187, 1960, (Cited on page 1.)

[Mari 12] A. Mari & J. Eisert. *Positive Wigner Functions Render Classical Simulation of Quantum Computation Efficient.* Phys. Rev. Lett., vol. 109, no. 230503, 2012, (Cited on page 2.)

[Marinelli 20] J. Duris ... A. Marinelli. *Tunable isolated attosecond X-ray pulses with gigawatt peak power from a free-electron laser.* Nature Photonics, vol. 14, 2020, (Cited on page 34.)

[Martin-Lopez 12] E. Martin-Lopez, A. Laing, T. Lawson, R. Alvarez, X-Q. Zhou & J. L. O'Brien. *Experimental realization of Shor's quantum factoring algorithm using qubit recycling.* Nature Photonics., vol. 6, 2012, (Cited on page 2.)

[Mascherpa 20] F. Mascherpa, A. Smirne, A. D. Somoza, P. Fernández-Acebal, S. Donadi, D. Tamascelli, S. F. Huelga & M.B. Plenio. *Optimized auxiliary oscillators for the simulation of general open quantum systems.* Phys. Rev. A, vol. 101, no. 052108, 2020, (Cited on page 117.)

[Maxwell 65] J. C. Maxwell. *VIII. A dynamical theory of the electromagnetic field.* Philosophical transations of the Royal Society of London, pages pp459–512, 1865, (Cited on pages 1 and 8.)

[Maxwell 96] J. C. Maxwell. A dynamical theory of the electromagnetic field. Wipf and StockPublishers, 1996. ISBN: 978-1-57910-015-5. (Cited on page 1.)

[Melnikov 17] A. A. Melnikov, A. Makmal, V. Dunjko & H. J. Briegel. *Projective simulation with generalization.* Scientific Repots, vol. 7, 2017, (Cited on page 97.)

[Melnikov 18] A. A. Melnikov, H. P. Nautrup, M. Krenn, V. Dunjko, M. Tiersch, A. Zeilinger & H. J. Briegel. *Active learning machine learns to create new quantum experiments.* Proceedings of the National Academy of Sciences, vol. 115, 2018, (Cited on page 97.)

[Menicucci 06] N. C. Menicucci, P. Van Loock, M. Gu, C. Weedbrook, T. C. Ralph & M. A. Nielsen. *Universal Quantum Computation with Continuous-Variable Cluster States.* Phys. Rev. Lett., vol. 97, no. 110501, 2006, (Cited on page 2.)

[Michel 21] T. Michel. *Optimization of the pump spectral shape in a parametric down conversion process to generate multimode entangled states.* PhD thesis, Sorbonne University ANU, 2021. (Cited on pages 67, 72, 90, 91, 92, 94, 97, 100, and 101.)

[Michelson] A-A. Michelson. (Cited on page 1.)

[Michelson 94] A-A. Michelson. *On the application of interference methods to astronomical measurements.* National Academy of Sciences., vol. 5, 1894, (Cited on page 1.)

[Milgram 67] S. Milgram. *The Small World Problem.* Psychology Today., vol. 2, 1967, (Cited on page 114.)

[Monmayrant 05] A. Monmayrant. *Façonnage et caractérisation d'impulsions ultracourtes. Contrôle cohérent de systèmes simples.* PhD thesis, UniversitṔaul Sabatier, Toulouse III, 2005. (Cited on pages 64, 65, and 71.)

[Monmayrant 10] A. Monmayrant, S. Weber & B. Chatel. *A newcomers guide to ultrashort pulse shaping and characterization.* Journal of Physics B: Atomic, Molecular and Optical Physics, vol. 43, no. 103001, 2010, (Cited on page 64.)

[Nokkala 16] J. Nokkala, F. Galve, R. Zambrini, S. Maniscalco & J. Piilo. *Complex quantum networks as structured environments: engineering and probing.* Scientific report, vol. 6, no. 26861, 2016, (Cited on page 118.)

[Nokkala 18a] J. Nokkala. *Quantum complex network.* PhD thesis, University of Turku, 2018. (Cited on pages 3 and 110.)

[Nokkala 18b] J. Nokkala, F. Arzani, F. Galve, R. Zambrini, S. Maniscalco, J. Piilo, N. Treps & V. Parigi. *Reconfigurable optical implementation* *of quantum complex networks.* NJP, vol. 20, no. 053024, 2018, (Cited on pages 3 and 119.)

[O'Brien 07] J. L. O'Brien. *Optical quantum computing.* Science, vol. 318, no. 5856, 2007, (Cited on page 2.)

[Osvay 04] K. Osvay, A.P. Kovacs, Z. Heiner, G. Kurdi, J. Klebniczki & M. Csatari. *Angular dispersion and temporal change of femtosecond pulses from misaligned pulse compressors.* IEEE Journal of Selected Topics in Quantum Electronics, vol. 10, no. 1, 2004, (Cited on page 37.)

[Ourjoumtsev 06] A. Ourjoumtsev, R. Tualle-Brouri, J. Laurat & P. Grangier. *Generating optical Schrödinger kittens for quantum information processing.* Science, vol. 312, no. 5770, 2006, (Cited on pages 2 and 22.)

[Ourjoumtsev 07] A. Ourjoumtsev, H. Jeong, R. Tualle-Brouri & P. Grangier. *Generation of optical Schrödinger cats from photon number states.* Nature, vol. 448, no. 7155, 2007, (Cited on page 2.)

[Patera 09] G. Patera. *Quantum properties of ultra-short pulses generated by SPOPOs: multi-mode squeezing and entanglement.* PhD thesis, Université Pierre et Marie Curie, 2009. (Cited on page 3.)

[Paul 90] W. Paul. *Electromagnetic traps for charged and neutral particles.* Rev. Mod. Phys, vol. 62, no. 531, 1990, (Cited on page 2.)

[Pinel 10] O. Pinel. *Optique quantique multimode avec des peignes de fréquence.* PhD thesis, Université Pierre et Marie Curie, 2010. (Cited on page 36.)

[P.Kok 07] P.Kok, W. J. Munro, K. Nemoto, T.C. Ralph, J. P. Dowling & G. J. Milburn. *Linear optical quantum computing with photonic qubits.* Rev. Mod. Phys., vol. 79, no. 135, 2007, (Cited on page 2.)

[Politi 09] A. Politi, J.C.F. Matthews & J. L. O'Brien. *Shor's quantum factoring algorithm on a photonic chip.* Science., vol. 325, no. 1221, 2009, (Cited on page 2.)

[Popoff 10] S. Popoff, G. Lerosey, R. Carminati, M. Fink, A. C Boccara & S. Gigan. *Measuring the transmission matrix in optics: an approach to the study and control of light propagation in disordered media.* Phys. Rev. Lett., vol. 104, no. 100601, 2010, (Cited on page 1.)

[Ra 20] Y.-S. Ra, A. Dufour, M. Walschaers, C. Jacquart, T. Michel, C. Fabre & N. Treps. *Non-Gaussian quantum states of a multimode light field.* Nat. Phys., vol. 16, pages 144–147, 2020, (Cited on pages 2 and 22.)

[Raussendorf 01a] R. Raussendorf & H. J. Briegel. *A One-Way Quantum Computer.* Phys. Rev. Lett., vol. 86, no. 5188, 2001, (Cited on page 2.)

[Raussendorf 01b] R. Raussendorf & H. J. Briegel. *A One-Way Quantum Computer.* Phys. Rev. Lett., vol. 86, no. 5188, 2001, (Cited on page 2.)

[Reynaud 97] S. Reynaud, E. Giacobino & J. Zinn-Justin. *Fluctuations Quantiques/Quantum Fluctuations: Les Houches Session LXIII, June 27-July 28, 1995. course 4 by C. Fabre.* Fluctuations Quantiques/Quantum Fluctuations, 1997, (Cited on page 57.)

[Rivas 10] Á. Rivas, S. Huelga & M. B Plenio. *Entanglement and non-Markovianity of quantum evolutions.* Phys. Rev. Lett., vol. 105, no. 050403, 2010, (Cited on pages 142 and 143.)

[Rivas 14] À. Rivas, S. F. Huelga & M. B. Plenio. *Quantum non-Markovianity: characterization, quantification and detection.* Rep. Prog. Phys., vol. 77, no. 094001, 2014, (Cited on pages 138 and 139.)

[Roslund 14] J. Roslund, R. Medeiros de Araùjo, S. Jiang, C. Fabre & N. Treps. *Wavelength-multiplexed quantum networks with ultrafast frequency combs.* Nature Photonics, vol. 8, 2014, (Cited on page 3.)

[Ruskai 94] M. B. Ruskai. *Beyond strong subadditivity? Improved bounds on the contraction of generalized relative entropy.* Reviews in Mathematical Physics, vol. 6, no. 05a, 1994, (Cited on page 141.)

[Segev 13] M. Segev, Y. Silberberg & D. N. Christodoulides. *Anderson localization of light.* Nature Photonics, vol. 7, 2013, (Cited on page 1.)

[Senitzky 60] J. R. Senitzky. *Dissipation in Quantum Mechanics. The Harmonic Oscillator.* Phys. Rev., vol. 119, no. 770, 1960, (Cited on page 110.)

[Shor 94] P. W. Shor. *Proceedings of the 35th Annual Symposium on Foundations of Computer Science.* IEEE Computer Society Press., 1994, (Cited on page 2.)

[Siegman 86] A. E. Siegman. Lasers. University Science Books, 1986. ISBN: 978-0-9357-0211-8. (Cited on page 9.)

[Spence 91] D. E. Spence, P. N. Kean & W. Sibbett. *60-fsec pulse generation from a self-mode-locked Ti:sapphire laser.* Optics Letter, vol. 16, no. 1, pages pp42–44, 1991, (Cited on page 34.)

[Strogatz 01] SH. Strogatz. Nonlinear dynamics and chaos: With applications to physics, biology, chemistry and engineering. Westview Press, 2001. ISBN: 978-0-7382-0453-6. (Cited on page 110.)

[Thiel 15] V. Thiel. *Modal analysis of an ultrafast frequency comb: From classical to quantum spectra correlations.* PhD thesis, Sorbonne Université, 2015. (Cited on pages 12 and 14.)

[Tranter 18] A. D. Tranter, H. J. Slatyer, M.R. Hush, A. C. Leung, J. L.Everett, K. V. Paul, P. Vernaz-Gris, P. K. Lam, B. C. Buchler & G. T. Campbell. *Multiparameter optimisation of a magneto-optical trap using deep learning.* Nature Communication, vol. 9, no. 4360, 2018, (Cited on page 98.)

[Travers 69] J. Travers & S. Milgram. *An Experimental Study of the Small World Problem.* Sociometry, vol. 32, 1969, (Cited on page 114.)

[Ugander 11] J. Ugander, B. Karrer, L. Backstrom & C. Marlow. *The Anatomy of the Facebook Social Graph.* ArXiv:1111.4503, 2011, (Cited on page 114.)

[Vasile 11] R. Vasile, S. Maniscalco, M. G. A. Paris, HP. Breuer & J. Piilo. *Quantifying non-Markovianity of continuous-variable Gaussian dynamical maps.* Phys. Rev. A., vol. 84, no. 052118, 2011, (Cited on pages 143 and 144.)

[Vasile 14] R. Vasile, F. Galve & R. Zambrini. *Spectral origin of non-Markovian open-system dynamics: A finite harmonic model without approximations.* Phys. Rev. A, vol. 89, no. 022109, 2014, (Cited on page 110.)

[Verstraete 09] F. Verstraete, M.M. Wolf & J. I. Cirac. *Quantum computation and quantum-state engineering driven by dissipation.* Nature Phys, vol. 5, no. 633, 2009, (Cited on pages 3 and 109.)

[Walls 83] D. F. Walls. *Squeezed states of light.* Nature, vol. 306, 1983, (Cited on pages 2 and 25.)

[Walschaers 21a] M. Walschaers. *Non-Gaussian Quantum States and Where to Find Them.* PRX Quantum, vol. 2, no. 030204, 2021, (Cited on pages 2 and 22.)

[Walschaers 21b] M. Walschaers, N. Treps, B. Sundar, L. D. Carr & V. Parigi. *Emergent complex quantum networks in continuous-variables non-Gaussian states.* arXiv:2012.15608., 2021, (Cited on page 158.)

[Wangsness 53] R. K. Wangsness & F. Bloch. *The dynamical theory of nuclear induction.* Phys. Rev., vol. 89, no. 728, 1953, (Cited on page 140.)

[Watts 98] D. J. Watts & S. H. Strogatz. *Collective dynamics of "small-world" networks.* Nature, vol. 393, 1998, (Cited on page 114.)

[Weedbrook 12] C. Weedbrook, S. Pirandola, R. Garcia-Patròn, N. Ceerf, T. C. Ralph, J. H. Shapiro & S. Lloyd. *Gaussian quantum information.* Rev. Mod. Phys., vol. 84, no. 621, 2012, (Cited on page 2.)

[Weiner 00] A. M. Weiner. *Femtosecond pulse shaping using spatial light modulators.* Review of Scientific Instruments, vol. 71, 2000, (Cited on page 71.)

[Weiner 11] A. M. Weiner. *Ultrafast optical pulse shaping: A tutorial review.* Optics Communications, vol. 284, 2011, (Cited on page 64.)

[Weiss 12] U. Weiss. Quantum dissipative systems. World Scientific, 2012. ISBN: 978-981-4374-91-0. (Cited on pages 108, 109, 110, and 117.)

[Wigner 32] E. P. Wigner. *On the quantum correction for thermodynamic equilibrium.* Phys. Rev., vol. 40, no. 5, pages 749–759, 1932, (Cited on page 22.)

[Williamson 36] J. Williamson. *On the algebraic problem concerning the normal forms of linear dynamical systems.* American journal of mathematics, vol. 58, 1936, (Cited on page 85.)

[Wissmann 12] S. Wissmann, A. Karlsson, EM. Laine, J. Piilo & HP. Breuer. *Optimal state pairs for non-Markovian quantum dynamics.* Phys. Rev. A, vol. 86, no. 062108, 2012, (Cited on page 145.)

[Wu 87] L-A. Wu, M. Xiao & H.J. Kimble. *Squeezed states of light from an optical parametric oscillator.* JOSA B, vol. 4, no. 10, 1987, (Cited on page 2.)

[Yokoyama 13] S. Yokoyama, R. Ukai, S. C. Armstrong, C. Sorphiphatphong, T. Kaji, S. Suzuki, H. Yonezawa J-I. Yoshikawa, N. C. Menicucci & A. Furusawa. *Ultra-large-scale continuous-variable cluster states multiplexed in the time domain.* Nature Photonics, vol. 7, 2013, (Cited on page 2.)

[You 05] JQ. You & F. Nori. *Superconducting circuits and quantum information.* arXiv:quant-ph/0601121, 2005, (Cited on page 2.)

[Yuen 83] H. P. Yuen & W. S. Chan. *Noise in homodyne and heterodyne detection.* Optics letters, vol. 8, 1983, (Cited on page 56.)